No 1

Volume 10

June, 2026

MINISTRY OF SCIENCE AND EDUCATION OF THE REPUBLIC OF AZERBAIJAN

TRANSACTIONS

OF THE INSTITUTE OF MOLECULAR BIOLOGY AND BIOTECHNOLOGIES

TRANSACTIONS OF THE INSTITUTE
OF MOLECULAR BIOLOGY & BIOTECHNOLOGIES
PUBLISHER: INSTITUTE OF MOLECULAR BIOLOGY
MINISTRY OF SCIENCE AND EDUCATION OF THE REPUBLIC OF AZERBAIJAN

2026 Volume X No 1

The journal has published according to the decision of the Scientific Council of the Institute of Molecular Biology & Biotechnologies, ANAS on May 19, 2017 (protocol No 2). The journal was registered by the decision of the Ministry of Justice of the Republic of Azerbaijan No 4282 of January 10, 2020.

ISSN: 2709-0744 - Print | 2709-0752 - Online
Publisher: Institute of Molecular Biology, Ministry of Science and Education of the Republic of Azerbaijan
11, Izzat Nabiyev Str., AZ 1073, Baku, Azerbaijan
E-mail: timbb@imbb.science.az

The human large-conductance, calcium-activated potassium channel covers cell resistance to oxidative damage

Fidan Gudratova[1], Nicoletta Savalli[2], Enrique Balderas[3], Sevda Mahmudova[1], Aysel Aliyeva[1], Gunay Aliyeva[1], Taleh Yusifov[1*]

[1]Institute of Molecular Biology, Ministry of Science and Education of the Republic of Azerbaijan, 117 Academician Zahid Khalilov Str., AZ1141, Baku, Azerbaijan
[2]Department of Anesthesiology, Division of Molecular Medicine, David Geffen School of Medicine, University of California, CA 90095-7115, Los Angeles, USA
[3]CVRTI, University of Utah, 95 S 2000 E., UT 84112, Salt Lake City, USA

[*]***For correspondence:*** *tjussifo@ucla.edu, talehy671@gmail.com*

Received: April 01, 2026; Reviewed: May 21, 2026; Accepted: June 01, 2026

Our recent studies have identified a novel module in the BK channel reminiscent of the cytochrome c domains of hemoproteins. This feature may explain the distinctive physiological functions of these widespread ion channels. To further elucidate the structural and functional implications, we investigated how BK channel activity responds to reactive oxygen species (ROS), with a particular focus on hydrogen peroxide (H_2O_2). We demonstrated that the human BK channel possesses enzymatic activity that efficiently cleaves H_2O_2. To elucidate this novel catalytic activity in a physiological context, we are conducting experiments using a biochemical assay of the human BK channel and studies in human embryonic kidney (HEK293) cell lines. Our experiments using ABTS and Amplex Red assay showed that the C-terminal protein, isolated from the soluble and incorporated fractions, catalyzes H_2O_2 cleavage unless heme is added, at which point the protein exhibits catalytic activity. Our experiments using the intact human BK channel revealed a significant protective effect of wild-type BK channels against oxidative stress by enhancing HEK cell tolerance to (H_2O_2): at 200 µM H_2O_2, 37%±6% of cells expressing only YFP survived. In contrast, 60%±4% of HEK cells expressing wild-type BK channels were viable. However, a mutant with a disrupted heme-binding site (*C615S/H616R*) did not provide protection. We demonstrated that the BK channel exhibits modulatory activity at the H_2O_2 level. Most importantly, this novel enzymatic activity of BK likely has physiological significance: non-conducting BK channels with intact heme-binding properties enhance cell survival against oxidative stress.

Keywords: *MaxiK, Slo1, heme regulatory motif, electronic absorption spectroscopy, heme sensor, ABTS oxidation, oxidative stress, ROS*

INTRODUCTION

Human BK channels provide a fundamental physiological mechanism whose activity modulates numerous biological signaling molecules, including heme (Hoshi et al., 2013; Pantazis & Olcese, 2016; Echeverría et al., 2024; Cui, 2021; Sancho & Kyle, 2021). The opening probability of BK channels (Slo1) is tightly regulated by heme, which binds to their intracellular C-terminal domain (Tang et al., 2003; Horrigan et al., 2005; Walewska et al., 2022; Toro et al., 2016; Yusifov et al., 2025). Heme is essential for numerous physiological processes in living organisms (Yusifov et al., 2025; Soladogun & Zhang, 2024; Dutt et al., 2022; Coletta et al., 2024), partly by modulating ion channel activity. Despite its importance, the mechanisms by which heme regulates these channels remain poorly understood (Wang et al., 2009; Burton et al., 2016; Sahoo et al., 2013; Coburger et al., 2020; Burton et al., 2020; Sahoo et al., 2022). We discovered that the gate ring region of the human BK channel, including the heme-binding site, shares structural homology with cytochrome c (CytC), a well-known multifunctional hemoprotein Figure 1 (Yusifov et al., 2026; Gudratova et al., 2026).

In addition to its role in electron transport, cytochrome c (CytC) exhibits diverse catalytic activities, including peroxidase activity, the oxidation of suitable substrates using peroxides (Kagan et al., 2005; Belikova et al., 2006a; Belikova et al., 2007; Bertini et al., 2006). The heme moiety can bind to a region of the BK channel that adopts a cytochrome c-like fold; this

binding likely drives a conformational transition from a disordered to an ordered state. These structural changes in the "gate ring" region appear to mediate the heme-dependent modulation of BK channel activity (Yusifov et al., 2025). The identification of a novel heme-sensitive site resembling cytochrome c (Cytcl) suggests that it may regulate BK channel activity through similar mechanisms (Kagan et al., 2005; Belikova et al., 2006; Bertini et al., 2006; Belikova et al., 2007). However, further research is required to elucidate the physiological role and consequences of this enzymatic activity. Recent biochemical studies proposed a role for BK channels in cell protection (Yusifov et al., 2026; Gudratova et al., 2026). Accordingly, we tested whether BK channels in HEK293 cells serve not only as a cytosolic domain for ligand binding but also as functional ion-conducting channels with specific consequences. Our data indicate that BK channels promote cell survival in the presence of H_2O_2, pointing to a novel physiological role for these channels in protecting cells against oxidative damage.

MATERIALS AND METHODS

In the experiments, Tris-HCl, EDTA, and ABTS (2,2'-azino-bis-(3-ethylbenzothiazoline-6-sulfonate) (Sigma-Aldrich, USA), ultra-pure urea (MP Biomedicals), MOPS (MP Biomedicals), AmplexRed. acrylamide, and imidazole (Thermo Fisher Scientific). All enzymes and buffers for DNA manipulations were obtained from New England Biolabs (USA). PCR purification kit and nickel-nitrilotriacetic acid-agarose column (Qiagen, Valencia, CA).

Preparation of heme solution. Heme stock solutions (4 mM) were freshly prepared in DMSO for the experiment. The heme concentrations in the stock solutions were determined spectrophotometrically using the heme molar extinction coefficient of 170,000 M^{-1} cm^{-1} at λ max 404nm (Javaherian et al., 2011).

Cloning, construction of the recombinant plasmid, and mutagenesis: cDNA for the C-terminus of the human BK (^{322}IIE⋯ALK^{1005}) was amplified by PCR using specific primers. To ensure correct orientation at the vector's multiple cloning sites, the forward primer incorporated a BamHI restriction enzyme site. In contrast, the reverse primer incorporated a HindIII site. Amplification of the DNA was achieved in a 25 µl reaction mixture using 30 cycles of denaturation at 94°C for 10 seconds, annealing at 57°C for 10 seconds, extension at 72°C for 90 seconds, and a final extension at 72°C for 10 minutes. The PCR products were recovered from the gel and purified using the PCR purification kit (Qiagen). The human BK channel constructs with mutant C615S/H616R genes were obtained by using Quick Change site-directed mutagenesis (Stratagene). The point mutations were confirmed by the determination of DNA sequences.

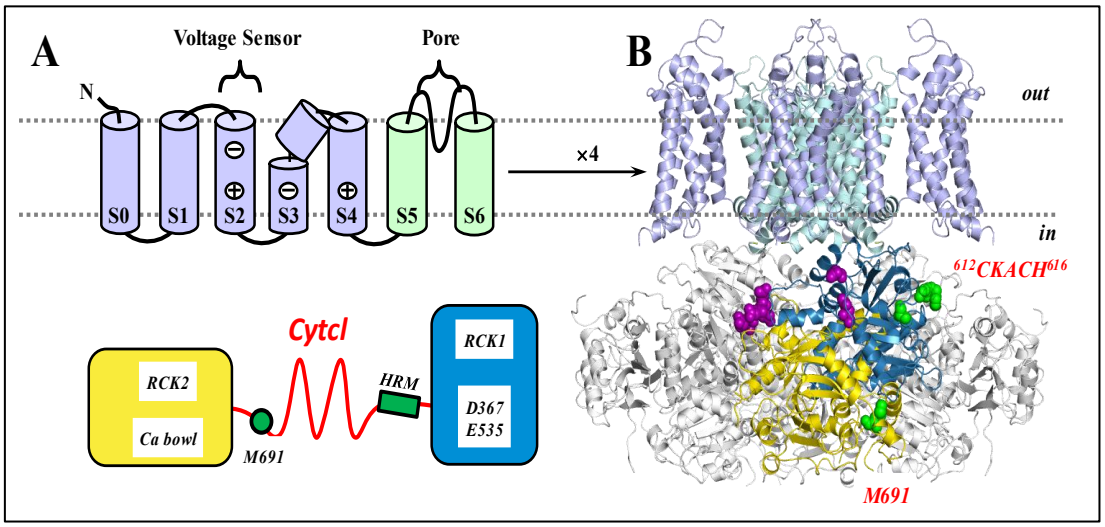

Fig. 1. BK channel topology and 3D structure, and the conservation of functionally important residues. **(A),** Membrane topology of a single BK α subunit. The intracellular C terminus is located below the transmembrane voltage-sensing domain (VSD) and ion-conducting (pore) region and consists of the Ca^{2+}-sensing RCK1 and RCK2 domains, which flank the Cytochrome c-like (Cytcl) domain with a conserved heme-regulatory motif (HRM, ^{612}CKACH^{616}) and M691. RCK1 possesses Ca^{2+}-sensing residues D367 and E535, while RCK2 encompasses the Ca bowl (^{894}DDDDD^{898}); **(B),** BK channels are homotetramers. Side view of a BK channel 3D structure.

Expression and purification of the C-terminus of the human BK from *E. coli*: M15(pREP4) bacterial cells were transformed with the pQE30 plasmid. Protein expression was induced by 1 mM isopropyl-β-D-thiogalactopyranoside (IPTG). Cells carrying the pQE-30-Cytcl plasmid were cultured at 37°C in 1 liter of Luria-Bertani (LB) medium containing 100 mg/ml ampicillin. When the optical density (at 600nm) reached 0.5, 1mM IPTG was added to induce the C-terminus of the human BK expression. The cells were incubated for an additional 1 h at 28°C and then harvested by centrifugation.

The collected cells were lysed by sonication. The supernatant was loaded onto a 5-ml nickel-nitrilotriacetic acid-agarose column (Qiagen, Valencia, CA), which was extensively washed with Tris buffer (25 mM Tris-HCl, 150 mM KCl, pH7.5). The His6 tag-C-terminus of the human BK fusion protein was then eluted with elution buffer (25 mM Tris-HCl, 150 mM KCl, 80 mM imidazole, pH 7.5), according to the manufacturer's instructions. We also purified CT protein from inclusion bodies as described previously by solubilizing them in 100 mM NaH_2PO4, 10 mM Tris·HCl, 8 M Urea (pH 8.0) containing 1 mg/ml lysozyme (Javaherian et al., 2011). The purity of the expressed proteins was analyzed using a 12.5% SDS-PAGE (Fig.2A). Protein concentrations were determined using the Biuret-Lowry assay.

Absorption spectroscopy. UV/Vis electronic absorption spectrometer measured on a Shimadzu UV-2700 UV-VIS spectrophotometer in a quartz cuvette of 1cm path length. The measurements were performed in the range of 240–600 nm in Tris buffer mM (150 KCl, 25 Tris, and 2 EDTA, pH 7.5).

ABTS assay. The peroxidase activity of the BK channel CT proteins purified from solubles and inclusion bodies was investigated using a colorimetric assay with 2,2′-azino-bis(3-ethylbenzothiazoline-6-sulfonate) (ABTS) as the electron donor. Reduced ABTS has a characteristic peak at 340 nm; when the peroxidase-catalyzed reduction of H_2O_2 to water is coupled to the oxidation of ABTS, an absorbance peak at 415 nm is formed. The reaction mixture (100 µL in a quartz cuvette) contained 20-50 µM ABTS, 10-500 µM H_2O_2, and 0.1–2 µM CT proteins.

Amplex RED assay. The stock solution of Amplex Red was prepared in analytically pure DMSO; the stock solution was diluted in 50 mM Tris–HCl buffer, pH 7.4. Amplex Red at 10 mM was incubated with 2 mM H_2O_2 and soluble fraction (CTsol) or from the inclusion body (CTin) (2µM) in 50 mM Tris, pH 7.4, at room temperature for 5 min, then diluted threefold before measurement. The emission spectra of Amplex Red and its oxidation product, resorufin, were measured by recording the fluorescence emission intensity at 580 nm (with an excitation wavelength of 500nm).

Cell viability assay. HEK293 cells (ATCC CRL-1573; kindly provided by Dr. Liqia Toro, UCLA) were transfected with either YFP alone or WT or C615S/H161R mutant BK channel constructs fused to YFP at the C-terminus using Lipofectamine 2000. Cells were grown in the presence of the specific BK channel blocker 1 µM paxilline (PAX) (Giangiacomo et al., 1992). After 72 h, collected cells were lysed in a buffer (50 mM Tris HCl, 2 mM EDTA, pH 7.4) in the presence of a protease inhibitor cocktail (Roche) and 1 mM PMFS using sonication (5–10 s) and then centrifuged at 3000× g for 5 min to clarify the lysates. The expression level of channel proteins was evaluated using the fluorescence intensity of the YFP signal (λext 500 nm/λem 527 nm). Protein concentration was measured using the DC protein assay kit (Bio-Rad Laboratories, Hercules, CA, USA). After 48h, cells were seeded in triplicate in a 96-well plate and, after 10h, treated with different concentrations of H_2O_2 (0-500 µM) in the presence of 100nM Iberiotoxin. Cell viability was tested after 16h using the MTT (3-(4, 5-dimethylthiazolyl-2)-2, 5-diphenyltetrazolium bromide) assay. The MTT salt is reduced by metabolically active cells, generating formazan that is solubilized and quantified by spectrophotometry (λ=570 nm) to estimate cell proliferation. Background absorbance of the medium alone was subtracted from the absorbance of wells containing cells at the corresponding (H_2O_2) and normalized to no-H_2O_2 absorbance values (100% viability).

Statistical analysis. Data are presented as mean±S.E.M, n≥6. Statistical comparisons were made using one-way ANOVA with Tukey's posttest (SPSS Windows software, Rel. 11.0). Statistical significance was assumed at $P < 0.05$ and indicated by asterisks in the figures.

RESULTS

The C-terminal (CT) protein of the human BK channel modulates the levels of reactive oxygen species (ROS), such as H_2O_2.

a) ABTS assay. The C-terminal (CT) sequence of the human BK channel protein ($^{322}IIE\ ALK^{1005}$), corresponding to >60% of the total channel, was cloned into a bacterial protein expression vector and obtained in high yield and purity from the soluble fraction, as described in Materials and Methods. After purification, the CT protein migrated as a single band corresponding to the expected mass (≈78 kDa), as shown in Fig. 2A.

This is very similar to the characteristics of the CT protein purified from CT protein inclusions (Belikova et al., 2007). However, the BK channel protein purified from the soluble fraction (CTsol) exhibits distinct characteristics from that purified from inclusions (CTin). We found that CT proteins have activity that modulates H_2O_2 levels by degrading in the absence of heme, but the CTin protein for similar activity requires the presence of heme.

The results of these experiments are shown in Fig. 2C, D. We performed a peroxidase reaction using the ABTS assay in the presence of CTsol and CTin proteins. As shown in Fig. 2D, CT sol oxidizes ABTS in the absence of heme, indicating its own heme. In contrast, the protein CTin isolated in inclusion bodies exhibits no peroxidase activity unless heme is added, after which the protein exhibits catalytic activity. This is likely because CTsol forms a protein-heme complex, in which the CTin protein does not exhibit the characteristic band at 41nm for heme (Fig. 2B).

The C-terminal (CT) protein of the human BK channel modulates the levels of reactive oxygen species (ROS), such as H_2O_2.

b) Amplex Red assay. To assess the activity of human BK channel proteins degraded in H_2O_2, we assessed peroxidase activity using the Amplex Red assay, which measures resorufin fluorescence upon oxidation of Amplex Red. Amplex Red is a colorless substrate that reacts with hydrogen peroxide (H_2O_2) to form highly fluorescent resorufin (excitation at 530 nm, emission maximum at approximately 580 nm) in the presence of peroxidases (Fig. 3A, B). The fluorescence intensity of resorufin formed in CTsol proteins was compared with the fluorescence intensity in CTin protein samples (Fig. C, D). This experiment showed high resorufin fluorescence intensity in CTsol protein samples compared to CTin proteins (Fig. 3E). These data demonstrated that the human BK channel protein CTsol can form resorufin by degradation in H_2O_2, similar to the results of previous experiments using the ABTS assay.

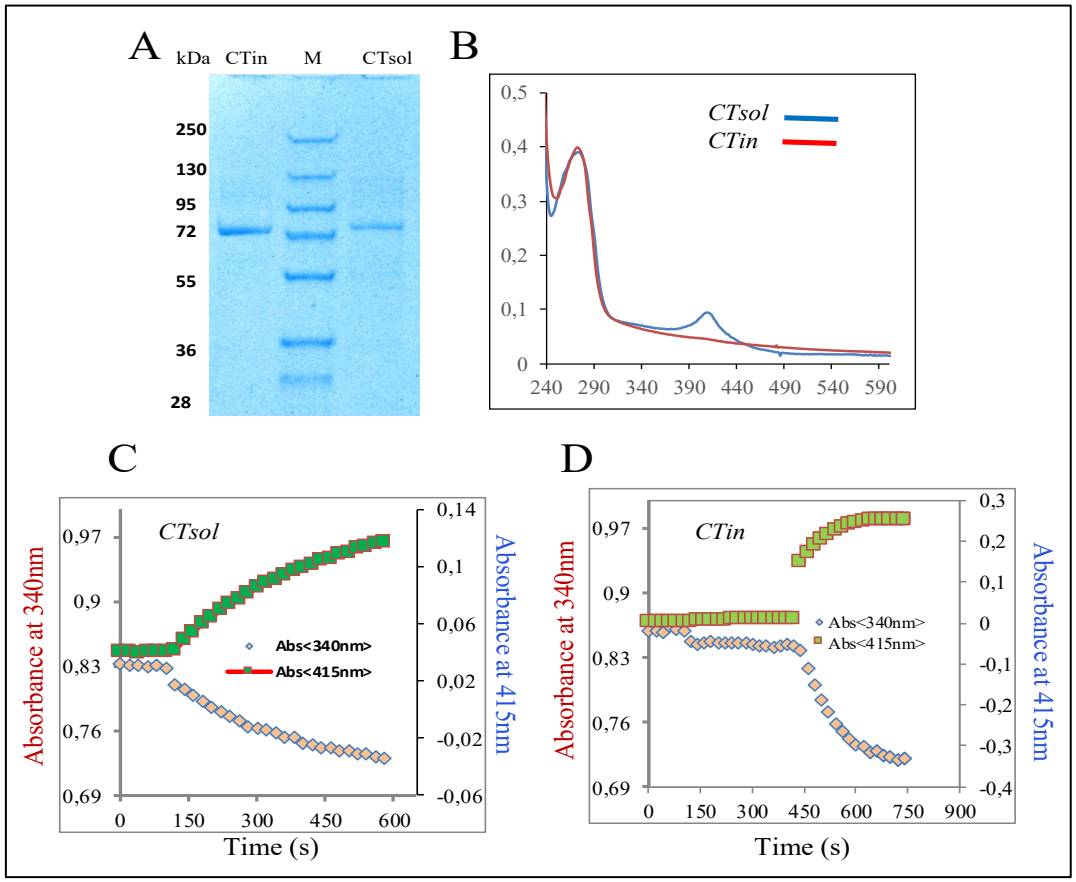

Fig. 2. **(A),** 10% SDS-PAGE of the purified GR from the inclusion fraction (CTin, 10µg) and soluble fraction. (CTsol, 5 µg) shows a single band of ~72 kDa **(B),** Electronic absorption spectra of purified CT from the soluble fraction (CTsol) and inclusion fraction (CTin). In the spectrum of CT, a band is observed near 412 nm (Soret band) that is characteristic of heme binding to proteins. However, this feature is absent in GRin. **(C),** Time course of ABTS oxidation in the presence of the CTsol (0.1 µM; 0–150 s), at 150 after the addition of H_2O_2 (500 µM, 150-600 s). **(D),** Time course of ABTS oxidation in the presence of the CTin (0.1 µM; 0–150 s), at 150 after the addition of H_2O_2 (500 µM, 150-300 s), and heme at 300 (2 µM 300-600 s).

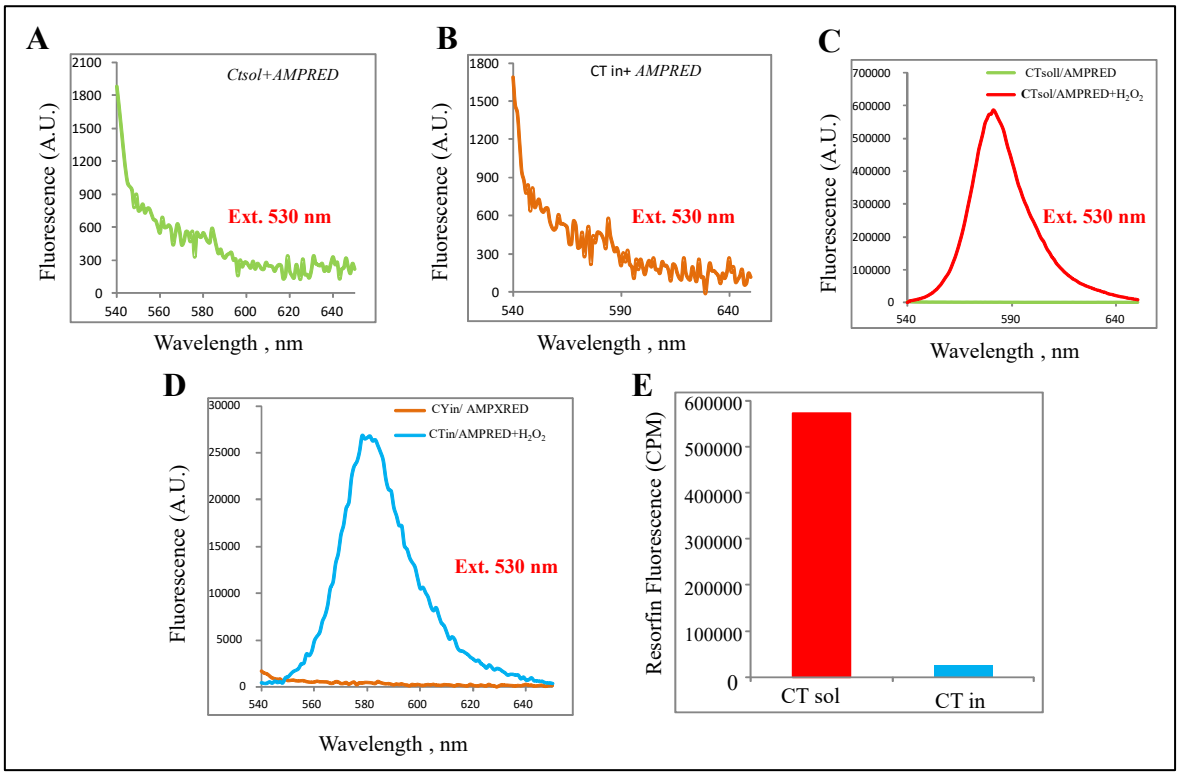

Fig. 3. (A) and **(B),** Emission spectra (with an excitation wavelength of 500nm). of Amplex Red solutions in the presence of CTsol and CTin the absence of H_2O_2, respectively. **(C)** and **(D),** Emission spectra of Amplex Red solutions in the presence of GR sol and CTin in the presence of H_2O_2, respectively. The addition of H_2O_2 led to the formation of fluorescence intensity at 580 nm, indicating the formation of Amplex Red oxidation product resorufin **(E)**, In the CTsol solution, unlike with CTin incorporated into the protein, the significant increase in emission intensity indicates the formation of resorufin, demonstrating that the CTsol protein exhibits peroxidase activity by decomposing H_2O_2.

Expression of the entire human BK channel protein in HEK293 cells

To evaluate the physiological relevance of CT protein activity on H_2O_2, HEK293 cells were transfected with yellow fluorescent protein (YFP) or YFP was fused to the C-terminus of human BK channel constructs (Fig. 4A-F). YFP fluorescence signal fused to the BK channel proteins allows the expression level with the emission peak at 527 nm to be quantified, at an excitation of 500 nm. To determine the concentrations of expressed YFP, as well as YFP fused to the BK proteins in HEK lysates, we utilized the fluorescence emission intensity of YFP at 527 nm (with an excitation wavelength of 500 nm). After measuring the total protein concentration in the HEK cell lysates, we used the emission intensity at 527 nm to standardize for the equal amount of expressed YFP, YFP fused to BK WT, and BK C615S/H616R proteins in the MTT assay.

The human BK Channel proteins increase cell survivability against oxidative stress

To evaluate the non-conducting properties (enzymatic activity) of the full BK channel in a cellular environment, we expressed the channel-forming α subunit of the human BK channel in tandem with YFP in HEK-293 cells and assessed cell viability under increasing oxidative stress (H_2O_2 0-500 µM). Cell viability was evaluated with the MTT assay, which measures the cell proliferation rate or, conversely, the reduction in cell viability when metabolic events lead to apoptosis or necrosis. The potency of H_2O_2 to induce cell death in BK-transfected cells was compared to that in cells expressing YFP alone and cells transfected with a BK HRM mutant with impaired heme binding ability (C615S/H616R). To pharmacologically eliminate the ion-conducting properties of the channels and restrict the investigation to the enzymatic activity of the gating ring, the cell medium was supplemented with 100nM Iberiotoxin, a highly selective and potent BK channel blocker with an effective K_d of ~1nM (Giangiacomo et al., 1992). Thus, the BK channel conductance was fully blocked, while native ionic conductances were unperturbed.

This experiment (Fig. 5) revealed a significant protective effect of BK channels against oxidative stress, increasing the tolerance of HEK cells to H_2O_2. E.g., with 200 µM H_2O_2, 37%±6% of the cells expressing only YFP survived (n=9), while 60%±4% (n=9) of HEK cells expressing WT BK channels were viable. While wild-type BK channels

endow resistance to H_2O_2 insult, a mutant with an impaired heme-binding site failed to confer protection: no statistical difference could be measured for the viability of cells transfected with YFP alone versus mutant BK.

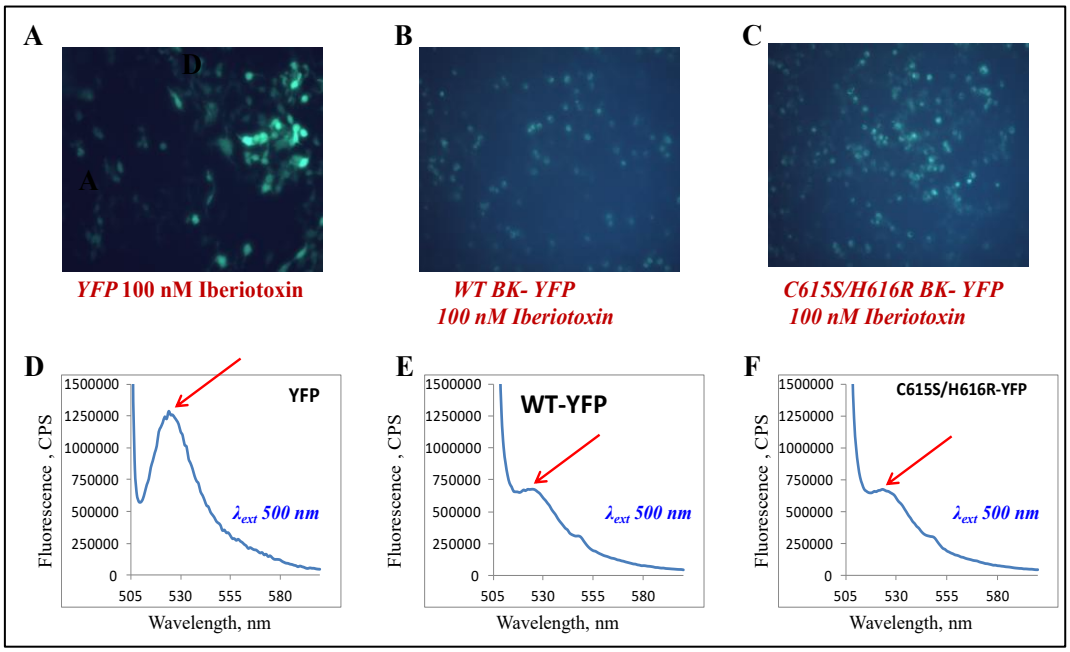

Fig. 4. Expression of the human BK channel in HEK293 cells. Lanes**, A-C** HEK293 cells transfected with WT BK-YFP, and C615S/H616R BK-YFP, YFP alone (control), respectively. Lanes**, D-F** Fluorescence spectra of the HEK293 cells lysates, which expressed with YFP alone **(D),** WT BK-YFP **(E)**, and C615S/H616R BK-YFP **(F)**. The expression level of channel proteins was assessed using the fluorescence intensity of the YFP signal, which revealed an emission peak at 527 (λem 527 nm) and excitation at 500 nm (λext 500 nm).

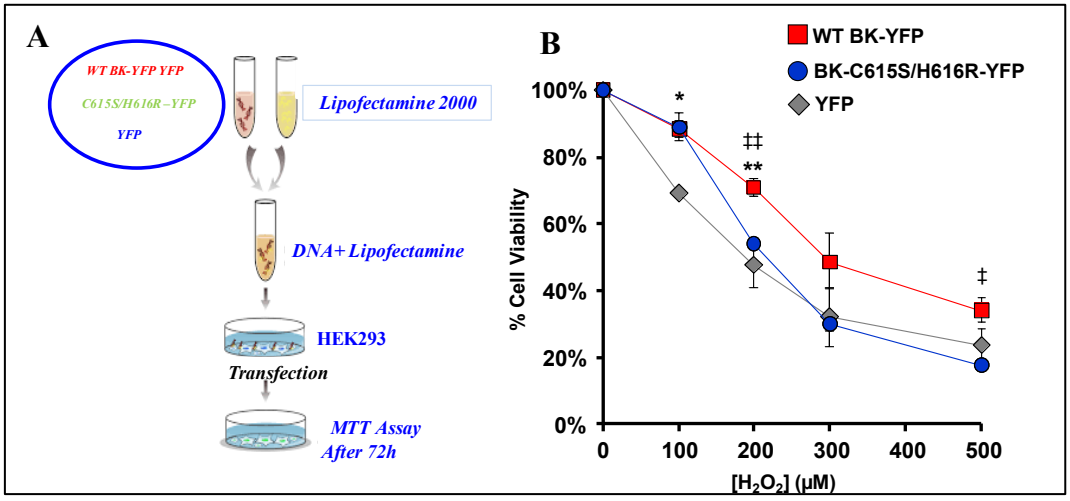

Fig. 5. BK channels with an intact heme regulatory motif protect cells from oxidative stress. (A), Cell viability of HEK-293 cells transiently transfected with BK-YFP channels (WT or BK-C615S/H616R, heme-binding mutant) or YFP alone was determined by MTT assay after 16 h incubation with various H_2O_2 concentrations in the presence of 100 nM Iberiotoxin to fully and selectively block BK ion conduction. **(B),** The statistical analysis was performed using one-way ANOVA with Tukey's post-test, comparing data from cells transfected with YFP alone (n=6) and cells expressing either BK-WT (n=6) or BK-C615S/H616R (n=6). Statistical significance ($p<0.05$) is indicated by the symbols above data points (∗, for comparison between cells with BK WT ■ and control cells ♦; ‡, for comparison between BK WT ■ and BK-C615S/H616R mutant ●). The viability of cells with BK-C615S/H616R was not significantly different from that of cells with YFP alone (except at 100μM). Error bars are SEM (bars not visible are within the symbols).

These results support the hypothesis that heme bound by BK channels, and their associated enzymatic activities, play a key role in protection from H_2O_2-induced cell death. Also, these results are in agreement with the data from our biochemical work that show significantly reduced peroxidase activity of the CT proteins carrying the C615S/H616R HRM mutations (Javaherian et al., 2011; Yusifov et al., 2025; Gudratova et al., 2025).

DISCUSSION

Human BK channels provide multifunctional molecular machinery

The discovery of novel enzymatic properties in these channels reinforces the view that ion channels are more than just proteins that facilitate ion transport and paves the way for attributing new physiological functions to these ubiquitously expressed channels. Channel-enzymes constitute a class of ion channels possessing enzymatic activity that is directly or indirectly linked to their channel function. Channel-enzymes (co-enzymes) form a unique group of ion channels that combine two key biological functions within a single polypeptide chain: ion permeability and enzymatic activity. Our discovery that the human BK channel exhibits peroxidase-like activity and degrades reactive oxygen species (ROS), hydrogen peroxide (H_2O_2) has led to its classification as a new member of the co-enzyme family (Huang et al., 2024). Thus, the coupling of electrical activity with functions unrelated to ion transport underlies the mechanism of the BK channel's functional versatility within the organism. The results of this study reveal new functions—distinct from those previously known (such as ion conductance and enzymatic activity) that characterize the multifunctional nature of human BK channels. Multifunctional proteins (also referred to as proteins with "combined functions" or "moonlighting proteins") are defined as proteins capable of performing multiple, unrelated biochemical or biophysical functions within a single polypeptide chain, where these functions do not arise from gene fusion or alternative RNA splicing. Consequently, the BK channel represents one of the multifunctional components of cellular organization; Such components are viewed not merely as highly specialized, monofunctional agents, but as dynamic participants in cellular processes, endowed with multiple functions (Espinosa-Cantú et al., 2020). Multifunctional proteins can influence the evolution of organisms by contributing to increased complexity and resilience. For instance, in early life forms as well as in organisms undergoing genome reduction, multifunctionality enables the expansion of the functional repertoire of a limited gene set (Kelkar & Ochman, 2013). Furthermore, multifunctional proteins can coordinate the interplay between diverse biological processes, a capability particularly important for organisms with large genomes and complex metabolic and regulatory pathways (Flores & Gancedo, 2011). Identifying and studying such proteins is essential for a deeper understanding of living systems, both in health and disease. Indeed, multifunctional proteins often act as virulence factors and determine disease progression, generating significant interest in this subject.

Catalytic activity of human BK channels regarding H_2O_2 decomposition: a function extending beyond electrical signaling

The current research demonstrates the diverse physiological functions of BK channels and their involvement in the pathogenesis of a wide range of diseases, driven by interactions with numerous signaling molecules. To elucidate the molecular mechanisms by which biological modulators such as Ca^{2+} and heme regulate BK channel activity, we identified that BK channel confers peroxidase activity, catalyzing H_2O_2 decomposition. Our findings indicate that the BK channels protect cells against H_2O_2-induced oxidative damage specifically through the catalytic activity of the BK channel. Thus, their K^+ conductance prevents abnormal cellular excitability, while their enzymatic activity may protect against oxidative damage. This discovery lays the groundwork for identifying additional physiological functions of these ubiquitously expressed ion channels and for understanding the mechanisms underlying this new cytochrome c-like activity, which is likely linked to cellular metabolism. These results open new avenues for developing therapeutic strategies for diseases associated with BK channel dysfunction, such as cancer and cardiovascular disorders.

CONCLUSION

BK channels are nearly ubiquitous membrane proteins, whose exceptionally large conductance for potassium has earned them the designation “universal suppressor of cellular excitability”. BK channel conductance is regulated by numerous cytosolic signaling molecules, including Ca, Mg, and heme. The latter, usually associated with oxygen transfer and storage, inhibits BK channel opening. Intriguingly, BK channels sense heme by means of a heme regulation motif (HRM), usually encountered in an altogether different class of proteins: cytochrome c (CytC), which are normally involved with electron shuttling and exhibit

catalytic properties. We know very little about the molecular structure of the area immediately downstream of the HRM, but in this work, we present compelling evidence that it adopts a CytC-like structure in the presence of heme. Such a molecular transition not only explains the regulation of BK conductance by heme; it also confers CytC-like enzymatic properties, specifically the ability to break down hydrogen peroxide, a product of damaging free radicals. We characterized the novel catalytic ability of BK channels and also found that, when overexpressed, they can protect cultured cells from H_2O_2-induced death. Our work demonstrates that, in addition to protecting against overt electrical excitability, BK channels may confer resistance to deleterious metabolic byproducts by virtue of their newly identified CytC-like domain.

CREDIT AUTHORSHIP CONTRIBUTION STATEMENT

Taleh Yusifov: Conceptualization, Writing – review & editing; Fidan Gudratova: Data curation, Visualization, Software; Enrique Balderas Data curation; Nicoletta Savalli: Data curation, Formal analysis; Sevda Mahmudova: Visualization, Software; Aysel Aliyeva: Visualization; Gunay Aliyeva: Software

DECLARATION OF INTERESTS

The authors declare no competing interests.

FUNDING SOURCES

This research did not receive any specific grant from funding agencies in the public, commercial, or not-for-profit sectors.

DATA AVAILABILITY

Data will be made available on request.

ACKNOWLEDGMENTS

The authors would like to express their deep gratitude to Doctors of Biological Science Karim Gasimov and Professor Oktay Gasimov for their incredible support in conducting the study and for their contributions to the manuscript.

AI STATEMENT

AI-assisted tools were used only for language translation, grammatical editing, and reference formatting.

REFERENCES

Belikova N.A., Vladimirov Y.A., Osipov A.N., Kapralov A.A., Tyurin V.A., Potapovich M.V. et al. (2006) Peroxidase activity and structural transitions of cytochrome *c* bound to cardiolipin-containing membranes. *Biochemistry*, **45(15):** 4998-5009.

Belikova N.A., Jiang J., Tyurina Y.Y., Zhao Q., Epperly M.W., Greenberger J. et al. (2007) Cardiolipin-specific peroxidase reactions of cytochrome c in mitochondria during irradiation-induced apoptosis. *International Journal of Radiation Oncology, Biology, Physics*, **69(1):** 176–186.

Bertini I., Cavallaro G., Rosato A. (2006) Cytochrome *c*: Occurrence and functions. *Chem. Rev*., **106(1):** 90–115.

Burton M.J., Cresser-Brown J., Thomas M., Portolano N., Basran J., Freeman S.L. et al. (2020) Discovery of a heme-binding domain in a neuronal voltage-gated potassium channel. *Journal of Biological Chemistry*, **295(38):**13277–13286.

Burton M.J., Kapetanaki S.M., Chernova T., Jamieson A.G., Dorlet P., Santolini J. et al. (2016) A heme-binding domain controls regulation of ATP-dependent potassium channels. *Proceedings of the National Academy of Sciences USA*, **113(14):**3785–90.

Coburger I., Yang K., Bernert A., Wiesel E., Sahoo N., Swain S.M. et al. (2020) Impact of intracellular hemin on N-type inactivation of voltage-gated K^+ channels. *Pflugers Arch*., **472(5):** 551-560.

Coletta M., Bolognesi M., Ascenzi P. (2024) Heme is pivotal for life. *J. Inorg. Biochem*., **250:** 112423.

Cui J. (2021). BK Channel Gating Mechanisms: Progresses Toward a Better Understanding of Variants Linked Neurological Diseases. *Frontiers in physiology*, **12:** 762175.

Dutt S., Hamza I., Bartnikas T.B. (2022) Molecular mechanisms of iron and heme metabolism. *Annu. Rev. Nutr*., **42(1):**311–35.

Echeverría F., Gonzalez-Sanabria N., Alvarado-Sanchez R., Fernández M., Castillo K., Latorre R. (2024) Large conductance voltage-and calcium-activated K+ (BK) channel in health and disease. *Frontiers in pharmacology*, *15*, 1373507.

Espinosa-Cantú A., Cruz-Bonilla E., Noda-Garcia L., DeLuna A. (2020) Multiple forms of multifunctional proteins in health and disease. *Front. Cell Dev. Biol*., **8:** 451; doi: 10.3389/fcell.2020.00451.

Flores C.L., Gancedo C. (2011) Unraveling moonlighting functions with yeasts. *IUBMB Life*,

63(7):457-62. doi: 10.1002/iub.454.

Giangiacomo K.M., Garcia M.L., McManus O.B. (1992) Mechanism of iberiotoxin block of the large-conductance calcium-activated potassium channel from bovine aortic smooth muscle. *Biochemistry*, **31(29):** 6719.

Gudratova F., Aliyeva A., Mahmudova S., Gasimov K., Yusifov T. (2025) ABTS oxidation reaction as a model of cytochrome c-driven electron transfer. *The Ukrainian Biochemical Journal*, **97(4):** 43-51.

Gudratova F., Savalli N., Aliyeva A., ...Yusifov T. (2026). Heme signaling through the cytochrome c-like domain of the human BK channel. *Biochimica et Biophysica Acta, Biomembranes*, **1868(3):** 184533; doi: 10.1016/j.bbamem.2026.184533

Horrigan F.T., Heinemann S.H., Hoshi T. (2005) Heme regulates allosteric activation of the Slo1 BK channel. *J. Gen. Physiol*., **126(1):** 7–21.

Hoshi T., Heinemann S.H. (2016). Modulation of BK channels by small endogenous molecules & pharmaceutical channel openers. *International review of neurobiology*, **128:** 193–237.

Hoshi T., Pantazis A., Olcese R. (2013) Transduction of voltage and Ca^{2+} signals by Slo1 BK channels. *Physiology*, **28(3):** 172–89.

Huang Y., Kumar S., Lee J., Lu W., Du J. (2024) Coupling enzymatic activity and gating in an ancient TRPM chanzyme and its molecular evolution. *Nat. Struct. Mol. Biol*., **31(10):**1509-1521; doi: 10.1038/s41594-024-01316-4.

Javaherian A.D., Yusifov T., Pantazis A., Franklin S., Gandhi C.S., Olcese R. (2011) Metal-driven operation of the human large-conductance voltage- and Ca^{2+}-dependent potassium channel (BK) gating ring apparatus. *J. Biol. Chem*., **286(23):**20701-20709; doi: 10.1074/jbc.M111.235234.

Kagan V.E., Tyurin V.A., Jiang J., Tyurina Y.Y., Ritov V.B., Amoscato A.A. et al. (2005) Cytochrome c acts as a cardiolipin oxygenase required for release of proapoptotic factors. *Nat. Chem. Biol*., **1(4):** 223–232.

Kelkar Y.D., Ochman H. (2013) Genome reduction promotes increase in protein functional complexity in bacteria. *Genetics*, **193(1):**303-307. doi: 10.1534/genetics.112.145656.

Pantazis, A., & Olcese, R. (2016). Biophysics of BK Channel Gating. *International Review of Neurobiology*, **128:** 1-49.

Sahoo N., Goradia N., Ohlenschläger O., Schönherr R., Friedrich M., Plass W. et al. (2013) Heme impairs the ball-and-chain inactivation of potassium channels. *Proceedings of the National Academy of Sciences of the United States of America*, *110*(42), E4036–E4044.

Sahoo N., Yang K., Coburger I., Bernert A., Swain S.M., Gessner G. et al. (2022) Intracellular hemin is a potent inhibitor of the voltage-gated potassium channel Kv10.1. *Sci. Rep*., **12(1):** 14645.

Sancho M., Kyle B.D., Sancho M., Kyle B.D. (2021). The Large-conductance, calcium-activated potassium channel: A big key regulator of cell physiology. *Frontiers in Physiology*, **12:** 750615.

Soladogun A.S., Zhang L. (2024) The neural palette of Heme: Altered Heme homeostasis underlies defective neurotransmission, increased oxidative stress, and disease pathogenesis. *Antioxidants*, **13(12):**1441.

Tang X.D., Xu R., Reynolds M.F., Garcia M.L., Heinemann S.H., Hoshi T. (2003) Haem can bind to and inhibit mammalian calcium-dependent Slo1 BK channels. *Nature*, **425(6957):** 531–535.

Walewska A., Szewczyk A., Koprowski P. (2022) External Hemin as an inhibitor of mitochondrial large-conductance calcium-activated potassium channel activity. *Int. J. Mol. Sci*., **23(21):**13391.

Wang S., Publicover S., Gu Y. (2009) An oxygen-sensitive mechanism in regulation of epithelial sodium channel. *Proceedings of the National Academy of Sciences USA*, **106(8):**2957–2962.

Yusifov T., Aliyeva A., Gudratova F., ... Aliyeva N. (2026) Ion channels and regulatory signals of heme. *European Journal of Biology*, **85(1):** 5765; doi: 10.26650/EurJBiol.2026.1756794

Yusifov T., Qudretova F., Aliyeva A. (2025) Cytochrome C-like domain within the human BK channel. *Int. J. Mol. Sci.*, **26(15):** 7053.

ORCIDs:

Fidan Qudretova: https://orcid.org/0009-0005-9597-5066
Nicoletta Savalli: https://orcid.org/0000-0001-7267-9655
Enrique Balderas: https://orcid.org/0000-0001-8780-9272
Sevda Mahmudova: https://orcid.org/0000-0001-8207-0544
Aysel Aliyeva: https://orcid.org/0009-0005-2826-0335
Gunay Aliyeva: https://orcid.org/0009-0002-1183-2593
Taleh Yusifov: https://orcid.org/0009-0002-8486-5695

Synthesis and characterization of magnetic Fe_3O_4/chitosan/ALA nanocomposite

Mahmut Yıldıztekin[1], Sultan Köşkeroğlu[1*], Mehmet Fırat Baran[2], Atilla Levent Tuna[3]

[1]Department of Herbal and Animal Production, Köyceğiz Vocational School, Mugla Sıtkı Kocman University, 48800, Köyceğiz, Muğla, Türkiye
[2]Department of Food Processing, Vocational School of Technical Science, 72060, Batman, Türkiye
[3]Department of Biology, Faculty of Science, Mugla Sıtkı Kocman University, 48000, Mugla, Türkiye

[*]***For correspondence:*** *skoskeroglu@mu.edu.tr*

Received: March 05, 2026; Reviewed: May 12, 2026; Accepted: May 25, 2026

Alpha-lipoic acid (ALA) is a naturally occurring antioxidant that has attracted considerable interest for its applications in nanobiotechnology, controlled drug delivery, and agricultural sciences. In the present study, a magnetic chitosan-coated liposomal nanocomposite incorporating ALA was synthesized and comprehensively characterized. Structural analyses demonstrated a spherical and well-dispersed morphology with an average crystallite size of 19.42 nm, as determined by X-ray diffraction. Elemental characterization confirmed the presence of Fe, C, O, and S, with iron accounting for 64% of the composition, while FT-IR analysis verified successful integration of the composite constituents through characteristic functional group interactions. The antioxidant properties of ALA are associated with its ability to suppress lipid peroxidation and reduce oxidative damage caused by reactive oxygen species. These effects are particularly relevant for plant systems, where oxidative balance directly influences growth, development, stress tolerance, and overall physiological performance. To enhance the stability, bioavailability, and targeted delivery of ALA, liposomal formulations were functionalized with magnetic iron oxide and chitosan, yielding a multifunctional nanocarrier platform. The developed ALA-conjugated nanocomposite exhibited favorable physicochemical properties, including improved stability, controlled morphology, and enhanced surface characteristics. Owing to the biocompatible nature of liposomal and chitosan-based systems, the synthesized material is expected to possess low toxicity while maintaining efficient delivery performance. This study highlights the potential of magnetic chitosan-coated liposomal nanoparticles as innovative carriers for ALA and provides a basis for future investigations into their biological activity, biocompatibility, and applications in plant-based and therapeutic delivery systems.

Keywords: *Magnetic Fe_3O_4/alpha-lipoic acid, chitosan, Spinacia oleracea, SEM-EDX, FTIR*

INTRODUCTION

In the evolving technological landscape, the synthesis of nanoparticles through various methodologies has emerged as a prominent field of research. This growing interest is driven by their unique properties in battery charge-discharge processes and energy storage, as well as their diverse applications, including drug delivery systems, environmental remediation (soil, air, and water), shelf-life extension of food products, and biosensors (Ertaş et al., 2025; Aslan et al., 2026; Priya et al., 2023). In recent years, incorporating natural bioactive compounds into the process has come to the fore to enhance the efficacy and biocompatibility of these nanomaterials. In this context, alpha-lipoic acid (ALA), frequently defined in the literature as the 'universal antioxidant', stands out as a natural redox compound widely distributed in flora and fauna. This molecule, which acts as a cofactor for critical enzyme complexes in mitochondrial bioenergetic processes, exists in cells in both oxidized and reduced (dihydrolipoic acid - DHLA) forms. Offering high antioxidant capacity through both of its chemical forms, the ALA/DHLA system not only neutralizes free radical damage but also restores the depleted endogenous antioxidant pool (Kagan et al., 1992; Han et al., 1997; Shay et al., 2009; Goraca et al., 2011). Capitalizing on these properties, recent research has focused on developing advanced drug delivery systems that leverage alternative antioxidant molecules conjugated with gold nanoparticle (AuNP)-ALA matrices to attenuate oxidative stress and repair cellular damage. Studies indicate that the deployment of such binary or ternary nanocomposites yields a powerful synergistic effect, significantly outperforming the therapeutic outcomes achieved by single-component administrations (Abdelkader et al., 2025). Alpha-lipoic acid (ALA) is a promising therapeutic candidate for addressing oxidative stress.

DOI: https://doi.org/10.62088/timbb/10.1.2

ALA is a potent, endogenous antioxidant and a necessary cofactor for mitochondrial enzymes. However, its therapeutic potential is constrained by physicochemical limitations, including instability, low bioavailability, and non-specific tissue distribution. To overcome these challenges, nanoparticle-based drug delivery systems offer an attractive solution. Such systems can enable targeted delivery while enhancing the stability and bioavailability of therapeutic compounds. Among various nanocarriers, chitosan has emerged as an excellent material due to its biocompatibility, biodegradability, and versatile formulation properties.

Furthermore, chitosan itself has demonstrated intrinsic antioxidant activity. To enable neuronal targeting, we functionalized chitosan nanoparticles with lipoic acid. Our goal in synthesizing this triple composite is to potentially increase the specificity and cellular uptake of the delivered therapeutic agent by leveraging the high expression of its receptors (Skibska et al 2015; Quitadamo et al., 2021; Bagheri et al., 2022; Singh et al., 2023; Kurul et al., 2025; Gheybi et al., 2026). Alpha-lipoic acid (ALA), also known as thioctic acid, is a dithiol-containing compound (Hahm et al., 2004; Smith et al., 2004; Sheikholeslami et al., 2021). Due to its potent antioxidant, hydroxyl radical scavenging, and anti-inflammatory properties, it is widely utilized in the treatment of various diseases and as a dietary supplement. However, ALA exhibits a short half-life and low bioavailability owing to its poor aqueous solubility and gastric instability; additionally, its in vitro stability is substantially limited. Lipids are crucial for maintaining physiological functions such as energy storage, membrane structure, and cell signaling. Studies have shown how metabolism regulates immune cell function and that cellular metabolism is a key regulator of immune function (Wientjens et al., 2026). Lipid metabolism, which involves the synthesis and breakdown of lipids, plays a vital role in cellular homeostasis, and research has highlighted its association with various pathological conditions. In recent years, research has emphasized lipids as key regulators of cellular function, particularly in immune cells. Lipid metabolism is known to influence immune responses, cell phenotypes, metabolic pathways, and cytokine levels (Li et al., 2026).

Consequently, various formulation strategies are being developed by researchers to enhance the bioavailability and improve the stability of ALA. Among these approaches, polymeric hybrid nanoparticles represent innovative core-shell nanocarrier systems in which a polymeric core is enveloped by a lipid bilayer. By merging the distinct advantages of liposomes and polymeric nanoparticles, these liposome-based nanostructures and nanocomposites offer critical merits, such as controllable particle size, facile surface modification, high encapsulation efficiency, biocompatibility, controlled drug release, and enhanced in vitro/in vivo stability. Nevertheless, the type and ratio of the lipids and polymers utilized, the fabrication method, and the corresponding process parameters (e.g., presence of crosslinkers, surfactant concentration, temperature, stirring speed, and active ingredient payload) can significantly influence the core physicochemical properties of these nanocarriers, including particle size, polydispersity index, zeta potential, and encapsulation efficiency (Salehi et al., 2021; Ye et al., 2021; Skibska et al., 2022; Çoban et al., 2025). To this end, the present study focuses on the biogenic synthesis of this novel core-shell/bimetallic nanocomposite, where its crystalline architecture, morphological features, surface chemistry, and structural stability were comprehensively elucidated through advanced spectroscopic characterization techniques.

MATERIALS AND METHODS

Iron (III) chloride hexahydrate ($FeCl_3 \cdot 6H_2O$), iron (II) chloride tetrahydrate ($FeCl_2 \cdot 4H_2O$), 3-chloro-1,2-epoxypropane (epichlorohydrin), ammonium hydroxide (NH4OH), sodium hydroxide (NaOH), chitosan, and α-Lipoic acid [5-(1,2-dithiolan-3-yl)pentanoic acid] used in this study were commercially available in analytical purity from Sigma-Aldrich and Merck.

Fe_3O_4 synthesis: The synthesis of magnetic (Fe_3O_4) nanoparticles was achieved by modifying the co-precipitation method described in the literature. Typically, 4.0 g of $FeCl_3 \cdot 6H_2O$ was dissolved in 125 mL of distilled water, then 4-5 drops of concentrated HCl were added to avoid hydrolysis, and the mixture was continuously stirred at 800 rpm and 80°C in a magnetic stirrer (in a N2 atmosphere). After approximately 25 minutes of stirring, a clear solution with a yellow tint was obtained. Then, 2.7 g of $FeCl_2 \cdot 4H_2O$ was added to this yellow solution and stirring continued for another 90 minutes. In addition, 5 mL of spinach (Spinacia oleracea) extract was added, and the mixture was stirred for another 30 minutes. After 45 minutes, 30 mL of 30% NH4OH solution was added to the reaction mixture, and stirring continued under these conditions for another 30 minutes. After stirring for 30 minutes, the reaction was stopped, and the precipitate was collected from the medium using a magnet and then washed 5 times with deionized (DI) water. After washing, the resulting product was dried under vacuum (Yadav et al, 2023; Cuana et al., 2022; Yusefi et al., 2021).

Fe_3O_4/chitosan synthesis: 0.25 g of the prepared Fe_3O_4 nanoparticles was dispersed in 50 mL of DI water in an ultrasonic bath at 50°C. Another solution was prepared by adding 250 mg of chitosan to 100 mL of acetic acid, and this solution was stirred continuously at 60°C. In addition, 250 µl of acetic acid was added to the chitosan solution and then stirred in an ultrasonic bath at 50°C for 30 minutes. In the next step, the chitosan solution was added dropwise to the Fe_3O_4 nanoparticle solution, which was kept at 40°C for stirring. Then, 250 µl of crosslinking agent epichlorohydrin (3-chloro-1,2-epoxypropane) was added to the mixture and stirring continued for 2 hours at 50°C. The prepared nanocomposite was then washed five times with successive distilled water. Finally, nanocomposites were collected and dried under vacuum to obtain chitosan-coated magnetic nanoparticles (chitosan@Fe_3O_4) (Tomke and Rathod, 2020; Istiqomah et al., 2024).

Synthesis of Fe_3O_4/chitosan/lipoic acid (LA): 500 mg of the prepared Fe_3O_4/chitosan nanoparticles were dispersed in 100 mL of deionized water in an ultrasonic bath at room temperature for 1 hour. After 1 hour, 100 mg of lipoic acid dissolved in 50 mL of ethanol was added to the solution. This solution was stirred in a shaker at 37°C in a nitrogen gas atmosphere for 24 hours to allow it to react. Then, the resulting product was removed from the environment using a magnet. To remove unreacted substances, the Fe3O4/chitosan/LA nanoparticles were washed 10 times with distilled water, and the resulting product was dried in a lyophilizer (Zhou et al., 2016; Abd Razak et al., 2018).

RESULTS AND DISCUSSION

UV-Vis study of Fe_3O_4/chitosan/LA synthesis

To determine the wavelength of formation of the synthesized Fe_3O_4/chitosan/LA nanoparticles, specific samples were taken using a spectrophotometer, and the formation of the nanoparticles and their maximum absorbance values were determined (Fig. 1).

This spectrum shows that Fe_3O_4/chitosan/lipoic acid nanoparticles exhibit high absorbance in the UV region, and the small absorbance shoulder around 335 nm supports the presence of Fe_3O_4/chitosan/lipoic acid. Low absorbance in the visible region may provide an advantage in terms of optical transparency in applications such as biomedical or drug delivery.

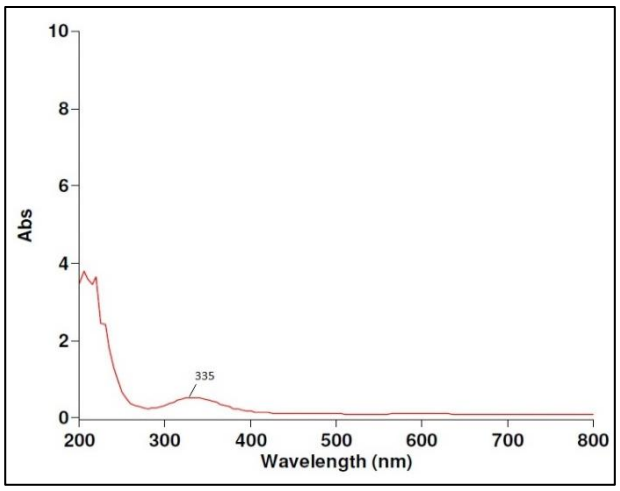

Fig. 1. Formation and maximum absorbance value of Fe_3O_4/Chitosan/LA NPs in UV-Vis spectroscopy.

XRD study of Fe_3O_4/chitosan/LA synthesis

The crystal sizes of Fe_3O_4/chitosan/LA nanoparticles were calculated using the Debye-Scherrer equation based on X-ray diffraction (XRD) data. This method is a reliable technique widely used to determine the average crystal size of nanoparticles. The obtained average crystal size of 19.42 nm indicates that these nanoparticles are small and have a nanometric structure (Fig. 2). This suggests that the material has properties that can provide advantages in various biomedical and industrial applications.

Scanning Electron Microscopy-Energy Dispersive X-ray Spectroscopy (SEM-EDX) analysis was performed to determine the morphological and elemental composition of the Fe_3O_4/chitosan/LA nanoparticle. Examination of the EDX spectrum clearly revealed characteristic peaks belonging to the added Fe element. Furthermore, the presence of C, S, and O elements in the spectrum supports the presence of chitosan and lipoic acid in the nanocomposite structure. According to the elemental analysis results, approximately 64% Fe element was detected in the nanocomposite structure, indicating that iron oxide cores are the dominant component within the nanocomposite (Fig. 3).

Scanning Electron Microscopy (SEM) analysis was performed to evaluate the morphological properties, particle size, surface topography, and distribution characteristics of Fe_3O_4/chitosan/LA nanoparticles (Fig. 4). SEM images revealed that under specific magnification and operating conditions, the nanoparticles generally have a spherical morphology and exhibit a nearly homogeneous distribution.

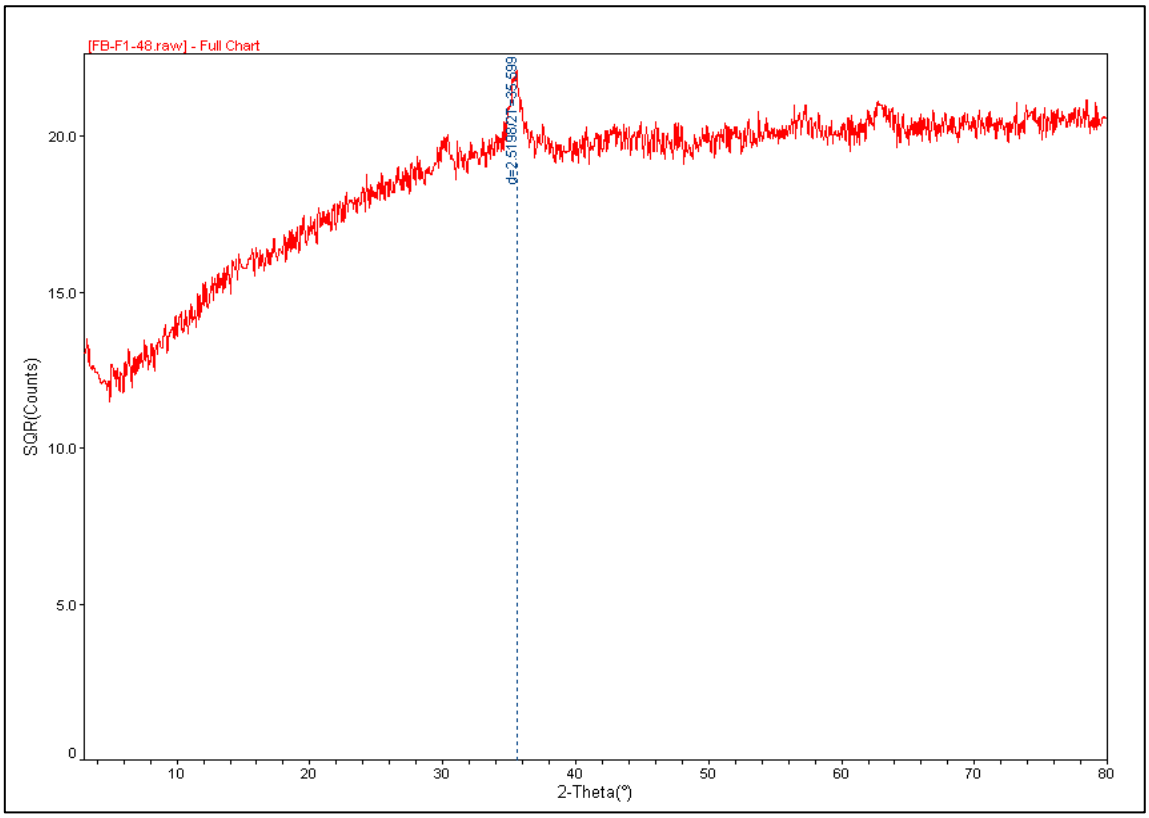

Fig. 2. XRD diagram of Fe_3O_4/chitosan/LA nanoparticle.

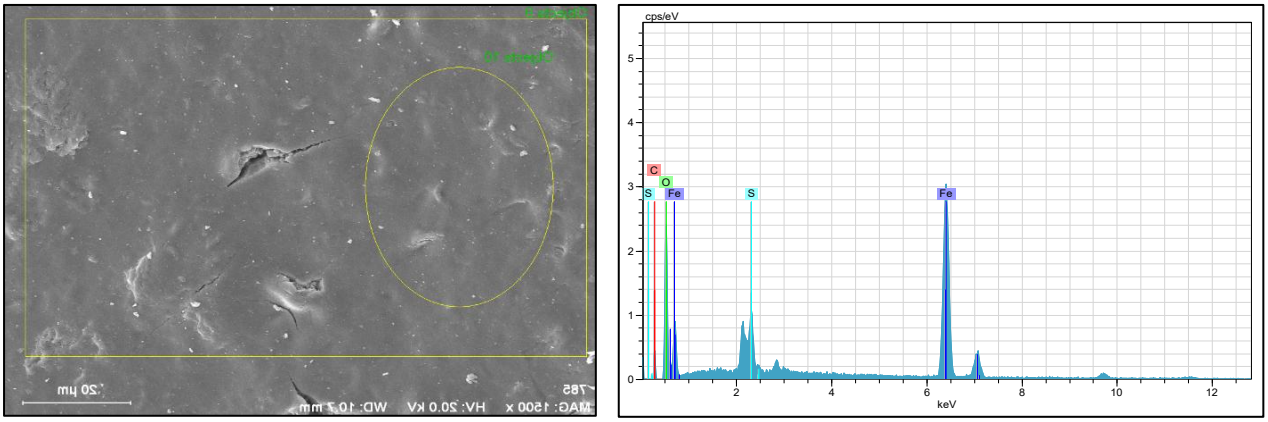

El	AN	Series	unn. C [wt.-%]	norm. C [wt.-%]	Atom. C [at.-%]	Error [%]
Fe	26	K-series	50.66	63.79	34.98	1.4
S	16	K-series	5.77	7.27	6.94	0.2
C	6	K-series	3.38	4.26	10.85	0.9
O	8	K-series	19.60	24.68	47.23	2.9
		Total:	79.42	100.00	100.00	

Fig. 3. SEM-EDX study of Fe_3O_4/chitosan/LA nanoparticle.

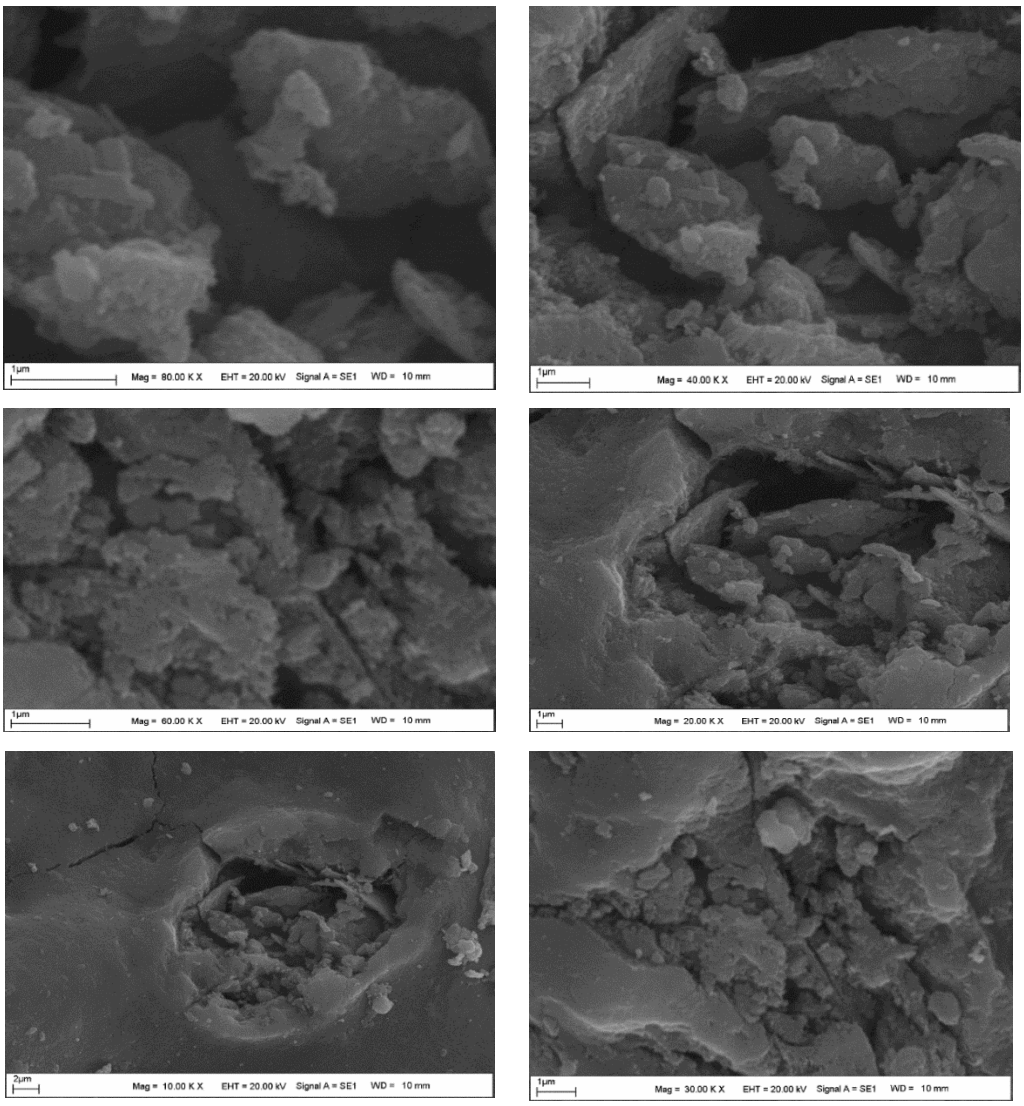

Fig. 4. SEM diagram of Fe_3O_4/chitosan/ALA nanoparticle.

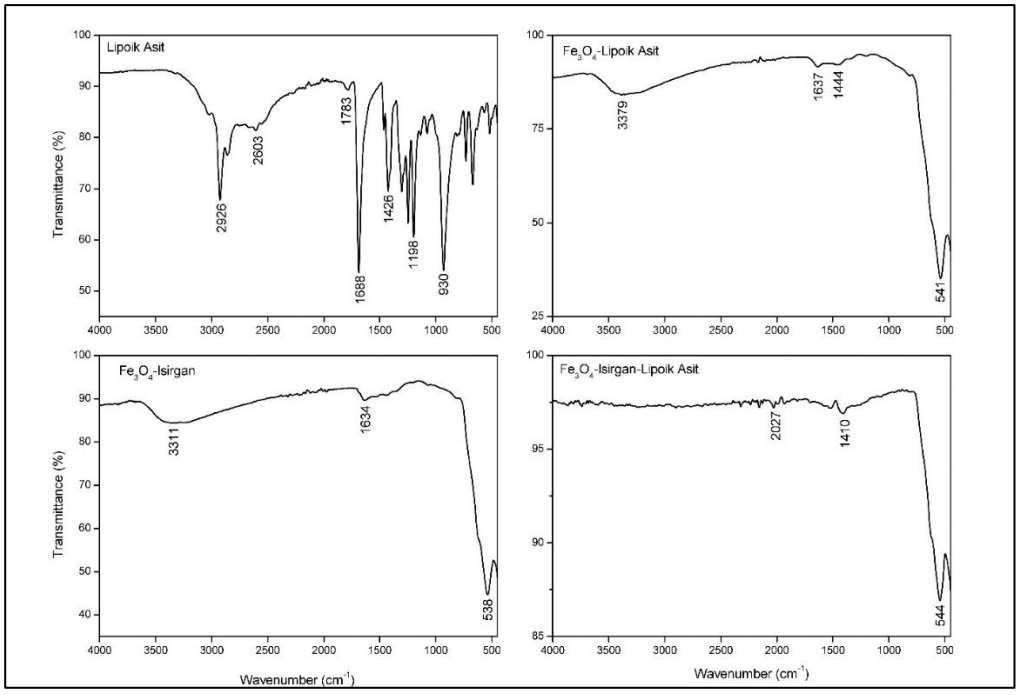

Fig. 5. FTIR diagram of Fe_3O_4/chitosan/ALA nanoparticle.

FTIR spectrum data analysis

Fourier Transform Infrared (FT-IR) spectroscopy was used to confirm the formation of Fe_3O_4/chitosan/ALA nanoparticle. This technique was used to examine changes in the functional groups in the structure and to evaluate the presence of chemical bonding between the components. As seen in Figure 5, it was observed that the characteristic functional groups in the lipoic acid structure showed shifting or, in some cases, completely disappeared in the Fe_3O_4/ALA composite. These spectral changes indicate that lipoic acid is chemically bonded to the magnetite surface and that the targeted Fe_3O_4/chitosan/ALA nanoparticle structure was successfully synthesized.

CONCLUSION

In this study, a hybrid liposomal carrier system (Fe_3O_4@α-LA/Chitosan) containing α-lipoic acid-chitosan complexes attached to a magnetic iron oxide (Fe_3O_4) core was synthesized and its structural properties were elucidated. Extensive characterization studies confirmed the successful achievement of the targeted nanostructure using various analytical techniques. Accordingly, the average crystal size, calculated using the Debye-Scherrer equation from XRD analysis data, was determined to be 19.42 nm, proving the nanometric-scale crystal structure of the material. SEM morphology studies revealed that the nanoparticles have a spherical geometry and exhibit a nearly homogeneous distribution without showing a significant agglomeration tendency. EDX analysis, which determined the elemental composition of the structure, detected the presence of 64% Fe element as well as C, O, and S, supporting the integration of chitosan and lipoic acid components into the matrix. Finally, the shifts observed in the bands belonging to characteristic functional groups and the extinction of some specific peaks in the FT-IR spectra demonstrated that lipoic acid successfully bound to the Fe_3O_4 surface and that strong structural interactions occurred. This overall assessment clearly shows that the synthesized Fe_3O_4/chitosan/LA nanocomposite was successfully produced with the targeted architecture, purity, and composition. Although the particle morphology was verified by SEM and XRD, the absence of dynamic light scattering (DLS) and zeta potential measurements is acknowledged as a limitation of this study, and these liquid-state analyses will be prioritized in future work.

ETHICAL CONSIDERATIONS

This study complies with internationally accepted research ethics standards. No human participants, personal data, or confidential information were involved, or all ethical approvals were obtained where required.

AUTHOR CONTRIBUTIONS

MY and MFB: Conceptualization, Methodology, Investigation, Writing-original draft. SK: Investigation, Writing – review and editing. ALT: Project administration, Supervision, Formal analysis, Data curation, Visualization.

ACKNOWLEDGEMENTS

The authors would like to thank all individuals and institutions that provided support or insights during the preparation of this study.

FUNDING

This work was supported by the Scientific Research Projects Coordination Unit of Muğla Sıtkı Koçman University (Project No. BAP-24/169/07/1).

CONFLICT OF INTEREST

The authors declare no conflict of interest related to this study.

AI STATEMENT

AI-assisted tools were used only for language translation, grammatical editing, and reference formatting.

REFERENCES

Abd Razak N.F., Shamsuddin M., Lee S.L. (2018) Adsorption kinetics and thermodynamics studies of gold (III) ions using thioctic acid functionalized silica coated magnetite nanoparticles. *Chemical Engineering Research and Design*, **130:** 18-28.

Abdelkader N.F., El-Batal A.I., Amin Y.M., Hawas A.M., Hassan S.H., Eid N.I. (2025) Possible mechanisms underlying the neuroprotective effects of gold nanoparticles and alpha-lipoic acid mixture on brain damage induced by radiation: a subacute study in rats. *Journal of Drug Delivery Science and Technology*, **109:** 106977.

Aslan K.S., Ertaş E., Baran M.F., Levent A., Tümür Ş., Eftekhari A., ... Katz E. (2026) Enhanced electrochemical performance of

supercapacitors using Fe_3O_4-doped biomass-derived activated carbon electrodes. *Electrochemical Science Advances*, **6(1):** e70014.

Bagheri M., Validi M., Gholipour A., Makvandi P., Sharifi E. (2022) Chitosan nanofiber biocomposites for potential wound healing applications: Antioxidant activity with synergic antibacterial effect. *Bioengineering & Translational Medicine*, *7***(1):** e10254.

Çoban Ö., Demirtaş H., Kaya-Yasar Y., Engin S., Yıldırım S., Morsali M.R. (2025) Formulation optimization and *in vitro–in vivo* evaluation of alpha lipoic acid-loaded lipid–polymer hybrid nanoparticles via design of experiments. *Journal of Pharmaceutical Innovation*, **20(2):** 50.

Cuana R., Panre A.M., Istiqomah N.I., Tumbelaka R.M., Wicaksono S.T., Suharyadi E. (2022) Green synthesis of Fe_3O_4/chitosan nanoparticles utilizing moringa oleifera extracts and their surface plasmon resonance properties. *ECS Journal of Solid-State Science and Technology*, **11(8):** 083015.

Ertaş E., Doğan S., Baran A., Baran M.F., Evcil M., Kurt B., ... Aslan K.S. (2025) Preparation and characterization of silver-loaded magnetic activated carbon produced from *Crataegus monogyna* for antimicrobial and antioxidant applications. *Chemistry Select.*, **10(16):** e202405558.

Gheybi E., Jalili Nik M., Hosseinzadeh P., Mirzaei S.M., AlAlikhan A., Soukhtanloo M. (2026) Evaluation of the neuroprotective effects of alpha lipoic acid-loaded folate-conjugated chitosan nanoparticles against 6-OHDA-induced apoptosis and oxidative stress in an *in vitro* Parkinson's disease model. *BMC Neuroscience*, **27 (1):** 7.

Gorąca A., Huk-Kolega H., Piechota A., Kleniewska P., Ciejka E., Skibska B. (2011) Lipoic acid–biological activity and therapeutic potential. *Pharmacological Reports*, **63(4):** 849-858.

Hahm J.R., Kim B.J., Kim K.W. (2004) Clinical experience with thioctacid (thioctic acid) in the treatment of distal symmetric polyneuropathy in Korean diabetic patients. *J Diabetes Complications*, **18(2):** 79-85; doi: 10.1016/S1056-8727(03)00033-3.

Han D., Handelman G., Marcocci L., Sen C.K., Roy S., Kobuchi H., ... Packer L. (1997) Lipoic acid increases de novo synthesis of cellular glutathione by improving cystine utilization. *Biofactors*, **6(3):** 321-338.

Istiqomah. N.I., Budianti S.I., Cuana R., Puspitarum D.L., Mahardhika L.J., Suharyadi E. (2024) Magnetically separable and reusable Fe_3O_4/chitosan nanocomposites green synthesized utilizing *Moringa oleifera* extract for rapid photocatalytic degradation of methylene blue. *Results in Chemistry*, **7:** 101245.

Kagan V.E., Shvedova A., Serbinova E., Khan S., Swanson C., Powell R., Packer L. (1992) Dihydrolipoic acid a universal antioxidant both in the membrane and in the aqueous phase: reduction of peroxyl, ascorbyl and chromanoxyl radicals. *Biochemical Pharmacology*, **44(8):** 1637-1649.

Kurul F., Turkmen H., Cetin A. E., Topkaya S. N. (2025). Nanomedicine: How nanomaterials are transforming drug delivery, bio-imaging, and diagnosis. *Next Nanotechnology*, **7:** 100129.

Li Z., Deng W., Yang L., Tang C., Yue J.M., Monteiro O., ... Li T. (2026) Lipid metabolism in homeostasis and disease. *Signal Transduction and Targeted Therapy*, **11(1):** 55.

Priya M., Venkatesan R., Deepa S., Sana S.S., Arumugam S., Karami A.M., Vetcher A.A., Kim S.C. (2023) Green synthesis, characterization, antibacterial, and antifungal activity of copper oxide nanoparticles derived from *Morinda citrifolia* leaf extract. *Sci. Rep*., **13(1):** 18838.

Quitadamo F., De Simone V., Beleggia R., Trono D. (2021). Chitosan-induced activation of the antioxidant defense system counteracts the adverse effects of salinity in durum wheat. *Plants*, **10(7):** 1365.

Salehi B., Yılmaz Y.B., Antika G., Boyunegmez Tumer T., Mahomoodally M.F., Lobine D. et al. (2019) Insights on the use of α-lipoic acid for therapeutic purposes. *Biomolecules*, **9(8):** 356; doi: 10.3390/biom9080356.

Shay K.P., Moreau R.F., Smith E.J., Smith A.R., Hagen T.M. (2009) Alpha-lipoic acid as a dietary supplement: molecular mechanisms and therapeutic potential. *Biochimica et Biophysica Acta (BBA)-General Subjects*, **1790(10):** 1149-1160.

Sheikholeslami S., Khodaverdian S., Dorri-Giv M., Hosseini S.M., Souri S., Abedi-Firouzjah R. et al. (2021) The radioprotective effects of alpha-lipoic acid on radiotherapy-induced toxicities: a systematic review. *Int. Immunopharmacol*., **96:** 107741; doi: 10.1016/j.intimp.2021.107741

Singh A., Mittal A., Benjakul S. (2023) Chitosan, chitooligosaccharides and their polyphenol conjugates: preparation, bioactivities, functionalities and applications in food systems. *Food Reviews Int.*, **39(4):**2297–2319.

Skibska B., Goraca A., Skibska A., Stanczak A. (2022) Effect of alpha-lipoic acid on rat ventricles and atria under LPS-induced oxidative stress. *Antioxidants (Basel)*, **11(4):** 734; doi: 10.3390/antiox11040734.

Skibska B, Goraca A (2015) The protective effect of lipoic acid on selected cardiovascular diseases caused by age-related oxidative stress. Oxidative

Med Cell Longev, 2015(1):313021.

Smith A.R., Shenvi S.V., Widlansky M., Suh J.H., Hagen T.M. (2004) Lipoic acid as a potential therapy for chronic diseases associated with oxidative stress. *Curr. Med. Chem*., **11(9):** 1135-46; doi: 10.2174/0929867043365387.

Tomke P.D., Rathod V.K. (2020) Facile fabrication of silver on magnetic nanocomposite (Fe_3O_4@ Chitosan–AgNP nanocomposite) for catalytic reduction of anthropogenic pollutant and agricultural pathogens. *International Journal of Biological Macromolecules*, **149:** 989-999

Yadav A., Raghav S., Jangid N.K., Srivastava A., Jadoun S., Srivastava M., Dwivedi J. (2023) *Myrica esculenta* leaf extract assisted green synthesis of porous magnetic chitosan composites for fast removal of Cd (II) from water: Kinetics and thermodynamics of adsorption. *Polymers*, **15(21):** 4339.

Ye N., Lv Z., Dai H., Huang Z., Shi F. (2021) Dietary alpha-lipoic acid supplementation improves spermatogenesis and semen quality via antioxidant and anti-apoptotic effects in aged breeder roosters. *Theriogenology*, **159:** 20-27; doi: 10.1016/j.theriogenology.2020.10.017.

Yusefi M., Yee O.S., Shameli K. (2021) Bio-mediated production and characterisation of magnetic nanoparticles using fruit peel extract. *Journal of Research in Nanoscience and Nanotechnology*, **1(1):** 53-61.

Zhou Y., Yu J., Feng X., Li W., Wang Y., Jin H., Fan D. (2016) Reduction-responsive core-crosslinked micelles based on a glycol chitosan–lipoic acid conjugate for triggered release of doxorubicin. *Rsc Advances*, **6(37):** 31391-31400;

Wientjens C., Doverman M., Zurkovic J., More T., Surendar J., Nesic S., ... Wilhelm C. (2026) Tolerance to ferroptosis facilitates lipid metabolism and pathogenic type 2 immunity in allergic airway inflammation. *Immunity*, **59(2):** 322-338.

ORCIDs:

Mahmut Yıldıztekin: https://orcid.org/0000-0002-0206-0117
Sultan Köşkeroğlu: https://orcid.org/0000-0001-6623-1862
Mehmet Fırat Baran: https://orcid.org/0000-0001-8133-6670
Atilla Levent Tuna: https://orcid.org/0000-0001-5123-0031

Association of salt-tolerant bacteria to support the growth of pasture grasses on saline soils

Irina Smirnova[1*], Amankeldi Sadanov[1], Gul Baimakhanova[1], Marat Aldabergenov[2], Yaira Rakhmetova[1]

[1]*Research and Production Center for Microbiology and Virology LLC, 105 Bogenbai Batyr Str., 050010, Almaty, Kazakhstan*
[2]*Research and Production Center for Agricultural Engineering LLC, 312 Raimbek Ave., Almaty, Kazakhstan*

[*]***For correspondence**: iesmirnova@mail.ru*

Received: April 08, 2026; Reviewed: June 03, 2026; Accepted: June 16, 2026

Soil salinization poses a serious threat to agriculture, as it causes soil degradation, negatively impacts crops, and reduces productivity. For Kazakhstan, the development of pasture livestock farming plays a key role in the country's economy, providing the population with essential food products. Soil salinization significantly reduces the forage value of pastures, as it leads to the displacement of valuable forage grasses by salt-tolerant weeds. A promising solution to this problem is the use of rhizobacteria, which promote grass growth in saline soils, thereby increasing the forage value of pastures. The aim of this study was to select salt-tolerant bacteria, study their ability to stimulate pasture grass growth under conditions of high salt stress, and create an effective association based on them to support growth in saline soils. Phosphate-solubilizing and nitrogen-fixing bacteria were isolated from saline pasture soils in the South-East of Kazakhstan, their salt tolerance was studied, and the most resistant strains were selected. It was shown that the bacteria actively fix atmospheric nitrogen and dissolve phosphates under salt stress. The ability of the bacteria to produce secondary metabolites (phytohormone and ACC deaminase), which relieve salt stress and promote plant growth, was established. Active bacterial strains were selected, and an effective association was created. Application of the association more than tripled the yield of green mass, which is an effective method for increasing grass productivity in saline pastures. Based on the bacterial association, it is planned to develop a biofertilizer for saline soils.

Keywords: *Nnitrogen-fixing bacteria, phosphate-solubilizing bacteria, salt tolerance, nitrogenase, phosphate solubilization, growth stimulation, salt stress, pasture grasses, productivity*

INTRODUCTION

The development of modern agriculture requires increased food production. Intensive agricultural technologies based on chemical production pollute the environment, reduce soil fertility, and negatively impact the quality of the final product (Nuruzzaman et al., 2025). Therefore, it is necessary to develop alternative methods for increasing crop yields. Soil salinization is currently a serious agricultural problem and is caused by several factors. One is climate change, which causes an increase in overall air temperature and leads to increased water evaporation from the soil, thereby increasing its salinity (Tarolli et al., 2024). Another problem is the shortage of fresh water and the use of saline water for irrigation. Currently, the extent of soil salinization continues to increase, and the FAO estimates that salinization will cause a 50% loss of arable land worldwide by 2050 (FAO, 2025).

In Kazakhstan, pasture livestock farming is a main industry, accounting for over 45% of total agricultural output (Esengalieva et al., 2024). Pasture monitoring in 2023 showed that 82% of pastures were in poor condition due to soil degradation and salinization (Eldala.kz report, 2024). In this regard, restoring pastures is a pressing issue. Several solutions exist, including breeding salt-tolerant crops and creating genetically modified salt-tolerant crops. However, traditional breeding is time-consuming and has a relatively low success rate, and the development of genetically modified salt-tolerant crops has not yielded any significant results (Afzal et al., 2023). The most promising approach is the use of salt-tolerant rhizobacteria, which promote plant growth in saline soils. These bacteria are live cultures of PGPR (Plant Growth Promoting Rhizobacteria), which possess valuable properties: they do not pollute the environment, are safe for humans and

 DOI: https://doi.org/10.62088/timbb/10.1.3

animals, and are non-phytotoxic and non-mutagenic (Zhang et al., 2024; Yang et al., 2024). Furthermore, they are natural components, as they are isolated from natural substrates (soil, plant roots, leaves, stems, etc.) (Liang et al., 2025). In agriculture, complex multifunctional biopreparations based on bacterial associations are used. The strains that comprise these associations can fix nitrogen, synthesize vitamins and phytohormones, convert unavailable phosphorus into a plant-available form, and colonize plant roots (Pathak et al., 2026). Rhizobacteria strains can also exhibit antagonistic activity against plant pathogens and synthesize antibiotics, siderophores, pigments, and other metabolites (Al Raish et al., 2025). The use of rhizobacteria is environmentally safe, does not pollute the environment, and does not disrupt the ecological balance of the agrocenosis. In this regard, the most promising approach is the use of salt-tolerant rhizobacteria that promote plant growth (PGPR) and produce metabolites that reduce salt stress and promote plant development in saline soils. Due to its wide range of applications, efficiency and environmental friendliness, this method is the most relevant for reducing soil salinity (Jabborova et al., 2025). However, the main mechanisms for maintaining plant growth on saline soils are nitrogen fixation and increasing the availability of soil phosphates. The aim of this study was to select salt-tolerant bacteria, study their ability to stimulate pasture grass growth under conditions of high salt stress, and create an effective association based on them to support growth in saline soils. The use of salt-tolerant rhizobacteria associations can be considered the best alternative for environmentally friendly and sustainable agriculture.

RESEARCH METHODOLOGY

The objects of the study were nitrogen-fixing and phosphate-solubilizing bacteria isolated from the rhizosphere soil of pasture grasses in the South-East of Kazakhstan, in the Almaty region.

Timothy grass (*Phleum pratense* L.), meadow fescue (*Festuca pratensis* L.), and perennial ryegrass (*Lolium perenne* L.) were used as pasture grasses. These plants are salt-tolerant, adapted to the soil and climatic conditions of Kazakhstan, and form the basis of pasture grasses in the South-East of the Republic.

Phosphate-solubilizing bacteria were isolated on NBRIP medium (National Botanical Research Institute's Phosphate growth medium) (De Zutter et al. 2022). Salt stress was created by adding 10% NaCl to the medium. To isolate bacteria, 10 g of soil was diluted with 90 ml of tap water and stirred on a shaker at 180 rpm for 1 hour. The water was sterilized in an autoclave at 120°C for 30 minutes. Then, 1 ml from the stock suspension was used to prepare serial dilutions in eight test tubes, each containing 9 ml of sterile distilled water. Inoculation of microorganisms was carried out by transferring 0.1 ml from dilutions 10^{-4}, 10^{-5}, 10^{-6}, 10^{-7} and 10^{-8} onto Petri dishes containing NBRIP agar medium. The inoculum volume was 1 ml of soil suspension. Each dilution was plated in triplicate. The dishes were incubated at 28°C until clear halo zones appeared around the bacterial colonies.

Free-living nitrogen-fixing bacteria were isolated from saline soil. Nitrogen-free Ashby agar (Shi et al., 2023) was used for bacterial isolation. Salt stress was created by adding 10% NaCl to the medium. Petri dishes were inoculated with microorganisms at dilutions of 10^{-3}, 10^{-4}, 10^{-6}, and 10^{-8}. Nitrogen-fixing bacteria were selected from large-diameter colonies. This selection was based on the assumption that bacteria capable of forming large colonies on nitrogen-free medium are characterized by increased nitrogen fixation activity.

Salt tolerance of phosphate-solubilizing bacteria was determined in a liquid medium containing NBRIP, while nitrogen-fixing bacteria were tested in Ashby's medium supplemented with 100, 250, and 500 mM NaCl. Bacteria were grown for 3-5 days at 28°C and 180 rpm. Bacterial growth was determined using a spectrophotometer (PD-303, Apel, Japan) at 540 nm. Bacterial growth was assessed using a scale where [-] - denotes the absence of growth, [+] - denotes the presence of growth, and [several +] - denotes the intensity of growth. The study was conducted in triplicate.

To study phosphate-solubilizing activity, bacteria were grown in liquid NBRIP medium at 28°C and 180 rpm for three days. Petri dishes were filled with NBRIP agar. After the agar solidified, wells were punched and 0.1 ml of the bacterial suspension at a concentration of 10^8 CFU/ml was added. The dishes were placed in an incubator at 28°C and incubated until clear halo zones (transparent zones of tricalcium phosphate dissolution) appeared around the wells. The presence of a clear halo around the bacterial colonies indicates the strain's ability to dissolve mineral phosphates. The phosphate-solubilizing activity of the bacteria was quantified by the diameter of the halo zones and expressed in mm. Wells containing bacteria-free medium served as a negative control. The study was performed in triplicate.

The nitrogenase activity of bacteria was determined by the acetylene method (ARA). Bacteria were grown in Ashby’s medium under

aeration to a concentration of 10^8 cells/ml. The suspension of bacteria was placed in 10 ml vessels; acetylene was introduced to a concentration of 10% (by volume). After incubation of bacteria for 1.5 h in an acetylene atmosphere, gas samples were taken with a 1 ml syringe from the vessel and the ethylene content was detected on an Agilent Technology 7890B (USA) gas chromatograph with a flame ionization detector (Montes-Luz et al., 2023).

To study the biocompatibility of nitrogen-fixing and phosphate-solubilizing bacteria, the perpendicular streak method was used (Hossain, 2024). To determine the ability of bacteria to produce the phytohormone Indole-3-Acetic Acid (IAA), the method described by B.G. Guardado-Fierros (Guardado-Fierros et al., 2024) was used. Bacteria were grown in LB medium supplemented with tryptophan at 28°C and 180 rpm for 5 days. The medium was then centrifuged at 10000 rpm for 10 min. Then, 2 ml of the supernatant was mixed with 4 ml of Salkowski's reagent. The solution was incubated in the dark for 30 min at 40°C. The IAA content was measured using an Apel PD-303 spectrophotometer (Japan) at a wavelength of 530 nm.

To determine the amount of ACC deaminase (1-Amino Cyclopropane-1-Carboxylate), the strains were cultured with Tryptic Soy Broth (TSB culture medium) (Sigma-Aldrich, Germany) at 28°C and 180 rpm. After 24 hours of growth, the bacteria were centrifuged at 10,000 x g for 5 min and then suspended in 5 ml of Dworkin and Foster medium containing 5 μmol L^{-1} ACC as the sole nitrogen source and incubated for 24 hours at 28°C. The ACC deaminase activity of bacteria was determined spectrophotometrically (Apel PD-303, Japan) at 540 nm and compared with a standard curve constructed using α-ketobutyrate solution (Sigma-Aldrich, Germany) (Kumari et al., 2025). The amount of α-ketobutyrate produced (mmol mg^{-1} protein h^{-1}) was used as a measure of ACC deaminase activity.

To study the effect of bacteria and association on PGP-activity, nitrogen-fixing and phosphate-solubilizing bacteria were grown separately in flasks: phosphate-solubilizing bacteria on NBRIP medium and nitrogen-fixing bacteria on Ashby's medium at 28°C and 180 rpm for 3-5 days. Then the bacterial suspensions were mixed in a 1:1 ratio. Timothy grass (*Phleum pratense* L.), meadow fescue (*Festuca pratensis* L.) and perennial ryegrass (*Lolium perenne* L.) were used as pasture grasses, which were mixed in equal proportion. The seeds were inoculated with bacteria or association (concentration 10^8 cells/ml) for two hours at 23°C, at the rate of 5 ml per 10 g of seeds. Then, 10 seeds were sown in vessels (500 ml) with sterilized vermiculite. A negative control was seeds treated with sterile water. Knop's solution was used as a nutrient solution for the seedlings (Le et al., 2025). The biometric characteristics of the plants were measured after 30 days. The experiments were carried out in a climatic growth chamber (Memmert HPP 750 Constant Climate Chamber, Germany) under the following regime: daylight hours - 14 h, temperature 25°C, illumination: cold white light - 6500 K, warm light 2700 K; night mode - 9 hours; temperature 20°C, humidity - 65%. Experiments were conducted in 3 replicates.

All the recorded data underwent statistical analysis using the software package STATISTICA 10.0, var. 6 (Borovikov, 2016). Tables and figures show the mean values (M) and standard errors of means (±SEM).

RESULTS AND DISCUSSION

Nitrogen-fixing and phosphate-solubilizing bacteria were isolated from the rhizosphere of pasture grasses growing on highly saline pasture soils in the Almaty region (South-East of Kazakhstan). The salt content in the aqueous extract of the soils ranged from 3.62% to 5.18%, pH was 8.7-9.2. Based on the HCO_3 ion content, the soils are highly alkaline. Such soils cause alkaline toxicity in plants, which negatively impacts their development. Nitrogen-fixing bacteria were isolated on nitrogen-free Ashby's medium, phosphate-mobilizing bacteria on NBRIP medium. A total of 57 free-living nitrogen-fixing and 46 phosphate-mobilizing bacteria were isolated. A primary screening of bacteria was conducted, and 19 nitrogen-fixing and 25 phosphate-mobilizing bacteria characterized by salt tolerance were selected.

To select salt-tolerant strains, their growth activity under high salt stress was studied. Bacteria were grown in elective media with varying NaCl concentrations: 100, 250, and 500 mM. Cultivation was carried out at 28°C on a shaker at 180 rpm for three days. Table 1 presents growth activity data for 17 strains of phosphate-solubilizing and nitrogen-fixing bacteria at varying NaCl concentrations in the medium.

Table 1 shows that not all bacterial strains isolated from highly saline soils exhibited high salt tolerance. Almost all strains grew at 100 mmol/L NaCl, while 17 strains grew at 250 mmol/L NaCl, with some strains showing very little growth. At 500 mmol/L NaCl, growth was observed only in five nitrogen-fixing strains (Az3/9, Az3/29, Azp6/2, Az22/1, Az24) and six phosphate-mobilizing strains (F7A, FC11, FC24, FT4, FY3, FY3/8). These strains were selected as the most salt-tolerant.

Table 1. Effect of salinity on bacterial growth.

Strains	NaCl concentration, mM		
	100	250	500
Nitrogen-fixing bacteria			
Az3/9	+++	+	+
Az3/23	+++	+	-
Az3/29	++++	+++	++
Azp6/2	++++	+++	++
Az22/1	++++	+++	++
Az23/4	+++	++	-
Az24	+++	++	+
Az43/2	+++	++	-
Phosphate-solubilizing bacteria			
F7A	++++	+++	+++
FC11	++++	++	+
FC24	++++	++	+
FM9/5	++++	+	-
FM12	++++	+	-
FT4	++++	+++	++
FY3	++++	+++	+++
FY3/8	++++	++	+
FY7/2	++++	+	-

Note: Qualitative assessment: [-] - indicates the absence of growth; [+] - indicates the presence of growth; additional [+] - indicates the growth intensity exhibited by the strains.

Table 2. Biomass and nitrogenase activity of nitrogen-fixing bacterial strains.

Strains	Duration of cultivation			
	3 days		5 days	
	Biomass*, g/l	Nitrogenase activity, µmol C_2H_4/ml/h	Biomass*, g/l	Nitrogenase activity, µmol C_2H_4/ml/h
Control	0	0	0	0
Az3/9	1.02±0.01	1.16±0.01	1.96±0.01	3.56±0.01
Az3/29	1.62±0.01	2.41±0.01	2,75±0,2	4,94±0,01
Azp6/2	1.81±0.02	2.55±0.02	2,81±0,1	5,27±0,03
Az22/1	1.73±0.01	2.32±0.02	2,71±0,1	4,71±0,01
Az24	1.12±0.01	2.17±0.01	2.25±0.01	3.87±0.02

Note: * - absolutely dry biomass of bacteria; $p < 0.05$, n = 3

Table 3. Phosphate-solubilizing activity of bacterial strains.

Strains	Cell titer, CFU/ml	Halo zone diameter, mm	pH
Control	0	0	6.8±0.01
F7A	3.3×10^8	33.9±0.2	4.5±0.01
FC11	3.1×10^8	28.5±0.1	5.0±0.01
FC24	2.8×10^8	33.7±0.1	4.1±0.02
FT4	3.6×10^8	35.3±0.2	4.7±0.01
FY3	3.4×10^8	34.5±0.1	4.4±0.01
FY3/8	2.9×10^8	28.3±0.2	4.8±0.01

Note: $p < 0.05$; n = 3

One of the main indicators of PGPR for use in agriculture on saline soils is their ability to fix atmospheric nitrogen and mobilize soil phosphates that are inaccessible to plants. In this regard, the nitrogenase activity and biomass accumulation capacity of selected nitrogen-fixing bacteria were studied under saline conditions. Biomass accumulation on nitrogen-free media is an indirect indicator of bacterial nitrogen fixation activity. To create salt stress, 500 mM NaCl was added to Ashby's medium. These experiments were conducted dynamically, and results were obtained after 3 and 5 days of cultivation. The data obtained are presented in Table 2.

It was found that the strains actively accumulated biomass and fixed nitrogen under saline conditions. Three strains had the highest nitrogenase activity, with biomass accumulation reaching 2.71–2.81 g/L (Table 2). Therefore, these three strains (Az3/29, Azp6/2, Az22/1) were selected as the most effective, as they were characterized by high nitrogenase activity and biomass accumulation when grown in nitrogen-free medium under high salinity conditions.

To select strains active in phosphate solubilization under high salt stress, selected bacterial strains were studied. To create salt stress, 500 mM NaCl phosphate was added to the culture

medium. Table 3 presents data for seven strains with higher phosphate solubilization activity when grown on NBRIP medium.

The data in Table 3 showed that the bacteria have a high capacity to solubilize phosphates under salt stress. Of the seven bacteria, three strains, F7A, FT4, FY3 demonstrated high phosphate solubility. The halo zone diameter for these strains ranged from 33.8 to 34.3 mm. These strains (F7A, FT4, FY3) were selected as the most effective. Strain FT4 demonstrated the highest phosphate solubility.

The main indicator for the use of bacteria in saline soils is their ability to synthesize metabolites that support plant growth and enhance plant adaptation to stress factors such as flooding, drought, and salinity. These metabolites include phytohormones and the enzyme ACC deaminase. The most common phytohormone is indole-3-acetic acid (IAA), which influences root formation, root and shoot growth, and plays a key role in plant adaptation to salt stress. Another metabolite that is crucial during plant stress is ACC deaminase. Under stress, plants produce ethylene, which inhibits root growth and phytohormone transport, accelerates tissue aging, causes defoliation, and delays fruit ripening. Rhizobacteria that produce ACC deaminase reduce ethylene levels in plants, which promotes the formation of longer roots and significantly increases resistance to stress factors. In this regard, the ability of the studied strains of bacteria to produce the enzyme ACC-deaminase and indole-3-acetic acid (IAA) under salt stress was studied. To create salt stress, 500 mM NaCl phosphate was added to the culture medium. The obtained data are presented in Table 4.

Table 4 shows that the studied rhizobacteria produce indole-3-acetic acid and the enzyme ACC-deaminase. It was found that nitrogen-fixing bacteria demonstrated a higher ability to synthesize these metabolites compared to phosphate-solubilizing bacteria. However, biomass accumulation was slightly higher in the phosphate-solubilizing bacterial strains. The results indicate that, through metabolite synthesis, these strains can reduce salinity stress and stimulate plant growth.

A biocompatibility study of the strains showed that all the studied strains were compatible and did not inhibit each other's growth. Based on these strains, 10 associations were created, containing strains of phosphate-mobilizing and nitrogen-fixing bacteria.

Table 4. Indole-3-acetic acid (IAA) production and ACC deaminase activity by bacterial strains.

Strains	Biomass*, g/l	ACC-deaminase, µmol α-ketobutyrate mg^{-1} protein h^{-1}	IAA, µg ml^{-1}
Az3/29	2,75±0.2	0.54 ±0.01	44.25±1.1
Azp6/2	2,81±0.1	0.56 ±0.02	48.45±1.1
Az22/1	2,71±0.1	0.52 ±0.02	46.17±1.6
F7A	3.04±0.2	0.43 ±0.01	43.42±1.2
FT4	3.12±0.1	0.47 ±0.01	38.37±1.1
FY3	3.01±0.1	0.45 ±0.01	43.25±1.1

Note: * - absolutely dry biomass of bacteria; $p < 0.01$; n = 3

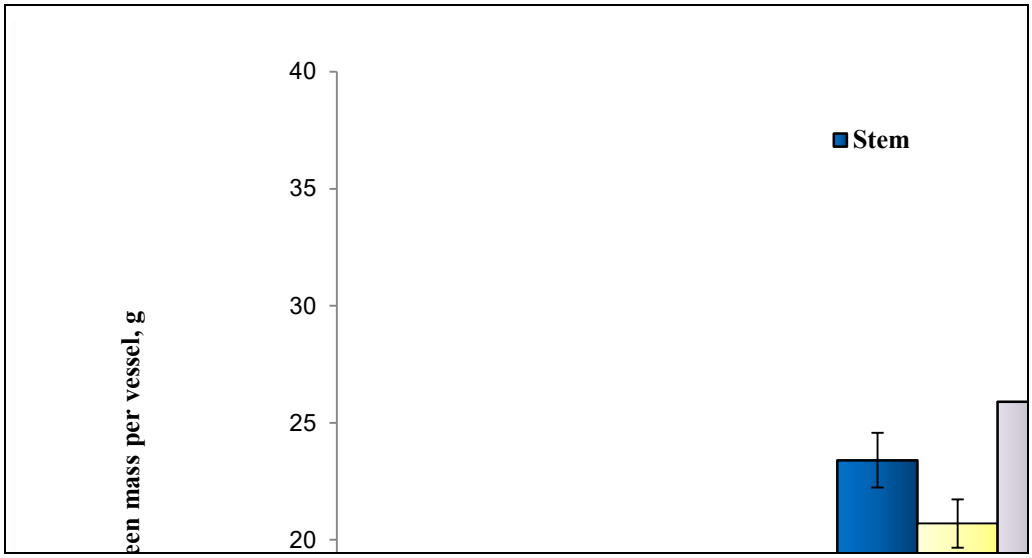

Fig. The effect of inoculation on the dry mass of stems, roots, and green mass productivity of pasture grasses on highly saline soils. Control without bacterial inoculation.

The effect of phosphate-solubilizing and nitrogen-fixing bacteria on pasture grass growth was studied. A mixture of timothy grass, meadow fescue, and perennial ryegrass seeds in a 1:1:1 ratio was used as pasture grass seeds. Experiments were conducted in vessels with highly saline soil with a salinity content of 3.62% in the aqueous extract and a pH of 8.9. Figure 1 presents data from the three associations that demonstrated the greatest stimulating effect on the growth and yield of pasture grass green mass.

The results showed that pre-sowing inoculation of grass seeds with the associations stimulated their growth, as evidenced by morphometric parameters (Fig. 1). Moreover, the dry weight of plant stems increased by an average of 1.8-2.2 times, root dry weight by 2.5-3.3 times, and green mass yield by 2.7-3.5 times compared to the control. Seed treatment also increased root length by 3.0-3.2 times, indicating grass adaptation to soil salinity. Based on the results of the study, an effective association №18 was selected, which increased the green mass yield of pasture grasses by 3.5 times.

Thus, the effect of associations of salt-tolerant bacteria on the growth and development of pasture grasses was studied. An effective association №18, consisting of salt-tolerant strains of phosphate-mobilizing (FT4) and nitrogen-fixing (Azp6/2) bacteria, was selected. It can be concluded that the use of associations stimulates the growth and alleviates salinity stress of pasture grasses.

CONCLUSION

The use of microbial associations in agriculture is an alternative to chemical fertilizers, as they are natural soil or rhizosphere agents and have no negative impact on the ecosystem. Currently, preference is given to using microbial associations that include several microbial species that perform beneficial functions for plants. Most often, associations include bacteria that fix nitrogen, mobilize phosphorus and potassium, stimulate plant growth, and suppress the development of phytopathogenic microorganisms. The use of such associations will reduce the toxic load on soil and plants. In our study, we obtained the following results:

- Nitrogen-fixing and phosphorus-solubilizing bacteria were isolated from saline pasture soils in the South-East of Kazakhstan, and salt-tolerant strains capable of growing under high salt stress (500 mM NaCl) were selected.
- The ability of the strains to fix atmospheric nitrogen and mobilize phosphates under high salinity was studied, and the most active strains were selected.
- The selected salt-tolerant bacterial strains were found to produce secondary metabolites: the phytohormone indole-3-acetic acid (IAA) and the enzyme ACC deaminase, which relieve salt stress and stimulate plant growth.
- Ten associations consisting of salt-tolerant strains of phosphate-solubilizing and nitrogen-fixing bacteria were created using the active strains.
- Pre-sowing seed inoculation with associations stimulates the growth of pasture grasses: stem dry weight more than doubled, root weight increased by 2.5-3.3 times, and green mass yield increased by 3.5 times. Seed treatment was shown to increase root length by 3.0-3.2 times, indicating plant adaptation to soil salinity. Based on the research results, association №18 was selected as the most effective.

Thus, an association of salt-tolerant bacteria has been created that improves nitrogen and phosphorus nutrition of plants, reduces salt stress, and positively impacts the growth and yield of pasture grasses on saline soils. Based on association, it is planned to develop a biofertilizer to support crop growth on saline soils.

FUNDING

The work was carried out within the framework of the grant project IRN AP23487733

CONFLICT OF INTEREST

The authors declare no conflict of interest related to this study.

DATA AVAILABILITY STATEMENT

The raw data supporting the conclusions of this article will be made available by the authors on request.

AUTHOR CONTRIBUTIONS

IS - supervision, writing, original preparation; AS - writing-review and editing; BG - formal analysis; MA - funding acquisition; YR - visualization. All authors have read and agreed to the published version of the manuscript.

AI STATEMENT

AI-assisted tools were used only for language translation, grammatical editing, and reference formatting.

REFERENCES

Afzal M., Hindawi S.E.S., Alghamdi S.S., Migdadi H.H. (2023) Potential breeding strategies for improving salt tolerance in crop plants. *Journal Plant Growth Regulation,* **42:** 3365-3387

Al Raish S.M., Sourani O.M., Abu-Elsaoud A M. (2025) Plant Growth-Promoting Microorganisms as Biocontrol Agents: Mechanisms, Challenges, and Future Prospects. *Applied Microbiology*, **5(2):** 44; doi: 10.3390/applmicrobiol5020044

Borovikov V.P. (2016) Popular introduction to modern data analysis in the STATISTICA 10.0 system, ver. 6. M.: Hot-Point Telecom. 288 p. (in Russian)

De Zutter N., Ameye M., Vermeir P., Verwaeren J., De Gelder L., Audenaert K. (2022) Innovative rhizosphere-based enrichment under P-limitation selects for bacterial isolates with high-performance P-solubilizing traits. *Microbiology Spectrum,* **10:** e02052-22; doi: 10.1128/spectrum.02052-22.

Eldala.kz report: Kazakhstan's pastures are in poor to very poor condition (2024) URL: https://eldala.kz/novosti/kazahstan/18026-82-pastbishch-kazahstana-v-plohom-i-ochen-plohom-sostoyanii (in Russian)

Esengalieva S.M., Mansurova M.A., Makhmudov A.D., Fedorchenko L.V. (2021) Current state and development trends of animal husbandry in the Republic of Kazakhstan. Economy: strategy and practice, **2(16):** 134-144 (in Russian)

FAO report: The State of the World's land and water resources for food and agriculture (2025) URL: https://www.unwater.org/news/fao-report-state-world's-land-and-water-resources-food-and-agriculture-2025

Guardado-Fierros B.G., Tuesta-Popolizio D.A., Lorenzo-Santiago M.A. et al. (2024) Comparative study between Salkowski reagent and chromatographic method for auxins quantification from bacterial production. *Frontiers of Plant Science*, **15:** 1378079; doi: 10.3389/fpls.2024.1378079

Hossain T.J. (2024) Methods for screening and evaluation of antimicrobial activity: A review of protocols, advantages, and limitations. *European journal of microbiology and immunology*, **14(2):** 97-115; doi: 10.1556/1886.2024.00035

Jabborova D., Nurmatova M., Bisht N., Jabbarov Z. et al. (2025) Multipotential rhizobacteria simultaneously mitigate salinity stress and improve growth and physiological traits in black cumin (*Nigella sativa* L.). *Science Reports,* **15(1):** 42807; doi: 10.1038/s41598-025-26925-x.

Kumari P., Gupta R.K., Singh A. (2025) Estimation of 1-Aminocyclopropane-1-Carboxylic Acid (ACC) Deaminase Enzyme in Bacteria. *Methods of Molecular Biology*, **2945**: 3-10; doi: 10.1007/978-1-0716-4650-2_1.

Le T.T., Nguyen P.T., Van Pham T., Nguyen T.O. (2025) Effects of nutrient solutions on growth, yield and quality of yardlong bean plant (*Vigna unguiculate subsp. Sesquipedalis* L.) grown in a hydroponic system. *Horticultural Science*, **52(4):** 333-341; doi: 10.17221/1/2025-HORTSCI

Liang R., Zhong L., Huang Z., Wang W., Lu G., Zhu T. (2025) Plant growth-promoting rhizobacteria isolated from natural habitats promote the growth of *Elymus sibiricus* and enhance its resistance to abiotic stress. *Plant-Environment Interactions*, **6(6):** e70106; doi: 10.1002/pei3.70106

Montes-Luz B., Conrado A. C., Ellingsen J. K., Monteiro R. A., deSouza E. M., Stacey G. (2023) Acetylene reduction assay: A measure of nitrogenase activity in plants and bacteria. *Current Protocols*, **3:** e766; doi: 10.1002/cpz1.766

Nuruzzaman M., Bahar M.M., Naidu R. (2025) Diffuse soil pollution from agriculture: Impacts and remediation. *Science of the total environment*, **962:** 178398; doi: 10.1016/j.scitotenv.2025.178398

Pathak A., Rabani M.S., Shrivastav M. et al. (2026) Mechanistic insights into plant growth promoting rhizobacteria with focus on root soil interactions, functional attributes and agricultural sustainability. *Discovery Biotechnology*, **3:** 1; doi: 10.1007/s44340-025-00046-7

Shi Z., Guo X., Lei Z. et al. (2023) Screening of high-efficiency nitrogen-fixing bacteria from the traditional Chinese medicine plant *Astragalus mongolicus* and its effect on plant growth promotion and bacterial communities in the rhizosphere. *BMC Microbiology,* **23:** 292; doi: 10.1186/s12866-023-03026-1.

Tarolli P., Luo J., Park E., Barcaccia G., Masin R. (2024) Soil salinization in agriculture: Mitigation and adaptation strategies combining nature-based solutions and bioengineering. *Science*, **27(2):** e108830; doi: 10.1016/j.isci.2024.108830

Yang P., Condrich A., Scranton S., Hebner C. et al. (2024) Utilizing plant growth-promoting

rhizobacteria (PGPR) to advance sustainable agriculture. *Bacteria*, **3(4):** 434-451; doi: 10.3390/bacteria3040030

Zhang T., Jian Q., Yao X., Guan L. et al. (2024) Plant growth-promoting rhizobacteria (PGPR) improve the growth and quality of several crops. *Heliyon*, **10 (10):** e31553; doi: 10.1016/j.heliyon.2024.e31553

ORCIDs:

Irina Smirnova: http://orcid.org/0000-0001-5854-1529
Amankeldi Sadanov: http://orcid.org/0000-0002-2593-6302
Gul Baimakhanova: http://orcid.org/0000-0001-5416-3209
Marat Aldabergenov: http://orcid.org/0000-0001-6421-2668
Yaira Rakhmetova: http://orcid.org/0009-0007-8259-7953

Carbon footprint-yield relationships in sorghum as influenced by agronomic input intensity

Zain ul Sajjad

Department of Agronomy, PMAS Arid Agriculture University Rawalpindi, 46300, Pakistan

***For correspondence**: zainulsajjad.edu@gmail.com*

Received: March 06, 2026; Reviewed: May 23, 2026; Accepted: June 05, 2026

The challenge of significantly increasing food demand while reducing greenhouse gas emissions represents a two-pronged challenge for sorghum production, but the relationship between agronomic intensity and carbon efficiency remains unresolved. The absence of integrated multi-season analyses limits the development of climate-smart management strategies. In this research paper, the researcher examined the impact of graded input levels on grain yield, biomass production, and the carbon footprint of sorghum under semi-arid conditions. A randomized complete block experiment was conducted across two consecutive growing seasons using low-, medium-, and high-input regimes, and fertilizer consumption, mechanization, and agrochemical inputs were measured. The absolute and yield-scaled carbon footprints were calculated using life cycle assessment, and linear mixed-effects models were employed to study treatment effects across seasons. Intensification increased grain yield (3.12 to 5.44 t ha^{-1}) and above-ground biomass (7.73 to 13.63 t ha^{-1}) significantly ($p < 0.001$), whereas absolute carbon emissions increased from 891 to 1645 kg CO_2-eq ha^{-1}. The carbon footprint scaled by yield remained relatively constant at 286–303 kg CO_2-eq ha^{-1}, indicating a structural relationship between biomass formation and emissions. These results indicate that intensification shifts the production curve along a predictable yield-emission trajectory without altering carbon efficiency, offering practical conclusions for sustainable intensification practices in semi-arid cereal production.

Keywords**:** *Sorghum, carbon footprint, yield-scaled emissions, agronomic intensification, life cycle assessment, biomass production, sustainable agriculture*

INTRODUCTION

Sorghum (*Sorghum bicolor* L.) is a widely cultivated cereal with significant agronomic and economic importance, especially in semi-arid and drought-prone regions, where its ability to withstand water shortages and extreme temperatures makes it an important food security crop (Hadebe et al., 2017; Hossain et al., 2022). As global agricultural production faces the dual challenges of increasing food demand and mitigating climate change, measuring the environmental impacts of crop production has become a central research priority (Toromade et al., 2024; Farooq et al., 2022). In this context, the carbon footprint, defined as the total greenhouse gas (GHG) emissions generated during crop production and expressed in CO_2-equivalents per unit area or yield, serves as an essential indicator linking agronomic management practices with climate impacts (Linquist et al., 2012).

The intensity of inputs, including synthetic fertilizers, mechanization, and chemical weed management techniques, has a direct impact on biomass accumulation, nitrogen transformations, fuel consumption, and the production of upstream agrochemicals, which are critical factors in agronomic management (Nath et al., 2024; Monteiro & Santos, 2022; Idris et al., 2026). Yield, in turn, affects the yield-scaled carbon footprint, which quantifies emissions per tonne of grain harvested and combines productivity and environmental efficiency into a single performance measure (Jagadesh et al., 2024). The literature has shown that high input intensity tends to boost yield and overall biomass but may simultaneously increase per-hectare GHG emissions, creating a multifaceted trade-off between productivity and environmental impact (Harrison et al., 2021; Henry et al., 2018; Hajiyeva, 2025).

Most research focuses only on total emissions or crop yields. Scientists rarely combine these factors into a single model. This makes it difficult to understand the real relationship between productivity and carbon efficiency (Shi et al., 2013). Moreover, inter-annual variability, which can strongly influence both yield and emissions, is rarely represented across multiple seasons in field-level research. These limitations affect the capacity to develop evidence-based strategies for climate-

 DOI: https://doi.org/10.62088/timbb/10.1.4

sensitive intensification of sorghum and other cereal systems (Wakjira et al., 2025; Panicker, 2025).

Although yield–carbon dynamics in cereals such as maize and wheat have been investigated, several gaps remain concerning sorghum. First, there is limited knowledge regarding the simultaneous quantification of absolute and yield-scaled carbon footprints at different levels of agronomic input intensity. This restricts the understanding of the effectiveness of intensive production systems. Second, previous studies are often based on single-season observations (Li et al., 2024). Such approaches limit the strength of inferences regarding whether observed patterns are maintained under climatic variability, particularly in the absence of hierarchical experimental designs (Johnston et al., 2021; Moore & MacDonald, 2024). Third, the mechanistic basis of the possible decoupling of per-hectare emissions and yield-based carbon footprints, resulting from biomass accumulation, nitrogen interactions, and mechanization, remains insufficiently investigated in sorghum.

Therefore, important questions remain: How do agronomic input intensities influence the structural relationship among yield, biomass, and absolute GHG emissions? Does an increase in input intensity impair or maintain yield-scaled carbon efficiency, and does this relationship vary across growing seasons? Answers to these questions are necessary to inform climate-smart strategies for sorghum production in which yield maximization is not accompanied by increased unit-based emissions.

The objective of this study is to rigorously quantify the relationship between sorghum productivity and carbon footprint under contrasting levels of agronomic input intensity across two successive growing seasons. We hypothesize that increasing intensification will augment grain yield and absolute emissions, yet may not substantially alter the yield-scaled carbon footprint because of the coupled scaling relationship between biomass production and emissions.

In order to confirm this hypothesis, we designed a randomized complete block field experiment with three levels of input intensity: low, medium, and high, while keeping the cultivar, sowing date, row spacing, and target plant population constant. Detailed field-level data on fertilizer and agrochemical application, mechanization, labour, and fuel consumption were used to perform a transparent life-cycle assessment of carbon emissions, including direct, indirect, and upstream contributions expressed in CO_2-equivalents per hectare and per tonne of grain. Grain yield, above-ground biomass, and harvest index were measured to help explain the mechanistic basis of productivity–emissions interactions.

The three crucial innovations of this paper are:

1. Systematic quantification of absolute and yield-scaled carbon footprints across graded input intensities, indicating trade-offs between productivity and emissions efficiency.

2. A combination of multi-season field data to measure inter-annual variability, enabling more robust inferences regarding the stability of yield–carbon relationships.

3. A biomechanistic linkage among biomass growth, harvest index, and carbon emissions, allowing the identification of structural limitations affecting the efficiency of intensified sorghum production.

Unlike previous studies that focus solely on yield response or per-hectare emissions, this work explicitly describes the structural linkage between productivity and emissions, providing a framework within which climate-smart management in sorghum and other cereal systems can be evaluated.

The remainder of the paper is organized as follows: Section 2 outlines the experimental design, agronomic treatments, and carbon footprint calculation methods. Section 3 presents the results for grain yield, biomass, absolute emissions, and yield-scaled emissions across two growing seasons. Section 4 discusses the implications for climate-smart agronomy, the mechanistic interpretation of yield–carbon coupling, and potential mitigation strategies. Finally, Section 5 summarizes the conclusions and future research directions.

MATERIALS AND METHODS

Study design and experimental site

The experiment was a multifactor field study designed to quantify the magnitude of yield–carbon footprint trade-offs in sorghum under varying levels of agronomic input intensity. A randomized complete block design was implemented across two successive growing seasons to specifically evaluate inter-annual variability. Each treatment was replicated three times per season.

Experimental plots were established on a semi-arid research farm characterized by homogeneous topography and loamy soil representative of regional sorghum production systems. To characterize baseline soil conditions (0–30 cm depth), soil texture, pH, organic carbon, total nitrogen, and available phosphorus were measured using standardized laboratory procedures to ensure comparability among plots.

Agronomic treatments and input intensity definition

Agronomic input intensity was defined a priori as a categorical management factor with three levels:

low, medium, and high. These levels differed systematically in fertilizer application rate, degree of mechanization, and weed control strategy, while cultivar, sowing date, row spacing, and target plant population remained constant. This approach enabled the isolation of management-related differences in productivity and emissions.

All field operations were recorded in real time, including machinery type, fuel consumption, fertilizer formulation, application timing, and labour inputs, thereby ensuring transparent carbon accounting.

Measuring yield and supporting agronomic data

Grain yield was determined at physiological maturity by harvesting the net plot area while excluding border rows. Grain moisture content was standardized to 12% prior to yield calculation, and results were expressed as tonnes per hectare (t/ha).

Subsamples were collected to determine above-ground biomass and harvest index in order to support the interpretation of yield responses under different input regimes. Daily weather data were obtained from an on-site automated meteorological station and were used descriptively to contextualize seasonal differences rather than as covariates in statistical analyses.

Quantification of carbon footprint

A cradle-to-farm-gate life cycle assessment framework was used to estimate the carbon footprint. Emission sources included upstream production of fertilizers and agrochemicals, direct and indirect field emissions associated with nitrogen application, and on-farm energy consumption resulting from mechanized operations.

Emission factors were primarily derived from the IPCC Tier 1 methodology and supplemented with regionally specific coefficients where available. Total greenhouse gas emissions were expressed as carbon dioxide equivalents (kg CO_2-eq ha^{-1}), allowing the aggregation of emissions from multiple sources into a single metric.

Formula & quantitative protocol

The total carbon footprint (CF) of each plot was given as:

"CFijk=" ∑_"m=1" ^"n" ▒"Am,ijk × EFm"

Where Am,ijk is the activity data of input m with input intensity i, year j, and block k, and EFm is the resultant emission factor (kg CO_2-eq $unit^{-1}$).

Yield-scaled carbon footprint (YCF) was determined as:

YCFijk=" "CFijk" / "Yijk

Yijk refers to the yield of grain (t ha^{-1}). Every amount was converted to SI units, and the equations were put in an editable form to comply with journal reproducibility criteria.

The life cycle analysis in this paper assumed a cradle-to-farm-gate method, which included upstream manufacturing of fertilizers and agrochemicals, on-farm energy consumption, and both direct and indirect N_2O emissions during fertilization. The change in soil carbon stock was not categorized as part of the LCA boundary because of the limited time scale of the experiment and the inherent uncertainty during measurement of small annual changes in soil organic carbon under field conditions (Sevenster et al., 2020).

Statistical analysis and model specification

Linear mixed-effects models were applied to analyse the data in order to reflect the hierarchical structure of the experiment and prevent inflation of Type I error. Agronomic input intensity was considered a fixed effect, whereas year and block were considered random effects within year. The following was the base model of the responses of yield and carbon footprint:

$$Yijk=\mu + Ii + uj + bk(j) + \varepsilon ijk$$

Equation 1, where μ denotes the general mean, Ii denotes the fixed effect of input intensity, uj denotes the random effect of year, bk(j) denotes the random effect of block within year, and εijk denotes the error term. Experimental and analytical procedures are summarized in Table 1.

Table 1: Overview of experimental design and methodology for sorghum yield–carbon footprint study

Component	Key Details
Design	Randomized complete block, 3 replicates, 2 consecutive seasons
Site & Soil	Semi-arid farm; loamy soil; baseline characterization: texture, pH, organic C, total N, available P
Input Intensity	Low, Medium, High; varied fertilizer, mechanization, weed control; cultivar, sowing, row spacing, plant population constant
Yield & Biomass	Grain harvested at physiological maturity (12% moisture); aboveground biomass and harvest index measured
Carbon Footprint	Cradle-to-farm-gate LCA including upstream inputs, N emissions, on-farm energy; reported as kg CO_2-eq ha^{-1} and t^{-1}
Analysis	Linear mixed-effects models (input fixed; year/block random); Tukey HSD for pairwise comparison; residual diagnostics for normality
Data Integrity	Standardized sampling, instrument calibration, independent cross-checks; analyses performed in R (v4.3.0, lme4 & emmeans)

Hypothesis tests on model assumptions of normality and homoscedasticity were performed using residual diagnostics. Where fixed effects were found to be important, pairwise analysis of treatment means was applied using the honestly significant difference (HSD) test at 0.05, in line with the editorial expectations of an agronomic field study. R

(4.3.0) was used to perform all analyses using the lme4 and emmeans packages.

Data quality control

The procedure of this study included instrument calibration, standardized sampling protocols, and cross-checking of data entry. None of the data points were eliminated except when measurement errors were clearly recorded. All statistical outputs were confirmed as internally consistent and then reported.

Ethics and compliance statement

The study did not involve human subjects or animals and therefore did not require the intervention of an ethics committee. Field testing and environmental evaluation were conducted in line with internationally recognized agronomic research criteria. As illustrated in Fig. 1, the data were not generated or statistically modeled using any artificial intelligence tools; all calculations were performed using traditional statistical software and equations.

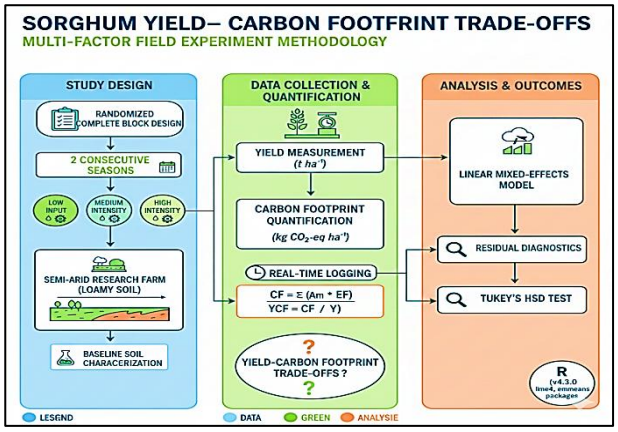

Fig. 1. Methodological framework for sorghum yield–carbon footprint assessment.

Combined decision process to assess the eco-efficiency of sorghum. The empirical basis of cradle-to-gate carbon accounting was based on a two-year RCBD trial with three management intensities: low, medium, and high. The data were collected through real-time field logging using standardized yield measures. Linear mixed-effects modelling was used to obtain yield-scaled carbon footprints (YCF), which measure the trade-offs between productivity and greenhouse gas emissions, and to isolate management signals from environmental variation.

RESULTS AND DISCUSSION

Effects of agronomic input intensity on grain yield and biomass production

The increase in above-ground biomass and grain yield occurred systematically with increasing agronomic input intensity during both growing seasons (Fig. 2; Table 2). At low input intensity, the mean grain yield was 3.12 t ha^{-1}, whereas at medium and high input intensities, it was 4.51 t ha^{-1} and 5.44 t ha^{-1}, respectively. Similarly, above-ground biomass ranged from 7.73±0.71 t ha^{-1} (low), to 11.00±0.87 t ha^{-1} (medium), and 13.63±0.51 t ha^{-1} (high).

The grain yield was significantly affected by input intensity ($F(2,12)=102.30$, $P < 0.001$) in the mixed-effects analysis (Table 4a). The effects of year ($F(1,12)=0.03$, $p=0.88$) and input intensity × year ($F(2,12)=1.15$, $p=0.35$) were not significant, suggesting that the treatment effects remained consistent across years. The fixed-effects estimates (Table 3a) showed that grain yield was lower by 2.44 t ha^{-1} at low input intensity ($z=-13.63$, $p < 0.001$) and 1.18 t ha^{-1} at medium input intensity ($z=-6.58$, $p < 0.001$) relative to high input. The year effect was minimal and non-significant (−0.23±0.18 t ha^{-1}; $z=-1.27$, $p=0.20$), and no interaction terms were significant ($p > 0.05$). All input intensities were significantly different from each other (Table 5), as determined by Tukey's HSD pairwise comparison.

High input yielded 2.31 t ha^{-1} more than low input (95% CI: −2.72 to −1.90, $p < 0.001$) and 0.93 t ha^{-1} more than medium input (95% CI: −1.34 to −0.52, $p < 0.001$), while medium input exceeded low input by 1.38 t ha^{-1} (95% CI: 0.97 to 1.79, $p < 0.001$), defining a strictly monotonic productivity gradient with increasing management intensity.

There was no significant difference in the harvest index between treatments or years (Fig. 2; Table 2), with mean values remaining very close, ranging from 0.40 to 0.41 ($p=0.148$). Thus, the variation in grain yield was a result of variation in total biomass production rather than differential partitioning of assimilates, consistent with well-known sorghum physiology (Bhattacharya, 2022).

This positive relationship between management intensity and grain yield and above-ground biomass is similar to findings from previous studies on sorghum and other C_4 cereals (Mullet, 2017), in which fertilizer inputs and mechanization influence canopy development and radiation interception (Olson et al., 2012; Punia et al., 2020).

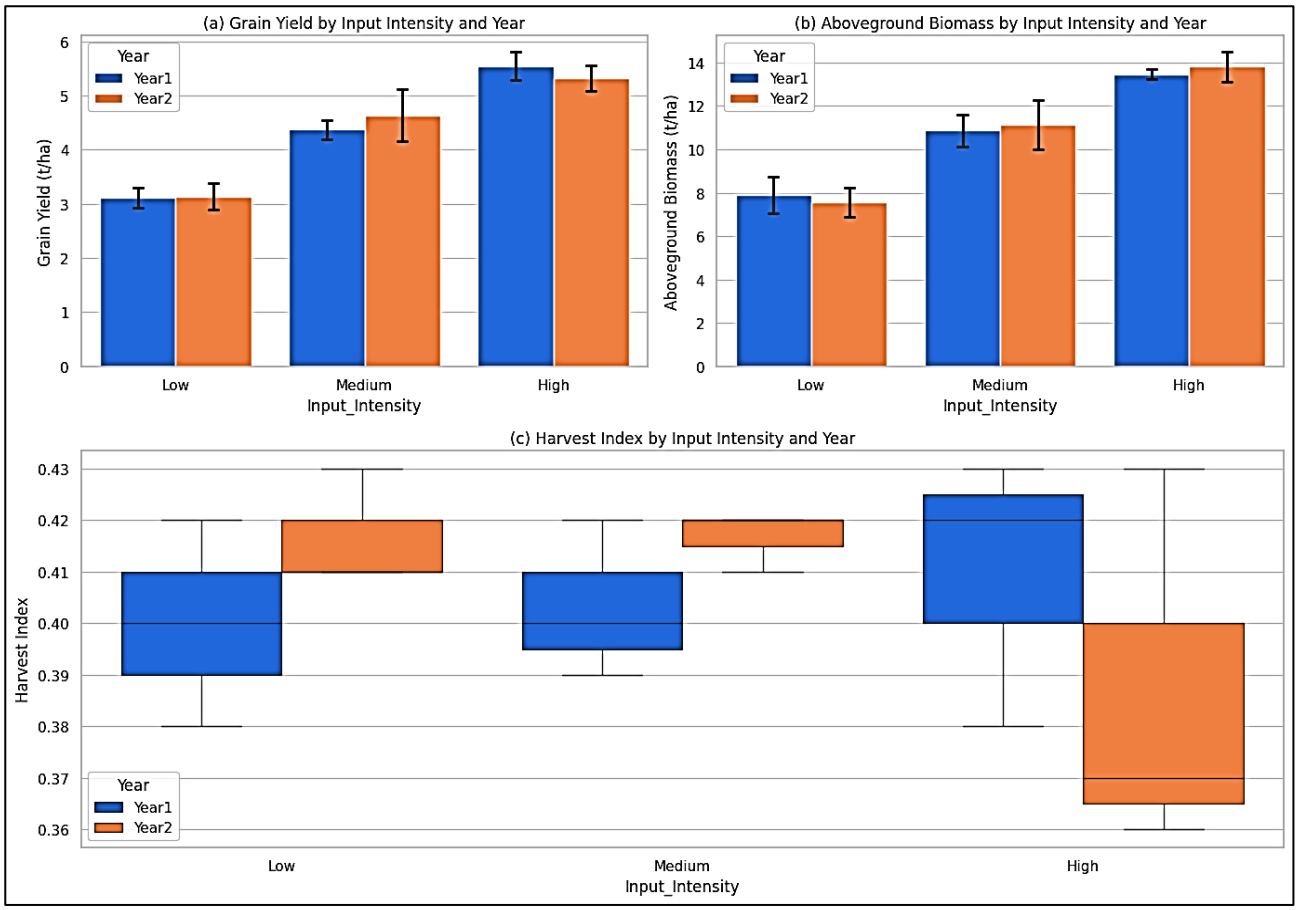

Fig. 2. Grain yield, above-ground biomass, and harvest index measured at two levels of input (low and medium) and two consecutive years (consecutive) plotted on a bar graph.

The overall robustness of treatment responses within the current climatic envelope is suggested by the absence of significant year and interaction effects, supporting the findings of Bareille and Chakir (2024). While this may imply that the high-input treatment was not close to the local agronomic optimum, yield increases were nearly linear across the range of input intensities tested, rather than exhibiting the diminishing marginal yield returns commonly observed under high nitrogen application (Reich et al., 2022).

Effects of agronomic input intensity on absolute carbon footprint

The higher the agronomic input intensity, the higher the absolute greenhouse gas emissions per hectare (Fig. 3; Table 2). The mean carbon footprints were 891.02±86.41 kg CO_2-eq ha^{-1} (low), 1296.58±117.23 kg CO_2-eq ha^{-1} (medium), and 1644.83±69.13 kg CO_2-eq ha^{-1} (high). The effect of input intensity on the carbon footprint was significant (Table 4b; $F(2,12)=109.51$, $p < 0.001$). The year effect ($F(1,12)=2.26$, $p=0.16$) and the interaction between input intensity and year ($F(2,12)=1.20$, $p=0.33$) were not significant, indicating that the emission response to management intensity did not vary by season.

The mixed-effects model (Table 3b) estimated emission reductions of 742.93±59.98 kg CO_2-eq ha^{-1} ($z=-12.39$, $p < 0.001$) and 410.57±59.98 kg CO_2-eq ha^{-1} ($z=-6.84$, $p < 0.001$) at low and medium intensities, respectively, relative to high intensity. The year effect was neither significant nor large (28.33±59.98 kg CO_2-eq ha^{-1}; $z=0.47$, $p=0.64$), and no interaction terms approached significance ($p > 0.14$).

As illustrated in Figure 3, these results indicate a close linear relationship between absolute emissions per unit land area and agronomic intensification, similar to the relationship observed for crop productivity. The linear trends between carbon footprint and input intensity can be explained by fertilizer-driven intensification, as observed in maize and wheat systems, where most emissions are associated with upstream input production (Fu et al., 2024; Han et al., 2024; Lin et al., 2025; Zhou et al., 2025). Unlike mechanized or irrigation-based systems, where the emissions budget may be more independent, the current fertilizer-based system generates proportional responses in both yield and emissions (Yang et al., 2023).

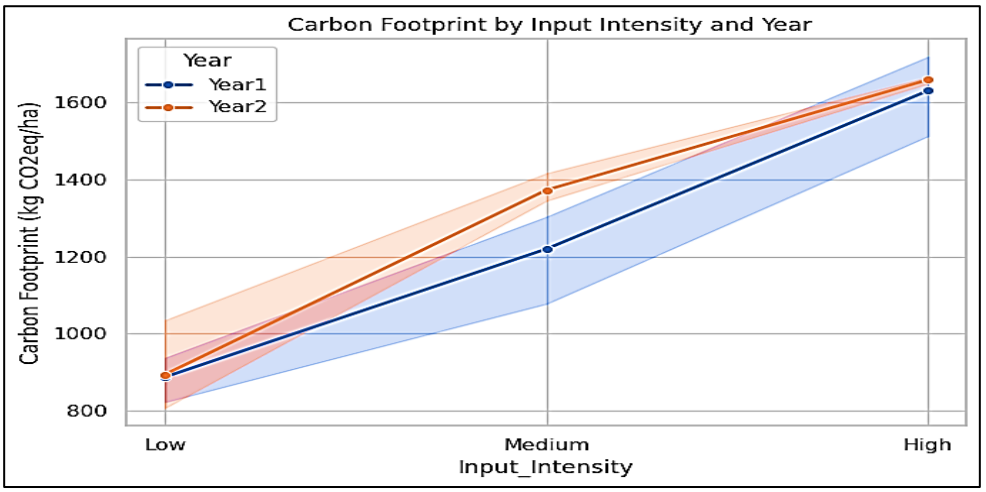

Fig. 3. Two growing seasons (Year 1 and Year 2) were calculated for each agronomic input intensity for the carbon footprint per hectare (kg CO_2-eq ha^{-1}).

Interannual climatic variability did not significantly affect this structural relationship, as evidenced by the small and non-significant year effect. This finding is consistent with observations reported for other semi-arid cereal systems (Zhang et al., 2023).

Yield-scaled carbon footprint and carbon efficiency

Although grain yield and absolute emissions differed significantly at the statistical level between treatments, the yield-scaled carbon footprint (kg CO_2-eq t^{-1} grain) was not significantly different among the input intensity treatments (Fig. 4; Tables 2 and 6). Mean values were 285.72±30.77 (low), 288.87±33.25 (medium), and 303.05±19.42 kg CO_2-eq t^{-1} (high). Tukey HSD tests (Table 6) confirmed no significant contrasts: high vs. low=−17.33 kg CO_2-eq t^{-1} (95% CI: −60.00 to 25.34, p=0.56); high vs. medium=−14.18 kg CO_2-eq t^{-1} (95% CI: −56.85 to 28.49, p=0.67); low vs. medium=3.15 kg CO_2-eq t^{-1} (95% CI: −39.52 to 45.82, p=0.98). Intensification resulted in a considerable increase in production and overall per-hectare emissions while maintaining the carbon efficiency of grain production on a yield-scaled basis.

As suggested by the findings of Adlan et al. (2025), this finding suggests that production intensification can move along a land-based emissions curve without altering the carbon intensity per unit product. This is in contrast to research that has shown reduced emission intensity under intensification (Costa et al., 2025; Infante & Aguilera, 2024), where significant yield improvements were made with relatively minor increases in inputs. The difference in the present case is probably because both yields and emissions were motivated by the same input, with a relatively small technological gradient. The moderate correlation between the yield-scaled carbon footprint and absolute emissions (r=0.44) also suggests that the input structure limits efficiency measures (Fig.4).

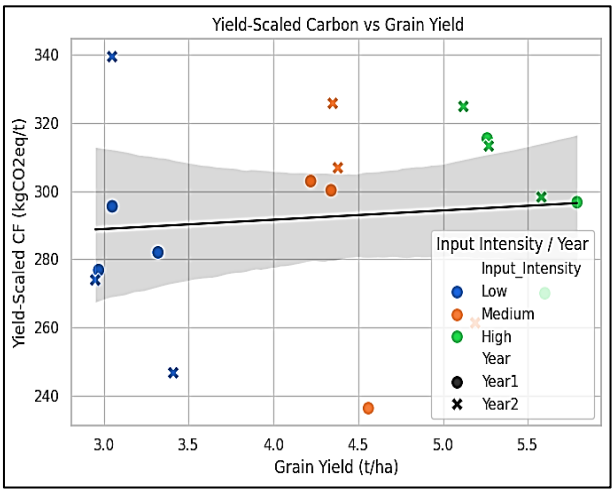

Fig. 4. Relationships between grain yield and yield-scaled carbon footprints, stratified by the level of inputs and the year of the growing season.

Relationships between yield, biomass, and carbon footprint

The absolute carbon footprint of the three input intensity treatments was positively correlated with grain yield for all years (Fig. 5), as low input intensity systems were in the low-yield/low-emission zone, medium input intensity systems were in the middle, and high input intensity systems were in the high-yield/high-emission zone. The Pearson correlation matrix (Fig. 6) quantifies this structure. Grain yield was strongly correlated with aboveground biomass (r=0.97) and carbon footprint/ha (r=0.93), and strongly correlated with aboveground biomass (r=0.92) for carbon footprint, indicating that higher-emitting systems had higher biomass production.

The yield-scaled carbon footprint was only

weakly related to grain yield (r=0.10) and moderately associated with the absolute carbon footprint (r=0.44), and had weak negative relationships with other variables. The harvest index showed only weak negative relationships with other variables, and the yield-scaled carbon footprint was only weakly associated with grain yield (r=0.10) and moderately associated with absolute emissions (r=0.44). The decoupling of the treatment effect on the absolute emission level from the lack of treatment effect on the yield-scaled level of emissions is explained by this correlation structure: intensification increased both yield and emission levels proportionally and did not significantly change the ratio of the two.

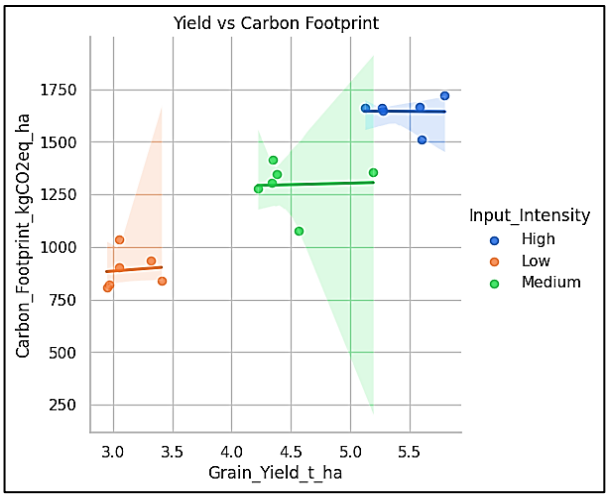

Fig. 5. Grain yield with observations colored by the level of absolute carbon intensity per hectare.

Causal architecture is reached when increases in yield are nearly perfectly correlated with increases in biomass (r=0.97) and biomass with carbon footprint (r=0.92), suggesting the existence of a single main axis of intensification, where more inputs are correlated with increased dry matter production and increased N-derived GHG emissions. Efficiency is achieved by using different (qualitatively) inputs and/or different ways of transforming nitrogen (Wang et al., 2025), noting that there is no efficiency gain in using more or less of the same input.

Model diagnostics and assumption checking

The linear mixed-effects models are presented with diagnostic plots in Figures 7, 8. The residual histogram was symmetric and unimodal, centered at zero, and the Q-Q plot indicated that the quantiles were close to the theoretical ones, with slight deviations at the tails. The patterns support the assumptions of normality and homoscedasticity and validate that the statistical inferences on yield and carbon footprint are valid.

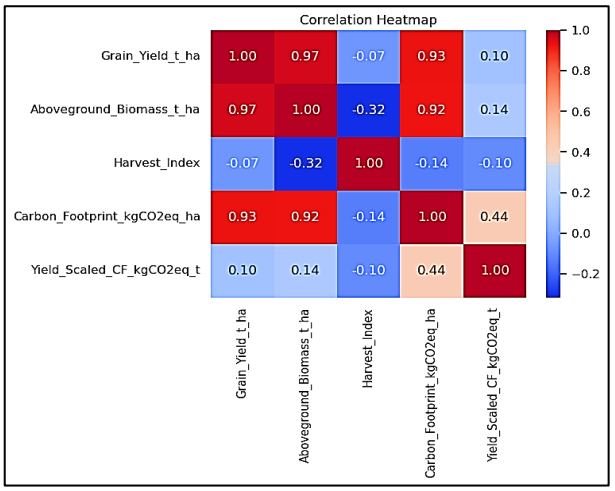

Fig. 6. All treatments and growing seasons were used to correlate key agronomic and environmental variables using a Pearson correlation heatmap.

Combined treatment effects and system-level interpretation

In both seasons, agronomic input intensity consistently and significantly improved grain yield, above-ground biomass, and absolute carbon footprint, but had no significant impact on harvest index or yield-scaled carbon footprint (Fig. 6). The interannual variation within treatments was small compared to treatment effects, as were the year and treatment year interaction terms in all mixed-effects models. Together, these results indicate that the intensification of sorghum production follows a regular yield-emission curve that does not compromise the C efficiency g kg-1 gr. This resolves an ongoing ambiguity in the intensification discussion and pinpoints the technology leverage point for emissions reductions (Singh, 2025; Biswas et al., 2022; Raseduzzaman et al., 2024; Pretty & Bharucha, 2014), which is the nature of inputs and not their intensity. In terms of land use, more grain per hectare at a known emission cost results in a higher input intensity. However, from a product perspective, intensification alone is insufficient to enhance carbon efficiency. This distinction is relevant to life cycle assessment methodology and mitigation policy (Schutzbach et al., 2025; McDonald et al., 2025): mitigation measures should focus on actions that will reduce the structural coupling between nitrogen throughput and biomass production (Tab.4a., 4b., Tab.5, Tab.6), such as using enhanced efficiency fertilizers, partial biological inhibition of N mineralization, or partial replacement of synthetic N.

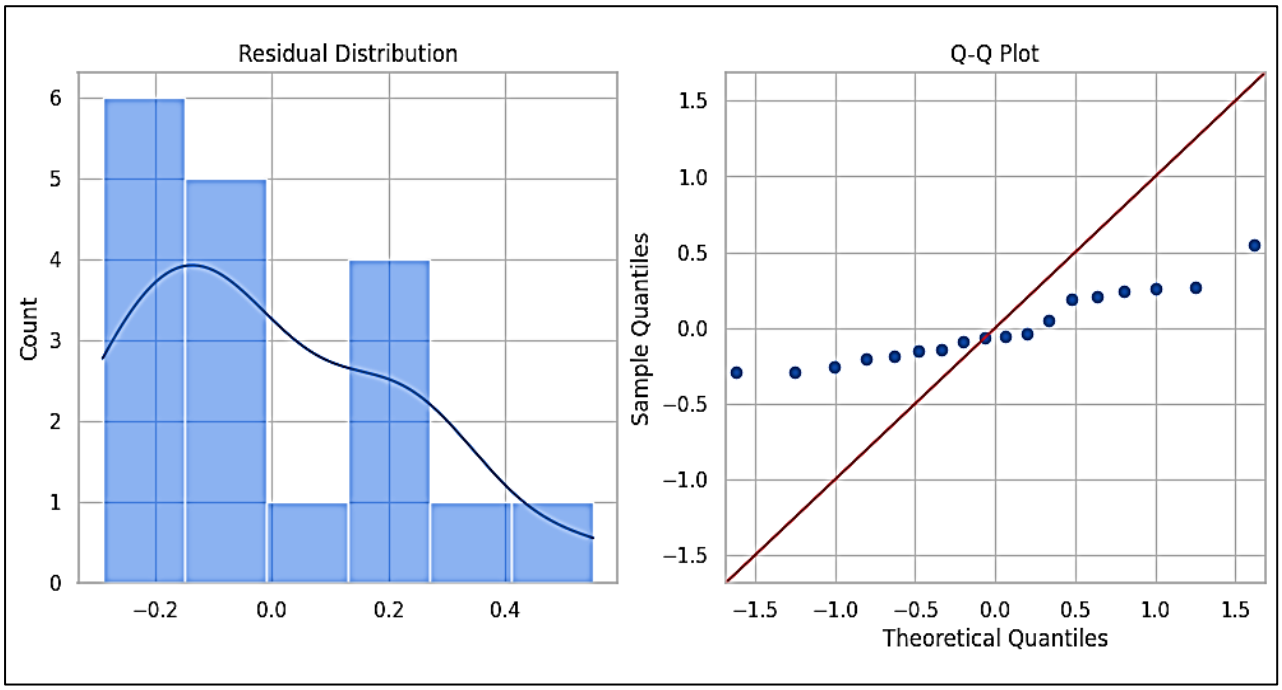

Fig. 7. Note the following diagnostic plots for the linear mixed-effects model: (a) a histogram of the residuals and (b) a normal Q-Q plot.

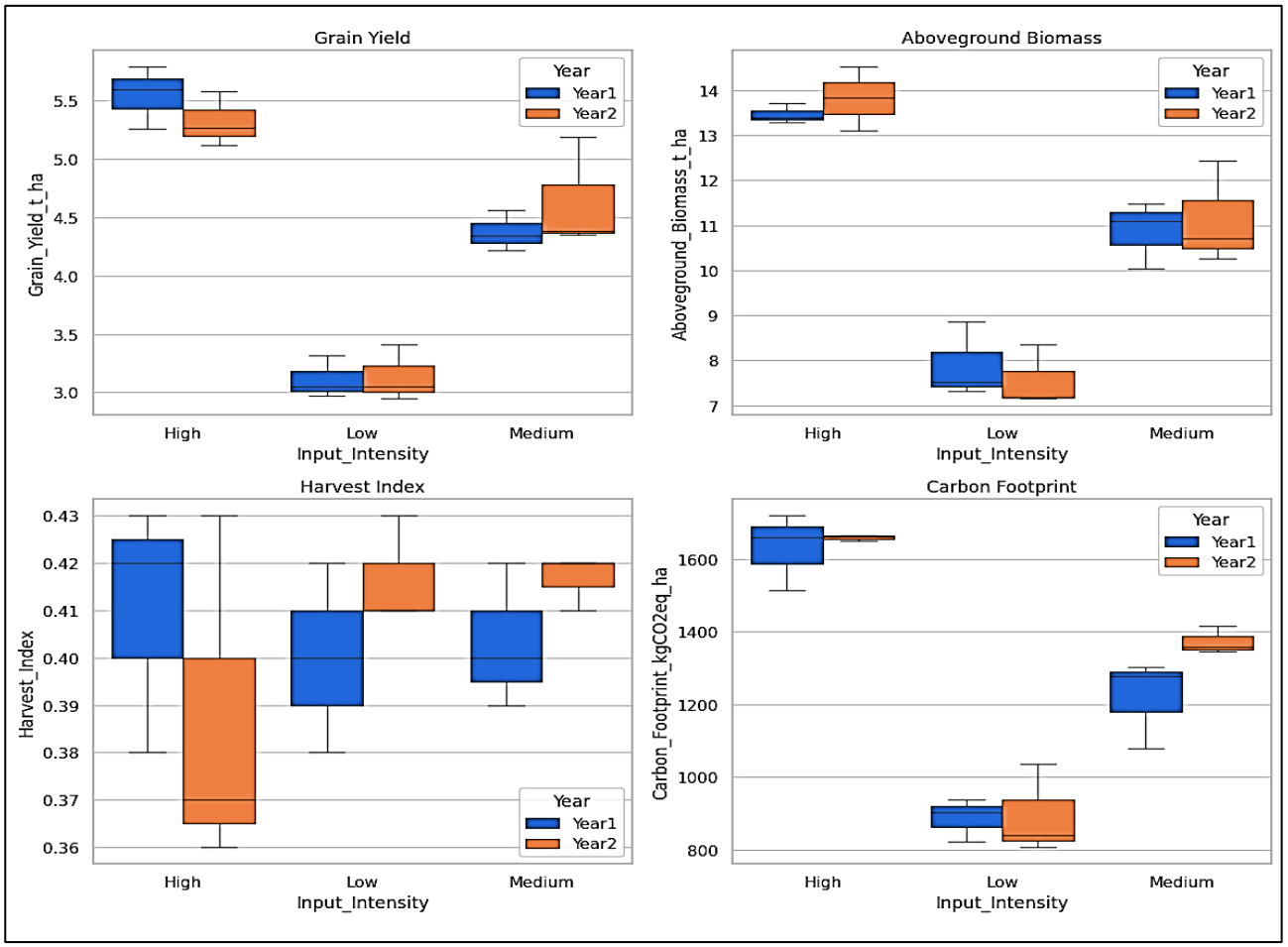

Fig. 8. For all input intensities and growing seasons, a summary of all measured response variables (grain yield, aboveground biomass, harvest index, and carbon footprint) was provided.

Table 2. Descriptive statistics by input intensity (p-values from mixed-effects models).

Variable	Mean	SD	Min	Max	p
A. High Input Intensity					
Grain Yield (t ha⁻¹)	5.44	0.26	5.12	5.79	<0.001
Above-ground Biomass (t ha⁻¹)	13.63	0.51	13.09	14.51	<0.001
Harvest Index	0.40	0.02	0.36	0.43	0.148
Carbon Footprint (kg CO_2-eq ha⁻¹)	1644.83	69.13	1512.90	1719.10	<0.001
Yield-Scaled C.F. (kg CO_2-eq t⁻¹)	303.05	19.42	270.00	324.80	0.468
B. Medium Input Intensity					
Grain Yield (t ha⁻¹)	4.51	0.35	4.22	5.19	<0.001
Above-ground Biomass (t ha⁻¹)	11.00	0.87	10.04	12.43	<0.001
Harvest Index	0.41	0.01	0.39	0.42	0.148
Carbon Footprint (kg CO_2-eq ha⁻¹)	1296.58	117.23	1077.80	1416.70	<0.001
Yield-Scaled C.F. (kg CO_2-eq t⁻¹)	288.87	33.25	236.30	325.70	0.468
C. Low Input Intensity					
Grain Yield (t ha⁻¹)	3.12	0.19	2.95	3.41	<0.001
Above-ground Biomass (t ha⁻¹)	7.73	0.71	7.16	8.86	<0.001
Harvest Index	0.41	0.02	0.38	0.43	0.148
Carbon Footprint (kg CO_2-eq ha⁻¹)	891.02	86.41	807.50	1035.30	<0.001
Yield-Scaled C.F. (kg CO_2-eq t⁻¹)	285.72	30.77	246.70	339.40	0.468

Table 3a. Mixed-effects model estimates of grain yield (t ha⁻¹).

Term	Coefficient	SE	z	p
Intercept	5.55	0.16	34.12	<0.001
Input Intensity [Low]	−2.44	0.18	−13.63	<0.001
Input Intensity [Medium]	−1.18	0.18	−6.58	<0.001
Year [Year 2]	−0.23	0.18	−1.27	0.20
Low × Year 2	0.25	0.25	0.99	0.32
Medium × Year 2	0.49	0.25	1.95	0.05
Group Variance	0.65	0.90	0.73	0.47

SE=standard error. Reference category: High input intensity, Year 1.

Table 3b. Mixed-effects model estimates of carbon footprint (kg CO_2-eq ha⁻¹).

Term	Coefficient	SE	z	p
Intercept	1630.67	50.98	31.98	<0.001
Input Intensity [Low]	−742.93	59.98	−12.39	<0.001
Input Intensity [Medium]	−410.57	59.98	−6.84	<0.001
Year [Year 2]	28.33	59.98	0.47	0.64
Low × Year 2	−21.77	84.83	−0.26	0.80
Medium × Year 2	124.63	84.83	1.47	0.14
Group Variance	0.44	0.67	0.66	0.51

SE=standard error. Reference category: High input intensity, Year 1.

Table 4a. Analysis of variance of grain yield.

Source	SS	df	F	p
Input Intensity	16.24	2	102.30	<0.001
Year	0.00	1	0.03	0.88
Input Intensity × Year	0.18	2	1.15	0.35
Residual	0.95	12	—	—

SS=sum of squares.

Table 4b. Analysis of variance of carbon footprint.

Source	SS	df	F	p
Input Intensity	1,708,003.90	2	109.51	<0.001
Year	17,646.94	1	2.26	0.16
Input Intensity × Year	18,720.11	2	1.20	0.33
Residual	93,578.02	12	—	—

SS=sum of squares.

Table 5. Tukey HSD pairwise comparisons of grain yield (t ha^{-1}).

Group 1	Group 2	Mean Diff.	p-adj	95% CI	Reject H_0
High	Low	−2.31	<0.001	−2.72 to −1.90	Yes
High	Medium	−0.93	<0.001	−1.34 to −0.52	Yes
Low	Medium	1.38	<0.001	0.97 to 1.79	Yes

Table 6. Tukey HSD pairwise comparisons of yield-scaled carbon footprint (kg CO_2-eq t^{-1}).

Group 1	Group 2	Mean Diff.	p-adj	95% CI	Reject H_0
High	Low	−17.33	0.56	−60.00 to 25.34	No
High	Medium	−14.18	0.67	−56.85 to 28.49	No
Low	Medium	3.15	0.98	−39.52 to 45.82	No

This study also highlights the need to report both area- and yield-scaled metrics because neither of these alone can adequately capture the performance of the system (Zong et al., 2025). Thus, this approach shows the importance of using mixed-effects modelling in combination with life-cycle analysis to unravel these relationships (Singh, 2025).

CONCLUSION

This experiment provides a quantitatively significant description of the agronomic yield-carbon footprint trade-off in sorghum at varying agronomic input intensities by showing that agronomic intensification increased grain yield by 3.12 to 5.44 t ha from 3.12 to 1.64 Mg CO_2-eq ha, respectively. Findings of this research imply that productivity and emission increase proportionally, hence maintaining yield-scaled carbon footprint among management regimes and explaining a structural relationship between biomass production and emissions. With the background of climate-smart agronomy, the findings can be used to construct a framework to differentiate between land-based efficiency and system-level mitigation. Although the study creates a strong seasonal consistency, its weakness lies in a two-year study and a one-site area. Responses at multiple locations should be experimented on in the future, and soil carbon dynamics and other nitrogen strategies should be incorporated. On the whole, the analysis shows that the reduction of emissions in sorghum systems will not rely as much on the intensity of inputs as it will depend on technological and biochemical points of leverage in intensified production systems.

DECLARATIONS

Funding

This research received no external funding.

Institutional Review Board Statement

Not applicable. This study did not involve human participants, human data, or animal subjects.

Data Availability Statement

The data supporting the findings of this study are available from the corresponding author upon reasonable request.

Conflicts of Interest

The author declares no conflict of interest.

Ethical Approval

The study was conducted in accordance with internationally accepted standards of agricultural and environmental research. No ethical approval was required because the research did not involve human participants or animals.

Acknowledgments

The author would like to thank the Department of Agronomy, PMAS Arid Agriculture University, Rawalpindi, Pakistan, for providing research facilities and technical support during the study.

Artificial Intelligence Statement

The author confirms that no artificial intelligence (AI) tools were used to generate, analyze, interpret, or manipulate the research data. Any use of AI-assisted tools for language improvement or proofreading, if applicable, did not influence the scientific content, results, interpretations, or conclusions of the study. The author takes full responsibility for the accuracy and integrity of the manuscript.

REFERENCES

Adlan C.A., **Hanssen S.V.**, **Luchtenbelt H.**, **Hendriks C.**, **Doelman J.C.**, **Stehfest E.**, **Wicke B.** (2025) Emissions footprints of agriculture around the world 1970–2020: Decreasing land conversion, regional exceptions and increasing management intensity. *Global Change Biology,* **31(10):** e70528.

Bareille F., **Chakir R.** (2024) Structural identification of weather impacts on crop yields: Disentangling agronomic from adaptation effects. *American Journal of Agricultural Economics,* **106(3):** 989–1019.

Bhattacharya A. (2022). Effect of low temperature on dry matter, partitioning, and seed yield: A review. In: *Physiological Processes in Plants Under Low Temperature Stress*, pp. 629–734.

Biswas J.C., **Haque M.M.**, **Hossain M.B.**, **Maniruzzaman M.**, **Zahan T.**, **Rahman M.M.**, ... **Hossain A.** (2022) Seasonal variations in grain yield, greenhouse gas emissions and carbon sequestration for maize cultivation in Bangladesh. *Sustainability,* **14(15):** 9144; doi: 10.3390/su14159144

Costa Jr.C., **Tedeschi L.O.**, **Gonzalez-Quintero R.**, **Arango J.**, **Burkart S.**, **Grosjean G.**, ... **Rao I.M.** (2025) South America's pasture intensification can increase beef production, reduce emissions by 30% and mitigate warming from methane by 2050. *Scientific Reports,* **15(1):** 35734; doi: 10.1038/s41598-025-35734-x

Farooq M.S., **Uzair M.**, **Raza A.**, **Habib M.**, **Xu Y.**, **Yousuf M.**, ... **Ramzan Khan M.** (2022) Uncovering the research gaps to alleviate the negative impacts of climate change on food security: A review. *Frontiers in Plant Science,* **13:** 927535; doi: 10.3389/fpls.2022.927535

Fu H., **Xie X.**, **Zhao K.**, **Chen D.**, **Hu S.**, **Li Y.**, ... **Shi L.** (2024) Tracking social-economic system nitrogen flow in China for emissions reduction and efficiency improvement. *Resources, Conservation and Recycling,* **207:** 107661; doi: 10.1016/j.resconrec.2024.107661

Hadebe S.T., **Modi A.T.**, **Mabhaudhi T.** (2017) Drought tolerance and water use of cereal crops: A focus on sorghum as a food security crop in sub-Saharan Africa. *Journal of Agronomy and Crop Science,* **203(3):** 177–191; doi: 10.1111/jac.12191

Hajiyeva S.T. (2025) Current aspects of small and medium entrepreneurship development in the agro-industrial sector of Azerbaijan. *Science, Education and Innovations in the Context of Modern Problems*, **8(2):** 144-167

Han K., **Li X.**, **Jia L.**, **Yu D.**, **Xu W.**, **Chen H.**, ... **Liu P.** (2024) Optimizing tillage and fertilization practices to improve the carbon footprint and energy efficiency of wheat-maize cropping systems. *Journal of Integrative Agriculture*.

Harrison M.T., **Cullen B.R.**, **Mayberry D.E.**, **Cowie A.L.**, **Bilotto F.**, **Badgery W.B.**, ... & **Eckard R.J.** (2021) Carbon myopia: The urgent need for integrated social, economic and environmental action in the livestock sector. *Global Change Biology,* **27(22):** 5726–5761; doi: 10.1111/gcb.15816

Henry B., **Murphy B.**, **Cowie A.** (2018). Sustainable land management for environmental benefits and food security: A synthesis report for the GEF. Global Environment Facility, Washington, DC, USA.

Hossain M.S., **Islam M.N.**, **Rahman M.M.**, **Mostofa M.G.**, **Khan M.A.R.** (2022) Sorghum: A prospective crop for climatic vulnerability, food and nutritional security. *Journal of Agriculture and Food Research,* **8:** 100300; doi: 10.1016/j.jafr.2022.100300

Idris S.A., **Saleh N.**, **Mikailu**, **Bashir L.R.** (2026) Impact of climate change on agriculture in Agatu Local Government Area, Benue State. *Science, Education and Innovations in the Context of Modern Problems,* **9(2):** 1–10; doi: 10.56334/sei/9.2.21

Infante-Amate J., **Aguilera E.** (2024) Beyond fossil fuels: Considering land-based emissions reshapes the carbon intensity of modern economic growth (Spain, 1860–2017). *Historical Methods: A Journal of Quantitative and Interdisciplinary History,* **57(4):** 226–241; doi: 10.1080/01615440.2024.2331315

Jagadesh M., **Dash M.**, **Singh S.K.**, **Kumari A.**, **Verma K.K.** (2024) Carbon footprints in agriculture: Challenges, mitigation strategies, and future prospects. In: *Carbon Footprint Assessments: Case Studies & Best Practices*, pp. 17–43. Springer Nature Switzerland: doi: 10.1007/978-3-031-58140-0_2

Johnston A., **Hochachka W.M.**, **Strimas-Mackey M.E.**, **Ruiz Gutierrez V.**, **Robinson O.J.**, **Miller E.T.**, ... **Fink D.** (2021) Analytical guidelines to increase the value of community science data: An example using eBird data to estimate species distributions. *Diversity and Distributions,* **27(7):** 1265–1277; doi: 10.1111/ddi.13271

Li X., **Li X.**, **Liu T.**, **Yin H.**, **Fu H.**, **Luo Y.**, ... **Chen Z.** (2024) Strategies for improving crop comprehensive benefits via a decision-making system based on machine learning in the rice-rape, rice-wheat and rice-garlic rotation systems in Southwest China. *Journal of Integrative Agriculture,* **23(9):** 2970–2988; doi: 10.1016/j.jia.2024.03.027

Lin S., **Liu K.**, **Lemke R.** (2025) Assessing cropping system effects on carbon footprint on the

Canadian prairies. *Soil Science Society of America Journal,* **89(2):** e70039; doi: 10.1002/saj2.70039

Linquist B., **Van Groenigen K.J.**, **Adviento-Borbe M.A.**, **Pittelkow C.**, **Van Kessel C.** (2012) An agronomic assessment of greenhouse gas emissions from major cereal crops. *Global Change Biology,* **18(1):** 194–209; doi: 10.1111/j.1365-2486.2011.02502.x

McDonald H., **Gardiner J.**, **Scheid A.**, **Siemons A.**, **Fallasch F.**, **Scheffler M.**, **Wiegmann K.** (2025) Temporary carbon units from carbon farming and EU agri-food climate policy. Assessment of risks, opportunities, and alternatives for promoting temporary carbon sequestration. Ecologic Institute, Berlin.

Monteiro A., **Santos S.** (2022) Sustainable approach to weed management: The role of precision weed management. *Agronomy,* **12(1):** 118; doi: 10.3390/agronomy12010118

Moore R.D., **MacDonald R.J.** (2024) James Buttle Review: Quantifying the influence of forestry and forest disturbance on stream temperature: Methodologies and challenges. *Hydrological Processes,* **38(7):** e15223; doi: 10.1002/hyp.15223

Mullet J.E. (2017) High-biomass C4 grasses—Filling the yield gap. *Plant Science,* **261:** 10–17; doi: 10.1016/j.plantsci.2017.05.015

Nath C.P., **Singh R.G.**, **Choudhary V.K.**, **Datta D.**, **Nandan R.**, **Singh S.S.** (2024) Challenges and alternatives of herbicide-based weed management. *Agronomy,* **14(1):** 126; doi: 10.3390/agronomy14010126

Olson S.N., **Ritter K.**, **Rooney W.**, **Kemanian A.**, **McCarl B.A.**, **Zhang Y.**, ... **Mullet J.** (2012) High biomass yield energy sorghum: Developing a genetic model for C4 grass bioenergy crops. *Biofuels, Bioproducts and Biorefining,* **6(6):** 640–655; doi: 10.1002/bbb.1357

Panicker A. (2025) Agriculture and climate change: Challenges ahead. Educohack Press.

Pretty J., **Bharucha Z.P.** (2014) Sustainable intensification in agricultural systems. *Annals of Botany,* **114(8):** 1571–1596; doi: 10.1093/aob/mcu205

Punia H., **Tokas J.**, **Malik A.**, **Satpal Rani A.**, **Gupta P.**, ... **Kumar S.** (2020). Solar radiation and nitrogen use efficiency for sustainable agriculture. In: *Resources Use Efficiency in Agriculture*, pp. 177–212. Springer Singapore. doi: 10.1007/978-981-15-6953-1_6

Raseduzzaman M., **Gaudel G.**, **Ali M.R.**, **Timilsina A.**, **Bizimana F.**, **Aluoch S.O.**, ... **Hu C.** (2024) Cereal-legume mixed residue addition increases yield and reduces soil greenhouse gas emissions from fertilized winter wheat in the North China Plain. *Agronomy,* **14(6):** 1167; doi: 10.3390/agronomy14061167

Reich P.B., **Bermudez R.**, **Montgomery R.A.**, **Rich R.L.**, **Rice K.E.**, **Hobbie S.E.**, **Stefanski A.** (2022) Even modest climate change may lead to major transitions in boreal forests. *Nature,* **608(7923):** 540–545; doi: 10.1038/s41586-022-05070-7

Schutzbach M., **Miehe R.**, **Sauer A.** (2025) Simplifying life cycle assessment: Basic considerations for approximating product carbon footprints based on corporate carbon footprints. *Ecological Indicators,* **176:** 113710; doi: 10.1016/j.ecolind.2025.113710

Sevenster M., **Luo Z.**, **Eady S.**, **Grant T.** (2020) Including long-term soil organic carbon changes in life cycle assessment of agricultural products. *The International Journal of Life Cycle Assessment,* **25(7):** 1231–1241; doi: 10.1007/s11367-019-01679-5

Sharma P. (2025) Modeling nitrous oxide (N_2O) emissions at different spatial and temporal scales Doctoral dissertation, Michigan State University.

Shi W., **Tao F.**, **Zhang Z.** (2013) A review on statistical models for identifying climate contributions to crop yields. *Journal of Geographical Sciences,* **23(3):** 567–576; doi: 10.1007/s11442-013-1039-5

Siddique I.A., **Grados D.**, **Chen J.**, **Lærke P.E.**, **Jørgensen U.** (2023) Soil organic carbon stock change following perennialization: A meta-analysis. *Agronomy for Sustainable Development,* **43(5):** 58; doi: 10.1007/s13593-023-00896-2

Singh N. (2025) Perenniality impacts on soil physical and hydraulic properties and ecosystem services: A review. *Sustainability,* **17(24):** 10988; doi: 10.3390/su172410988

Toromade A.S., **Soyombo D.A.**, **Kupa E.**, **Ijomah T.I.** (2024) Reviewing the impact of climate change on global food security: Challenges and solutions. *International Journal of Applied Research in Social Sciences,* **6(7):** 1403–1416; doi: 10.51594/ijarss.v6i7.1331

Ume C., **Kalu U.F.**, **Ezeibe A.B.C.**, **Ume C.S.**, **Ugwuoke C.O.**, **Onah O.**, **Joseph D.C.** (2025) Critical perspectives on the use of methanotrophs in rice farming: Advances in microbial climate mitigation. *Cleaner Food Systems,* **2:** 100005; doi: 10.1016/j.clfs.2025.100005

Wakjira M.T., **Peleg N.**, **Six J.**, **Molnar P.** (2025) Green water availability and water-limited crop yields under a changing climate in Ethiopia. *Hydrology and Earth System Sciences,* **29(4):** 863–886; doi: 10.5194/hess-29-863-2025

Wang F., **Arora C.**, **Liu Y.**, **Huang K.**, **Tantithamthavorn C.**, **Aleti A.**, ... **Lo D.** (2025) Multi-modal requirements data-based acceptance criteria generation using LLMs. *arXiv Preprint*, arXiv:2508.06888;

Yang Y., **Jin Z.**, **Mueller N.D.**, **Driscoll A.W.**, **Hernandez R.R.**, **Grodsky S.M.**, ... **Lobell D.B.** (2023) Sustainable irrigation and climate feedback. *Nature Food,* **4(8):** 654–663; doi: 10.1038/s43016-023-00796-0

Zhang J., **Zhu Z.**, **Hao H.** (2023) The effects of climate variation and anthropogenic activity on karst spring discharge based on the wavelet coherence analysis and the multivariate statistical approach. *Sustainability,* **15(11):** 8798; doi: 10.3390/su15118798

Zhou J., **Shao G.**, **Liu E.**, **Liu Q.**, **Yan C.**, **Alharbi S.A.**, ... **Kuzyakov Y.** (2025) Climate warming and agronomic practice interactively alter soil carbon stock in dry farmland in China. *Communications Earth & Environment,* **6(1):** 788; doi: 10.1038/s43247-025-01862-5

Zong M., **Yang X.**, **Li S.**, **Manevski K.**, **Jiaduo M.**, **Zhou S.**, ... **Abalos D.** (2025) Mismatch between soil nitrate and cumulative crop nitrogen uptake shape stage-specific N_2O emissions with legume cover crops under nitrogen reduction in dryland wheat systems. *Field Crops Research,* **333:** 110110; doi: 10.1016/j.fcr.2025.110110

ORCID:
Zain ul Sajjad: https://orcid.org/0009-0003-8354-8134

The effects of traditionally produced olive oil "Kara Yağ" and extra virgin olive oil from Northern Cyprus on hct-116 colon cancer cells

Özge Özden[1*], H. Seda Vatansever[2,3], Şebnem Güler[4], Salih Gücel[1], Cenk Serhan Özverel[3,5], Burak Durmaz[3,6], Meryem Demir[3], Mehmet Karagözlü[4], Tamer Şanlıdağ[3]

[1]Department of Landscape Architecture, Faculty of Agriculture, Near East University, Northern Cyprus
[2]Department of Histology and Embryology, Faculty of Medicine, Manisa Celal Bayar University, Manisa, Türkiye
[3]DESAM Research Institute, Near East University, Northern Cyprus
[4]Department of Food Engineering, Faculty of Agriculture, Near East University, Northern Cyprus
[5]Department of Basic Medical Sciences, Faculty of Dentistry, Near East University, Northern Cyprus
[6]Department of Medical Biochemistry, Faculty of Medicine, Near East University, Northern Cyprus

[*]***For correspondence:*** *ozge.ozden@neu.edu.tr*

Received: April 27, 2026; Reviewed: June 02, 2026; Accepted: June 15, 2026

Olive oil, a cornerstone of the Mediterranean diet, is renowned for its high content of phenolic compounds and its protective effects on human health. However, variations in production methods and raw material quality can significantly influence its chemical composition and biological activity. *Kara yağ*, a traditionally produced, unrefined olive oil unique to Northern Cyprus, is obtained through ancient artisanal extraction techniques and is rich in bioactive phenolics. This study aimed to investigate and compare the effects of *Kara yağ* and extra virgin olive oil (EVOO) on proliferation, viability, and apoptosis in HCT-116 human colon cancer cells. Samples of *Kara yağ* and EVOO were obtained from local producers in Northern Cyprus. Their physicochemical parameters, including free acidity, peroxide value, moisture content, and water activity, were analyzed in accordance with the Turkish Food Codex standards. Total phenolic content was determined using the Folin–Ciocalteu method, and antioxidant capacity was assessed spectrophotometrically. The high peroxide value (121.35 meq/kg) of *Kara yağ* is very high, which means that it was heavily oxidized throughout its conventional manufacturing process, and that heat treatment enhanced the chemical breakdown. Ochratoxin A (2.6 µg/kg) and aflatoxin B1 (0.8 µg/kg) were found in low levels of *Kara yağ* and therefore, the study is one of the first in the literature to analyze the toxin profile of the *Kara yağ*. The sensory analysis revealed that EVOO had distinct positive flavor qualities, but *Kara yağ* did not have them and high concentration of defects. HCT-116 cells were treated with different concentrations (1:1, 1:2, and 1:4) of each oil for 24, 48, and 72 hours. Cell viability was assessed by MTT assay, while morphological and apoptotic changes were evaluated by microscopy and immunocytochemical staining for Ki-67, Caspase-3, and c-Myc. *Kara yağ* exhibited significantly higher total phenolic content (278.95 mg GAE/kg) and antioxidant activity compared to EVOO. Treatment with *Kara yağ* led to a marked reduction in cell viability and proliferation in a time- and dose-dependent manner. Enhanced apoptotic activity, characterized by increased caspase-3 expression and decreased Bcl-2 levels, was observed following *Kara yağ* exposure. Both oils showed comparable c-Myc staining patterns. The findings suggest that *Kara yağ*, due to its superior phenolic composition and antioxidant potential, exerts stronger cytotoxic and pro-apoptotic effects on HCT-116 colon cancer cells than extra virgin olive oil. These results highlight the potential of traditionally produced *Kara yağ* as a natural source of bioactive compounds with promising chemopreventive and therapeutic properties against colon cancer. Further studies are warranted to elucidate the underlying molecular mechanisms and confirm its safety and efficacy in vivo.

Keywords: *Kara yağ; extra virgin olive oil, hct-116 colon cancer cell, ochratoxin A, aflatoxin B1*

INTRODUCTION

The species *Olea europaea*, belonging to the genus *Olea*, comprises six known subspecies: *europaea*, *guanchica*, *cerasiformis*, *maroccana*, *laperrinei*, and *cuspidata*. Three of these subspecies are found naturally in Europe and are found in parts of southwestern Atlantic Europe as well as the

Mediterranean basin, which includes Spain, Italy, Türkiye, Greece, Portugal, France, Cyprus, Slovenia, and Malta (Adun and Guler, 2025). Olives contain phenolic compounds that appear to have important health benefits because of their antioxidant nature, low-density lipoprotein (LDL) oxidative protection, and the possibility of inhibiting oxidative damage. Olive oil, recognized as a cornerstone of the Mediterranean diet, is distinguished by its rich composition of phenolic compounds and well-documented health-promoting properties. These phenols, flavonoids and phenolic acids play important roles in sensory properties and health effects of olive oil. It has been reported that the low prevalence of colorectal cancer in the Mediterranean basin is due to the antioxidant properties of hydroxytyrosol, tyrosol, oleuropein and their derivatives, especially found in olive oil. Oleuropein, one of the major secoiridoids in olive and olive oil, is a very powerful antioxidant and a natural defense against pests (Serra et al., 2021; Güler et al., 2024; Uzundumlu & Ateş, 2025). Factors such as production technique, raw material quality, and processing conditions can substantially influence the chemical composition and biological activity of olive oil. The meta-analysis of more than 800,000 participants revealed that 25 g of olive oil consumed daily reduced the risks of cardiovascular disease by 16%, risks of type 2 diabetes by 22%, and the rate of mortality in general by 11% (Martínez-Gonzalez et al., 2022). During Ancient times, olive oil was the main ingredient of cosmetics and medicine. Hippocrates termed it as the great healer and Homer made a famous saying that it was liquid gold. It is also important to note that Galen also focused on its medicinal use, and olive oil was considered an expensive luxury product in ancient Greece (Adun and Guler, 2025). According to the ARIMA model, world olive production is expected to reach 23.38 million tons in the 2023–2027 period; this increase indicates that the importance of olive oil in both nutrition and health will increase further in the future (Uzundumlu & Ateş, 2025).

Extra virgin olive oil (EVOO) is a juice of an olive that is produced using healthy fruits at the optimal point of their maturity and correctly processed. It reproduces the sensory characteristics of the aroma and flavor of the fruit from which it comes, while also preserving all the nutritional elements characteristic of these oils (Uceda et al. 2017).

Olive production in Cyprus can be traced back several thousand years, its origin can be traced to the Early Bronze Age. The presence of olive trees dating back 1,000 years, particularly in the Guzelyurt–Kalkanlı area, is strong evidence of this agricultural tradition (Karanfiloğlu et al., 2025). It is predominantly of the Ada Yerlisi variety, which is local to Cyprus and is what is more commonly referred to as the Local Olive. This is also a local variety that is mostly utilized in producing *Kara yağ* (Karanfiloğlu et al., 2025). *Kara yağ* is a type of olive oil produced using traditional methods, particularly in Cyprus. It is fermented, boiled, and dried; therefore, its production process is completely different compared to EVOO. During the production process, Ada Yerlisi are carefully harvested and cleaned of any foreign material such as leaves and branches. The olives are then boiled for approximately one hour until softened and then allowed to dry. However, this boiling process causes a certain loss of the naturally occurring phenolic compounds in the olives. Its most notable characteristics are its dark color and strong musty aroma. It also oxidizes more easily and has a shorter shelf life compared to EVOO. In Cyprus, *Kara yağ* is referred to as “mavrolado” (Μαυρολάδο). “Mavro” is black in the Greek language and “lado” is oil. Thus, “mavrolado” is translated literally as Kara yağ. The local people considered it to be a cure of longevity in ancient times and especially utilized it to cure gallbladder and stomach problems (MR Olive Oil, 2025). The Paphos and Karpaz regions are the traditional areas of *Kara yağ* production. However, due to its bitterness and production technique, it is considered a low-quality product and is gradually disappearing, as it no longer appeals to modern taste preferences. Its bottling has been prohibited by law since 1983 (Kıbrıs Postası, 2018). The methods utilized during the production of olive oil are determinants of the chemical composition and the toxicological profile of the oil. The processing of the oil can be made to oxidatively degrade more rapidly by the heat applied and can also result in more polar compounds and heat-treated byproducts (Uckun and Var, 2014; Var and Uckun, 2021). Therefore, it is essential to know how traditional heat treatment methods change the biological characteristics of oil to gain food safety as well as knowledge about its functional properties.

The literature review emphasizes that most of the existing literature is on EVOO and has no mechanistic or cellular research on heat-treated or fermented oils (Martínez-Gonzalez et al., 2022; Saad and Kmail, 2025). Therefore, scientific investigation of the biological effects of *Kara yağ* is important both for the identification of a traditional product and for determining the possible effects of the production process on health. Therefore, the present study provides the first experimental data concerning the biological activity of traditionally manufactured *Kara yağ*.

In the present study, the effects of *Kara yağ,* a traditionally produced unrefined olive oil and extra virgin olive oil at varying concentrations were investigated on cell viability, proliferation, and apoptosis in HCT-116 human colon cancer cells.

MATERIALS AND METHODS

Sample Collection and Preparation

Kara yağ was produced from freshly harvested olives supplied by the Ministry of Agriculture and Natural Resources, originating from the Girne Region of Northern Cyprus. The EVOO sample was obtained from a certified local producer. All samples were stored in dark glass bottles at 4°C until analysis to minimize oxidative degradation.

Physicochemical Analysis

Free fatty acidity and peroxide value determinations were carried out according to the *Turkish Food Codex Regulation on the Methods of Analysis for Olive Oil and Olive-Pomace Oil (No:2023/20)* (COI/T.20/Doc. No34 and COI/T.20/Doc. No 35).

Total Phenolic Content

Total phenolic content (TPC) analysis was carried out according to the method described by Gutfinger (1981) and Hrncirik and Fritsche (2004). Results were expressed as milligrams of caffeic acid equivalents per kilogram of oil (mg CAE/kg). 0.5 ml of olive oil and 0.5 ml of methanol were added to a 2 ml Eppendorf reaction tube. The tubes were shaken for 1 minute and centrifuged for 7 minutes at 15,000 rpm in a "Hettich" brand microcentrifuge. The upper methanolic phases were transferred to another tube, combined, and analyzed.

Aflatoxin Analysis

Aflatoxin analysis was carried out according to the method described by AOAC 991.31 (2002). Ten grams of oil sample was transferred into a centrifuge tube and extracted with 10 mL of methanol–water (80:20, v/v). The mixture was vortexed at high speed for 2 minutes and centrifuged at 6000 rpm for 20 minutes at +4 °C. After centrifugation, 1 mL of the upper layer was diluted with 9 mL of ultrapure water and vortexed for 20 seconds. The resulting 10 mL solution was loaded onto the immunoaffinity column (IAC) at a flow rate of 1 mL/min. The column was washed twice with 10 mL of water to remove non-specific impurities. Aflatoxin retained on the column was eluted with 1 mL of methanol followed by 1 mL of ultrapure water, and the combined eluate (2 mL) was collected in a vial. The final extract was vortexed for 30 seconds, filtered through a 0.45 µm Teflon membrane, and injected into the HPLC-FLD system.

HPLC-FLD conditions are as follows: Column: C18 Mobile Phase: Ultrapure Water: Acetonitrile: Methanol (600:200:300/v:v:v) (120 mg KBr and 350 µL 4 Molar Nitric Acid per liter of solution) Flow Rate: 1 mL/min Injection Volume: 100 µL Excitation wavelength: 360 nm Emission wavelength: 430 nm Column temperature: 25°C Derivatization Device: Coring Cell.

Ochratoxin Analysis (OTA)

OTA was carried out according to the method described by Tekin (2023). 50 ml oil sample was extracted using 100 mL of methanol–water (80:20, v/v) and homogenized for two minutes in order to perform an ochratoxin analysis. After filtering the extract using a coarse filter (Whatman No. 4), 2 mL of the filtrate was diluted with 40 mL of PBS and vortexed. After passing the diluted extract through the immunoaffinity column at a rate of two milliliters per minute, it was cleaned with distilled water and allowed to air dry. One milliliter of methanol–acetic acid (98:2) and one milliliter of ultrapure water were used to elute OTA. The eluate was injected into the HPLC-FLD system after being vortexed and filtered through a 0.45 µm Teflon membrane (Table 1).

Table 1. HPLC Conditions.

Parameter	Value
Column	C18 ODS-3 Column (5 µm, 250 × 4.5 mm)
Flow Rate	1 mL/min
Temperature	30°C
Excitation Wavelength	333 nm
Emission Wavelength	477 nm
Mobile Phase	Acetonitrile : Water : Acetic Acid (48:51:1)
Injection Volume	100 µL

Moisture and Volatile Matter and Water Activity (aw)

Moisture and volatile matter were measured using a Shimadzu Moc-63u instrument, and water activity (aw) was measured using a Novasina LabStart-aw instrument. Water activity (aw) analyses were performed following the AOAC Official Method 993.20 (2002) protocol. Measurements were carried out under controlled laboratory conditions (25 ± 1°C, 60% relative humidity).

Sensory Analysis

In the sensory analyses, forms based on the IOC method COI/T.20/Doc. No. 15/Rev. 10 were used.

Cell Culture and Treatment Protocol

The human colorectal carcinoma cell line (HCT-116) was used in this study and was obtained

from the Cell Culture Stock of the DESAM Research Institute, Near East University (Nicosia, TRNC). Cells were maintained in 75 cm² culture flasks containing Dulbecco's Modified Eagle Medium (DMEM, Capricorn-HPA) supplemented with 10% fetal bovine serum (FBS; Biological Industries, 04-127-1A), 2 mM L-glutamine (Biological Industries, 03-020-1B), and 1% penicillin–streptomycin (Biological Industries, 03-031-1B). Cultures were incubated at 37°C in a humidified atmosphere containing 95% air and 5% CO_2 under sterile conditions.

Cell Viability and MTT analysis

Cells were routinely monitored under an inverted light microscope to assess viability, proliferation, and possible microbial contamination. The Trypan Blue exclusion assay was used to evaluate cell viability. For this purpose, 50 µL of the cell suspension was mixed with an equal volume of Trypan Blue solution, and the mixture was loaded onto a Neubauer hemocytometer. Cell counting was performed under a light microscope in four 4×4 grid fields. Cells that excluded the dye and appeared bright were considered viable, while blue-stained cells were regarded as non-viable. The total number of viable cells per milliliter was calculated as the mean viable cell count multiplied by 20,000.

Cytotoxicity was assessed using the MTT [3-(4,5-dimethylthiazol-2-yl)-2,5-diphenyltetrazolium bromide] assay. HCT-116 cells were seeded in 96-well plates at a density of 3 × 10³ cells per well and allowed to adhere for 24 hours before treatment. HCT-116 cells were treated with varying ratios of *Kara yağ* and EVOO at 1:1, 1:2, and 1:4 for 24, 48, and 72 hours**.** *Kara yağ* and EVOO-untreated cells were prepared as the control group.

At the end of each incubation period (24, 48, and 72 hours), MTT reagent was added to each well and incubated for an additional 2 hours. The optical density (OD) was then measured at 570 nm using a microplate reader (Thermo Scientific, Multiskan FC, Finland). Cell viability was calculated as a percentage of the control group.

Immunocytochemistry Analysis in HCT-116 Cells

Indirect immunoperoxidase staining was performed according to the previously described method (Özduran et al., 2022) and the distribution of Ki-67, indicating proliferation, Caspase-3, indicating apoptosis from cell death pathways and proton-oncogene protein C-myc triggering cell growth and division were evaluated in HCT-116 cells. Both cell types were seeded and cultured until they reached approximately 70% confluency. Cells were then fixed with 4% paraformaldehyde (158127–25 G; Sigma-Aldrich) in phosphate-buffered saline (PBS) at 4°C for 30 minutes. Following fixation, cells were washed three times with PBS. Permeabilization was performed using 0.1% Triton X-100 (AppliChem, A4977-0100) in PBS for 15 minutes on ice. After washing with PBS, endogenous peroxidase activity was quenched using 3% hydrogen peroxide (H_2O_2; Merck, K31355100303) for 10 minutes and washed again with PBS. Non-specific binding was blocked using a commercial blocking solution (HRP, 859043; Thermo Fisher) for 1 hour at room temperature. Without washing, cells were incubated overnight at 4°C with primary antibodies against anti-caspase-3 (BT-AP01199; BT LAB), anti-Ki-67 (RB-081-A1; NeoMarkers) and anti-c-myc (9402, Cell Signaling Technology). The next day, cells were washed with PBS and incubated with a biotinylated secondary antibody (HRP, 859043; Thermo Fisher) for 30 minutes and subsequently washed again three times with PBS. Afterward, 100 µL of streptavidin-peroxidase complex was added to the cells and incubated for 30 minutes. Cells were then rinsed again with PBS. To enhance immunolabeling, diaminobenzidine (DAB) (D7304; Sigma-Aldrich) was applied for 3 minutes. Counterstaining was performed using Mayer's hematoxylin (09-168-1; DDK, Italia) and washed with distilled water for 3 minutes. Finally, the cells were mounted using mounting medium (Merck Millipore, 107961). Stained samples were examined using a light microscope (Olympus BX40). The intensity of caspase-3, Ki-67 and c-myc staining was quantified using the H-SCORE method, as described in Equation 2.

$$\textbf{H-SCORE}=\sum \boldsymbol{n}\ (\boldsymbol{i}+1)$$

where i is the intensity of dyeing with a value of 1, 2, or 3 (mild, moderate, or strong, respectively) and л is the percentage of cells stained with each intensity, varying between 0% and 100%.

Statistical Analysis

All experiments were performed in triplicate for each experimental group to ensure reproducibility and statistical validity. Quantitative data were expressed as mean ± standard deviation (SD)**.** Statistical differences among groups were analyzed using one-way analysis of variance (ANOVA) at a 95% confidence interval ($p < 0.05$)**.** Tukey's post-hoc test was applied to determine pairwise comparisons between experimental groups. Graphical representations of cytotoxicity data were generated using GraphPad Prism version 5.10.0. Additionally, a two-way ANOVA followed by the Bonferroni post-hoc test was conducted to assess the significance of interactions between treatment duration and concentration. Statistical significance was set at $p < 0.05$ for all analyses.

RESULTS AND DISCUSSION

The free acidity, peroxide value, moisture, volatile matter, and water activity of *Kara yağ* and extra virgin olive oil are given in Table 1. One of the most crucial factors in assessing the quality and geographic features of an olive oil is its peroxide and acidity levels. This study found that EVOO had lower free acidity, peroxide values moisture and volatile matter than *Kara yağ*. One indicator of the level of oxidation is the peroxide value. The maximum permissible limit is 20 meq/kg (meq active oxygen/kg oil), but *Kara yağ*'s peroxide value was found to be 121.35 meq active oxygen/kg oil (FAO, 2024). This suggests that there has been substantial oxidation of the *Kara yağ* made by traditional processing. According to Uckun and Var (2014), although heat treatments do not entirely remove toxins, they hasten the oxidative degradation rate by elevating the peroxide value in oils. It is believed that these oxidative byproducts due to heat are the factors that result in the high cytotoxicity of Kara yağ.

The total phenol content in Kara yağ was determined to be 28.5 mg CAE/kg (Table 2). Phenolic compounds such as hydroxytyrosol, oleocanthal and oleacein contained in EVOO have been shown to have mechanisms that reduce proliferation, suppress COX-2 and ERK1/2 pathways and increase apoptosis in colon cancer cells (Serra et al., 2021). The effects of EVOO on these are also linked mainly to the presence of phenols, antioxidants, and anti-inflammatory effects. The cellular mechanisms, by which this occurs, however, have not been completely illuminated. Therefore, in our study, EVOO was evaluated against traditional *Kara yağ* in terms of biological effects. According to Amaral et al. (2022), bagasse that is generated during the production of olive oil has 98-99.5% of total phenolic compounds, whereas only about 2 percent is extracted into the oil phase. This leads one to assume that the biological effects of the Kara yağ, which are altered due to a modification in the composition of the phenols, might be determined by the heat treatment and fermentation processes to a larger extent. Among ochratoxins, only ochratoxin A has a toxic effect in humans, while aflatoxins, produced by Aspergillus species and found in foods, are the most potent carcinogenic mycotoxins (Gil-Serna et al., 2018; Veršilovskis & Mikhook˜elsone, 2006).

Toxin analyses revealed contamination levels of ochratoxin A (2.6 µg/kg) and aflatoxin B1 (0.8 µg/kg). Although large meta-analyses have linked olive oil consumption to chronic diseases, contamination of the products by mycotoxins has not been conducted (Martínez-Gonzalez et al., 2022). It is reported that aflatoxins are degraded only in the range of 237–306 °C, and heat-resistant toxic and semi-toxic compounds can survive in the oil matrix (Var & Uçkun, 2021). The low concentration of OTA and AFB1 observed in *Kara yağ* in this research also indicates the risk to food safety of conventional production processes. The fact that *Kara yağ* has never been studied in literature before increases the scientific importance of the findings and shows that the health effects of such traditional products should be investigated in depth. Var and Uçkun (2021) demonstrated that various oil mining techniques have a significant impact on aflatoxin migration, and the toxic transfer rises especially in heat-based press procedures. This observation corroborates the idea that the old high-heat operations cause chemical degradation of the oil and can enhance the rate of heat-induced degradation product formation, therefore justifying the extreme chemical transformation seen in *Kara yağ*. Additionally, the solubility of aflatoxins in polar solvents is high, and this could be related to the presence of polar constituents in oils subjected to heating. Polar fraction is enhanced during oil processing that influences the transfer of toxins. This agrees with our results that when the temperature is high during Kara yağ production, the polar constituents of the oil significantly differentiate its chemical structure from EVOO.

Diraman et al. (2009) demonstrated that *Kara yağ* samples have significant structural changes that can be attributed to high heat exposure during processing, meaning that the observed high heat-induced changes in structure could be the cause of the specific biological profile of the samples on comparison with EVOO. Furthermore, PCA analysis of the *Kara yağ* has also been reported to have differentiated it with other countries as it has high POO and low content of gadoleic acid. Such a distinct TAG profile suggests the idea that there is a structural difference in the composition of *Kara yağ* and that heat treatment can also influence its chemical composition. Var and Uçkun (2021) demonstrated that various oil mining techniques have a significant impact on aflatoxin migration, and the toxic transfer rises especially in heat-based press procedures. This observation corroborates the idea that the old high heat operations cause chemical degradation of the oil and can enhance the rate of heat-induced degradation product formation, therefore justifying the extreme chemical transformation seen in *Kara yağ*.

Heat treatments have been extensively demonstrated in the literature to have significant effects on the chemical integrity of oils. It has been

reported that aflatoxins and other toxic metabolites remain stable up to 270°C, and therefore, heat treatment does not eliminate these compounds; on the contrary, it can lead to the formation of new toxic byproducts through increased peroxide production and oxidative degradation (Uckun and Var, 2014). These findings support the notion that the boiling and drying stages used in *Kara yağ* production can alter biological activity by causing thermal changes in the oil matrix.

For sensory analysis, the evaluation form shown in Fig. 1 was administered to a panel of seven individuals. According to the sensory analysis results, fruitiness (green) was perceived as a positive trait in EVOO at a rate of 8/10, bitterness at 6.4/10, and pungency at 7.7/10; while these traits were not detected in *Kara Yağ*. In *Kara Yağ*, a negative trait was perceived as a defect at a rate of 7.5/10.

Cell culture analysis results

Following 24 hours of incubation, treatment with *Kara yağ* and EVOO at a 1:1 ratio induced noticeable cytotoxic effects in HCT-116 cells. However, at the 1:4 ratio**,** a marked reduction in cytotoxicity was observed in the *Kara yağ*-treated group, whereas no cytotoxic effect was detected in cells treated with EVOO (Fig. 2)

After 48 hours of incubation, both *Kara yağ* and EVOO treatments at a 1:1 ratio exhibited pronounced cytotoxic effects in HCT-116 cells. However, at the 1:4 ratio, *Kara yağ* demonstrated notably lower cytotoxicity compared to EVOO at the same concentration, indicating a concentration-dependent reduction in toxicity specific to *Kara yağ* (Fig. 3). It has been stated that polyphenols contained in olive oil increase the cytotoxicity of chemotherapy drugs (Anwar et al., 2025). This could be explained by the fact that the high cytotoxicity of *Kara yağ* was also accompanied by a similar increase in the cellular sensitivity of polyphenolic compounds under heat treatment. Saad and Kmail (2025) state that the activity of the polyphenols found in olives is very sensitive to processing and temperature, which may cause a shift in their antioxidant–prooxidant activity and bioactivity. Accordingly, the extreme heat exposure in the production of *Kara yağ* could produce structurally altered phenolics that have enhanced cytotoxic and reduced stable dose-dependent effects.

Following 72 hours of incubation, *Kara yağ* treatment at the 1:1 ratio induced higher cytotoxicity in HCT-116 cells compared to EVOO. In contrast, the 1:4 *Kara yağ* treatment exhibited lower cytotoxicity relative to EVOO at the same ratio. (Fig. 4). The antioxidant to pro-oxidant effect relationship through concentration, as reported by Saad and Kmail (2025), accounts for the finding that *Kara yağ* has high cytotoxicity under high concentration and significantly lower cytotoxicity at low concentration.

Protective effects were particularly found in the category of cold-pressed EVOO in the meta-analysis (Martínez-Gonzalez et al., 2022). Nevertheless, the *Kara yağ* production method, which requires high temperatures and thermal treatment, might result in the production of various oxidative products and this might be the cause of the pro-cytotoxic action on the cancer cells.

Table 2. Physicochemical, Toxin, and Sensory Properties of Olive Oil Samples.

	EVOO	Kara Yağ
Free Acidity (% as oleic acid)	0.79 ± 0.08	1.97 ± 0.32
Peroxide Value (meq active oxygen/kg oil)	9.94 ± 1.45	121.35 ± 17.53
Moisture & Volatile Matter (%)	0.15 ± 0.07	0.35 ± 0.06
Water Activity (aw)	0.33±0.00	0.46±0.00
Total Phenolics (mg caffeic acid equivalent (CAE)/kg oil)	60.09±1.20	28.52±0.00
Toxin Analyses (µg/kg)	-	Ochratoxin A: 2.60; Aflatoxin B1: 0.80
Sensory Analyses	Median of Defects: – Positive Attributes: Fruitiness (green): 8.0 Bitterness: 6.4 Pungency: 7.7	Median of Defects: 7.5 Positive Attributes: Fruitiness : – Bitterness: – Pungency: –

COI/.20/Doc. No15/Rev. 10

AGROVET LABORATORY

PROFILE SHEET FOR VIRGIN OLIVE OIL

INTENSITY OF PERCEPTION OF DEFECTS

Fusty/muddy sediment _____

Musty/humid/earthy _____

Winey/vinegary acid/sour _____

Frostbitten olives (wet wood) _____

Rancid _____

Other negative attributes: _____

Descriptor: Metallic ☐ Dry hay ☐ Grubby ☐ Rough ☐

Brine ☐ Heated or burnt ☐ Vegetable water ☐

Esparto ☐ Cucumber ☐ Greasy ☐

INTENSITY OF PERCEPTION OF POSITIVE ATTRIBUTES

Fruity _____

Green ☐ Ripe ☐

Bitter _____

Pungent _____

Name of taster: **Taster code**:

Sample code: **Signature**:

Date:

Comments:

Fig. 1. Sensory Analysis Form (COI/.20/Doc. No15/Rev. 10).

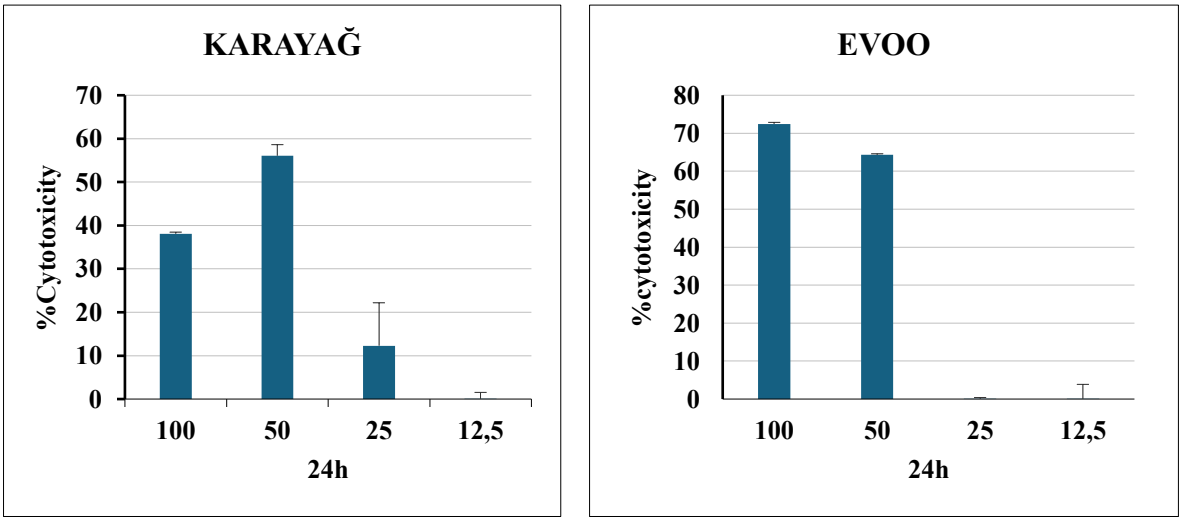

Fig. 2. A 1:1 treatment ratio resulted in a significant decrease in cell viability ($p < 0.05$), while cytotoxicity markedly declined at the 1:4 ratio in the Kara yağ group and was completely absent in the EVOO-treated cells.

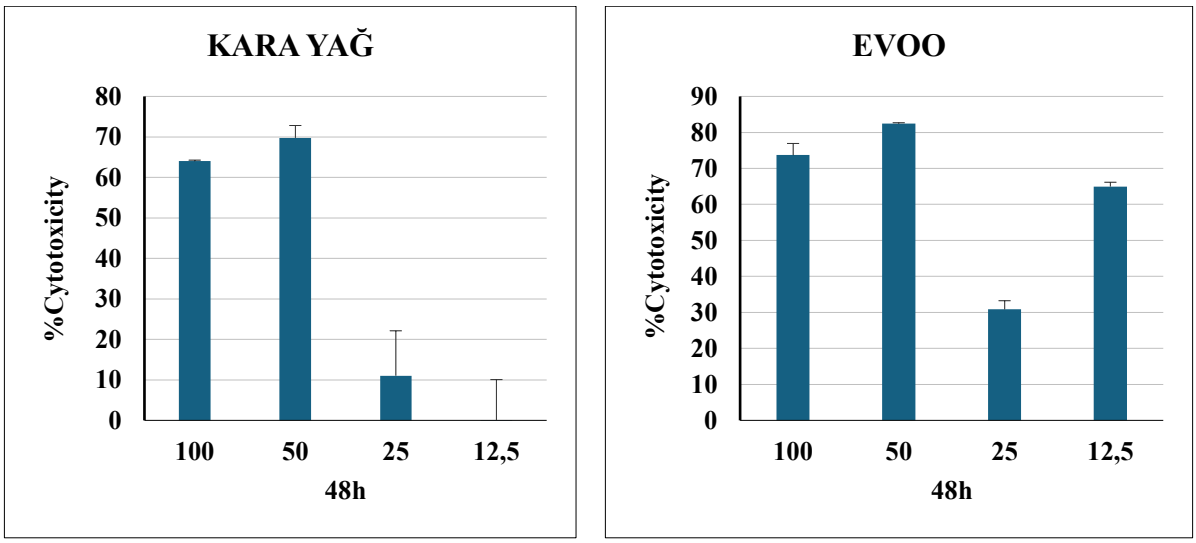

Fig. 3. Cytotoxic effects of Kara *yağ* and EVOO on HCT-116 cells following 48 hours of incubation. Both oils exhibited marked cytotoxicity at the 1:1 treatment ratio; however, *Kara yağ* demonstrated significantly reduced toxicity at the 1:4 ratio compared to EVOO, which showed no detectable cytotoxicity at the same concentration ($p < 0.05$).

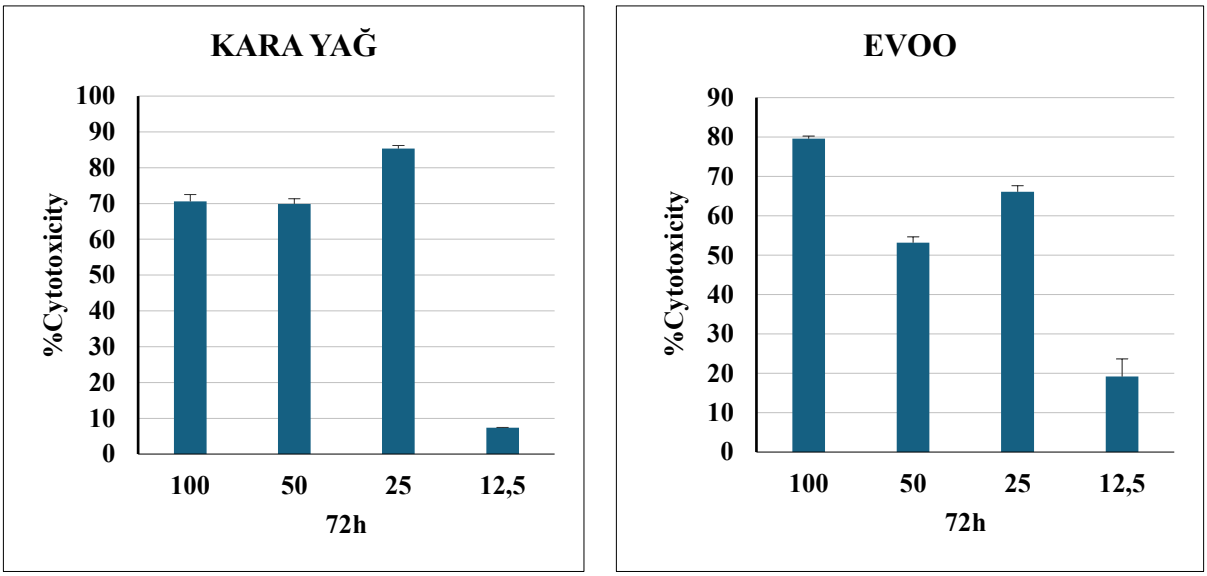

Fig. 4. Comparative cytotoxic effects of *Kara yağ* and EVOO on HCT-116 cells after 72 hours of incubation. At the 1:1 ratio, *Kara yağ* demonstrated greater cytotoxicity than EVOO, whereas at the 1:4 ratio, the cytotoxic potential of *Kara yağ* was reduced and remained lower than that observed for EVOO ($p < 0.05$).

Immunocytochemistry analysis results

Following the 48-hour incubation, the treatment ratios exhibiting the most pronounced cytotoxic effects (1:1) and the lowest cytotoxicity (1:4) for both oils were further evaluated using immunocytochemistry to visualize the subcellular localization of proteins associated with cell viability and death. Immunocytochemical analyses targeted Ki-67, a proliferation marker; caspase-3, a key executioner protein in the apoptotic pathway; and c-Myc, a proto-oncogene involved in promoting cell growth and division.

In the *Kara yağ* 1:1 treatment group, Ki-67 immunoreactivity was weakly positive (Fig. 5A), caspase-3 immunoreactivity was negative (Fig. 5B), and c-Myc immunoreactivity was moderately positive (Fig. 5C). These findings indicate that the *Kara yağ* 1:1 treatment reduced cellular proliferation, as reflected by the diminished Ki-67 staining, while failing to activate apoptosis, given the absence of caspase-3 staining. Moreover, the moderate c-Myc immunoreactivity suggested that proliferative signaling pathways related to cell growth and division may have remained partially active despite the observed cytotoxicity.

Following the 1:1 treatment with EVOO, both Ki-67 (Fig. 6A) and caspase-3 (Fig. 6B) immunoreactivities were strongly positive. The

marked immunolabelling of Ki-67 and caspase-3 observed after the 1:1 EVOO treatment suggests, in agreement with the MTT results, that EVOO may simultaneously promote cellular proliferation while also triggering apoptotic cell death in HCT-116 cells. The low but mild apoptotic cellular response accompanied by low cytotoxic response that is observed in our study is congruent with the oxidative-inflammatory controlling functions of the phenolic compounds in EVOO (Martínez-Gonzalez et al., 2022).

Following the 1:4 *Kara yağ* treatment, Ki-67 immunoreactivity was absent (Fig. 7A), while caspase-3 (Fig. 7B) and c-Myc (Fig. 7C) immunoreactivities were moderately positive. The lack of Ki-67 staining indicates a marked suppression of proliferative activity in HCT-116 cells, whereas the moderate expression of caspase-3 suggests the activation of apoptotic cell death pathways. Concurrently, the moderate c-Myc immunoreactivity implies that cellular growth and division–related mechanisms were partially maintained despite the overall reduction in proliferation.

According to Memmola et al. (2022) and Tarun et al. (2025) oleic acid in EVOO can induce apoptosis through the early downregulation of COX-2 and suppression of Bcl-2 expression. The mechanisms mentioned might be the reason that the apoptotic tendency was observed in EVOO-treated HCT-116 cells in our research. Its long-term clinical safety profile is also in keeping with the absence of high-dose cytotoxicity of EVOO. Proliferation and increase in apoptosis of colon cancer cells have been reported to be inhibited and induced by EVOO-specific phenolic compounds, including olecanthal, oleacein, and oleuropsenin (Anwar et al.,2025). These processes are in line with the moderate apoptotic effect of EVOO at low concentrations in our study. In contrast, the heat exposure in the traditional production of Kara yağ is quite extensive, and it is possible that it changes or degrades heat-sensitive phenolics; the structural changes could be the reason why the cytotoxicity profile has a concentration effect, being the highest at high concentrations and decreasing at lower dilutions.

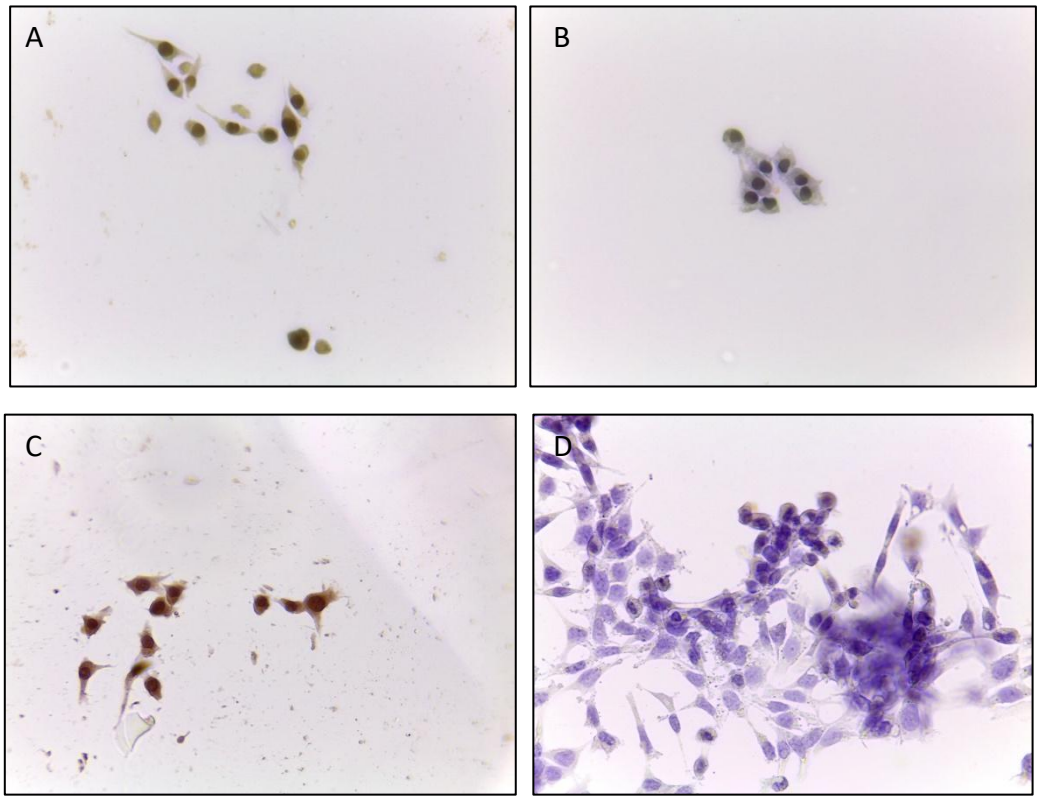

Fig. 5. Immunocytochemical staining of HCT-116 cells treated with *Kara yağ* at a 1:1 ratio for 48 hours, showing Ki-67 (A), caspase-3 (B), and c-Myc (C) expression, along with the negative control (D). Magnifications ×400.

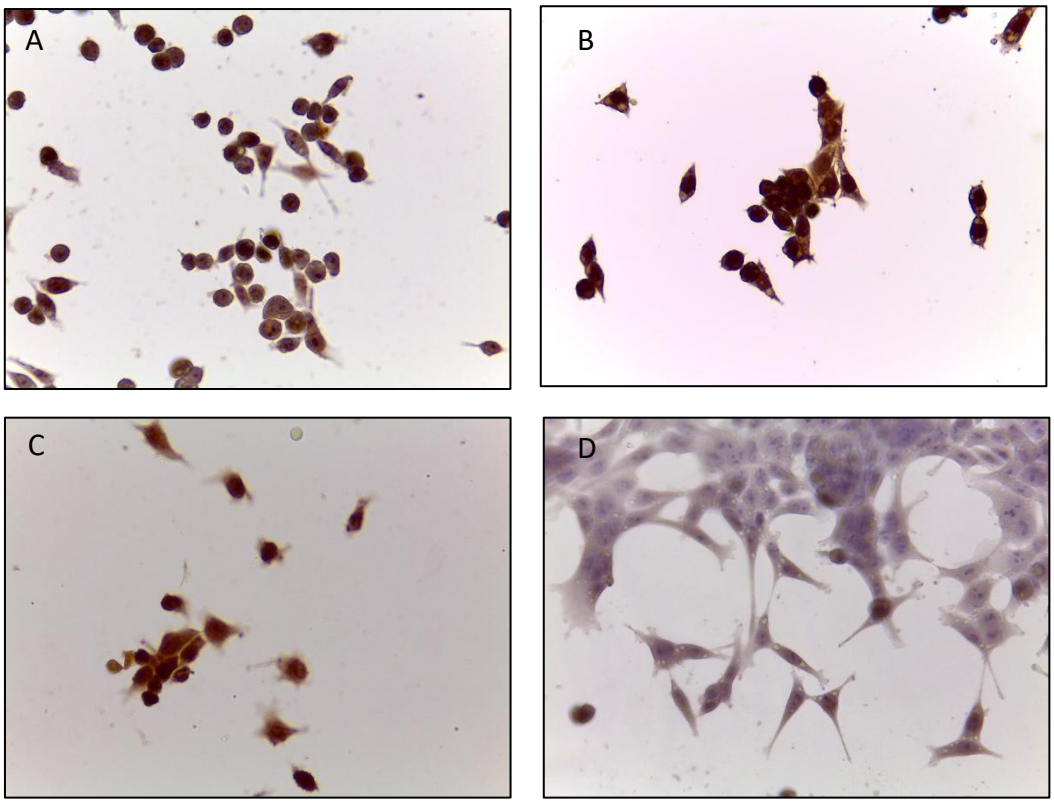

Fig. 6. Immunocytochemical staining of HCT-116 cells treated with EVOO at a 1:1 ratio for 48 hours, showing Ki-67 (A), caspase-3 (B), and c-Myc (C) expression, along with the negative control (D). Magnifications ×400.

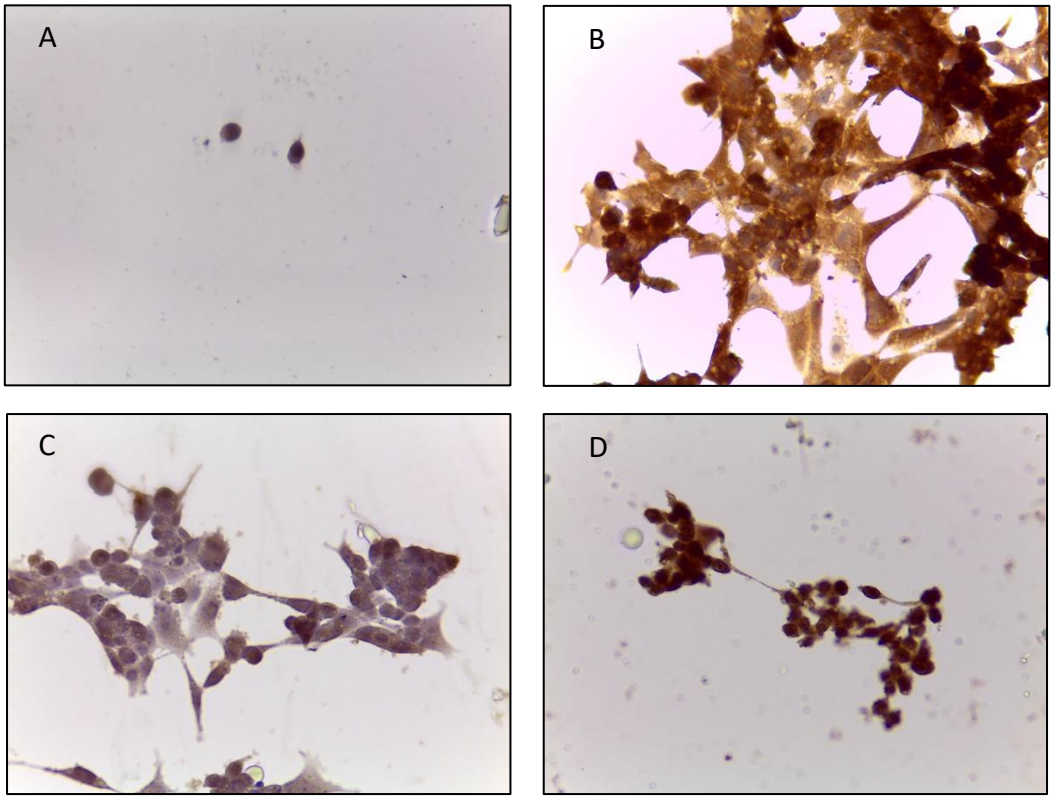

Fig. 7. Immunocytochemical staining of HCT-116 cells treated with *Kara yağ* at a 1:4 ratio for 48 hours, showing Ki-67 (A), caspase-3 (B), and c-Myc (C) expression, along with the negative control (D). Magnifications ×400.

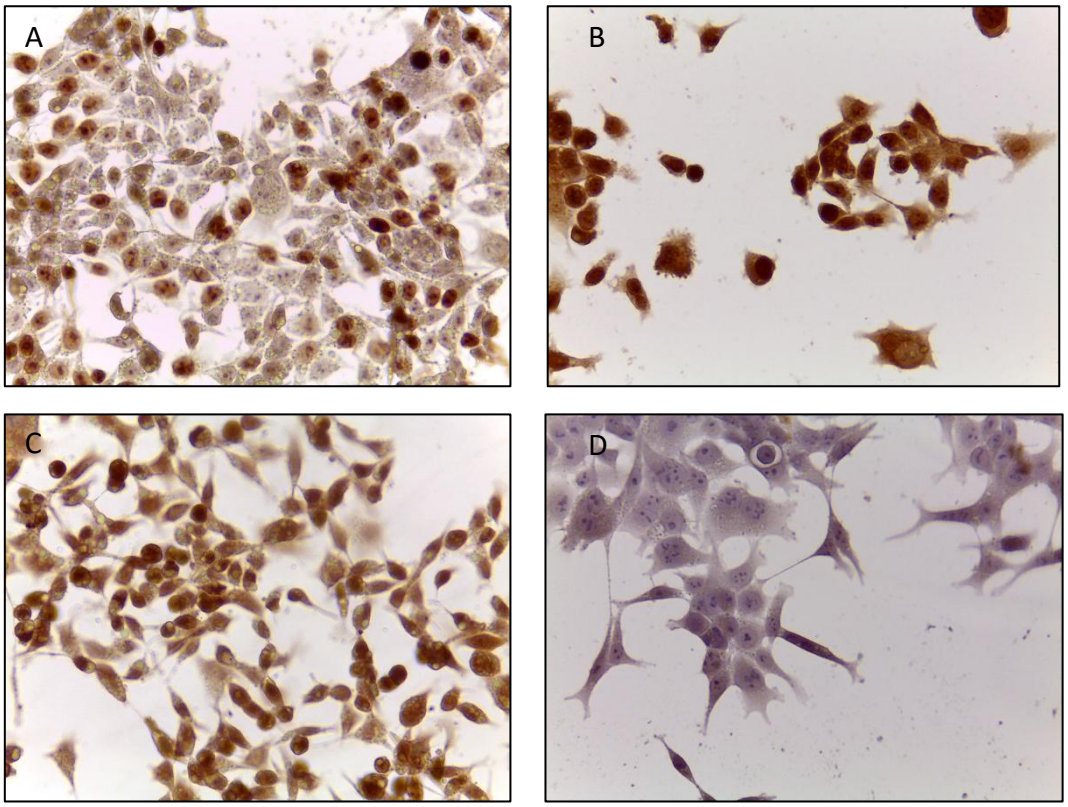

Fig. 8. Immunocytochemical staining of HCT-116 cells treated with EVOO at a 1:4 ratio for 48 hours, showing Ki-67 (A), caspase-3 (B), and c-Myc (C) expression, along with the negative control (D). Magnifications ×400.

Following the 1:4 treatment with EVOO, Ki-67 immunoreactivity was moderately positive in some cells (Fig. 8A), while caspase-3 immunoreactivity was strongly positive across the cell population (Fig. 8B). In addition, c-Myc immunoreactivity was diffusely moderate throughout the cells (Fig. 8C). These findings indicate that, after the 1:4 EVOO treatment, cellular proliferation persisted in a subset of cells, whereas apoptotic cell death was prominently induced in most HCT-116 cells. The EVOO polyphenols were also found to inhibit the molecular pathways that are vital in cancer development, including integrin 2, COX-2, and FAS, in colon cancer cells (Serra et al., 2021). The mechanisms are congruent with the low proliferation inhibition exhibited by EVOO at low concentrations in our study. In the study conducted by Serra et al. (2021), it was shown that the anti-inflammatory, antioxidant and microbiota-regulating effects of EVOO play a critical role in reducing the risk of colorectal cancer; these mechanisms are compatible with the limited apoptotic effect of EVOO with low cytotoxicity in our study.

The effects of varying concentrations of *Kara yağ* and EVOO on the proliferation and death of HCT-116 colorectal cancer cells were evaluated. Neither concentration of *Kara yağ* promoted cellular proliferation; however, apoptosis was observed predominantly at the 1:4 dilution, indicating a concentration-dependent response. In contrast, EVOO exhibited the highest cytotoxic effect at both dilutions after 48 hours of exposure. Notably, the 1:4 EVOO treatment led to a modest reduction in proliferation compared to the 1:1 ratio, while apoptotic cell death was primarily induced at the 1:4 dilution. These findings suggest that EVOO at a 1:4 ratio may exert a more pronounced pro-apoptotic effect on HCT-116 cells. Although *Kara yağ* at 1:4 also enhanced cell death compared to its 1:1 treatment, the concurrent expression of the proto-oncogene c-Myc implies that its overall cytotoxic efficacy on HCT-116 cells was lower than that of EVOO. Phenolic compounds have been discovered to prevent the production of ATP by interfering with the membrane permeability, which is fatal to both bacteria and cancer cell types (Amaral et al., 2022). This process is in line with the high cytotoxicity of *Kara yağ* in the HCT-116 cells.

CONCLUSIONS

The analyzed *Kara yağ* was identified as "raw olive oil" according to the Turkish Food Codex. Compared to EVOO, additional food safety assessments are required not only for its chemical and sensory qualities but also for its mycotoxin content.

The physicochemical results were further confirmed by sensory assessment, which showed that EVOO had high positive characteristics (fruitiness, bitterness, and pungency) and no negative ones (*Kara yağ*), with a high score in defects (as expected due to its high oxidation and low quality). The concentrations of OTA and AFB1 in the *Kara yağ* point to the fact that the traditional production methods are potentially dangerous to food safety and that there is a need to further investigate this product in terms of toxicological analysis.

This study demonstrated that traditionally produced *Kara yağ* and EVOO from Northern Cyprus exert distinct biological effects on the HCT-116 human colorectal cancer cell line. *Kara yağ* exhibited pronounced cytotoxicity and suppressed proliferation at higher concentrations, whereas at lower concentrations it induced only limited apoptotic activity. In contrast, EVOO, particularly at a 1:4 ratio, activated apoptotic pathways without markedly reducing proliferative activity, suggesting its potential as a functional food component or complementary anticancer agent**.**

Overall, the findings indicate that the biological effects of olive oils are strongly influenced by production method, phenolic composition, and treatment concentration**.** These results contribute to a deeper understanding of the bioactivity of traditionally produced olive oils and provide a valuable scientific basis for future in vivo investigations.

Consequently, it should be considered that these chemical alterations, because of heat treatment, can be used to tune the biological effects to some degree, and any future research on the health impact of traditional types of olive oil ought to include the thermal conditions associated with the production process as a variable.

FUNDING

This study did not receive any specific grant from the state, commercial, or non-commercial organizations.

CONFLICT OF INTEREST

The authors confirm the absence of a conflict of financial/non-financial interests related to the writing of the article.

ACKNOWLEDGMENTS

We would like to thank Prof. Dr. Işıl Var, Dr. Ali Tekin, and Hasan Yıldırım for conducting the toxin analyses.

AI STATEMENT

AI-assisted tools were used only for language translation, grammatical editing, and reference formatting.

REFERENCES

Adun P., Güler Ş. (2025) Mediterranean treasures: Olive varieties for table and olive oil. *Olives and Olive Related Products-Innovations in Production and Processing. In Agricultural Sciences. IntechOpen.* p. 107, doi: 10.5772/intechopen.1008263.

Kıbrıs Postası (2018) The possibility of obtaining a patent for Kara Yağ in Cyprus is being investigated. (Güney'de kara yağın patentinin alınıp alınamayacağı inceleniyor.) March, 11 2025. URL: https://www.kibrispostasi.com/c58-GUNEY_KIBRIS/n261567-guneyde-kara-yagin-patentinin-alinip-alinamayacagi-inceleniyor.

MR Olive Oil (2025) Black Oil (Kara Yağ): Traditional Cypriot Olive Oil Production and Characteristics. *March, 12 2025.* URL: https://mroliveoil.com/services/black-oil.

Anwar M.J., Anwar M.H., Imran M., Noman A.M., Hussain M., Raza H., ... Selim S. (2025) Olive oil polyphenols: A promising approach for cancer prevention and therapy. *Food Science & Nutrition*, **13(9):** e70976.

AOAC (2002) Official Method 991.31. Aflatoxins in Corn, Raw Peanuts, and Peanut Butter. In: *Official Methods of Analysis of AOAC International*, 17th ed. AOAC International, Gaithersburg, MD, USA.

Diraman H., Cam M., Ozder Y. (2009) Chemometric classification of foreign-origin virgin olive oils based on fatty acid and triacylglycerol composition. (Yabancı Ülke Kökenli Natürel Zeytinyağlarının Yağ Asitleri ve Triaçilgliserol Bileşenlerine Göre Kemometrik Sınıflandırılması.). *Gıda Teknolojileri Elektronik Dergisi*, **4(2):** 22-34.

FAO (2024) Codex Alimentarius Commission Standard For Olive Oils And Olıve-Pomace Oils. CXS 33-1981. 2024 Revisions. Rome, Italy.

Ferreira do Amaral V., Santos A.C.M.D., Moura J.G.L., Castilhos J.D., Gemelli T., Hoffmann J.F., ... Ferreira C.D. (2022) Antimicrobial and cytotoxic activity to human colon adenocarcinoma cell lines (HT-29) potential of olive oil extraction residue. *Natural Product Research*, **36(17):** 4486-4491.

Gil-Serna J., Vázquez C., González-Jaén M.T., Patiño B. (2018) Wine contamination with ochratoxins: A review. *Beverages*, **4(1):** 6; doi: 10.3390/beverages4010006.

Güler Ş., Erten H., Karagözlü M. (2025) Phenolic profile and antioxidant properties of sarıulak olive fermented with red beetroot. *Cyprus Journal of Medical Sciences*, **10(1):** 106-110.

Gutfinger T. (1981) Polyphenols in olive oils. *Journal of the American Oil Chemists' Society*, **58(11):** 966-968; doi: 10.1007/BF02659771

Hrncirik K., Fritsche S. (2004) Comparability and reliability of different techniques for the determination of phenolic compounds in virgin olive oil. *European Journal of Lipid Science and Technology*, **106(8):** 540-549; doi: 10.1002/ejlt.200400942

Karanfiloğlu H., Dikkaya Y.R., Mete N., Çetin Ö., Hakan M., Kaya H. (2025) Characterization of the 'Ada Yerlisi' olive variety native to the Turkish Republic of Northern Cyprus. (Kuzey Kıbrıs Türk Cumhuriyeti Orijinli "Ada Yerlisi" Zeytin Çeşidinin Karakterizasyonu). *Mustafa Kemal University Journal of Agricultural Sciences*, **30(2):** 267–276.

Martinez-Gonzalez M.A., Sayon-Orea C., Bullon-Vela V., Bes-Rastrollo M., Rodriguez-Artalejo F., Yusta-Boyo M.J., Garcia-Solano M. (2022) Effect of olive oil consumption on cardiovascular disease, cancer, type 2 diabetes, and all-cause mortality: A systematic review and meta-analysis. *Clinical Nutrition*, **41(12):** 2659-2682.

Memmola R., Petrillo A., Di Lorenzo S., Altuna S.C., Habeeb B.S., Soggiu A., ... Ghidini M. (2022) Correlation between olive oil intake and gut microbiota in colorectal cancer prevention. *Nutrients*, **14(18):** 3749.

Özduran G., Becer E., Vatansever H.S., Yücecan S. (2022) Neuroprotective effects of catechins in an experimental Parkinson's disease model and SK-N-AS cells: Evaluation of cell viability, anti-inflammatory and anti-apoptotic effects. *Neurological Research*, **44(6):** 511-523; doi: 10.1080/01616412.2021.2024715.

Saad B., Kmail A. (2025) Olive oil polyphenols in cancer: Molecular mechanisms and therapeutic promise. *Immuno*, **5(3):** 36.

Serra F., Spatafora F., Toni S., Farinetti A., Gelmini R., Mattioli A.V. (2022) Polyphenols, olive oil and colonrectal cancer: The effect of Mediterranean diet in the prevention. *Acta Bio. Medica: Atenei Parmensis*, **92(6):** e2021307.

Tarun M.T.I., Elsayed H.E., Ebrahim H.Y., El Sayed K.A. (2025) The olive oil phenolic S-(-)-oleocanthal suppresses colorectal cancer progression and recurrence by modulating SMYD2-EZH2 and c-MET activation. *Nutrients*, **17(3):** 397.

Uceda M., Aguilera M.P., Mazzucchelli (2017) Manual de cata y maridaje del aceite de oliva (Manual de cata y maridaje del aceite de oliva) 2nd ed. Editorial Almuzara, Córdoba, Spain, 155 pp.

Uçkun O., Var, I. (2014) Monitoring of aflatoxins in peanuts. *Turkish Journal of Agricultural and Natural Sciences*, **1(Özel Sayı-1):** 1310-1314.

Uzundumlu A.S., Ateş T. (2025) Olive production forecasts in the leader countries for 2023–2027. *Applied Fruit Science*, **67(2):** 56.

Var I., Tekin A. (2023) Investigation of aflatoxin presence in sunflower and corn oils offered on the market for consumption. (Piyasada tüketime sunulan ayçiçek ve mısırözü yağlarında aflatoksin varlığının araştırılması). *Gıda*, **48(6):** 1304-1317; doi: 10.15237/gida.GD23126

Var I., Uçkun O. (2021) Extraction methods' effects on aflatoxin concentration during sunflower oil processing: First Report. *European Journal of Agriculture and Food Sciences*, **3(5):** 136-143.

Veršilovskis A., Mikhookelsone V. (2006) Reduction of aflatoxin B1 and B2 in pistachio nuts by extraction with ethanol and ethanol-water solutions. *Maisto Chemija ir Technologija (Food Chemistry and Technology),* **40(2):** 64–68.

ORCIDs:

Özge Özden: https://orcid.org/0000-0001-7938-6927
H. Seda Vatansever: https://orcid.org/0000-0002-7415-9618
Şebnem Güler: https://orcid.org/0009-0002-8050-8850
Salih Gücel: https://orcid.org/0000-0001-5331-8379
Cenk Serhan Özverel: https://orcid.org/0000-0001-9932-4774
Burak Durmaz: https://orcid.org/0000-0002-5285-3641
Meryem Demir: https://orcid.org/0009-0004-9234-6881
Mehmet Karagözlü: https://orcid.org/0000-0002-6737-6702
Tamer Şanlıdağ: https://orcid.org/0000-0002-6015-8032

Biochemical components of *Juniperus communis* L. under the conditions of Northern Kazakhstan and the study of essential oils of some *Juniperus* L. species from the flora of Azerbaijan

Gulnar Aidarkhanova[1], Arzu Çığ[3], Elman Iskender[2], Minara Hasanova[2*], Zumrud Mamedova[2], Gullu Aliyeva[2]

[1]*Limited Liability Partnership "Republican Collection of Microorganisms", 43 Valikhanov Str., Z05P2K0, Astana, Kazakhstan*
[2]*Institute of Botany, Ministry of Science and Education of the Republic of Azerbaijan, 29 Sharg Str., AZ1044, Baku, Azerbaijan*
[3]*Siirt University, Faculty of Agriculture, Department of Horticulture, Kezer Campus, Veysel Karani Neighborhood, 1 University Str., Merkez, 56100, Siirt, Türkiye*

[*]***For correspondence:*** *minare.hasanova@inbox.ru*

Received: April 18, 2026; Reviewed: June 02, 2026; Accepted: June 12, 2026

Given the widespread popularity of common juniper in folk and traditional medicine, as well as in landscape design, this study aimed to investigate the phytochemical composition of *Juniperus communis* L. growing within the territory of the Burabay State National Nature Park in Northern Kazakhstan to determine its pharmacological potential, and to conduct a comparative study of the biochemical components of *Juniperus communis* L. and *Juniperus sabina* L. collected from the study areas Khizi, Altiagaj and Shabran, in Azerbaijan. The distribution and geobotanical characteristics of *Juniperus communis* L., growing in the Burabay State National Nature Park in northern Kazakhstan, were studied. The phytochemical composition of alcoholic extracts of common juniper included 54 components belonging to 15 classes of organic compounds: Ester, Carboxylic acid, Hydrocarbon, Lactone, Pyranone, Diketone, Ketone, Oxime, Phenol, Alcohol, Epoxide, Ether, Aldehyde, Disaccharide, and Anhydrosugar. Essential oils of 3 juniper species were obtained and their yield percentage was calculated. The yield of essential oil for *Juniperus communis* L. – 1.4% and and *Juniperus sabina* – 1.2%. The highest yield of essential oil was recorded in the type of multi-fruited juniper. The article presents the results of the analysis of the essential oil of *Juniperus communis* L. by gas chromatography and the composition of the essential oil. Chromatographic analysis revealed that thiujone (35.21%) and alpha-terpinene (19.78%) components had higher concentrations, while camphor (0.33%) and estragole (0.16%) components had the lowest concentrations. Turkish scientists have scientifically proven that the biochemical composition of juniper species growing in natural conditions depends on environmental conditions and soil characteristics, especially their richness in potassium (5.02-6.81%), and their macro and micro element composition.

Keywords: *Juniperus communis L., biochemical components, component composition chromatogram*

INTRODUCTION

Among the many species of medicinal plants, representatives of the genus *Juniperus* L. have been known since prehistoric times. Ancient healers used remedies prepared from parts of the juniper plant for treating wounds and drying ulcers (Karomatov, Davlatova, 2018), as well as for shortness of breath, asthma, ascites, and hemorrhoids. The berry-like cones of the plant were used for cleansing the stomach and liver, while crushed leaves were applied in the treatment of meningitis (Novikov et al., 2013).

Residents of Central Asian countries hold juniper in high esteem. They use juniper berries as food ingredients, making fruit drinks and compotes, and marinating meats (Asgary et al., 2014).

In Kazakhstan, the peoples of Central Asia hold juniper in particularly high esteem. They use juniper berries as food ingredients, prepare fruit drinks and compotes from them, and use them in meat marination. In Kazakhstan, juniper species grow in the mountainous regions of the Trans-Ili Alatau, Kungey Alatau, and Terskey Alatau (Northern and Southern Kazakhstan), where they form juniper woodlands. They are also distributed in the Altai Mountains (Eastern Kazakhstan) and the Tarbagatai Mountains (Southeastern Kazakhstan). Juniper phytocoenoses occur in

 DOI: https://doi.org/10.62088/timbb/10.1.6

granite rock crevices, on exposed granite cliffs, along rocky slopes, and under the canopy of pine forests in the Karkaraly and Degelen mountain ranges, as well as in the Bektauata Mountains. This information is based on long-term floristic studies of the Kazakh Uplands (Kupriyanov, 2020).

Thickets of common juniper grow within specially protected natural territories of the republic. In particular, they are widespread in the West Altai, Markakol, and Naurzum Nature Reserves, as well as in the Burabay, Ereimentau, Bayanaul, and Katon-Karagay State National Nature Parks, among others (Specially protected natural areas).

Due to their adaptability to soil and climatic conditions, junipers are highly decorative and promising for landscape design. Therefore, they are widely used in the landscaping of parks and public gardens in urbanized areas.

The biochemical composition of juniper species may vary depending on ecological conditions and soil properties. For instance, Gülser, Çığ and Türkoğlu (2012). reported that the fruits of *Juniperus excelsa* Bieb. growing naturally in Van, Turkiye, were particularly rich in potassium (5.02–6.81%) and their macro- and micronutrient contents were closely related to the soil characteristics of the growing environment. Beyond mineral nutrients, juniper plants also contain significant amounts of primary metabolites such as sugars. Türkoğlu, Balta and Cığ (2008) reported that fresh leaves and berries of *Juniperus excelsa* from Turkey contained fructose (44.0–70.2 mg/100g), glucose (22.0–26.0 mg/100g) and sucrose (10.0–25.0 mg/100g), with higher sugar levels observed in north-facing slopes compared to south-facing ones.

Given the widespread popularity of common juniper in folk and traditional medicine, as well as in landscape design, this study aimed to investigate the phytochemical composition of *Juniperus communis* L. growing within the territory of the Burabay State National Nature Park in Northern Kazakhstan to determine its pharmacological potential, and to conduct a comparative study of the biochemical components of *Juniperus communis* L. and *Juniperus sabina* L. collected from the study areas Khizi, Altiagaj and Shabran, in Azerbaijan.

MATERIALS AND METHODS

Juniperus communis L., known as a valuable medicinal and ornamental plant, was selected as the object of the study. Samples of *Juniperus communis* L. shoots were collected from sites in the Borovoe Forestry (Compartment 1) in the foothills of Mount Kokshe. According to the administrative division, this territory belongs to the regions of Northern Kazakhstan with a sharply continental climate of the temperate zone. The average annual air temperature is +3.2°C, and annual precipitation amounts to 320 mm. Due to the location of the natural park far from all oceans, the region is characterized by extremely cold winters and moderately hot, dry to semi-dry summers.

The ecological and phytocoenotic structure of *J. communis* L. associations was studied according to the floristic zoning of Kazakhstan (Flora of Kazakhstan, 1956). To investigate the phytocoenotic characteristics of *J. communis* L. associations, traditional field geobotanical methods based on the ecological-physiognomic approach described by Bykov (1970) were applied. The structure of the associations was studied according to the methods of T.A.Rabotnov (1964). Plant communities belonging to the same ecobiomorph and ecologically similar species groups were combined into ecological-physiognomic types according to the dominant principle. Plant nomenclature follows WCSP (wcsp.science.kew.org).

Within the territory of the Burabay State National Nature Park, three sampling plots were established during expeditionary work conducted in August - September 2020. Sampling was carried out early in the morning, avoiding the hottest period of the day, to ensure the representativeness of the results reflecting the condition of all plants and the study site. Shoots were cut using clean, dry secateurs from four directions (north, south, east, and west) and placed into clean paper bags. The total sample weight ranged from 500 to 550 g. In the laboratory, the juniper shoot samples were spread out and dried at room temperature. For phytochemical analysis, mixed shoot samples were prepared to obtain an average sample.

Analytical studies of the phytochemical composition of common juniper were carried out in the Laboratory of Physicochemical Methods of Analysis at Al-Farabi Kazakh National University. Alcoholic extracts of the shoots were used for phytochemical analysis. The analysis was performed by gas chromatography–mass spectrometry using an Agilent 7890A/5975C system. A sample volume of 1.0 μL was injected with a split ratio of 10:1 using a DB-35MS chromatographic column (Agilent, USA), 30 m × 0.25 mm, film thickness 0.25 μm. The column temperature program ranged from 50°C (held for 1 min) with a heating rate of 10°C/min up to 270°C (held for 15 min). The injector temperature was 250°C, and ion monitoring was carried out within the m/z 34–750 range. The phytochemical analysis method is well known and widely applied in laboratory practice in accordance with (Fatima et al., 2025; Gerling et al., 2016).

The structure and dynamics of forest phytocenoses of the North-Eastern part of the Greater Caucasus (Azerbaijani territory), and the impact of climate change on the development of species belonging to the genus *Juniperus* L. were scientifically investigated. Scientific research has been conducted in the Khizi, Altiagach, and Shabran research areas on the study of forest ecosystems, protection of biodiversity, sustainable forest management, and assessment of the impact of climate change.

Three juniper species belonging to the genus *Juniperus* L. were also used as research objects: *Juniperus communis* L. and *Juniperus sabina* L. These species are widespread in Azerbaijan within the lower and middle mountain belts and are sometimes found on rocky slopes up to the subalpine zone. They are economically valuable medicinal plants used in the production of essential oils and vitamins.

RESULTS AND DISCUSSION

Common juniper is characterized by uneven and fragmented distribution within the territory of the Burabay State National Nature Park. *Juniperus communis* L. mainly grows under the canopy of pine and pine-birch forests on podzolic soils along the slopes of Mount Kokshetau (Sinyukha). In the understory among pine, birch, and poplar trees, together with various shrubs such as rosehip, rowan, hawthorn, currant, cherry, and bird cherry, junipers are also present.

Aspen occurs as an admixture in pine-birch forests. In some depressions, pure aspen stands may occur. Towards the foothills, vegetation cover changes into communities dominated by semi-shrubs and herbaceous species. Overall, 754 plant species have been recorded within the territory of the Burabay State National Nature Park. Among them, 20 species are classified as rare and endangered plants listed in the Red Book of the Republic of Kazakhstan, and 79 species are considered relict plants. According to family representation, the flora is distributed as follows: *Asteraceae* (12.1%), *Poaceae* (6.8%), *Rosaceae* (6.2%), *Cyperaceae* (6.1%), *Scrophulariaceae* (3%), *Lamiaceae* (2.8%), *Callitrichaceae* (2.7%), *Apiaceae* (2.4%), and others.

In the experimental plots, generative individuals predominate in the cenopopulations of common juniper (up to 63%), while the proportion of juvenile individuals averages up to 9%, virginile individuals up to 17%, and senescent plants up to 11%. Healthy individuals (within 51–67%) were identified in each cenopopulation at every sampling site, although isolated weakened individuals were also observed.

Due to the special status of the region as a specially protected natural territory and its proximity to the national capital, a high level of fire safety and biological (phytopathological) security is maintained within the territory of the Burabay State National Nature Park. The flora and fauna of the park are under long-term monitoring, and many types of anthropogenic impact are strictly controlled. Therefore, the condition of the local flora, including common juniper, can be assessed as satisfactory.

It is well known that the pharmacological potential of plants directly depends on their biochemical composition. In this regard, the phytochemical composition of *Juniperus communis* L. was determined.

The results of the laboratory analysis of the phytochemical composition of *Juniperus communis* L. showed that 54 components were identified in the alcoholic extract of common juniper (Table).

All 54 components isolated from the alcoholic extracts of juniper belonged to 15 classes of organic compounds: esters, carboxylic acids, hydrocarbons, lactones, pyranones, diketones, ketones, oximes, phenols, alcohols, epoxides, ethers, aldehydes, disaccharides, and anhydrosugars. Taviano et al. (2013) compared the phenolic profiles of *Juniperus oxycedrus* subsp. *oxycedrus* and *J. oxycedrus* subsp. *macrocarpa* berries from Turkey. The total phenolic content was approximately threefold higher in *J. oxycedrus* subsp. *macrocarpa* (17.89 mg GAE/g extract) compared to subsp. *oxycedrus* (5.14 mg GAE/g extract). HPLC-DAD-ESI-MS analysis revealed similar flavonoid fingerprints but quantitative differences (12.644 μg/g vs. 4,632 μg/g). Notably, three phenolic acids were detected exclusively in subsp. *macrocarpa* (5,765 μg/g extract), with protocatechuic acid being the most abundant. In terms of antioxidant activity, subsp. *macrocarpa* showed stronger activity in DPPH and TBA tests, while subsp. *oxycedrus* exhibited higher reducing power and metal chelating activity. Both extracts displayed antimicrobial efficacy only against Gram-positive bacteria and showed no toxicity against *Artemia salina.*

In the phytochemical composition of the common juniper extract, 25 out of 54 substances were present at concentrations exceeding 1%. Among them, 21 substances were found within the range of 1–5%, while four substances exceeded 5%. The highest concentrations were observed for components such as Germacrene D isomer (7.57%), Humulene (7.97%), β-Caryophyllene (10.54%), and γ-Elemene (19.28%).

Miceli et al. (Miceli et al., 2009) investigated the flavonoid profiles and biological activities of *Juniperus communis* var. *communis* and var.

saxatilis berries from Turkey. Total polyphenol content was threefold higher in var. *communis* (59.17 mg GAE/g extract) than in var. *saxatilis* (17.64 mg GAE/g extract). HPLC-DAD-ESI-MS analysis revealed that flavonoid and biflavonoid content was significantly higher in var. *communis* (25.947 μg/g and 4.346 μg/g, respectively) compared to var. *saxatilis* (5.387 μg/g and 1.944 μg/g, respectively).

Table. Phytochemical Components of *Juniperus communis* L. extract.

№	Name of substance	RT, min	Content of components	Class of organic compounds
1	3-Methyl-3-buten-1-yl 3-methylbutanoate	10.83	0.28	Ester
2	Ethyl glycolate	11.85	0.28	Ester
3	Acetic acid	12.63	0.84	Carboxylic acid
4	Methyl pyruvate	12.91	2.29	Ester
5	Elixene (Isomer I)	13.42	0.40	Hydrocarbon
6	2-Hydroxy-γ-butyrolactone	15.17	0.68	Lactone
7	(S)-(-)-Methyl citronellate	15.47	0.45	Ester
8	β-Ylangene	15.58	1.54	Hydrocarbon
9	Bornyl acetate	15.77	1.07	Ester
10	Valencene	16.03	3.57	Hydrocarbon
11	β-Caryophyllene	16.13	10.54	Hydrocarbon
12	Elixene (Isomer II)	16.75	0.50	Hydrocarbon
13	γ-Elemene	17.16	19.28	Hydrocarbon
14	2,3-Dihydro-3,5-dihydroxy-6-methyl-(4H)-pyran-4-one (DDMP)	17.33	1.06	Pyranone
15	Methylenecyclopropanecarboxylic acid	17.58	0.27	Carboxylic acid
16	β-Copaene	17.64	0.43	Hydrocarbon
17	Humulene	17.79	7.97	Hydrocarbon
18	γ-Muurolene	18.24	1.23	Hydrocarbon
19	Terpinyl acetate	18.46	4.35	Ester
20	Germacrene D isomer	18.71	7.57	Hydrocarbon
21	β-Selinene	18.90	0.54	Hydrocarbon
22	α-Selinene	19.02	0.51	Hydrocarbon
23	Elixene (Isomer III)	19.23	0.43	Hydrocarbon
24	δ-Cadinene	19.79	1.75	Hydrocarbon
25	1,2-Cyclopentanedione	19.96	0.42	Diketone
26	2-Methyl-2-(3-methyl-2-oxobutyl)-1-cyclohexanone	20.12	0.60	Ketone
27	Methoxy phenyl oxime	20.13	0.58	Oxime
28	p-Vinylguaiacol	20.74	0.58	Phenol
29	Myrtenyl acetate	21.53	0.67	Ester
30	Epishyobunol	23.57	1.17	Alcohol
31	4-epi-Cubebol	23.79	0.40	Alcohol
32	Caryophyllene oxide	25.33	0.72	Epoxide
33	Humulene epoxide II	25.64	0.44	Epoxide
34	1-Hydroxy-1,7-dimethyl-4-isopropyl-2,7-cyclodecadiene	25.92	2.26	Alcohol
35	Elemol	26.54	1.22	Alcohol
36	trans-Longipinocarveol	26.84	0.52	Alcohol
37	Manoyl oxide	31.26	0.48	Ether
38	Palmitic acid	31.73	1.42	Carboxylic acid
39	Spathulenol	31.75	1.62	Alcohol
40	7R,8R-8-Hydroxy-4-isopropylidene-7-methylbicyclo [5.3.1] undec-1-ene	33.16	0.49	Alcohol
41	3-Isopropyl-6,7-dimethyltricyclo [4.4.0.0(2,8)] decane-9,10-diol	33.56	0.54	Alcohol
42	5-Hydroxymethylfurfural	33.80	2.62	Aldehyde
43	Phytol	34.06	0.80	Alcohol
44	Myristic acid	37.10	0.42	Carboxylic acid
45	Biformene	38.04	0.28	Hydrocarbon
46	Retinol	38.49	0.99	Alcohol
47	1-Docosene	39.23	1.79	Hydrocarbon
48	13β-Methyl-13-vinylpodocarp-7-en-3-one	40.02	1.78	Ketone
49	Tetratetracontane	40.50	0.39	Hydrocarbon
50	Behenyl alcohol	41.98	1.23	Alcohol
51	Sclareol	42.48	2.28	Alcohol
52	Tetratetracontane	44.28	1.15	Hydrocarbon
53	Sucrose	47.26	3.31	Disaccharide
54	Levoglucosan	49.42	1.00	Anhydrosugar
Total			**100.00**	

Sixteen flavonoids were separated in var. communis, with hypolaetin-7-pentoside and quercetin-hexoside as the main compounds, while eight flavonoids were identified in var. saxatilis. Notably, gossypetin-hexoside-pentoside and gossypetin-hexoside were identified for the first time in *J. communis* berries. In antioxidant assays, var. communis was more active than var. saxatilis in DPPH (IC_{50}: 0.63 vs. 1.84 mg/mL) and TBA (IC_{50}: 4.44 vs. 120.07 μg/mL) tests, whereas var. saxatilis exhibited higher Fe^{2+} chelating ability. Both extracts showed antimicrobial activity exclusively against Gram-positive bacteria.

The use of decoctions, extracts, ointments, and essential oils derived from *Juniperus* species in medicinal practice directly depends on their phytochemical composition. Some authors have demonstrated that *Juniperus excelsa* extracts exhibit antidiarrheal effects due to the presence of anthraquinones, flavonoids, saponins, sterols, terpenes, and tannins (Zhao et al., 2013). Aqueous and alcoholic extracts of juniper leaves and fruits are known to possess anticholinesterase and antioxidant activities (Jegal et al., 2017).

The scientific literature contains information indicating that certain components of juniper, such as α-pinene, apigenin, sabinene, β-sitosterol, campesterol, limonene, amentoflavone, and cupressuflavone, possess antiarthritic properties. The authors of studies (Jegal et al., 2016; Adams et al., 2010) found that juniper fruit extracts exhibit antityrosinase activity and are promising for the treatment of skin pigmentation disorders due to the presence of hypolaetin 7-O-β-xylopyranoside.

Several studies have demonstrated that the phytochemical composition of juniper depends on environmental growth conditions and that the biologically active substances of juniper are characterized by geographic variability (Butkiene et al., 2009; Koenig et al., 2004).

In a study conducted on J. excelsa leaves from Türkiye, the essential oil obtained by hydro-distillation was analyzed by GC-MS, revealing 27 compounds. The main components were identified as α-pinene (40.59%), α-cedrol (18.15%), β-myrcene (4.53%), and limonene (3.84%), accounting for 91.54% of the total essential oil composition. The oil exhibited weak antibacterial activity against both Gram-positive and Gram-negative bacterial strains, as well as low but valuable antioxidant activity as determined by TEAC/$ABTS^{+}$ radical scavenging assay (Eryigit et al., 2023).

Thus, *Juniperus communis* L., growing under the conditions of Northern Kazakhstan, demonstrates considerable potential due to its rich phytochemical composition for applications in the pharmacological, food, and perfume industries, as well as in landscape design.

A comparative study of the biochemical components of *Juniperus communis* L. growing in Northern Kazakhstan (Aleshina et al., 2004; Tkachev, 2008) and the species *Juniperus communis* L. and *Juniperus sabina* L. collected from the study areas Khizi, Altiagaj and Shabran in Azerbaijan, was conducted.

Elsherif et al. (2024) analyzed the phytochemical composition and elemental content of *Juniperus phoenicea* L. The ethanol extract contained higher concentrations of most phytochemicals compared to the aqueous extract, with total phenols at 49.36 mg/g, total flavonoids at 20.61 mg/g, and total antioxidant activity at 34.82 mg/g. Elemental analysis revealed that calcium was the most abundant macroelement (26,860 mg/kg), followed by sodium (1,705.4 mg/kg) and magnesium (944.4 mg/kg). Among microelements, iron (315.4 mg/kg) was predominant, followed by copper (55.52 mg/kg) and zinc (35.66 mg/kg).

Corresponding amounts of biomass (plant leaves) were collected from *Juniperus communis* L. and *Juniperus sabina*. Essential oils were obtained using the pharmacopoeial method (Aleshina and Velichko, 2004; OFS.1.5.3.0010.15).

A total of 160 g of each sample was measured, water was added to a 1000 mL flask using a Ginsberg apparatus, and the mixture was boiled for the period specified in the regulations. To calculate the amount of essential oil obtained as a volume–weight percentage (X) of the absolutely dry raw material, the following formula was used:

$$X = \frac{V * 100}{m}$$

V - is the volume of oil obtained, in milliliters;
m - is the weight of the raw material used, in grams.

The component composition of the isolated essential oils was analyzed by gas chromatography using a CRYSTAL-2000M gas chromatograph (Russia) (Salman et al., 2015). The analysis was completed in 22 min 48 s.

Essential oils obtained by any method or technology retain their quality even during long-term storage (for years) and remain both safe and effective. The replacement of imported pharmaceuticals with locally produced herbal remedies, as well as the increasing use of essential oil–bearing plants in various economic sectors, requires a comprehensive study of this group of plants. For this purpose, essential oils of three juniper species sourced from the Khizi, Altiagach, and Shabran regions of Azerbaijan are being studied.

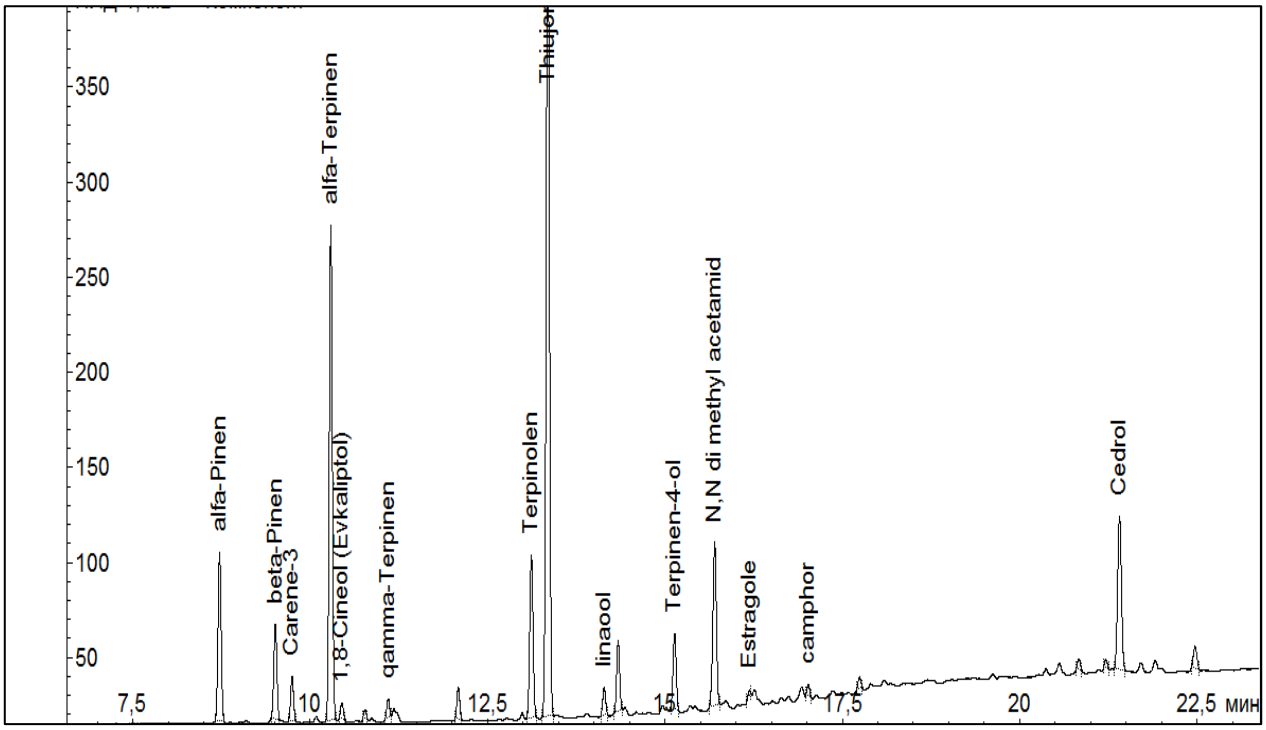

Fig. Component composition (chromatogram) of the essential oil isolated from *Juniperus communis* L.

The essential oil yields were 1.4% for *Juniperus communis* L. and 1.2% for *Juniperus sabina*. The highest essential oil yield was recorded for *Juniperus polycarpos*. The obtained essential oils had a greenish-yellow color and a characteristic pleasant aroma.

The article presents the results of gas chromatographic analysis of the essential oil of *Juniperus communis* L. and its chemical composition.

Chromatographic analysis revealed that thujone (35.21%) and α-terpinene (19.78%) were the major components, while camphor (0.33%) and estragole (0.16%) were present in the lowest concentrations (Aleshina, Velichko, 2004).

Let's take a look at the analysis of the component composition of the essential oil isolated from the studied *Juniperus communis* species. In the component composition of the essential oil, 14 peaks were identified, while 7 peaks could not be identified (Fig.). This was due to the lack of sufficient witness substances in the chromatograph. The results of the calculation of the identification of peaks are given in the table (Adams et al., 2010).

CONCLUSION

The distribution and geobotanical characteristics of *Juniperus communis* L. growing in the Burabay State National Nature Park in Northern Kazakhstan and the essential oils of some *Juniperus* L. species from the flora of Azerbaijan were studied.

The phytochemical composition of alcoholic extracts of common juniper included 54 components belonging to 15 classes of organic compounds: esters, carboxylic acids, hydrocarbons, lactones, pyranones, diketones, ketones, oximes, phenols, alcohols, epoxides, ethers, aldehydes, disaccharides, and anhydrosugars.

The yield of essential oil for *Juniperus communis* L. – 1.4%; and for *Juniperus sabina* – 1.2%. The highest yield of essential oil was recorded in the type of multi-fruited juniper.

CONFLICT OF INTEREST

There are no conflicts of interest to declare.

FUNDING

This study was carried out within the framework of Project AP05136154 “Resource Potential of Non-Wood Forest Materials and Their Environmental Safety for the Socio-Economic Development of the Regions of Kazakhstan”, financed by the Ministry of Education and Science of the Republic of Kazakhstan during 2018-2020.

ACKNOWLEDGMENTS

The authors express their sincere gratitude to V.Yu.Kirillov for consultation in interpreting the chemical analysis results and to A.N.Ebel for assistance with the expedition work.

AI STATEMENT

AI-assisted tools were used only for language translation, grammatical editing, and reference formatting.

REFERENCES

Adams R.P., Beauchamp P.S., Dev V., Bathala R.M. (2010) *The leaf essential oils of Juniperus communis* L. varieties in North America and the NMR and MS data for Isoabienol. *Journal of Essential Oil Research*, **22(23):** 23–28. doi:10.1080/10412905.2010.9700258.

Aleshina E.N., Velichko N.A. (2004) Research of the chemical composition features of essential oils of two *Juniperus species* L. *Chem. Plant Raw Mat.*, **4:** 35-37 (in Russian)

Asgary S., Naderi G.A., Shams Ardekani M.R., Sahebkar A., Airin A., Aslani S., Kasher T., Emami S.A. (2014) Inhibition of protein glycation by essential oils of branchlets and fruits of *Juniperus communis* subsp. *hemisphaerica*. *Res. Pharm. Sci*., May-Jun., **9(3):** 179-185; PMID: 25657787

Butkiene R., Nivinskiene O., Mockufc D. (2009) Two chemotypes of essential oils produced by the same *Juniperus communis* L. growing wild in Lithuania. *Chemija*, **20(3):** 195-201.

Bykov BA (1970) Introduction to phytocenology. Alma-Ata: ANKazSSR Publishing House, 226 p. (in Russian)

Elsherif K.M., Sulaiman M.A., Mlitan A. (2024) Chemical composition and phytochemical screening of *Juniperus phoenicea* L.: Evaluation of antioxidant activity, minerals, and bioactive compounds. *Journal of the Turkish Chemical Society* Section A: Chemistry, 11(2): 709-722; doi: https://doi.org/10.18596/jotcsa.1330273

Eryigit T., Yildirim B., & Ekici K. (2023) Chemical composition, antioxidant and antibacterial properties of *Juniperus excelsa* M. Bieb. leaves from Türkiye. *Acta Scientiarum Polonorum: Hortorum Cultus*, **22(1)**; doı: 10.24326/asphc.2023.4577

Fatima T., Shahzad M.I., Shah A.N., Yi Z., Gillani B., Hussain I., Gillani A., Çiftçi Z., Locatelli M., Hatamleh A.A., Al-Dosary M. (2025) Phytochemical analysis and in vitro and in vivo pharmacological activities of *Cordia myxa* extracts. *Turkish Journal of Agriculture and Forestry* **49 (1):** 169-181; doi: 10.55730/1300-011X.3256 (in Turkish)

Flora of Kazakhstan (1956) Alma-Ata: SciA of Kaz SSR, **V.1.:** 71 pp**.** (in Russian)

Gerling N.V., Punegov V.V., Gruzdev I.V. (2016) Component composition of essential oil of common juniper (*Juniperus communis* L.) under the canopy of spruce forests in the European North-East Russia. *Chem. Plant Raw Mat*., **2:** 89-96; doi: 10.14258/jcprm.2016021028 (in Russian)

Gülser F., Çığ A., Türkoğlu N. (2012) The determination of nutrient contents of native juniper (*Juniperus excelsa* Bieb.) and soil properties of plant growing areas in Van. *Journal of the Institute of Science and Technology*, **2(2):** 93-98. (in Turkish)

Jegal J., Chung K.W., Chung H.Y., Jeong E.J., Yang M.H. (2017) The standardized extract of *Juniperus communis* alleviates hyper-pigmentation *in vivo* HRM-2 hairless mice and in vitro murine B16 melanoma cells. *Biol. Pharm. Bull*., **40(9):** 1381-1388; doi: 10.1248/bpb.b17-00122

Jegal J., Park S.A., Chung K., Chung H.Y., Lee J., Jeong E.J., Kim K.H., Yang M.H. (2016) Tyrosinase inhibitory flavonoid from *Juniperus communis* fruits. *Biosci. Biotechnol. Biochem*., **80 (12):** 2311-2317; doi: 10.1080/09168451.2016.1217146

Karomatov I.D., Davlatova M.S. (2018) JUNIPER in traditional and scientific medicine. *Electronic scientific journal "Biology and Integrative Medicine"*, **1(18):** 87-106 (in Russian).

Khan M., Khan A.U., Najeeb-ur-Rehman, Gilani A.H. (2012) Pharma-ecological explanation for the medicinal use of *Juniperus excelsa* in hyperactive gastrointestinal and respiratory disorders, *J. Nat. Med.*, **66(2):** 292-301; doi: 10.1007/s11418-011-0605-z

Koenig W.A., Joulain D., Hochmuth D.H. (2004) Terpenoids and related constituents of essential oils. Mass Finder 3 in convenient and rapid analysis of GC/MS. D.H.Hochmuth (Ed.), Hochmuth Scientific Consulting: Hamburg, Germany, 493 p.

Kupriyanov A.N. (2020) Conspectus of flora of Kazakh hillocky area. Rus. Acad. Science, Sib. Department, Institute of Man Ecology, Cusbas Botanical Garden. Novosibirsk: Academical Publ. «Geo», 358 pp. (in Russian)

Miceli N., Trovato A., Dugo P., Cacciola F., Donato P., Marino A., Bellinghieri V., La Barbera T.M., Güvenç A., Taviano M.F. (2009) Comparative analysis of flavonoid profile, antioxidant and antimicrobial activity of the berries of *Juniperus communis* L. var. *communis* and *Juniperus communis* L. var. *saxatilis* Pall. from Turkey. *Journal of Agricultural and Food Chemistry*, **57(15):** 6570-6577; doi: 10.1021/jf9012295

Novikov O.O., Pisarev D.I. Zhilyakova E.T., Trifonov B.V., Levchenko V.E., Kornienko I.V. (2013) General knowledge and state of research in

pharmacology of the genus *Juniperus* L. plants (with retrospective review) *Scientific Bulletin of Belgorod State University. Series: Medicine,* 24, 1 (168): 5-9; URL: http://dspace.bsu.edu.ru/handle/123456789/57423 (in Russian)

Oztürk M., Tümen I., Uğur A., Aydoğmuş-Öztürk F., Topçu G. (2011) Evaluation of fruit extracts of six Turkish *Juniperus* species for their antioxidant, anticholinesterase and antimicrobial activities, *J. Sci. Food Agric*., **91(5):** 867-876; doi: 10.1002/jsfa.4258

Rabotnov T.A. (1964) Determination of the age composition of species populations in a community. Field geobotany. M-L.: Publishing House of the Academy of Sciences of the USSR, - pp. 132-145 (in Russian)

Salman M., Abdel Hamed E.S.S.; Bazaid A.S., Dabi M.M. (2015) Chemical composition for hydro distillation essential oil of Mentha longifolia by gas chromatography-mass spectrometry from North regions Kingdom of Saudi Arabia. Der Pharma Chimica. 7: 34-40.

Specially protected natural areas: URL: https://gis-terra.kz›spisok-gosudarstvennyh-osobo-ohra (in Russian)

Taviano M.F., Marino A., Trovato A., Bellinghieri V., La Barbera T.M., Güvenç A., Miceli N. (2013) *Juniperus oxycedrus* L. subsp. *oxycedrus* and *Juniperus oxycedrus* L. subsp. *macrocarpa* (Sibth. & Sm.) Ball. "berries" from Turkey: Comparative evaluation of phenolic profile, antioxidant, cytotoxic and antimicrobial activities. *Food and Chemical Toxicology*, **58:** 22-29; doi: 10.3390/molecules24030502

Tkachev A.R. (2008) Study of plant volatiles. Novosibirsk, 969 pp. (in Russian)

Türkoğlu N., Balta M.F., Cığ A. (2008) Sugar contents of juniper plants. *Asian Journal of Chemistry*, **20(4):** 3307-3309.

Zhao J., Liu T., Xu F., You S., Xu F., Li C., Gu Z. (2016) Anti-arthritic effects of total flavonoids from *Juniperus sabina* on complete Freund's adjuvant induced arthritis in rats. *Pharmacogn. Mag*., **12(47):** 178-183; doi: 10.4103/0973-1296.186346

ORGIDs:

Gulnar Aidarkhanova: https://orcid.org/0000-0002-5108-8036
Arzu Çığ: https://orcid.org/0000-0002-2142-5986
Elman Iskender: https://orcid.org/0009-0004-0790-2784
Minara Hasanova: https://orcid.org/0000-0001-5222-9366
Zumrud Mamedova: https://orcid.org/0000-0001-5116-0520
Gullu Aliyeva: https://orcid.org/0000-0001-8020-6583

A rationally designed Wuhan-sequence-based COVID-19 vaccine that maintained effectiveness against diverse SARS-CoV-2 variants, including Omicron: What was the key to success?

Tarlan Mamedov

Institute of Molecular Biology, Ministry of Science and Education of the Republic of Azerbaijan, 11 Izzat Nabiyev Str., AZ1073, Baku, Azerbaijan

* ***For correspondence:*** *tmammedov@gmail.com*

Received: April 19, 2026; Reviewed: May 26, 2026; Accepted: June 5, 2026

The continuous emergence of SARS-CoV-2 variants of concern has highlighted important limitations of first-generation COVID-19 vaccines developed against the ancestral Wuhan spike protein. Although these vaccines provided strong protection against severe disease and mortality, the accumulation of mutations in the spike protein, particularly within the receptor-binding domain (RBD), progressively reduced their ability to prevent infection and facilitated immune escape. In contrast, vaccine approaches that combine multiple complementary viral antigens have shown greater potential to maintain broad protective immunity despite ongoing viral evolution and immune escape. In this article, we discuss the scientific basis of a plant-produced recombinant COVID-19 cocktail vaccine that demonstrated sustained immunogenicity and cross-variant effectiveness despite being designed from the ancestral Wuhan SARS-CoV-2 sequence. Based on our experimental studies, we propose that this broad protective potential results from the integration of three key design elements: (i) targeting conserved and functionally constrained epitopes within the RBD, (ii) combining RBD and nucleocapsid (N) proteins in a multi-antigen vaccine formulation, and (iii) applying glycoengineering strategies to optimize antigen structure and immune recognition, thereby broadening the immune response and reducing susceptibility to viral immune escape. We further discuss the advantages of plant molecular farming, particularly transient expression in *Nicotiana benthamiana*, as a rapid, scalable, and cost-effective platform for recombinant vaccine production. Our studies demonstrated that plant-produced glycosylated and deglycosylated RBD antigens retain functional receptor-binding activity and induce strong neutralizing antibody responses. Moreover, when combined with the N protein, these antigens maintained effectiveness against highly divergent SARS-CoV-2 variants, including Omicron. Importantly, the principles underlying this vaccine design may extend beyond COVID-19. The strategic combination of conserved and immunologically complementary antigens provides a rational framework for the development of broadly protective vaccines against future pandemic threats and other rapidly evolving emerging pathogens. In particular, our findings suggest that integrating conserved and immunologically complementary antigens may represent a universal vaccine design strategy to combat future pandemics caused by rapidly evolving pathogens.

Keywords: *SARS-CoV-2, COVID-19 vaccine, receptor-binding domain, glycoengineering, nucleocapsid protein, plant molecular farming, Nicotiana benthamiana, cross-variant immunity, Omicron, vaccine design*

INTRODUCTION

The COVID-19 pandemic, caused by SARS-CoV-2, emerged from Wuhan, China, in late 2019 and rapidly became the most significant global public health crisis of the 21st century. The pandemic resulted in more than 7.1 million deaths worldwide and imposed an unprecedented burden on healthcare systems, economies, and societies across the globe.

The rapid global spread of SARS-CoV-2 prompted unprecedented efforts in vaccine development, resulting in the authorization and deployment of multiple first-generation vaccines within less than one year after the initial outbreak. Most of these vaccines, including Pfizer-BioNTech COVID-19 Vaccine (Polack et al., 2020), Moderna COVID-19 Vaccine (Baden et al., 2021), Oxford-AstraZeneca COVID-19 Vaccine (Ramasamy et al., 2020), Sputnik V COVID-19 Vaccine (Logunov et al., 2020), and plant-based Medicago Covifenz COVID-19 VPL-vaccine (Benvenuto et al., 2023), were designed based on the full-length spike (S) glycoprotein sequence of SARS-CoV-2 derived from

 DOI: https://doi.org/10.62088/timbb/10.1.7

the original Wuhan-Hu-1 isolate (NCBI Reference Sequence: NC_045512.2). These first-generation vaccine platforms demonstrated remarkable efficacy in preventing severe disease, hospitalization, and mortality during the early stages of the pandemic (Barda et al., 2021; Dagan et al., 2021; Roest et al., 2021; Bouillon et al., 2022).

However, the continued evolution of SARS-CoV-2 has resulted in the emergence of multiple variants of concern (VOCs), including the Alpha, Delta, and especially Omicron (He et al., 2021) variants, the latter being characterized by extensive mutations within the spike glycoprotein, particularly in the receptor-binding domain (RBD) (Harvey et al., 2021; Cao et al., 2022). These mutations substantially altered viral antigenicity, enhanced transmissibility, and facilitated immune escape from neutralizing antibodies induced by prior infection or vaccination (Harvey et al., 2021; Cao et al., 2022). Consequently, the protective efficacy of first-generation vaccines against infection declined considerably, although protection against severe disease remained relatively preserved (Cao et al., 2022).

The widespread reliance on the full-length spike protein, without sufficient emphasis on conserved and functionally constrained epitopes, may have limited the breadth and durability of cross-variant immunity. Immunodominant yet highly mutable regions within the receptor-binding motif (RBM) can preferentially attract antibody responses; however, amino acid substitutions within these regions may readily facilitate viral immune escape. In contrast, structurally constrained regions involved in receptor engagement, membrane fusion, and spike conformational stability are less tolerant to mutation and therefore represent more durable vaccine targets (Yuan et al., 2020; Walls et al., 2020).

Subunit vaccine strategies based on recombinant RBD antigens have emerged as a promising alternative to full-length spike formulations. Recombinant RBD proteins preserve critical neutralizing epitopes while reducing exposure to highly variable or non-protective regions of the spike protein. Experimental studies have demonstrated that RBD of the SARS-CoV-2 spike protein is one of the most promising targets for structure-based antigen design (Liu et al., 2020).

An important enabling technology for the development of such next-generation vaccines is the use of plant-based expression systems. Plant molecular farming, particularly transient expression in *Nicotiana benthamiana*, has emerged as a highly promising platform for the rapid and scalable production of recombinant biopharmaceuticals (Rybicki et al., 2010; Klimyuk et al., 2014; Křenek et al., 2015; Mamedov et al., 2020; Yuksel et al., 2025; Gun & Mamedov, 2022; Thuenemann et al., 2013). This system has been successfully utilized for the production of vaccine antigens, monoclonal antibodies, diagnostic proteins, and industrial enzymes for both human and veterinary applications (Mamedov et al., 2016; Mamedov et al., 2017; Mamedov et al., 2021a; Mamedov et al., 2021b; Mamedov et al., 2021c; Mammadova et al., 2022; Mamedov et al., 2023a; Mamedov et al., 2023b). Plant-based systems offer several important advantages, including low production costs, absence of contamination with human pathogens, rapid scalability, and compatibility with glycoengineering strategies that enable customized post-translational modifications (Gun & Mamedov, 2022).

In previous studies, our research group demonstrated that plant-produced glycosylated and *in vivo* deglycosylated RBD antigens retain functional receptor-binding activity and induce strong neutralizing antibody responses in experimental animal models (Mamedov et al., 2021a; Mamedov et al., 2021b). Furthermore, cocktail formulations combining RBD and nucleocapsid (N) proteins exhibited enhanced immunogenic breadth and maintained effectiveness against emerging variants, including highly mutated lineages, such as Omicron (Mamedov et al., 2021b; Mamedov et al., 2023a). Notably, these studies represented the first and only report that a rationally designed vaccine based on the original Wuhan sequence could have significant protective potential against antigenically distinct SARS-CoV-2 variants, including Omicron (Mamedov et al., 2023a). These findings provide experimental evidence that antigen engineering, glycan modulation, and multiantigen formulations can significantly enhance vaccine efficacy against the virus. (Mamedov et al., 2021b; Mamedov et al., 2023a; Mamedov et al., 2023b).

Despite these advances, a fundamental question remains regarding how the COVID-19 vaccine platform, rationally designed and developed by our research group, maintained broad cross-variant effectiveness despite the rapid antigenic evolution of SARS-CoV-2. We hypothesized that sustained cross-variant effectiveness depends on three interconnected principles: (i) targeting conserved and functionally constrained regions of the spike protein; (ii) rational glycoengineering to optimize antigen exposure and immune recognition; and (iii) incorporation of a multi-antigen (“cocktail”) strategy to broaden the immune repertoire and minimize immune escape (Mamedov et al., 2021a; Mamedov et al., 2021b; Mamedov et al., 2023a; Mamedov et al., 2023b).

Here, we present a hypothesis-driven vaccine design framework built upon these principles. Although the primary antigen design is based on the original Wuhan sequence, the strategy intentionally focuses on structurally conserved regions that remain immunologically relevant across subsequent variants. By integrating structural biology, evolutionary analysis, glycoengineering, and immunological principles, we propose that rationally designed plant-produced recombinant antigens have the potential to provide broad cross-variant protection, including Omicron (Mamedov et al., 2023a; Mamedov et al., 2023b).

RATIONAL HYPOTHESIS FOR A CROSS-VARIANT COVID-19 VACCINE TARGETING CONSERVED VIRAL EPITOPES

The central hypothesis of this study was based on three interconnected assumptions derived from viral evolutionary constraints and functional biology. First, we hypothesized that if the virus remains viable and capable of replication, the N protein must be highly conserved, since significant mutations in this protein would likely disrupt essential viral processes such as RNA packaging and replication, thereby compromising viral survival.

Second, it was hypothesized that if the virus is capable of infecting human cells, the RBD must retain functional integrity, meaning that key ACE2-interacting residues are not substantially altered by mutations, as such changes would reduce or abolish viral infectivity. Therefore, the receptor-binding interface is functionally constrained despite ongoing antigenic variation.

Third, it was considered that spike protein antigens expressed in heterologous systems are subject to host-specific glycosylation, which can mask antigenic epitopes and influence immune recognition. This glycosylation effect was therefore treated as an additional design constraint that must be accounted for in antigen selection and presentation.

Based on these three hypotheses, a rational multi-component (“cocktail”) vaccine strategy was invented and developed (Mammedov & Hasanova, EP90295649A1; US30230165995A; Mamedov et al., 2021b), combining a conserved internal antigen (N protein) with a functionally constrained RBD of the spike protein, while also incorporating glycosylation-aware design considerations. This integrated approach was intended to target multiple levels of viral constraint simultaneously, thereby increasing the likelihood of broad, cross-variant immune protection.

Multi-antigen cocktail vaccine design

To address mutations of SARS-CoV-2 and the challenges of viral evolution and immune escape, the idea of a multi-antigen (“cocktail”)-based vaccine was created (Mammedov & Hasanova, EP90295649A1; US30230165995A; Mamedov et al., 2021b; Mamedov et al., 2021b), and a COVID-19 vaccine cocktail comprising N-protein and RBD was developed. This formulation combines RBD variants, including both glycosylated and deglycosylated forms, with the highly conserved N protein.

The rationale behind this design is to broaden immune recognition by targeting multiple viral antigens and epitopes, thereby reducing reliance on a single antigen that may be susceptible to mutation-driven immune evasion. In addition, the inclusion of both structural and non-structural antigenic components is intended to promote complementary humoral and cellular immune responses, potentially enhancing the breadth and durability of protective immunity.

As we reported previously, plant-produced N protein alone did not elicit detectable neutralizing antibody responses in mice. However, we hypothesized that its incorporation into a multi-antigen vaccine formulation could provide additional immunological benefits by stimulating broader T-cell responses and contributing to more durable protective immunity when combined with RBD-based antigens (Mamedov et al., 2021b). This combinatorial approach, therefore, represents a promising strategy for improving vaccine resilience against viral variation and emerging SARS-CoV-2 variants.

This formulation combines:

- RBD variants (both glycosylated and deglycosylated forms)
- The conserved N protein

Such a design aims to:

- Broaden immune coverage across multiple viral epitopes
- Engage both humoral and cellular immune responses
- Reduce dependence on any single antigen susceptible to mutation

This combinatorial strategy is intended to enhance the breadth and robustness of protective immunity.

Our multivalent or cocktail-based antigen strategy, involving the combined use of SARS-CoV-2 structural proteins such as RBD and nucleocapsid, has been widely supported in recent plant-based vaccine studies and highlighted in review literature (Maharjan and Choe, 202; Venkataraman, 2022; Ruocco and Strasser, 2022) as a promising approach for enhancing

immunogenicity and variant coverage. The study further highlighted a novel plant-based expression strategy, reporting, according to the authors' claim, the first production of the N antigen both individually and in combination with the RBD. In contrast, most prior plant-based vaccine platforms have largely focused on S1-, S-, or RBD-based immunogens (Maharjan and Choe, 2021).

RBD as a rationally selected antigenic target

Among the structural proteins of SARS-CoV-2, the spike (S) glycoprotein rapidly emerged as the principal target for vaccine development due to its central role in viral attachment and entry into host cells via interaction with the angiotensin-converting enzyme 2 (ACE2) receptor (Tai et al., 2020). More specifically, the RBD of the S protein became one of the most strategically important antigenic regions because it contains the major neutralizing epitopes responsible for blocking virus–receptor interaction. The substantially stronger binding affinity of the SARS-CoV-2 RBD to ACE2 compared with SARS-CoV provided a molecular explanation for the enhanced infectivity and transmissibility of SARS-CoV-2 and further emphasized the importance of targeting this region in vaccine design.

The RBD-based vaccine concept offered several important advantages. First, the domain contains multiple conformational epitopes that can elicit highly potent neutralizing antibodies. Second, focusing immune responses on the receptor-interacting region reduced unnecessary antigenic complexity while maximizing the generation of functional antibodies directly associated with viral neutralization. Third, despite the emergence of multiple SARS-CoV-2 variants, critical structural and functional constraints within the RBD limited the extent of permissible mutations, allowing several conserved neutralizing epitopes to remain preserved across variants.

An additional critical consideration in rational vaccine design was the preservation of native-like protein folding and glycosylation. Both the SARS-CoV-2 spike protein and the ACE2 receptor are heavily glycosylated, and glycan structures located near the interaction interface influence protein conformation, receptor recognition, immune accessibility, and viral entry efficiency (Lan et al., 2020; Wang et al., 2018; Yan et al., 2020; Shajahan et al., 2020; Mamedov et al., 2021b). Consequently, the successful production of a properly folded and functionally active recombinant RBD required an expression system capable of supporting complex post-translational modifications and correct disulfide bond formation (Mamedov et al., 2021a; Gun & Mamedov, 2022).

In this context, the plant transient expression platform based on *Nicotiana benthamiana* provided several important advantages for rapid and scalable vaccine antigen production (Yuksel et al., 2025; Gun & Mamedov, 2022; Mamedov et al., 2020). Notably, flexible approaches are required for the successful production of recombinant proteins in plants (Gun & Mamedov, 2022; Mamedov et al., 2017; Mamedov et al., 2019a; Mamedov et al., 2021b; Mamedov et al., 2021c). This expression system has been successfully used for the production of many difficult-to-express proteins, such as Pfs48/45 of Plasmodium falciparum (Mamedov et al., 2019b), G protein of rabies virus (Mammadova et al., 2022) as vaccine candidates for malaria transmission blocking vaccine and rabies, respectively, as well as human furin and Factor IX (Mamedov et al., 2019a).

However, efficient production of functional RBD antigens required careful structural optimization of the expressed protein. One of the key factors contributing to successful expression was the rational selection of the RBD amino acid boundaries. The RBD construct encompassing amino acids R319–S591 contained an even number of cysteine residues, thereby enabling proper disulfide bridge formation and stabilization of the native protein conformation (Lan et al., 2020; Mamedov et al., 2021a). In contrast, previously reported constructs containing unpaired cysteine residues demonstrated substantially lower expression yields and reduced protein stability (Diego-Martin et al., 2020; Shin et al., 2021; Siriwattananon et al., 2021; Rattanapisit et al., 2020).

These findings highlighted an important principle in rational vaccine antigen engineering: successful antigen design depends not only on antigen selection itself but also on preservation of structural integrity, conformational stability, and native-like biochemical properties. The ability to produce highly soluble, properly folded, and functionally active RBD antigens was a critical factor in the immunogenicity and cross-variant effectiveness of the vaccine concept (Mamedov et al., 2021b; Mamedov et al., 2023a; Mamedov et al., 2023b).

Nucleocapsid protein as a rationally selected second target for cocktail-based vaccine development

The rapid global spread of SARS-CoV-2 since its emergence in Wuhan in 2019, together with the continuous appearance of new variants of concern such as Alpha, Beta, Gamma, and Delta, has highlighted the limitations of single-antigen vaccine strategies. Although multiple vaccine platforms,

including mRNA-, DNA-, viral vector, and recombinant protein-based vaccines, have been successfully developed and deployed, accumulating evidence indicates a reduction in vaccine effectiveness against emerging variants, particularly those carrying multiple mutations within the spike (S) protein RBD and N-terminal domain (NTD). These mutations have been shown to directly affect ACE2 binding affinity, viral transmissibility, and immune escape mechanisms, thereby challenging the durability of spike-focused immune responses.

Variants such as Delta (B.1.617.2) exemplify the evolutionary plasticity of SARS-CoV-2, harboring multiple mutations in the spike protein, including key substitutions within the RBD (e.g., L452R and T478K), which have been associated with reduced sensitivity to neutralizing antibodies. Collectively, these observations underscore a critical limitation of RBD-centered vaccine strategies: while highly effective in inducing neutralizing antibodies, they may be vulnerable to antigenic drift driven by spike mutations.

In this context, the N protein emerges as a rationally selected second antigenic target for next-generation cocktail vaccine design. Unlike the spike protein, the N protein is functionally constrained and highly conserved across SARS-CoV-2 variants and related coronaviruses, with significantly lower mutation frequency over time (Gao et al., 2021; Drosten et al., 2023; Wrapp et al., 2020; Holmes, K.V.; Enjuanes, 2003; Rota et al., 2003; Grifoni et al., 2020; Mamedov et al., 2020). Structurally, the N protein plays an essential role in viral RNA packaging and ribonucleoprotein assembly, and it is abundantly expressed during infection, making it a highly immunogenic antigen capable of inducing robust humoral and cellular immune responses.

Importantly, immune responses against the N protein are not primarily dependent on neutralizing antibodies but are strongly associated with T-cell-mediated immunity, which is generally more conserved and less affected by viral mutations. This provides an additional layer of immune protection that complements RBD-induced neutralizing antibody responses. Therefore, combining RBD and N antigens in a single formulation introduces a dual-mechanism vaccine strategy: (i) RBD-driven neutralization of viral entry, and (ii) N protein-driven enhancement of broad cellular and long-term immune memory.

Experimental evidence further supports this rationale. Although N protein alone may not induce strong neutralizing antibody responses, its inclusion in an antigen cocktail with RBD significantly enhances overall immunogenicity (Mamedov et al., 2021b). In plant-based expression systems such as *Nicotiana benthamiana*, co-expression of RBD and N proteins has demonstrated the feasibility of producing a multivalent antigen formulation capable of inducing high-titer antibody responses *in vivo*. Notably, the antigen cocktail elicited stronger humoral responses compared to individual antigens, suggesting a synergistic immunological effect (Mamedov et al., 2021b).

Taken together, these findings support the concept that rational vaccine design against rapidly evolving RNA viruses should extend beyond single-target neutralization strategies. The N protein, due to its evolutionary conservation, high immunogenicity, and role in inducing cellular immune responses, represents a strategically important second antigen in cocktail-based vaccine development. The combined N+RBD approach therefore provides a broader and potentially more durable protective immune profile, addressing both viral entry inhibition and long-term immune surveillance across SARS-CoV-2 variants.

Deglycosylation strategy: *in vivo* (cell-based) post-expression deglycosylation

Glycosylation plays a pivotal role in shaping antigen structure, stability, and immune recognition. Glycan moieties can shield immunogenic epitopes from antibody recognition, thereby modulating immune responses. To overcome challenges associated with aberrant glycosylation, an in vivo deglycosylation platform technology has been developed for the efficient production of recombinant proteins in native-like deglycosylated forms in eukaryotic cells (Mammedov, WO2012170678A1, EP2718444B1, US11673926B2, CA2839932C, CN103906840B; Mammedov, CN108463550A, US11041163B2, RU2741347C2, CA3005304C, IL259301B2, EP3374500A1, MX2018006001A; Mamedov et al., 2012; Mamedov et al., 2017). This technology has enabled the production of a broad range of recombinant proteins in their native-like, non-glycosylated forms (Mamedov et al., 2016; Mamedov et al., 2019a; Mamedov et al., 2019b; Mamedov et al., 2021a; Mamedov et al., 2021b; Mamedov et al., 2021c; Mamedov et al., 2023a; Mamedov et al., 2025). In particular, the Endo H-mediated in vivo deglycosylation approach has been successfully employed for the production of non-glycosylated forms of several biologically and medically important proteins, including the protective antigen PA83 of *Bacillus anthracis* (Mamedov et al., 2024), full-length Pfs48/45 of *Plasmodium falciparum* (Mamedov et al., 2019a), the rabies virus G protein (Mammadova et al., 2022), and the SARS-CoV-2 RBD (Mamedov et al., 2021a; Ruocco & Strasser, 2022). These studies facilitated the development of vaccine candidates

against anthrax, malaria, rabies, and several vaccine candidates against COVID-19 (Mamedov et al., 2021a, Mamedov et al., 2021b, Mamedov et al., 2023a; Mamedov et al., 2023b; Royal et al., 2021; Pillet et al., 2022; Shanmugaraj et al., 2020), as well as a soluble human angiotensin-converting enzyme 2 (ACE2) molecule as a potential therapeutic agent against COVID-19 (Mamedov et al., 2021c; Mammedov, Patent Application, 2022).

Building upon these advances in glycoengineering and *in vivo* deglycosylation technologies, the vaccine design described in this study incorporates a rational glycan-engineering strategy to optimize antigen presentation. First, glycoengineered receptor-binding variants may enhance epitope accessibility and improve antibody binding. In addition, targeted modification of glycosylation patterns can optimize antigen recognition and promote more effective immune responses. This dual glycoengineering strategy integrates complementary immunological mechanisms within a single vaccine design framework, with the potential to enhance both antigen recognition and the breadth of protective immunity.

PLANT TRANSIENT EXPRESSION SYSTEMS AS A COST-EFFECTIVE, SAFE, RAPID, AND SCALABLE VACCINE PRODUCTION

The plant transient expression platform based on *Nicotiana benthamiana* provided several important advantages for rapid, scalable, and cost-effective vaccine antigen production (Yuksel et al., 2025; Gun & Mamedov, 2022; Mamedov et al., 2020b). In addition to its rapid production timeline, flexibility, and low risk of contamination by human pathogens, this platform has recently emerged as a highly versatile expression technology for producing structurally complex and difficult-to-express recombinant proteins, including viral glycoproteins, multimeric antigens, monoclonal antibodies, and glycosylated therapeutic proteins. Furthermore, advances in agroinfiltration strategies, glycoengineering, deconstructed viral vectors, and transient co-expression technologies have significantly expanded the applicability of plant-based systems for next-generation vaccine development and rapid pandemic response platforms.

This expression system has been successfully used for the production of many difficult-to-express proteins, such as Pfs48/45 of *Plasmodium falciparum* (Mamedov et al., 2019b), G protein of rabies virus (Mammadova et al., 2022), Protective Antigen from *Bacillus anthracis* (Mamedov et al., 2016; Mamedov et al., 2017; Mamedov et al., 2024) as vaccine candidates for malaria transmission-blocking, rabies, and anthrax vaccines, respectively, as well as recombinant human furin and coagulation Factor IX (Mamedov et al., 2019a). In addition, plant transient expression systems have demonstrated considerable potential for the rapid production of monoclonal antibodies (Farrance et al., 2011; Shanmugaraj et al., 2020), growth factors and virus-like particles (VLPs) (Royal et al., 2021; Moon et al, 2022; Pillet et al., 2022; O'Kennedy et al., 2023; Tottey et al., 2023), immune complexes, and multicomponent vaccine formulations targeting emerging infectious diseases, thereby supporting their increasing relevance for future Disease X preparedness and outbreak-responsive biomanufacturing strategies.

FUTURE PERSPECTIVE: COCKTAIL ANTIGEN DESIGN AS A PLATFORM STRATEGY FOR EMERGING INFECTIOUS DISEASES (DISEASE X PREPAREDNESS)

The rational combination of RBD and N antigens represents more than a SARS-CoV-2-specific vaccine approach; it introduces a platform-based concept for next-generation vaccine design against emerging infectious diseases, including potential “Disease X” scenarios. This dual-antigen strategy integrates two complementary immunological axes: (i) the RBD-driven neutralizing antibody response targeting viral entry, and (ii) the nucleocapsid-driven conserved T-cell response supporting broad and durable immune memory.

From a systems vaccinology perspective, this cocktail-based design addresses a fundamental limitation of single-antigen vaccines, namely their vulnerability to antigenic drift in rapidly evolving RNA viruses. While spike-based immunogens are highly effective in inducing neutralizing antibodies, they remain susceptible to escape mutations. In contrast, nucleocapsid-based immunity provides a more evolutionarily constrained and conserved target, thereby stabilizing vaccine efficacy across divergent variants.

Importantly, the RBD+N combination should be viewed as modular vaccine architecture rather than a pathogen-specific formulation. Such an approach aligns with the broader concept of “preparedness vaccinology,” in which antigen selection is guided not only by current circulating strains but also by structural conservation, functional constraints, and immunological redundancy across related viral families. In this framework, cocktail antigen design may serve as a flexible technological platform for rapid adaptation against future emerging pathogens with pandemic potential.

Thus, the RBD and nucleocapsid-based

cocktail strategy may represent a foundational step toward next-generation rational vaccine platforms designed for rapid response to emerging threats, including potential “Disease X”.

CONCLUSION

The ongoing evolution of SARS-CoV-2 and the continuous emergence of variants of concern have clearly demonstrated the limitations of single-antigen vaccine strategies. In particular, spike antigen-focused approaches, while highly effective in inducing neutralizing antibodies, remain vulnerable to immune escape driven by mutations within the RBD and adjacent antigenic regions.

In this article, we highlight a rational dual-antigen vaccine design strategy combining the spike protein RBD with the N protein of SARS-CoV-2. The RBD induces potent neutralizing antibody responses targeting viral entry, whereas the N protein provides a highly conserved antigenic target associated with robust T-cell-mediated immunity and long-term immune memory. Together, this cocktail approach generates a complementary immune profile that supports both viral neutralization and long-term immune protection.

Notably, the COVID-19 vaccine platform developed by our group (Mamedov et al., 2021a; Mamedov et al., 2021b; Mamedov et al., 2023a; Mamedov et al., 2023b) demonstrated broad effectiveness against multiple SARS-CoV-2 variants despite the virus's rapid antigenic evolution. We demonstrated that plant-produced RBD and cocktail-based vaccine candidates are highly effective against SARS-CoV-2, independently of its emerging variants (Mamedov et al., 2023). As we described (Mamedov et al., 2023b), this was the first and only report worldwide on a COVID-19 vaccine SARS-CoV-2, effective against all emerging SARS-CoV-2 variants, including Delta and Omicron. The findings presented here suggest that this broad protection can be attributed to the synergistic combination of variant-sensitive neutralizing targets within the RBD and highly conserved immune targets within the N protein, together with optimized antigen design and presentation. This integrated strategy may help explain the sustained cross-variant immune responses observed with the vaccine platform.

Furthermore, plant-based transient expression systems provide a flexible and scalable platform for rapidly producing multivalent antigens, enabling timely responses to emerging viral threats. Collectively, these findings support developing multi-antigen vaccine platforms as a promising strategy to achieve broad, durable, and variant-resilient protection against current and future coronavirus threats.

Overall, the RBD+N cocktail vaccine strategy provides a rationale and framework for next-generation vaccine design that may be extended to other emerging infectious diseases and future pandemic threats. By combining complementary antigens, this platform provides a conceptual framework for the rapid development of vaccines against future emerging infectious diseases, including a potential “Disease X”. Such an approach may facilitate the selection of conserved and immunologically relevant antigens, thereby supporting the development of broadly protective and adaptable next-generation vaccines.

AUTHOR CONTRIBUTIONS

Tarlan Mamedov conceived the review topic, performed the literature search and analysis, interpreted the findings, and wrote and revised the manuscript. The author has read and approved the final manuscript.

ETHICAL CONSIDERATIONS

This article is a review study based exclusively on previously published literature and does not involve human participants, animals, or the collection of primary data. Therefore, ethical approval and informed consent were not required.

FUNDING

No specific funding was received for the preparation of this review article. However, the scientific background, technological developments, and vaccine design concepts discussed in this review were developed through research projects awarded to Tarlan Mamedov and supported by TÜBİTAK (Project Nos. 114Z258, 114Z863, 115S077, 218S723 and 222Z043) and TÜSEB (Project No. 8611).

CONFLICT OF INTEREST

The author declares no conflict of interest.

AI STATEMENT

The author declares that no artificial intelligence (AI) tools were used to generate, analyze, interpret, or validate the clinical data, statistical results, or scientific conclusions presented in this study. Any AI-assisted technologies, if used, were limited to language editing, grammar correction, or formatting support. The author assumes full responsibility for the accuracy, originality, and integrity of the manuscript.

REFERENCES

Baden L.R., El Sahly H.M., Essink B. et al. (2021) Efficacy and safety of the mRNA-1273 SARS-CoV-2 vaccine. *N. Engl J. Med.,* **384:** 403–416; doi:10.1056/NEJMoa2035389.

Bally J., Jung H., Mortimer C. et al. (2018) The rise and rise of *Nicotiana benthamiana*: A plant for all reasons. *Annu. Rev. Phytopathol.,* **56:**405–426.

Barda N., Dagan N., Balicer R.D. (2021) BNT162b2 mRNA COVID-19 vaccine in a nationwide mass vaccination setting. *N. Engl. J. Med.,* **384(20):** 1970; doi: 10.1056/NEJMc2104281.

Benvenuto E., Broer I., D'Aoust M.A., Hitzeroth I., Hundleby H., Menassa R., Kirsi-Marja Oksman-Caldentey K.M. et al. (2023) Plant molecular farming in the wake of the closure of Medicago Inc., 2023. *Nature Biotechnology,* **41:** 893–894.

Bouillon K., Baricault B., Botton J., Jabagi M.J., Bertrand M., Semenzato L., Vu S.L., Drouin J. et. al. (2022) Effectiveness of BNT162b2, mRNA-1273, and ChAdOx1-S vaccines against severe COVID-19 outcomes in a nationwide mass vaccination setting: cohort study. *BMJ Me*d., **1(1):** e000104; doi: 10.1136/bmjmed-2021-000104.

Cao Y., Wang J., Jian F., Xiao T., Song W., Yisimayi A, Huang W. et al. (2022) Omicron escapes the majority of existing neutralizing antibodies. *Nature*, **602:** 657–663.

Chen Q., Lai H. (2015) Gene delivery into plant cells for recombinant protein production. *BioMed. Research International*, **2015:** 932161.

Dagan N., Barda N., Kepten E., Miron O., Perchik O, Katz M.A., Miguel A Herná M.A. et al. (2021) BNT162b2 mRNA COVID-19 Vaccine in a Nationwide Mass Vaccination Setting. *N. Engl. J. Med*., **384(15):** 1412-1423.

Farrance C.E., Chichester J.A., Musiychuk K. et al. (2011) Antibodies to plant-produced Plasmodium falciparum sexual stage protein Pfs25 exhibit transmission-blocking activity. *Hum. Vaccin*., **7(sup1):** 191-198.

Gleba Y., Klimyuk V., Marillonnet S. (2007). Viral vectors for the expression of proteins in plants. *Current Opinion in Biotechnology*, **18:** 134–141.

Goulet M.C., Gaudreau L., Gagné M. et al. (2019) Production of biopharmaceuticals in *Nicotiana benthamiana* - Axillary stem growth as a key determinant of total protein yield. *Front. Plant Sci*. **10:** 735.

Gun N., Mamedov T. (2022) Flexible approaches are required for successful production of recombinant proteins in plants. *Med Science*, 2022, **11:** 1.

Harvey W.T. et al. (2021) SARS-CoV-2 variants, spike mutations and immune escape. *Nat. Rev. Microbiol*., **19:** 409–424.

He X., Hong W., Pan X., Lu G., Wei X. (2021) SARS-CoV-2 Omicron variant: Characteristics and prevention. *Med. Comm.,* **2 (4):** 838–845.

Klimyuk V., Pogue G., Herz S., Butler J., Haydon H. (2014) Production of recombinant antigens and antibodies in *Nicotiana benthamiana* using 'magnifection' technology: GMP-compliant facilities for small- and large-scale manufacturing. *Curr. Top. Microbiol. Immunol.*, **375:** 127–154; PMID: 22527176

Křenek P., Šamajová O., Luptovčiak I., Doskočilová A., Komis G., Šamaj J. (2015) Transient plant transformation mediated by *Agrobacterium tumefaciens*: Principles, methods and applications. *Biotechnol. Adv.,* **33(6 Pt 2):** 1024–1042.

Logunov D.Y. et al. (2021) Safety and immunogenicity of an rAd26 and rAd5 vector-based heterologous prime-boost COVID-19 vaccine in two formulations: two open, non-randomised phase 1/2 studies from Russia. *Lancet,* **396:** 887–897.

Mamedov T., Ghosh A., Jones M., Mett M., Farrance C., Musiychuk K., Horsey A., Yusibov V. (2012) Production of non-glycosylated recombinant proteins in *Nicotiana benthamiana* plants by co-expression with bacterial PNGase F. *Plant Biotechnology Journal*, **10:** 773–782.

Mamedov T., Chichester J.A., Jones R.M. et al. (2016) Production of functionally active and immunogenic non-glycosylated protective antigen from *Bacillus anthracis* in *Nicotiana benthamiana* by co-expression with peptide-n glycosidase f (PNGase F) of *Flavobacterium meningosepticum*. *PLoS One*, **11(4):** e0153956.

Mamedov T., Cicek K., Gulec B., Ungor R., Hasanova G. (2017) *In vivo* production of non-glycosylated recombinant proteins in *Nicotiana benthamiana* plants by co-expression with Endo-β-N-acetylglucosaminidase H (Endo H) of *Streptomyces plicatus*. *PLoS One*, **12(8):** e0183589.

Mamedov T., Musayeva I., Acsora R. et al. (2019a) Engineering and production of functionally active human Furin in *N. benthamiana* plant: *In vivo* post-translational processing of target proteins by Furin in plants. *PLoS One*, **14(3):** e0213438.

Mamedov T., Cicek K., Miura K. et al. (2019b) A plant-produced *in vivo* deglycosylated full-length

Pfs48/45 as a transmission-blocking vaccine candidate against malaria. *Sci Rep.*, **9(1):** 9868.

Mamedov T., Soylu I., Mammadova G., Hasanova G. (2020a) Sequence analysis and amino acid variations of structural proteins deduced from novel coronavirus SARS-CoV-2 strains, isolated in different countries. *PrePrint*, doi: 10.20944/preprints202005.0026. **v1:** PPR: PPR1

Mamedov T., Gulec B., Mammadova G. (2020b) Plant molecular pharming is a promising system for cost-effective production of veterinary vaccines. *Mediterranean Agricultural Sciences*, **33(3):** 375-380.

Mamedov T., Yuksel D., Ilgın M. et al. (2021a) Plant-produced glycosylated and in vivo deglycosylated receptor-binding domain proteins of SARS-CoV-2 induce potent neutralizing responses in mice. Viruses. 2021a, 13(8):1595.

Mamedov T., Yuksel D., Ilgın M. et al. (2021b) Production and characterization of nucleocapsid and RBD cocktail antigens of SARS-CoV-2 in *Nicotiana benthamiana* plant as a vaccine candidate against COVID-19. *Vaccines (Basel*), **9(11):** 1337.

Mamedov T., Gurbuzaslan I., Yuksel D. et al. (2021c) Soluble human angiotensin converting enzyme 2 as a potential therapeutic tool for COVID-19 is produced at high levels in *Nicotiana benthamiana* plant with potent anti-SARS-CoV-2 activity. *Front. Plant Sci*., **12:** 742875.

Mammadova G., Gurbuzaslan I., Yuksel D. et al. (2022) Engineering, production, and immunogenicity studies of a truncated form of rabies virus glycoprotein produced in *Nicotiana benthamiana* plant. *Med. Science*, **11(2):** 478.

Mamedov T., Gun G., Gulec G., Khozeini H., Ungor R. et al. (2024) Immunogenicity and efficacy studies of Endo H *in vivo* deglycosylated protective antigen from *Bacillus anthracis* as a vaccine candidate against anthrax. *Research Square*, doi: 10.21203/rs.3.rs-3928112/v1.

Mamedov T, Hasanova G. (2023) Engineering, production and characterization of plant-produced nucleocapsid and spike structural proteins of SARS-CoV-2 as vaccine candidates against COVID19. EP4029569A1 Patent App., US Patent App. 17/457,138, 2023.

Mammedov T. (2022) Engineering, production and characterization of plant-produced, soluble human angiotensin converting enzyme-2 as a therapeutic target in COVID-19. US Patent App.17534479, US2022220465A1, WO2022115083A1; Publication date 2022/7/14.

Mammedov T. (2015) Production of *in vivo* N-deglycosylated recombinant proteins by co-expression with Endo H. **Patents:** CN108463550A, US11041163B2, RU2741347C2, CA3005304C, IL259301B2, EP3374500A1, MX2018006001A.

Mammedov T., Hasanova G. (2020) Production and characterization of plant-produced nucleocapsid and spike structural proteins of SARS-CoV-2 as vaccine candidates against COVID-19. European Patent Application EP90295649A1; U.S. Patent Application US30230165995A1.

Liu L., Wang P., Nair M.S., Yu J., Rapp M., Wang Q., Luo Y., J. F.-W. Chan J.F-W. et al. ((2020) Potent neutralizing antibodies against multiple epitopes on SARS-CoV-2 spike. *Nature*, **584:** 450–456.

O'Kennedy M.M., Abolnik C., Smith T., Motlou T., Goosen K., Sepotokele K.M. et al. (2023). Immunogenicity of adjuvanted plant-produced SARS-CoV-2 Beta spike VLP vaccine in New Zealand white rabbits. *Vaccine,* **41(13):** 2261–2269.

Polack F.P., Thomas S.J., Kitchin N. et al. (2020) Safety and efficacy of the BNT162b2 mRNA COVID-19 vaccine. *N. Engl. J. Med.*, **383:** 2603–2615.

Pillet S., Arunachalam P. S., Andreani G., Golden N., Fontenot J., Aye P.P. et al. (2022) Safety, immunogenicity, and protection provided by unadjuvanted and adjuvanted formulations of a recombinant plant-derived virus-like particle vaccine candidate for COVID-19 in nonhuman primates. *Cell Mol. Immunol.,* **19:** 222–233; doi: 10.1038/s41423-021-00809-2.

Ramasamy M.N., Minassian A.M., Ewer K.J. et al. (2020) Safety and immunogenicity of ChAdOx1 nCoV-19 vaccine administered in a prime-boost regimen in young and old adults (COV002): a single-blind, randomized, controlled, phase 2/3 trial. *Lancet*, **396:** 1979–93.

Royal J.M., Simpson C.A., McCormick A.A., Phillips A., Hume S., Morton J. et al. (2021) Development of a SARS-CoV-2 vaccine candidate using plant-based manufacturing and a tobacco mosaic virus-like nanoparticle. *Vaccines,* **9:** 1347; doi: 10.3390/vaccines9111347

Rybicki E.P. (2010) Plant-made vaccines for humans and animals. *Plant Biotechnol. J.*, **8:** 620-637.

Ruocco V., Strasser R. (2022) Transient expression of glycosylated SARS-CoV-2 antigens in *Nicotiana benthamiana*. *Plants,* **11:** 1093; doi: 10.3390/plants11081093.

Shanmugaraj B., Rattanapisit K., Manopwisedjaroen S., Thitithanyanont A., Phoolcharoen W. (2020). Monoclonal antibodies B38 and H4 produced in *Nicotiana benthamiana*

neutralize SARS-CoV-2 in *vitro*. *Front. Plant Sci.,* **11:** 589995.

Tottey S., Shoji Y., Mark Jones R., Musiychuk K., Chichester J.A., Miura K. et al. (2023) Engineering of a plant-produced virus-like particle to improve the display of the *Plasmodium falciparum* Pfs25 antigen and transmission-blocking activity of the vaccine candidate. *Vaccine,* **41(4):** 938–944; doi: 10.1016/j.vaccine.2022.12.048.

Thuenemann E.C., Lenzi P., Love A.J, Taliansky M., Bécares M., Zuñiga S. et al. (2013) The use of transient expression systems for the rapid production of virus-like particles in plants. *Curr. Pharm. Des.,* **19:** 5564–5573.

Venkataraman S. (2022) Plant molecular pharming and plant-derived compounds towards generation of vaccines and therapeutics against coronaviruses. *Vaccines*, **10(11):** 1805.

Walls A.C. et al. (2020) Structure, function, and antigenicity of SARS-CoV-2 spike glycoprotein. *Cell*, **181(2):** 281-292.

Ward B.J. et al. (2021) Phase 1 randomized trial of a plant-derived virus-like particle vaccine for COVID-19. *Nature Medicine*, **27:** 1071–1078.

Yuan M et al. (2020) Structural basis of shared antibody responses to SARS-CoV-2. *Science*, **369:** 6507, 1119-1123.

Yuksel D., Yusifova G., Hasanova A.S., Mammedov T. (2025) Enhancing recombinant protein production by optimizing nutrient replenishment, light, and humidity in a *Nicotiana benthamiana* bioreactor. *European Journal of Biology*, **4:** 4.

ORCID:
Tarlan Mamedov: https://orcid.org/0000-0002-5747-4990

Note: *This manuscript was reviewed by two independent external reviewers who are not members of the journal's Editorial Board.*

Molecular docking analysis of glycyrrhizin interactions with ACE2 and tyrosinase: implications for inflammatory and pigmentation-associated pathways

Leyla Galandarli[1*], Ralphreed Gasanov[2], Gulnara Akverdieva[3]

[1] "Young Talents" Lyceum, Baku State University, 53 Ahmad Jamil Str., AZ1141, Baku, Azerbaijan
[2] Bioengineering Research Laboratory, Baku State University, 33 Academician Zahid Khalilov Str., AZ1148, Baku, Azerbaijan
[3] Institute for Physical Problems, Baku State University, 33 Academician Zahid Khalilov Str., AZ1148, Baku, Azerbaijan

[*] ***For correspondence:*** *leyla_aktau@mail.ru*

Received: February 25, 2026; Reviewed: April 08, 2026; Accepted: May 29, 2026

Currently, traditional herbal medicines are used as complementary agents in the management of viral and inflammatory disorders. In the present study, the interactions of glycyrrhizin (ChemSpider ID: 14263) with ACE2 (PDB ID: 6LZG) and tyrosinase (PDB ID: 2ZMX) were investigated to evaluate its potential relevance to ACE2-associated inflammatory pathways and pigmentation-related molecular mechanisms. Docking simulations were performed using AutoDock Vina software. It was shown that the ligand molecule binds to the active sites of the selected receptors and forms several key intermolecular interactions. Glycyrrhizin exhibited binding affinity values of −7.4 and −7.1 kcal/mol with 6LZG and 2ZMX protein targets, respectively. These findings suggest that glycyrrhizin may serve as a promising molecular scaffold for further investigation of ACE2- and tyrosinase-associated pathways. Based on the calculated results and SAR data analysis, pharmacophore models for glycyrrhizin interaction with the specified receptors were proposed. Although the obtained docking results indicate favorable ligand–receptor interactions, further molecular dynamics simulations and experimental validation are required to confirm the biological relevance of these findings.

Keywords: *Glycyrrhizin, ACE2, tyrosinase, molecular docking, pharmacophore model*

INTRODUCTION

The identification of biological targets and elucidation of molecular mechanisms underlying drug activity are important for both fundamental pharmacological research and the development of novel therapeutic agents. Glycyrrhizin (glycyrrhizic acid) is a glycosidic saponin extracted primarily from the roots of Glycyrrhiza glabra (licorice), traditionally used in various medical systems, including Siddha medicine (Sharma et al., 2017).

Chemically, glycyrrhizin is a triterpenoid saponin consisting of a hydrophilic moiety formed by two glucuronic acid residues and a hydrophobic glycyrrhetinic acid core. The molecular structure and atomic numbering are presented in Fig. 1(a–c) (El-Saber Batiha et al., 2020).

Glycyrrhizin and its aglycone have demonstrated antiviral-related biological activity against several viruses, including HSV-1/2, EBV, HCV, HIV-1, SARS-CoV, and influenza. Proposed mechanisms include disruption of viral entry, modulation of membrane fluidity, inhibition of viral gene expression, and stimulation of host interferon production. In addition to antiviral-related activity, glycyrrhizin has attracted attention because of its potential immunomodulatory effects associated with the renin–angiotensin system (RAS) (Al Dehlawi et al., 2023; Graebin 2017; Rasool et al., 2025).

Recent studies have also reported interactions of glycyrrhizic acid with SARS-CoV-2 main protease (M^{pro}), suggesting possible relevance of this compound for further investigation of virus-associated molecular pathways (Chen et al., 2024).

Moreover, ACE2 plays a critical protective role in the renin–angiotensin system through regulation of the ACE2/Ang-(1–7) axis, which is associated with anti-inflammatory, cardioprotective, and vasoprotective effects under chronic pathological conditions (Patel et al., 2016).

In addition to enzyme inhibition, glycyrrhizic acid may interfere with the early stages of viral infection by affecting interactions between viral surface proteins and host cell receptors, including ACE2 (Li et al., 2021).

 DOI: https://doi.org/10.62088/timbb/10.1.8

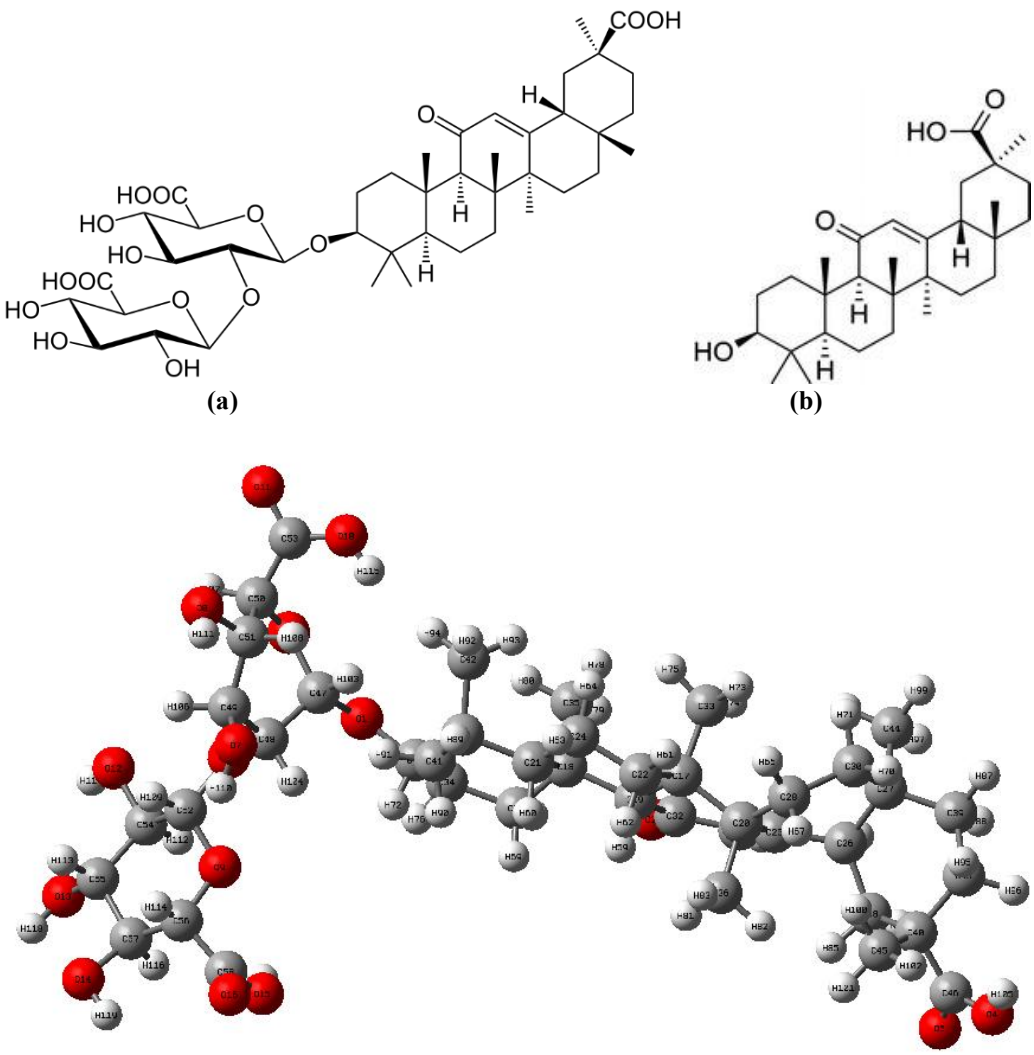

Fig. 1. Molecular structure of glycyrrhizin (a) and its part - glycyrrhetic acid (b); chemical structure and numbering scheme for glycyrrhizin (c).

Beyond antiviral-related activity, glycyrrhizic acid also demonstrates immunomodulatory effects through the regulation of interferon production and inflammatory cytokines, thereby contributing to host antiviral defense mechanisms (Zuo et al., 2023). While CD4 remains the primary receptor for HIV-1, systemic complications of chronic HIV infection are associated with dysregulation of the renin–angiotensin system (RAS), in which ACE2 may play a protective role (Murck., 2020). In the context of chronic HIV infection, ACE2 was investigated not as a direct viral entry receptor, but as a component of the renin–angiotensin system potentially associated with inflammatory dysregulation and systemic complications. Chronic HIV infection is associated with persistent systemic inflammation and RAS imbalance characterized by elevated angiotensin II levels and reduced ACE2 expression (Buder et al., 2022). Previous molecular docking studies have demonstrated that glycyrrhizin and structurally related compounds exhibit favorable binding interactions with the ACE2 receptor, supporting their potential relevance in investigations of virus-associated molecular pathways (Ahmad et al., 2021).

In parallel, melanogenesis represents a complex biological process regulated by oxidative stress, inflammatory mediators, enzymatic activity, and intracellular signaling pathways involved in melanocyte function and pigmentation (Videira et al., 2013). Because oxidative and inflammatory mechanisms are also implicated in pigmentary disorders such as vitiligo, the investigation of glycyrrhizin interactions with melanogenesis-related proteins may provide additional insights into its potential cytoprotective and immunomodulatory properties. Vitiligo is associated with autoimmune and inflammatory mechanisms, including oxidative stress and immune dysregulation, which may be triggered or exacerbated by viral infections (Schmidt et al., 2022). Rather than emphasizing direct inhibition of

tyrosinase activity, the present study explores possible stabilizing interactions of glycyrrhizin with tyrosinase-associated molecular structures under oxidative stress conditions (Zeng et al., 2024).

The Siddha system of medicine includes therapeutic approaches for dermatological disorders such as Vitiligo (Venpulli) (Thas., 2008). Vitiligo is a chronic depigmentation disorder characterized by melanocyte destruction and loss of skin pigmentation (Marchioro et al., 2022). Tyrosinase, a copper-containing enzyme involved in melanogenesis, catalyzes melanin biosynthesis within melanocytes (Wang et al., 2025). Glycyrrhiza glabra has also been investigated in dermatological research because of its anti-inflammatory and biologically active properties (Liu et al., 2025).

In the present study, potential molecular interactions of glycyrrhizin with ACE2 and tyrosinase were investigated in the context of inflammatory and pigmentation-associated pathways.

COMPUTATIONAL METHODS

The successful development of new, life-saving drugs is highly dependent on the collaborative efforts of physicists, biologists, biophysicists, biochemists, and synthetic chemists. Molecular docking has become a particularly valuable tool in this process, accelerating the selection of molecules that can act as potential drugs (Meng et al., 2022). By enabling the prediction of a ligand's selective binding to a specific target protein, one responsible for a particular pathology, molecular docking can effectively block its erroneous function (Megantara et al., 2025).

Molecular docking is a widely used computational approach in drug discovery that predicts the interaction patterns and binding affinities between a ligand and a target protein (Xu et al., 2023). Molecular docking is a computational molecular modeling method used to predict the binding pose of a small ligand molecule within the active site of a receptor (Agu et al., 2023). The core objective of molecular docking is to identify the most energetically favorable binding conformation of an inhibitor molecule at the target protein's active site, based on its intermolecular interactions. Mathematically, this is equivalent to searching for the global minimum on a complex, high-dimensional energy landscape (Celik et al., 2023).

The method predicts the optimal orientation and position of one molecule relative to another for the formation of a stable complex. The docking procedure is highly valuable during the initial stages of drug discovery and development, representing one of the most crucial steps in the process. It enables the generation of an ensemble of ligand conformations that are optimally positioned within the receptor's binding pocket, thereby predicting the most favorable orientation of the ligand and receptor for forming a stable complex (Rai et al., 2021).

The ligand molecules are held within the binding site through various non-covalent intermolecular forces, such as electrostatic (Coulombic), van der Waals, and hydrogen bonding interactions. For instance, AutoDock utilizes a semi-empirical scoring function to estimate the free energy of atom-atom interactions. This function incorporates terms corresponding to molecular-mechanical interactions as well as empirical terms that account for desolvation effects, including interactions with water (Srivastava et al., 2022).

In this study, molecular docking was employed to explore the interaction mechanisms of glycyrrhizin with two target proteins: ACE2 angiotensin-converting enzyme 2 (PDB ID: 6LZG) and tyrosinase (PDB ID: 2ZMX), using AutoDock Vina software (Trott et al., 2010). The 3D structure of glycyrrhizin (ChemSpider ID: 14263) was obtained from the ChemSpider database (http://www.chemspider.com) (Keiko et al., 2009). The crystal structures of ACE2 and tyrosinase were retrieved from the RCSB Protein Data Bank (http://www.rcsb.org) (Turner et al., 2022, Matoba et al., 2008). Prior to docking, all water molecules and native ligands were removed from the protein structures. Polar hydrogen atoms were added, and Kollman charges were assigned to the receptors. The partial charges of the ligand were computed using the Gasteiger method. Throughout the docking process, the protein targets were treated as rigid, while the ligand remained fully flexible to explore conformational space. Rectangular grid box covering the ligand-binding sites was of dimensions 40 x 40 x 40Å for 6LZG and 50 x 50 x 50 Å for 2ZMX. The center of the gridbox was defined by the bound inhibitor using the respective ligand - enzyme biological assembly pdb1 file. The binding energy (affinity) of a ligand was calculated by the Vina module. Visualization and analysis of receptor–ligand interactions were conducted using PyMOL and Discovery Studio 3.0 (De Lano, 2010), which provided both 2D interaction maps and 3D structural visualizations.

The predicted inhibition constants (K_i) were calculated according to the equation: $\mathbf{K_i=K_D=exp(\Delta G/RT)}$, where ΔG is the binding free energy of glycyrrhizin; R-gas constant equal to 1.986 cal/(mol·K)**;** T-absolute temperature in Kelvin (298 K).

MOLECULAR DOCKING RESULTS AND DISCUSSION

Docking simulations indicated that glycyrrhizin binds at the active sites of both angiotensin-converting enzyme 2 (ACE2, PDB ID: 6LZG) and tyrosinase (PDB ID: 2ZMX) target proteins, forming key stabilizing interactions.

The predicted binding affinities (-7.4 and -7.1 kcal/mol) with these proteins indicate a favorable thermodynamic interaction.

For large natural glycosides such as glycyrrhizin, these scores represent a significant molecular affinity threshold for identifying bioactive hits in virtual screening (Chen et al., 2025).

The binding affinities and binding modes were determined. To understand the stability of the minimized complexes, the important ligand-receptor interactions were visualized and analyzed. The molecular docking results and molecular interactions are shown in Tables 1-6, Fig. 2 and 3. The most important contacts are shown in dotted lines. Let's look at both docking results separately. There are the distances (in Å) between functional ligand groups and the interacting receptor residues in the minimized complex, also indicated

Molecular docking of glycyrrhizin with 6LZG

It was found that the binding affinity (ΔG) for the best binding pose between glycyrrhizin and 6LZG is -7.4 kcal/mol (Table 1). It has been revealed that ten receptor residues contribute to the stability and specificity of the receptor-ligand complex through a combination of hydrogen bonding and van der Waals interactions. The 3D (a) and 2D (b) visualizations of the receptor-ligand interactions are shown in Fig. 2.

It was found that several amino acid residues, namely Glu35, Gln76 of A-chain, and Gln493, Ser494 of B-chain, play a pivotal role in anchoring glycyrrhizin within the binding site of the 6LZG receptor. The detailed characteristics of the intermolecular interactions between glycyrrhizin and these receptor residues are presented in Table 2.

Table 1. Binding affinities between glycyrrhizin and 6LZG.

mode	affinity (kcal/mol)	distance from the best mode (Å)	
		rmsd l.b.	rmsd u.b.
1	-7.4	0.000	0.000
2	-6.4	2.288	3.544
3	-6.1	1.460	2.348
4	-5.7	3.028	5.708
5	-5.5	2.168	4.651
6	-5.2	2.369	3.593
7	-5.2	3.117	4.739
8	-5.1	5.130	8.978
9	-5.1	1.840	2.874

It was found that the hydrophilic moiety of glycyrrhizin is centrally positioned within a complex interaction network comprising both polar and nonpolar contacts with the surrounding amino acid residues. So, the H119 and O16 atoms of the terminal glucuronic ring of glycyrrhizin engage in two conventional hydrogen bonds with the O and HN atoms of the amide plane of the B-chain receptor residue Ser494 at distances of 2.48 Å and 2.38 Å, respectively. Moreover, the H118 atom of this moiety of glycyrrhizin also takes part in the conventional hydrogen bonding with the OE1 atom of the A-chain receptor residue Glu35. This interaction occurs at a distance of approximately 1.92 Å, indicating a strong and specific hydrogen bonding. Additionally, the O16 atom of the terminal glucuronic acid also participates in a carbon-hydrogen bonding with the HA atom of the B- chain of receptor residue Gln493, at a distance of 2.74Å, suggesting a stabilizing, albeit weaker, polar interaction.

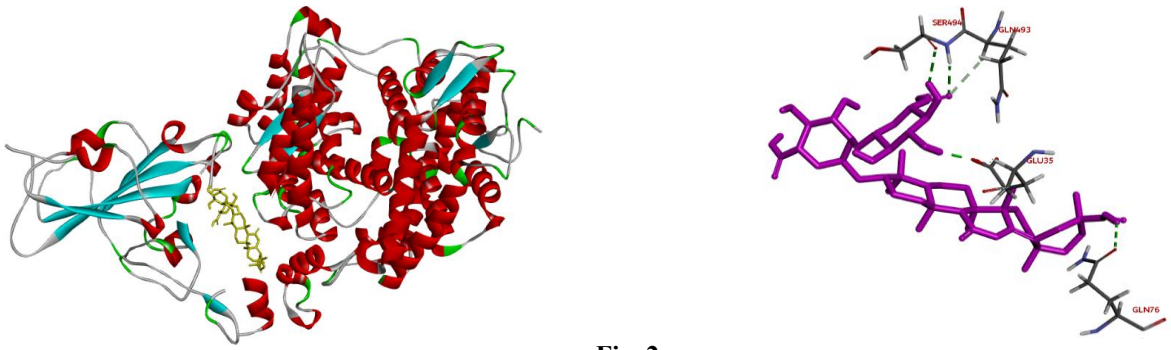

Fig. 2.

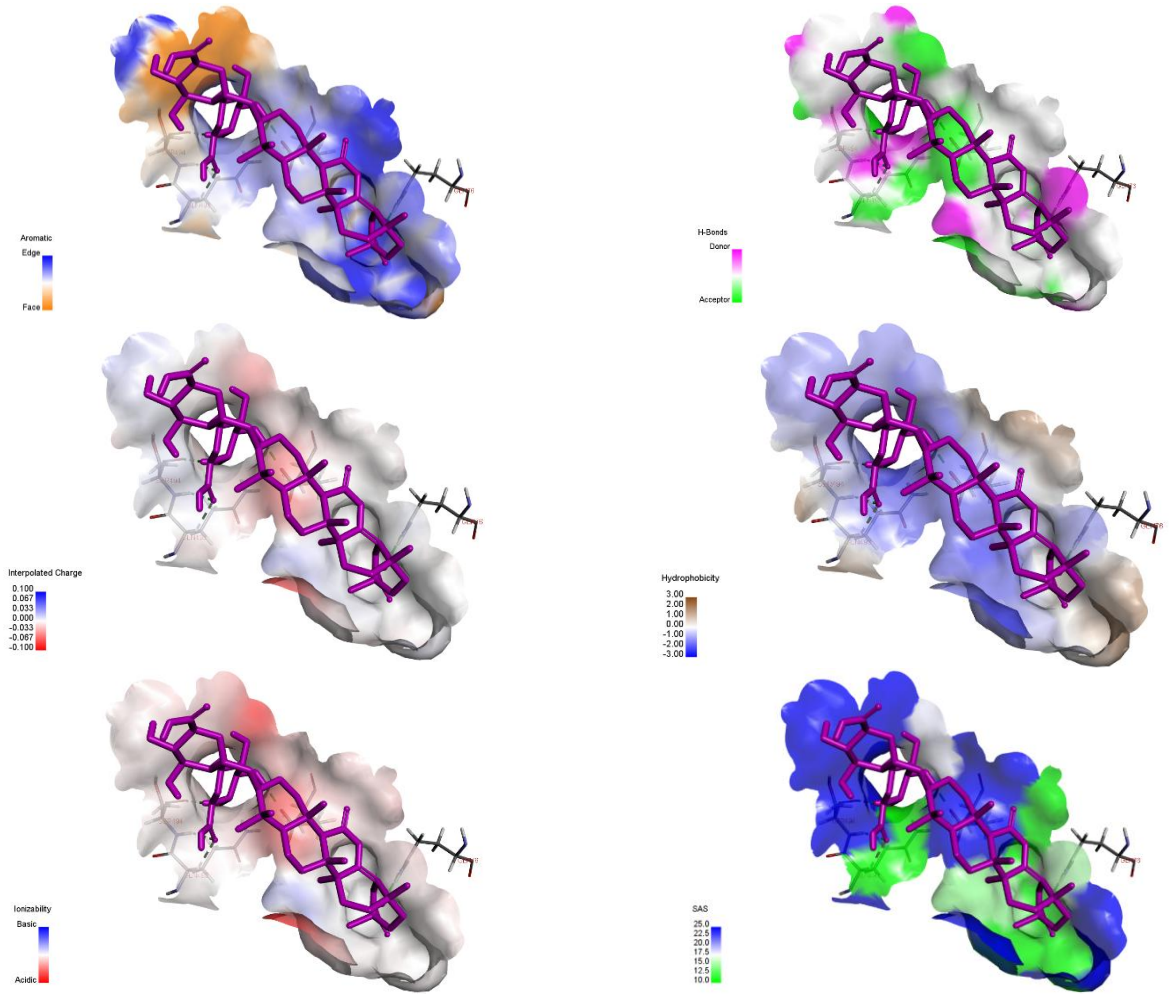

(a)

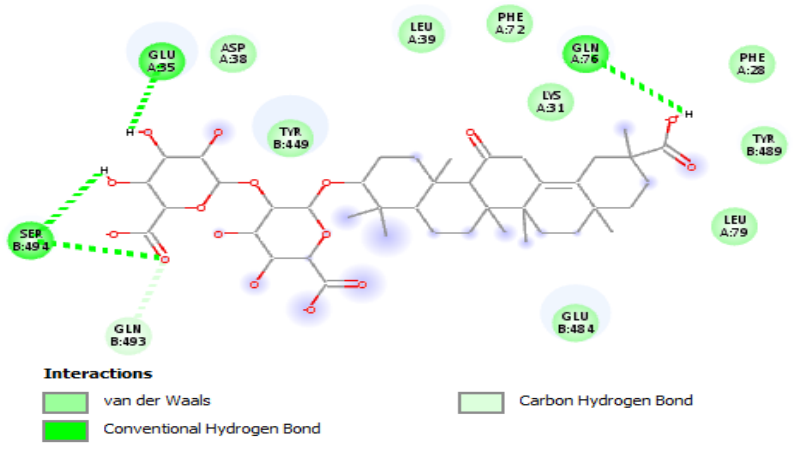

(b)

Fig. 2. The molecular docking results of glycyrrhizin to 6LZG: 3D visualization of the ligand-receptor interactions (a), 2D diagram of the receptor-ligand interactions (b).

Table 2. The attributes of the glycyrrhizin – 6LZG intermolecular interactions.

Contacts	Types interactions	Distances (Å)	∠DHA (degree)	∠HAY (degree)
Glycyrrhizin:H119 - B:SER494:O	Conventional HB	2.48	114.74	97.95
B:SER494:HN - : Glycyrrhizin:O16	Conventional HB	2.38	142.76	104.63
Glycyrrhizin:H118 - A:GLU35:OE1	Conventional HB	1.92	167.84	168.95
B:GLN493:HA - : Glycyrrhizin:O16	Carbon HB	2.74	145.55	142.06
Glycyrrhizin:H105- A:GLN76:OE1	Conventional HB	2.65	133.47	101.84

Comment: The numbering of glycyrrhizin atoms is given following Fig. 1(c); HB – hydrogen bond, D – Donor, A – Acceptor, Y – atom connected with Acceptor.

Table 3. The parameters of the intramolecular interactions for the 6LZG active site residues.

Contacts	Types interactions	Distances (Å)	∠DHA (degree)	∠HAY (degree)
A:LEU39:HN - **A:GLU35:O**	Conventional HB	2.22	164.57	150.96
A:GLU35:HN - A:PHE32:O	Conventional HB	2.63	109.46	95.80
A:GLU35:HN - A:LYS31:O	Conventional HB	2.05	160.49	154.25
B:SER494:HA - B:TYR451:O	Carbon HB	2.71	133.47	128.62
A:ALA80:HN - **A:GLN76:O**	Conventional HB	2.06	147.15	136.54
A:GLN76:HN - A:PHE72:O	Conventional HB	1.97	158.11	145.77
B:GLN493:HE21 - A:HIS34:O	Conventional HB	2.90	119.80	90.54
B:GLN493:HN - B:TYR453:O	Conventional HB	1.85	169.61	174.02
B:TYR453:HN - **B:GLN493:O**	Conventional HB	1.91	160.37	161.64
B:LEU452:HA - **B:GLN493:O**	CarbonHB	2.51	126.74	132.45

Comment: Amino acid residues that interact with glycyrrhizin are highlighted in bold; HB –Hydrogen Bond, D – Donor, A – Acceptor, Y – atom connected with Acceptor.

Thus, these interactions further reinforce the binding of the ligand's hydrophilic region within the active site. Interestingly, the OE1 atom of the Gln76 residue of A-chain forms a conventional hydrogen bond with the H105 atom of the terminal carboxyl group of the hydrophobic part of the glycyrrhetinic acid of the ligand at a distance of 2.65 Å. This indicates that polar interactions also extend to the more hydrophobic region of the ligand, contributing to the favorable binding conformation. Beyond hydrogen bonding, the orientation and positioning of glycyrrhizin within the receptor's binding pocket are further stabilized by a network of van der Waals interactions. These non-covalent interactions involve several residues from A-chain, including Lys31, Phe28, Leu39, Asp38, Phe72, and Leu79, as well as residues from the B-chain, such as Tyr449, Gln493, Glu484, and Tyr489. These contacts contribute to the overall affinity and proper spatial arrangement of the ligand within the binding pocket.

So, the abovementioned receptor residues are important for binding with glycyrrhizin, and affect the overall loop conformation and the favorable binding conformation. Collectively, the combination of hydrogen bonds and van der Waals forces involving both hydrophilic and hydrophobic regions of glycyrrhizin underscores the specificity and strength of its binding to the 6LZG receptor, offering insights into potential mechanisms of biological activity and therapeutic targeting.

In addition to the considered intermolecular interactions, a detailed assessment of the receptor's internal hydrogen bonding network revealed several key intramolecular contacts that likely contribute to maintaining the receptor's structural integrity and functional conformation. The detailed characteristics of these intramolecular interactions are presented in Table 3.

The structural configuration of the 6LZG protein reveals a highly organized network of intramolecular hydrogen bonds localized within its active site, comprising both intra- and inter-chain interactions. These non-covalent contacts contribute significantly to the conformational stability, spatial orientation of functional residues, and potentially, to the protein's catalytic or binding activity.

A particularly strong conventional hydrogen bond is formed between the amide hydrogen atom of A:LEU39 and the backbone carbonyl oxygen atom of A:GLU35, with a donor–acceptor distance of 2.22 A. This interaction is likely critical for maintaining the local β-strand or loop conformation in this region. The residue A:GLU35 further acts as a hydrogen bond donor through its amide hydrogen, engaging in two additional conventional hydrogen bonds. One of these is established with the carbonyl oxygen of A:PHE32, spanning a distance of 2.63 A, which suggests a moderately strong stabilizing interaction. The second bond, with a shorter length of 2.05 A, is formed between the amide hydrogen of A:GLU35 and the carbonyl oxygen of A:LYS31, reflecting a stronger hydrogen bond that may reinforce the secondary structural motif in this segment.

Further along the sequence, A:ALA80 donates its amide hydrogen to the carbonyl oxygen of A:GLN76, forming a hydrogen bond at 2.06 A. This interaction likely contributes to the maintenance of local helical or loop geometry. Additionally, A:GLN76, through its amide hydrogen, forms a close-range hydrogen bond with the carbonyl oxygen of A:PHE72, characterized by a particularly short distance of 1.97 A. This strong bond suggests a critical role in anchoring the residue conformation, possibly within a turn or coil structure.

Cross-chain hydrogen bonds further enhance the structural complexity and stability of the active site. A conventional hydrogen bond is formed between the side chain amide hydrogen (HE21) of B:GLN493 and the backbone carbonyl oxygen of A:HIS34, with a distance of 2.90 A. Though relatively longer, this interaction could still contribute to inter-domain communication or positioning. Notably, B:GLN493 also participates in a much shorter hydrogen bond (1.85 A) via its backbone amide hydrogen, interacting with the carbonyl oxygen of B:TYR453. A reciprocal bond is observed in the opposite direction, wherein

B:TYR453, via its amide hydrogen, donates a hydrogen bond to the carbonyl oxygen of B:GLN493, with a bond length of 1.91 A. This bidirectional interaction likely plays a key role in stabilizing the relative orientation of these two residues, potentially mediating a functionally relevant contact surface within the protein.

In addition to conventional hydrogen bonding, the active site features weaker yet structurally relevant carbon-hydrogen bonds, which arise from interactions involving C–H donors. One such interaction is observed between the alpha hydrogen of B:SER494 and the carbonyl oxygen of B:TYR451, with a bond distance of 2.71Å. A similar carbon-hydrogen bond is present between the alpha hydrogen of B:LEU452 and the carbonyl oxygen of B:GLN493, with a slightly shorter distance of 2.51 A. Although weaker than their conventional counterparts, these interactions may contribute to fine-tuning residue packing and local folding, especially in hydrophobic or partially buried regions.

Our docking results suggest possible interactions of glycyrrhizin with ACE2-associated molecular pathways potentially relevant to inflammatory regulation. Collectively, the intricate network of intramolecular hydrogen bonds observed within the 6LZG active site underscores the delicate balance of interactions required to maintain the protein's structural fidelity. Both conventional and carbon-hydrogen bonds, involving a range of donor and acceptor atoms across backbone and side chain moieties, contribute to the fine-tuning of local geometry and global conformation. The presence of short, directional hydrogen bonds suggests regions of significant structural rigidity, while longer or weaker interactions may provide the flexibility necessary for dynamic functional roles. This hydrogen bonding architecture not only stabilizes secondary and tertiary structural elements but may also be essential for aligning catalytically or functionally important residues within the active site. Thus, the observed pattern of interactions contributes to the structural organization and conformational stability of the 6LZG protein. The inhibition constants (Ki) were estimated using the equation **Ki=Kd=exp(ΔG/RT).** For a binding free energy of –7.4 kcal/mol, this calculation yields a dissociation constant of approximately

3.7×10-6 M, indicating a micromolar level of binding affinity. This value reflects a micromolar binding affinity, indicating a moderately strong interaction between the ligand and the target.

Molecular docking of glycyrrhizin with 2ZMX

The docking results for the glycyrrhizin–2ZMX complex revealed that the top-ranked binding pose (mode 1) exhibited the most favorable binding free energy of −7.1 kcal/mol, indicating a favorable docking pose. In contrast, modes 2 and 3 showed reduced affinities of −5.6 and −4.4 kcal/mol, respectively, along with RMSD values exceeding 3.0Å, suggesting considerable conformational deviation from the reference pose. These findings support the selection of mode 1 as the most favorable predicted binding conformation, as detailed in Table 4.

Table 4. Binding affinities between glycyrrhizin and 2ZMX.

mode	affinity (kcal/mol)	dist from best mode	
		rmsd l.b.	rmsd u.b.
1	-7.1	0.000	0.000
2	-5.6	3.025	10.939
3	-4.4	3.049	10.780

Structural analysis has demonstrated that multiple amino acid residues, including Asp99, Ser146, Val195, Ser142, Glu114, Arg140, Gly113, Gln116, and Pro102, contribute to the stabilization of glycyrrhizin within the binding pocket of the 2ZMX receptor. These residues collectively contribute to the affinity and specificity of the receptor-ligand contacts through an intricate network of non-covalent forces, predominantly hydrogen bonding and van der Waals interactions.

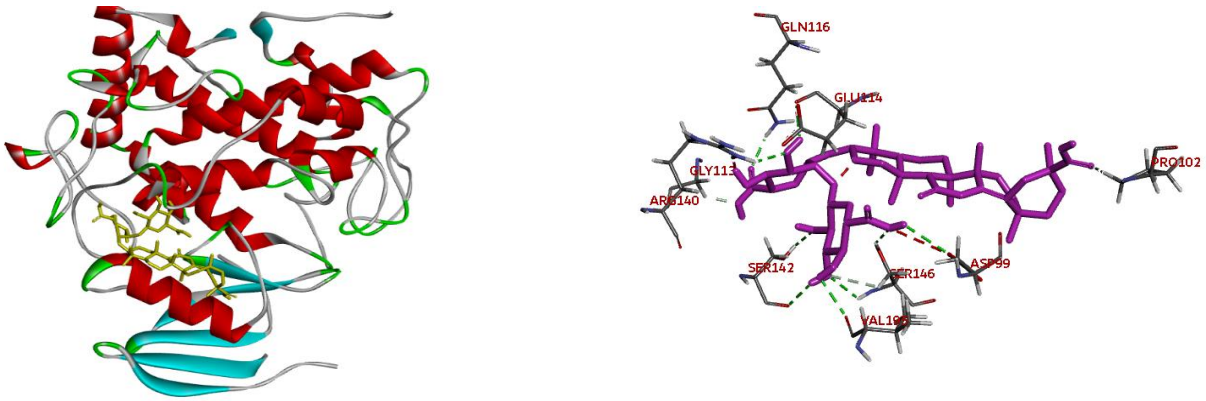

Fig. 3.

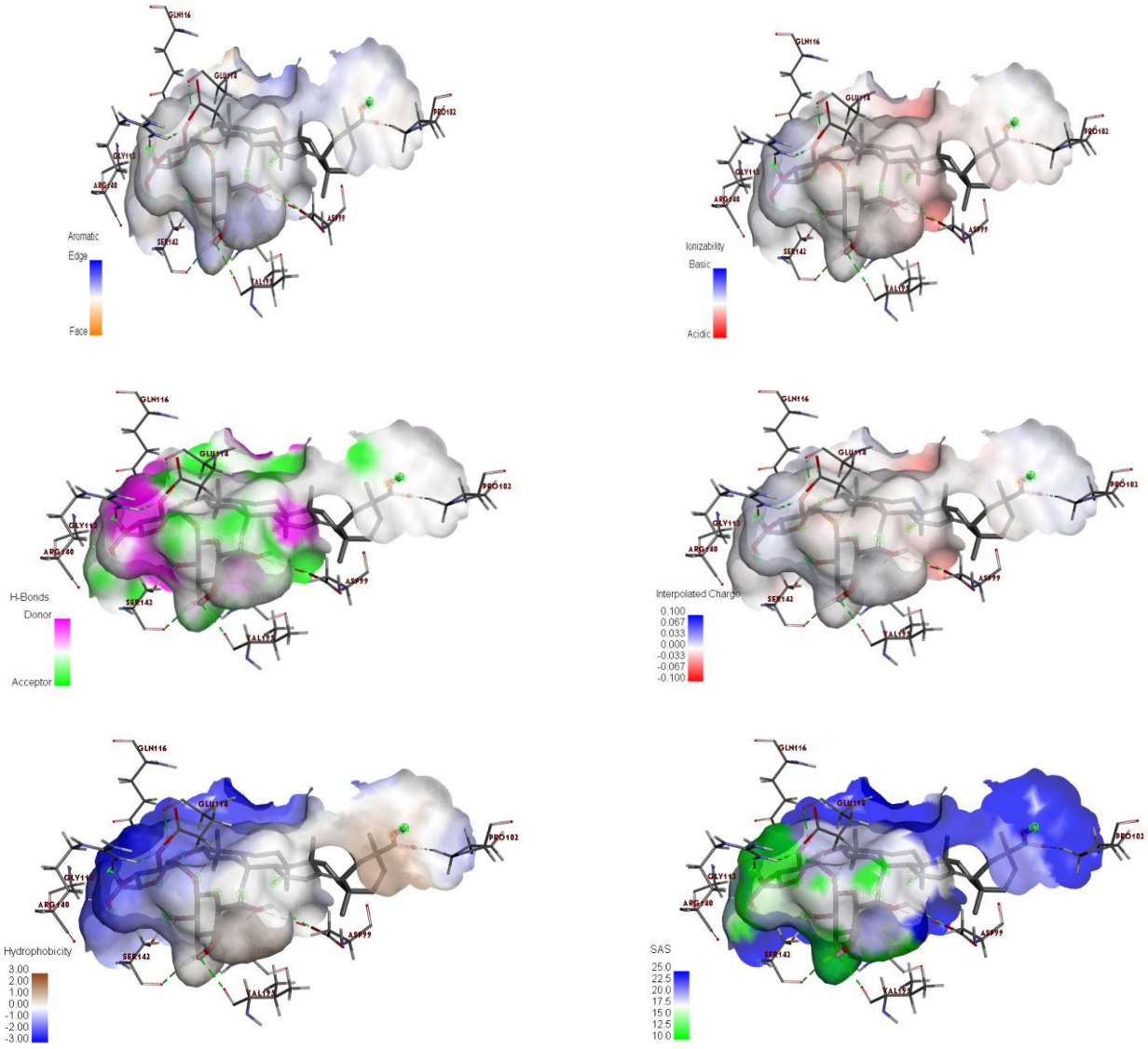

(a)

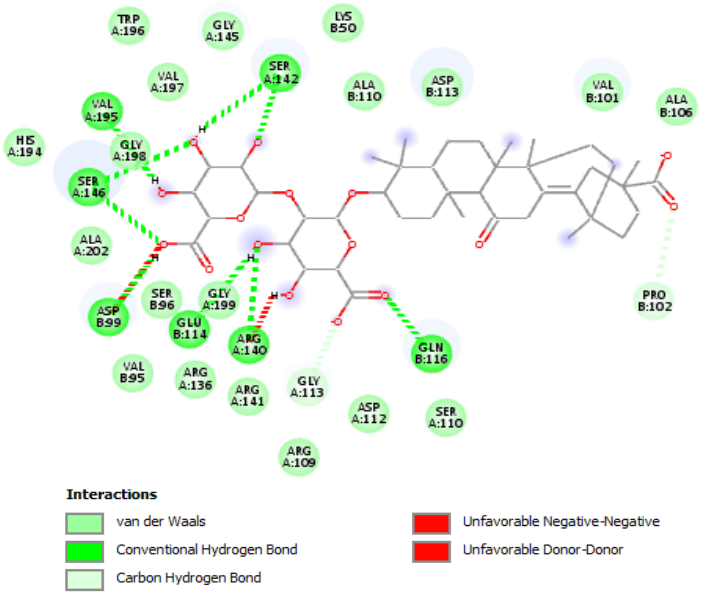

(b)

Fig. 3. The molecular docking results of glycyrrhizin into 2ZMX: 3D visualization of the ligand-receptor interactions (a); 2D diagram of the ligand-receptor interactions (b).

Table 5. The attributes of the glycyrrhizin – 2ZMX intermolecular interactions.

Contacts	Types interactions	Distances (Å)	∠DHA (degree)	∠HAY (degree)
A:SER142:HG - : Glycyrrhizin:O12	Conventional HB	2.60	115.48	93.62
Glycyrrhizin: H118 - A:SER142:O	Conventional HB	2.52	128.81	128.89
Glycyrrhizin:H120 - B:ASP99:OD2	Conventional HB	2.79	128.23	141.49
B:PRO102:HD2 - : Glycyrrhizin:O5	Conventional HB	2.43	133.32	107.66
A:SER146:HN - : Glycyrrhizin:O15	Conventional HB	2.48	125.60	115.20
A:SER146:HG - : Glycyrrhizin:O13	Conventional HB	2.39	152.26	93.21
A:SER146:HB2 - : Glycyrrhizin:O15	Carbon-Hydrogen Bond	2.88	103.51	98.52
Glycyrrhizin:H110 - B:GLU114:O	Conventional HB	2.04	124.80	110.62
A:ARG140:HH11 - : Glycyrrhizin:O7	Conventional HB	2.36	113.25	115.69
B:GLN116:HE22 - : Glycyrrhizin:O11	Conventional HB	2.01	149.21	140.65
A:GLY113:HA2 - : Glycyrrhizin:O10	Carbon HB	1.86	120.96	111.76
Glycyrrhizin:H119 - A:VAL195:O	Conventional HB	2.50	94.05	138.86
B:ASP99:OD2 - : Glycyrrhizin:O15	Unfavorable N-N	3.40		
A:ARG140:HH12 - : Glycyrrhizin:H111	Unfavorable D-D	1.36		

Comment: The numbering of glycyrrhizin atoms is given following Fig. 1(c); HB – hydrogen bond, N – negative, D – Donor, A – Acceptor, Y-atom connected with Acceptor.

The 3D (a) and 2D (b) visualizations of the receptor-ligand interactions are shown in Fig. 3. Each of these contacts plays a distinct role in maintaining the proper orientation and conformational stability of glycyrrhizin within the active site. Notably, some of these residues are located in the different chains of the receptor, indicating a cooperative involvement of multiple domains in ligand recognition

A comprehensive overview of these intermolecular interactions, including bond types, participating atoms, and interaction distances, is summarized in Table 5. It has been revealed that O12 and H118 atoms of the terminal moiety of the hydrophilic region of glycyrrhizin, specifically the distal glucuronic acid residue, form two conventional hydrogen bonds with HG and O atoms of Ser142 at distances of 2.60 Å and 2.52 Å, respectively. Additionally, H119 of the same glucuronic acid of glycyrrhizin forms a conventional hydrogen bond with the O atom of the amino acid residue Val195, at a distance of 2.5 Å. Moreover, amino acid residue Ser146 forms three hydrogen bonds with the oxygen atoms of the hydrophilic acid of glycyrrhizin. So, HG atom of this residue takes part in the hydrogen bonding with O13 atom of the carbonyl group at a distance of 2.39Å, but its HN and HB2 atoms forms both the conventional and carbon-hydrogen bonds with O15 atom of the carboxyl group of the same glucuronic acid at a distance of 2.39 Å and 2.48 Å, respectively, although one of them is not visually distinguishable in the 2D diagram due to overlapping bonds. Notably, the hydrogen atom H120 of this hydroxyl group also forms a hydrogen bond with the oxygen atom of the side chain of the amino acid residue Asp99, at a distance of 2.79Å. In turn, Asp99 forms an Unfavorable Negative-Negative bond with the oxygen atom of the same hydroxyl group at a distance of 3.4Å.

Thus, the terminal glucuronic acid residue is involved in seven conventional hydrogen bonds with four amino acid residues, Ser142, Val195, Ser146, and Asp99, one unfavorable negative-negative bond with Asp99. It is also important to note that the first three amino acid residues Ser142, Val195, and Ser146 of the A-chain of the receptor are involved in hydrogen bonding interactions. In contrast, Asp99 belongs to the B-chain of the receptor. This distinction highlights the involvement of both receptor chains in stabilizing the interaction with glycyrrhizin.

The second glucuronic acid unit, which also constitutes part of the hydrophilic region of glycyrrhizin, forms a conventional hydrogen bond characterized by a donor–acceptor distance of 2.04 Å between the H110 atom of the ligand and the O atom of receptor Glu114 (B-chain). This interaction contributes to the stabilization of the ligand within the binding site by establishing a specific and directional polar contact, reinforcing the affinity and precise positioning of glycyrrhizin through its hydrophilic moiety.

Conventional hydrogen bonding is observed between residue Arg140 (A-chain) and glycyrrhizin, where the HH11 hydrogen atom of Arg140 donates a hydrogen bond to the oxygen atom O7 of the ligand. This interaction occurs at a distance of 2.36 Å, indicating a strong and directionally favorable bond that contributes significantly to the stabilization and specificity of the receptor–ligand complex. Such polar interactions are crucial for maintaining the precise orientation of glycyrrhizin within the binding pocket.

In contrast, an unfavorable donor–donor contact is identified between the HH12 hydrogen atom of Arg140 and the H111 hydrogen atom of glycyrrhizin at a very close distance of 1.36 Å. This interaction is energetically disfavored due to repulsive electrostatic forces between two positively polarized hydrogen

atoms, which may induce local strain and necessitate conformational adjustments to mitigate steric and electronic clashes.

Together, these interactions involving Arg140 illustrate a nuanced balance within the binding interface: while the conventional hydrogen bond stabilizes ligand binding, the proximate donor–donor contact may reflect dynamic flexibility or an induced fit mechanism, essential for accommodating the ligand and maintaining the functional conformation of the receptor.

A conventional hydrogen bond is formed between the side chain amide hydrogen (HE22) of Gln116 (chain B) and the oxygen atom O11 of glycyrrhizin. This interaction occurs at a distance of 2.01 Å, indicative of a strong and highly directional hydrogen bond. The precise alignment and short donor–acceptor distance suggest that this polar contact plays a significant role in stabilizing the glycyrrhizin molecule within the receptor binding site. By facilitating specific recognition through the polar side chain of Gln116, this hydrogen bond contributes to the overall affinity and specificity of the ligand–receptor complex, supporting proper ligand positioning and effective molecular interaction.

In addition to this, a carbon-hydrogen bond is observed between the α-hydrogen (HA2) of Gly113 (A-chain) and the oxygen atom O10 of glycyrrhizin, with a remarkably short interaction distance of 1.86 Å. Although carbon-hydrogen bonds are generally weaker than conventional hydrogen bonds, the short distance and favorable geometry here indicate a significant stabilizing contribution. This interaction likely enhances the local packing and contributes to the fine-tuning of the ligand's orientation within the binding pocket, complementing the stronger polar contacts and thus collectively strengthening the receptor–ligand association.

Within the hydrophobic region of glycyrrhizin, a single carbon-hydrogen bond has been identified that connects the side-chain hydrogen atom HD2 of Pro102 (B-chain) with the oxygen atom O5 of the carboxyl group in the glycyrrhetinic acid moiety. This interaction occurs at a distance of 2.43 Å, reflecting a moderate yet meaningful non-conventional hydrogen bond. Although weaker than classical hydrogen bonds, this C–H···O contact plays an important role in stabilizing the hydrophobic core of the ligand within the receptor's binding pocket. By bridging Pro102 with the carboxyl group, this interaction likely contributes to maintaining the precise spatial arrangement of the ligand's hydrophobic segment, thereby complementing the network of stronger polar and van der Waals interactions that underpin the overall ligand–receptor affinity.

It was revealed that some residues of both A- and B-chains of the receptor are not involved in the receptor-ligand interactions, but they stabilize the positions of certain active site residues. The comprehensive mapping of intramolecular interactions for the, as summarized in Table 6, reveals a multifaceted network of non-covalent contacts that collectively contribute to the stability, specificity, and proper orientation of the 2ZMX active site residues. These interactions include classical hydrogen bonds, salt bridges, carbon-hydrogen bonds, alkyl (hydrophobic) contacts, and electrostatic attractions.

Conventional hydrogen bonds dominate the interaction landscape, characterized by donor–acceptor distances ranging primarily from 1.90 to 2.89 Å and favorable donor–hydrogen–acceptor (DHA) angles generally exceeding 130°, consistent with strong and directional polar interactions. Key examples include the hydrogen bond between the atoms HN of SER142 and O of VAL197 at a distance of 1.90 Å with a DHA angle of 153.88°, and the HN atoms of GLY145 in the A-chain forming a hydrogen bond with the O atom of SER142 in the same chain at 1.96 Å, reinforcing the structural integrity of the receptor's binding pocket. Similarly, VAL195 engages in multiple conventional hydrogen bonds with backbone oxygens of ASN191 and ARG192 in chain A, suggesting its pivotal role in stabilizing the ligand environment via backbone-mediated interactions.

Electrostatic forces are substantially represented by salt bridges and attractive charge interactions, notably between positively charged residues such as Arg140 and Arg136 and negatively charged glutamate residues, primarily Glu114. The salt bridge between HH21 of ARG140 in A-chain and OE2 of GLU114 in B-chain at 2.10 Å exemplifies a strong ionic bond with a near-ideal interaction distance, critical for ligand anchoring. Multiple salt bridges involving Arg140's guanidinium hydrogens and Glu114's carboxylate oxygens suggest a cooperative network of charged interactions, enhancing ligand affinity through electrostatic complementarity and spatial precision.

Carbon-hydrogen bonds, which typically exhibit weaker electrostatic components compared to classical hydrogen bonds, are nevertheless prevalent and contribute significantly to ligand positioning. For instance, interactions such as HA atoms of ARG140 in A-chain with O atom of GLY113 at 2.15 Å and HA1 atoms of GLY108 with O atom of GLY113 in the same chain at 2.13Å, with corresponding favorable angular geometries, indicate their role in stabilizing both polar and hydrophobic regions of the ligand–receptor interface. These subtle contacts likely aid in minimizing conformational entropy and optimizing ligand fit within the hydrophobic pockets.

Table 6. The parameters of the intramolecular interactions for the 2ZMX active site residues.

Contacts	Types interactions	Distances (Å)	∠DHA (degree)	∠HAY (degree)
B:ASP99:HN - B:SER96:O	Conventional HB	2.89	151.60	108.77
A:SER142:HN - A:VAL197:O	Conventional HB	1.90	153.88	147.34
A:GLY145:HN - **A:SER142:O**	Conventional HB	1.96	152.18	138.30
A:VAL195:HN - A:ASN191:O	Conventional HB	2.15	156.45	149.37
A:VAL195:HN - A:ARG192:O	Conventional HB	2.65	111.93	90.94
A:GLY198:HN - **A:VAL195:O**	Conventional HB	2.74	112.39	94.07
A:VAL147 - **A:VAL195**	Alkyl	4.82		
A:ARG140:NH1 - B:GLU114:OE1	Attractive Charge	4.57		
A:ARG140:HH11 - B:GLU114:OE2	Salt Bridge;Attractive Charge	2.43		
A:ARG140:NH2 - A:ASP134:OD1	Attractive Charge	4.12		
A:ARG140:HH21 - B:GLU114:OE2	Salt Bridge;Attractive Charge	2.10		
A:ARG140:HN - A:GLN200:OE1	Conventional HB	1.89	165.83	133.33
A:GLN200:HN - **A:ARG140:O**	Conventional HB	2.78	135.39	126.82
A:GLY199:HA1 - **A:ARG140:O**	Carbon HB	2.13	168.37	97.39
A:ARG140:HA - A:GLY113:O	Carbon HB	2.15	133.47	131.95
A:ARG140:HD2 - A:ASP112:O	Carbon HB	2.92	109.68	143.53
A:ARG140:HD1 - A:ASP112:O	Carbon HB	3.10	99.20	175.71
A:TYR138 - **A:ARG140**	Pi-Alkyl	5.16		
A:GLY113:HN - A:ARG109:O	Conventional HB	2.14	128.79	149.86
A:GLY113:HA2 - A:ARG109:O	Carbon HB	2.62	107.11	150.27
A:GLY108:HA1 - **A:GLY113:O**	Carbon HB	2.13	151.91	98.50
A:ARG140:HA - A:GLY113:O	Carbon HB	2.15	133.47	131.95
A:ARG141:HN - **A:GLY113:O**	Conventional HB	2.06	154.03	152.50
B:GLU114:HN - B:ALA110:O	Conventional HB	1.97	149.44	143.43
B:GLU114:HN - B:ALA111:O	Conventional HB	2.51	112.53	91.61
B:LEU115:HA **- B:GLU114:OE1**	Carbon HB	3.05	121.27	134.36
A:ARG136:HH22 **- B:GLU114:OE1**	Salt Bridge; Attractive Charge	1.89		
A:ARG140:NH1 - B:GLU114:OE1	Attractive Charge	4.57		
A:ARG136:NH1 **- B:GLU114:OE2**	Attractive Charge	4.65		
A:ARG140:HH21 - B:GLU114:OE2	Salt Bridge; Attractive Charge	2.10		
A:ARG140:HH11 - B:GLU114:OE2	Salt Bridge; Attractive Charge	2.43		
B:GLN116:HN - B:ASP113:O	Conventional HB	2.85	137.51	97.07
B:GLN116:HN - B:VAL112:O	Conventional HB	2.51	146.33	151.79
A:ASP112:HA - **B:GLN116:OE1**	Carbon HB	2.67	132.92	114.87
B:ALA106 - **B:PRO102**	Alkyl	4.54		

Comment: Amino acid residues that interact with glycyrrhizin are highlighted in bold; HB – Hydrogen Bond, D – Donor, A – Acceptor, Y – atom connected with Acceptor.

Hydrophobic (alkyl) interactions also form an integral part of the binding mechanism. The alkyl contact between VAL147 and VAL195 in the A-chain at 4.82 Å exemplifies van der Waals forces that promote ligand retention by reinforcing hydrophobic packing. Similarly, the alkyl interaction between ALA106 and PRO102 in the B-chain at 4.54 Å stabilizes the receptor structure surrounding the ligand-binding site, contributing to overall conformational rigidity and ligand accommodation.

Moreover, the data reveal a cooperative involvement of residues from both receptor chains, with hydrogen bonds and electrostatic interactions crossing chain boundaries, thereby emphasizing the multimeric nature of the receptor and the distributed binding interface. This cross-chain interaction network suggests a dynamic yet specific ligand engagement that can accommodate subtle conformational changes while preserving binding specificity.

The angular parameters (DHA and HAY angles) recorded for these hydrogen bonds and carbon-hydrogen bonds further corroborate the strength and specificity of these interactions. Larger DHA angles (close to linearity) generally indicate stronger hydrogen bonding, which is consistently observed across the key contacts in Table 6. Such geometrical optimization is critical for efficient molecular recognition and receptor–ligand interaction patterns.

In summary, the detailed characterization of contacts in Table 6 demonstrates that the positions of the residues in the 2ZMX active site are governed by a balanced interplay of strong directional hydrogen bonds, ionic salt bridges, supportive carbon-hydrogen bonds, and stabilizing hydrophobic interactions. The dual presence of conventional stabilizing hydrogen bonds alongside some energetically less favorable donor–donor contacts suggests a dynamic binding mode that may facilitate induced fit and specificity. This complex interaction

network not only secures the ligand in a precise orientation but also enhances the receptor's ability to recognize and respond to the ligand with high specificity and affinity, providing valuable insights into the molecular basis of ligand recognition and potential avenues for drug design optimization.

The inhibition constants (Ki) were estimated using the equation $Ki=Kd=\exp(\Delta G/RT)$. For a binding free energy of –7.1 kcal/mol, this calculation yields a dissociation constant of approximately 6.2×10^{-6} M, indicating a micromolar level of binding affinity.

Pharmacophore models of glycyrrhizin for the interaction with 6LZG and 2ZMX

Based on the calculated results, pharmacophore elements and their locations were identified and, as a result, pharmacophore models were constructed for glycyrrhizin interactions both with 6LZG and 2ZMX (Fig.4 and Fig.5). It was revealed, that that carboxyl groups (-COOH), –hydroxyl radical(-OH) of glycyrrhizin are predicted to play the important role in the interactions with amino acid residues of the active site.

As seen from Fig.4, the H118 and H119 atoms of the carbonyl group and the O16 atom of the carboxyl group of the terminal glucuronic acid, H105 atom of the terminal carboxyl group of the hydrophobic fragment are the elements of pharmacophore moieties of glycyrrhizin for its intermolecular interactions with the ACE2.

Table 7. The respective geometrical arrangement of pharmacophore moieties of glycyrrhizin for its interaction with 6LZG.

Distances	In Å	Angles	In degrees
O16 – H105	11.61	H105 – H119 – O116	56.11
H119 – H105	12.99	H118 – H119 – H105	115.8
H118 – H105	10.81	H118 – O16 – H105	87.34
O16 – H118	4.76	O16 – H119 – H118	87.03
H119 – H118	3.89	H105 – H118 – H119	115.8
O16 – H119	2.94	H119 – O16 – H105	56.11

*Comment:*The numbering of the ligand atoms is given in accordance with Fig.1(c).

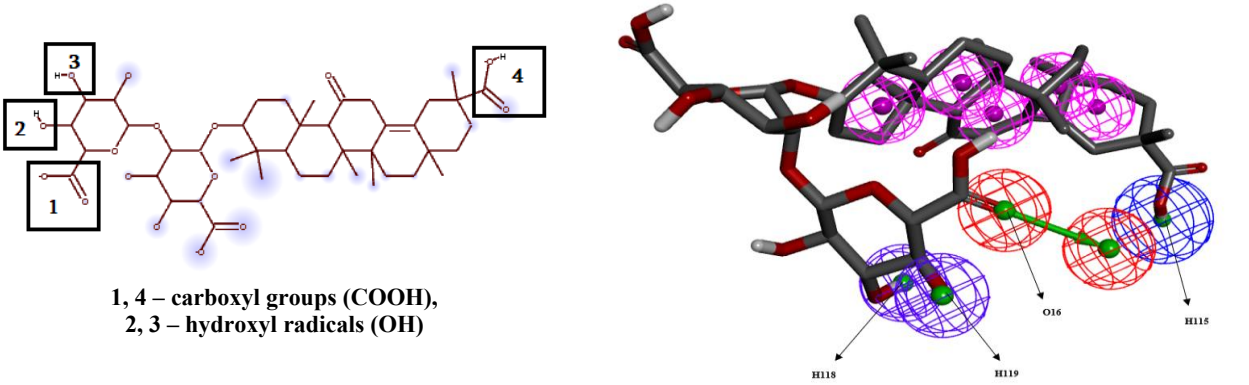

Fig. 4. Pharmacophore model of glycyrrhizin for its interaction with 6LZG /the pharmacophore moieties 1 – 4 (a) are shown: H-acceptors – in red, H-donors – in blue, hydrophobic groups – in violet, their elements are indicated by labels and symbols (b).

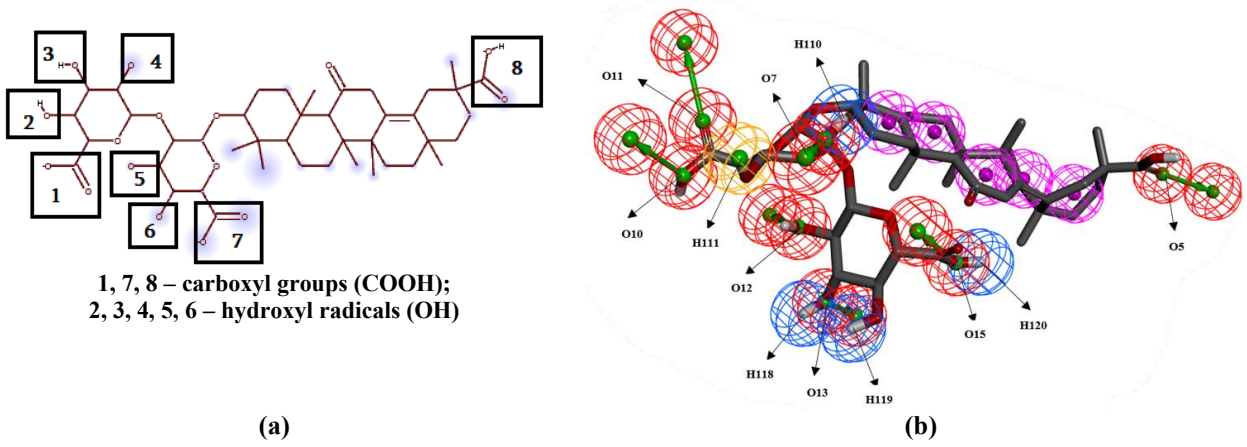

Fig. 5. Pharmacophore model of glycyrrhizin for its interaction with 2ZMX /the pharmacophore moieties 1 - 8 (a) are shown; H-acceptors – in red, H-donors – in blue, cation -in orange , hydrophobic groups – in violet, their elements are indicated by labels and symbols (b).

Table 8. The respective geometrical arrangement of pharmacophore moieties of glycyrrhizin for its interaction with 2ZMX.

Distances	In Å	Angles	In degrees
O15-H118	6.71	H118-H110-O5	80.92
H119-O12	4.63	O15-H110-O5	36.56
O15-H110	7.41	O12-H11-O5	45.48
H119-O7	7.4	H119-O10-O5	7.07
H118-O7	7.68	O15-O12-O5	124.74
O12-O7	5.5	H120-H110-O10	56.51
H120-O5	10.49	O12-O10-O5	28.01
H118-O5	10.16	O12-H110-O5	35.34
H110-O5	15.48	H119-O12-O5	138.66
O11-O5	19.02	H118-H111-O12	99.29

Comment: The numbering of the ligand atoms is given in accordance with Fig.1(c)

As seen from Fig.5, O12, O13, H118, and H119 atoms of the – hydroxyl radical, O15, H120 atoms of the carboxyl group of the terminal glucuronic acid; O7, H110, H111 atom of the – hydroxyl radical, and O10, O11 atoms of the carboxyl group of the aromatic ring of the next glucuronic acid in the sequence of the hydrophilic part; O5 atom of the terminal carboxyl group of the hydrophobic fragment are the elements of pharmacophore moieties of glycyrrhizin for its intermolecular interactions with the tyrosinase.

The relative positions of pharmacophore areas of glycyrrhizin for interaction with 6LZG and 2ZMX were characterized by a set of distances and angles, represented in Tables 7 and 8, respectively. The proposed models may support future structure-based design studies of glycyrrhizin-derived compounds.

LIMITATIONS OF THE STUDY

A limitation of the present study is the absence of comparative docking analysis with experimentally validated reference inhibitors or control compounds. In addition, molecular dynamics simulations and in vitro validation experiments were beyond the scope of the current investigation. Therefore, the obtained results should be considered preliminary and require further experimental confirmation.

CONCLUSION

Molecular docking simulations revealed that glycyrrhizin demonstrates favorable binding interactions with both ACE2 and tyrosinase protein targets.

The important intermolecular interactions of glycyrrhizin were observed with residues Glu35 and Gln76 of the A-chain, and Gln493 and Ser494 of the B-chain of the ACE2 receptor (6LZG), thereby contributing to the stabilization of the ligand within the binding pocket through conventional and carbon-hydrogen bonds.

The key intermolecular interactions of glycyrrhizin with residues Ser142, Gly113, Arg140, Ser146 and Val195 of the A-chain, and Asp99, Glu114, Gln116, and Pro102 of the B-chain of the tyrosinase enzyme (2ZMX) were identified. These residues contributed to ligand stabilization through a network of conventional hydrogen bonds, carbon-hydrogen bonds, and electrostatic interactions.

The obtained docking results provide structural insights into the spatial organization of pharmacophore elements involved in target recognition. The proposed pharmacophore models may support future structure-based design of glycyrrhizin-derived compounds targeting ACE2-associated inflammatory pathways and pigmentation-related molecular mechanisms.

However, the present findings are based solely on computational docking analysis and should therefore be interpreted cautiously. Further molecular dynamics simulations, comparative docking studies with reference compounds, and experimental validation are required to confirm the biological relevance and potential therapeutic applicability of glycyrrhizin interactions with the investigated targets.

AI STATEMENT

AI-assisted tools were used only for language translation, grammatical editing, and reference formatting.

REFERENCES

Agu P.C., Afiukwa C.A., Orji O.U. et al. (2023) Molecular docking as a tool for the discovery of molecular targets of nutraceuticals in diseases management. *Sci. Rep*., **13:** 13398; doi: 10.1038/s41598-023-40160-2

Ahmad S., Waheed Y., Abro A., Abbasi S.W., Ismail S. (2021) Molecular screening of glycyrrhizin-based inhibitors against ACE2 host receptor of SARS-CoV-2. Journal of Molecular Modeling, 27(7): 206; doi: 10.1007/s00894-021-04816-y. PMID: 34169390; PMCID: PMC8225399.

Al Dehlawi H., Jazzar A. (2023) The power of licorice (*Radix glycyrrhizae*) to ımprove oral health: A comprehensive review of ıts pharmacological properties and clinical ımplications. *Healthcare* (Basel), **11(21):** 2887; doi: 10.3390/healthcare11212887

Buder F., Selejan S-R., Hohl M., Kindermann M., Herr C., Lepper P.M. et al. (2022) Glycyrrhizin through liquorice intake modulates

ACE2 and HMGB1 levels - A pilot study in healthy individuals with implications for COVID-19 and ARDS. *PLoS ONE*, **17(10):** e0275181; doi: 10.1371/journal.pone.0275181.

Celik S., Yilmaz G., Akyuz S., Ozel A.E. (2023) Shedding light into the biological activity of aminopterin, via molecular structural, docking, and molecular dynamics analyses. *J. Biomol. Struct. Dyn.,* **42 (15):** 7773-7794; doi: 10.1080/07391102.2023.2245493

Chen H.-Y. et al. (2025) Mechanism of Salvia miltiorrhiza in the treatment. *BMC Complementary Medicine and Therapies*, **25:** 291; doi: 10.1186/s12906-025-05040-4

Chen R.-Y., Shi J.-J., Liu Y.-J., Yu J., Li C.-Y., Tao F., Cao J.-F., Yang G.-J., Chen J. (2024) The state-of-the-art antibacterial activities of glycyrrhizin: A comprehensive review. *Microorganisms*, **12:** 1155; doi: 10.3390/microorganisms12061155

De LanoW.L. (2010) The PyMOL molecular graphics system. URL: https://www.ccp4.ac.uk/newsletters/newsletter40/11_pymol.pdf

Discovery studio 3.1. (2016) Discovery Studio Visualization [Internet]. [cited 2 Dec 2016]. http://accelrys.com/products/collaborative-science/biovia-discovery-studio/visualization-download.php

El-Saber Batiha G., Magdy Beshbishy A., El-Mleeh A.M., Abdel-Daim M., Prasad Devkota, H. (2020) Traditional uses, bioactive chemical constituents, and pharmacological and toxicological activities of *Glycyrrhiza glabra* L. (*Fabaceae*). *Biomolecules*, **10:** 352; doi: 10.3390/biom10030352

Graebin C.S. (2017) The pharmacological activities of glycyrrhizinic acid ("Glycyrrhizin") and glycyrrhetinic acid. *Sweeteners*, **31:** 245–261; doi: 10.1007/978-3-319-27027-2_15

Xu F., Huang X., Wu H., Wang X. (2023). Screening compounds for treating the diabetes and COVID-19 from Miao medicine by molecular docking and bioinformatics. *Arab. J. Chem.*, **16(9):** 105001; doi: 10.1016/j.arabjc.2023.105001

Keiko Y-S., Kazuki S. (2009) Functional genomics for plant natural productbiosynthesis, *Nat. Prod. Rep.*, **26:** 1466; doi: 10.1039/B817077K

Li J., Xu D., Wang L., Zhang M., Zhang G., Li E., He S. (2021) Glycyrrhizic acid ınhibits SARS-CoV-2 ınfection by blocking spike protein-mediated cell attachment. *Molecules,* **26(20):** 6090; doi: 10.3390/molecules26206090.

Liu J., Xu X., Jian M., Guo Y., Zhai L., Sun G., Sun L., Jiang R. (2025) *Glycyrrhiza glabra* extract as a skin-whitening Agent: Identification of active components and CRTC1/MITF pathway-inhibition mechanism. *J. Ethnopharmacol*., **349:** 119948; doi: 10.1016/j.jep.2025.119948.

Marchioro H.Z., Silva de Castro C.C., Fava V.M., Sakiyama P.H., Dellatorre G., Miot H.A. (2022) Update on the pathogenesis of vitiligo. *An. Bras. Dermatol*., **97(4):** 478-490; doi: 10.1016/j.abd.2021.09.008.

Matoba Y., Sugiyama M. (2008) Crystal structure of the met1-form of the copper-bound tyrosinase in complex with a caddie protein from *Streptomyces castaneoglobisporus* obtained by soaking in cupric sulfate solution for 36 hours. *PDB entry 2ZMX*; doi: 10.2210/pdb2zmx/pdb

Megantara S., Rusdin A., Budiman A., Puluhulawa, L.E., Ikram N.K.B.K., Muchtaridi M. (2025) Demonstrating the absence of correlation between molecular docking and *in vitro* cytotoxicity in anti-breast cancer research: Root causes and practical resolutions. *Breast Cancer: Targets and Therapy*, **17:** 1005–1023; doi: 10.2147/BCTT.S549682.

Meng X.Y., Zhang H.X., Mezei M., Cui M. (2022) Molecular docking: a powerful approach for structure-based drug discovery. *Curr. Comput. Aided Drug Des*., **7(2):** 146-157; doi: 10.2174/157340911795677602.

Murck H. (2020) Glycyrrhizin: The highly active compound of liquorice and its potential in COVID-19. *Front Immunol*., **11:** 1232; doi: 10.3389/fimmu.2020.01232.

Patel V.B., Zhong J.C., Grant M.B., Oudit G.Y. (2016) Role of the ACE2/Angiotensin-(1–7) axis of the renin–angiotensin system in heart failure. *Circulation Research*, **118(8):** 1313–1326; doi: 10.1161/CIRCRESAHA.116.307708. PMID: 27081186.

Rai H., Barik A., Singh Y.P. (2021) Molecular docking, binding mode analysis, molecular dynamics, and prediction of ADMET/toxicity properties of selective potential antiviral agents against SARS-CoV-2 main protease: an effort toward drug repurposing to combat COVID-19. *Mol. Divers*, **25:** 1905–1927; doi: 10.1007/s11030-021-10188-5

Rasool A., Dar T.A. (2025) Glycyrrhizin and its derivatives: an emerging secondary metabolite arsenal of *Glycyrrhiza glabra. Med. Chem. Res*, **34:** 745–763; doi: 10.1007/s00044-025-03376-7

Schmidt A.F., Rubin A., Milgraum D., Wassef C. (2022) Vitiligo following COVID-19: A case report and review of pathophysiology. *JAAD Case Rep.*, **22:** 47-49; doi: 10.1016/j.jdcr.2022.01.030.

Sharma V., Katiyar A., Agrawal R.C. (2017) *Glycyrrhiza glab*ra: Chemistry and pharmacological activity. *Sweeteners*, **31:** 87–

100; doi: 10.1007/978-3-319-27027-2_21. PMCID: PMC7124151.

Srivastava V., Yadav A., Sarkar P. (2022) Molecular docking and ADMET study of bioactive compounds of Glycyrrhiza glabra against main protease of SARS-CoV2. *Materials Today: Proceedings*, **49(8):** 2999-3007; doi: 10.1016/j.matpr.2020.10.055.

Thas J.J. (2008) Siddha medicine--background and principles and the application for skin diseases. *Clin Dermatol.*, **26(1):** 62-78; doi: 10.1016/j.clindermatol.2007.11.010.

Trott O., Olson A.J. (2010) AutoDock Vina: Improving the speed and accuracy of docking with a new scoring function, efficient optimization, and multithreadin. *Journal of Computational Chemistry*, **31:** 455-461; doi: 10.1002/jcc.21334

Turner A.J., Nalivaeva N.N. (2022) Angiotensin-converting enzyme 2 (ACE2): Two decades of revelations and re-evaluation. *Peptides*, **151:** 170766; doi: 10.1016/j.peptides.2022.170766.

URL: https://www.chemspider.com/Chemical-Structure.14263.html

Videira I.F.D.S., Moura D.F.L., Magina S. (2013) Mechanisms regulating melanogenesis. Anais Brasileiros de Dermatologia, 88(1): 76–83; doi: 10.1590/S0365-05962013000100009. PMID: 23539007; PMCID: PMC3699929.

Wang M., He L., Yan P. (2025) Integrated network pharmacology, molecular docking and experimental validation to investigate the mechanism of tannic acid in nasopharyngeal cancer. *Sci Rep*., **15:** 5645; doi:10.1038/s41598-025-90211-z.

Zheng Z., Lu Y., Wu H., Lam P.U., Sun X., Song Y. et al. (2024) Clinical outcomes of Omicron infection and vaccine acceptance among pediatric liver transplant recipients: insights from a cross-sectional survey. *Virol. J*., **21:** 299; doi: 10.1186/s12985-024-02531-7.

Zuo J., Meng T., Wang Y., Tang W. (2023) A review of the antiviral activities of glycyrrhizic acid, glycyrrhetinic acid and glycyrrhetinic acid monoglucuronide. *Pharmaceuticals (Basel),* **16(5):** 641; doi: 10.3390/ph16050641.

ORCIDs:

Leyla Galandarli: https://orcid.org/0009-0006-3290-9157
Ralphreed Gasanov: https://orcid.org/0000-0002-8102-7154
Gulnara Akverdieva: https://orcid.org/0000-0003-1851-2234

Expression analysis of HSP17.3, WRKY14, and WRKY36 genes in bread wheat genotypes under heat stress

Saida Zulfugarova, Samira Rustamova, Irada Huseynova*

Institute of Molecular Biology, Ministry of Science and Education of the Republic of Azerbaijan, 11 Izzat Nabiyev Str., AZ1073, Baku, Azerbaijan

****For correspondence: i.huseynova@imbb.science.az***

Received: February 25, 2026; Reviewed: April 08, 2026; Accepted: May 29, 2026

Heat stress is one of the major environmental factors limiting wheat productivity under changing climatic conditions. In this study, the expression patterns of HSP17.3, WRKY14, and WRKY36 genes were analyzed in four bread wheat (*Triticum aestivum* L.) genotypes differing in heat tolerance. Two heat-tolerant genotypes, Murov 2 and Zirva 85, and two heat-sensitive genotypes, Aran and Gyzyl bugda, were exposed to heat stress, and relative transcript levels were determined using quantitative real-time PCR. Heat treatment induced clear genotype-dependent changes in the expression of all three genes. The tolerant genotypes showed markedly higher transcript accumulation than the sensitive ones. HSP17.3 was strongly upregulated in Zirva 85 and Murov 2, indicating an active chaperone-mediated protective response under elevated temperature. Among the studied genes, WRKY36 showed the most pronounced induction, reaching approximately a 30-fold increase in Murov 2. WRKY14 also exhibited stronger expression in tolerant genotypes compared with sensitive genotypes. The concurrent upregulation of HSP17.3, WRKY14, and WRKY36 in heat-tolerant wheat genotypes suggests that these genes are involved in molecular mechanisms contributing to thermotolerance. The obtained results indicate that these genes may be considered promising candidate markers for evaluating heat stress tolerance in bread wheat breeding programs.

Keywords: *Triticum aestivum* L., *heat stress, HSP17.3, WRKY14, WRKY36, thermotolerance, qRT-PCR*

INTRODUCTION

In the context of global warming, improving the tolerance of crop plants to high temperatures is considered a critical challenge for the development of global agriculture (IPCC, 2023). Extremely high temperatures associated with climate change directly affect yield, respiration, reproduction, growth, and other biochemical processes in plants **(**Jagadish et al., 2021). Under stress conditions, elevated temperatures negatively impact plant development by disrupting intermolecular interactions essential for growth (Mahajan et al., 2025). To mitigate stress conditions, plants have evolved various adaptive responses, including deeper root growth into moist soil layers, stomatal closure to prevent water loss during transpiration, stabilization of cellular membranes, and reorganization of the genetic apparatus to regulate the synthesis of stress-related proteins. At the biochemical level, high temperatures lead to the denaturation of thermolabile proteins and significantly increase the accumulation of damaging reactive oxygen species (ROS) in plant cells **(**Mittler et al., 2017**)**. Depending on the intensity and duration of heat stress, protein metabolism is profoundly affected, resulting in protein degradation, inhibition of protein accumulation, and induction of the synthesis of specific stress-related proteins. Under high-temperature stress, however, plants activate additional protective mechanisms, among which heat shock proteins (HSPs) play a central role. HSPs are widely recognized as stress proteins and function as molecular chaperones involved in preventing aggregation of misfolded proteins, protein refolding, disaggregation, and degradation under heat stress conditions (Kang et al., 2022). In plants, HSPs are classified into several major families based on their molecular weight and sequence homology, including HSP100, HSP90, HSP70, HSP60, and small heat shock proteins (sHSPs), which typically range from 15 to 42 kDa (van Montfort et al., 2001). Among these, sHSPs represent a highly diverse and abundant group, with numerous isoforms identified in higher plants (Waters & Vierling, 2020). The diversity of HSP families reflects their essential role in plant adaptation to a wide range of abiotic stresses, including heat, drought, and salinity (Hasanuzzaman et al., 2020). Functionally, HSPs act as molecular chaperones that regulate protein

folding, assist newly synthesized polypeptides in achieving their native conformation, prevent non-specific protein aggregation, and facilitate protein refolding under stress conditions. A characteristic feature of many HSPs is the presence of conserved domains associated with chaperone activity, which are essential for substrate binding and protein stabilization (Peters et al., 2024). The expression of *HSP* genes is tightly regulated by heat shock transcription factors (HSFs), which act as key transcriptional activators under stress conditions (Ohama et al., 2017). Under non-stress conditions, *HSP* expression is generally low and is mainly associated with specific developmental processes such as embryogenesis, seed germination, pollen development, and fruit ripening. However, under heat stress, *HSP* genes are rapidly induced, contributing to cellular protection and stress adaptation. Among these families, HSPs, particularly members of the HSP17 group such as HSP17.3**,** have attracted significant attention due to their rapid induction and crucial role in protecting cellular proteins under heat stress conditions (Mukesh Sankar et al., 2021). HSP17.3 contributes to maintaining protein stability by preventing aggregation of denatured proteins and supporting their refolding, thereby enhancing stress tolerance in plants. In addition to heat shock proteins, transcription factors play a crucial role in regulating plant responses to heat stress. Among them, members of the *WRKY* family have attracted considerable attention due to their involvement in stress signaling networks. *WRKY* transcription factors regulate the expression of numerous stress-responsive genes associated with antioxidant defense, hormonal signaling, and abiotic stress adaptation. Several studies have demonstrated that *WRKY* genes are induced by elevated temperatures and contribute to thermotolerance by activating downstream protective mechanisms (Ma et al., 2024; Zhang et al., 2025). Among the *WRKY* family members, *WRKY14* and *WRKY36* are considered potential regulators of stress-responsive pathways associated with antioxidant defense, signal transduction, and cellular protection, suggesting their possible involvement in plant adaptation to heat stress (Li et al., 2024).

However, their contribution to heat stress responses in wheat remains insufficiently understood. Therefore, the coordinated activation of heat shock proteins and *WRKY* transcription factors may represent an important component of the complex regulatory network underlying heat stress tolerance. Wheat (*Triticum aestivum* L.) is one of the most important cereal crops and a staple food source for a large proportion of the global population, with annual production exceeding 700 million tons (FAO, 2023). This crop is constantly exposed to various abiotic stresses. In many regions worldwide, wheat is subjected to heat stress during the grain-filling stage, which adversely affects plant growth, yield, and grain quality (Zhao et al., 2017). Heat stress during reproductive stages is a major constraint in wheat production, affecting approximately 40% of wheat-growing areas globally (Yadav et al., 2022). Studies have shown that heat-tolerant wheat genotypes exhibit a stronger molecular response to high-temperature stress compared to sensitive ones, largely due to the activation of stress-responsive proteins (Kumar et al., 2020**)**. Among these stress-responsive proteins, low-molecular-weight heat shock proteins (sHSPs), including members of the HSP17 family, play a central role in the heat stress response in wheat. However, the genotype-dependent expression patterns and functional roles of *HSP17.3, WRKY14,* and *WRKY36* in the molecular response of wheat to elevated temperature remain insufficiently characterized. Therefore, the aim of this study was to investigate the expression patterns of *HSP17.3*, *WRKY14,* and *WRKY36* in bread wheat genotypes exposed to heat stress and to evaluate their potential contribution to the molecular mechanisms underlying thermotolerance.

MATERIALS AND METHODS

Plant material and growing conditions

Four local bread wheat (*Triticum aestivum* L.) genotypes were selected from the Gene Fund of the Research Institute of Crop Husbandry (Azerbaijan), including two tolerant genotypes (Murov 2 and Zirva 85) and two sensitive genotypes (Aran and Gyzyl bugda). To ensure the reliability of gene expression analysis, the experiment was designed using a randomized complete block layout with two treatments, comprising 10 biological replicates and 3 technical replicates. Plants were cultivated under controlled environmental conditions in a growth chamber with a 16/8 h light/dark photoperiod, day/night temperatures of 24/18 °C, and relative humidity maintained at 50%. Seedlings were grown individually in plastic containers filled with a soil–sand mixture (1:3 ratio). Fourteen-day-old plants were subjected to heat stress treatment. Heat stress was applied under laboratory conditions using a thermostat at 38 °C for 30 min, 40 °C for 30 min, and 42 °C for 2 h. Leaf samples were collected immediately after treatment, rapidly frozen in liquid nitrogen, and stored at −80 °C until further analysis.

Quantitative Real-Time PCR

Quantitative Real-Time PCR (qRT-PCR) analysis was performed using a Mic Real-Time PCR (Bio Molecular Systems, Upper Coomera,

QLD, Australia) system with a total reaction volume of 20 µL. Each reaction contained 10 µL of Luna Universal qPCR Mix (New England Biolabs, Ipswich, MA, USA), 1 µL of cDNA template diluted 1:5, 0.5 µL of each forward and reverse primer (10 µM), and 7 µL of nuclease-free water. The amplification protocol consisted of an initial denaturation step at 94 °C for 60 s, followed by 45 cycles of denaturation at 95 °C for 15 s and annealing/extension at 60 °C for 30 s. No-template controls (NTCs) were included for each primer set to verify the absence of contamination. All reactions were carried out in three technical replicates for each of the three independent biological replicates. The elongation factor 1-alpha gene (Elf1-α) was used as an internal reference due to its stable expression across experimental conditions. Primer sequences are provided in Table.

Primer efficiency was evaluated using a standard curve generated from serial dilutions of cDNA and calculated according to the following equation:

$$Efficiency\ (\%) = \left(10^{-\frac{1}{slope}} - 1\right) \times 100$$

Melting curve analysis was performed for each amplicon to confirm amplification specificity. Relative gene expression levels were calculated using the $2^{-\Delta\Delta Ct}$ method (Livak, 2001), comparing heat-treated samples with the corresponding controls.

Statistical analysis was performed using Student's t-test to compare control and heat-stressed samples within each genotype, and differences were considered statistically significant at $p < 0.05$.

RESULTS AND DISCUSSION

Heat stress markedly increased *HSP17.3* expression in all studied wheat genotypes (Fig. 1A). The magnitude of induction was genotype-dependent, with the strongest response observed in the heat-tolerant genotypes Zirva 85 and Murov 2, where transcript levels increased approximately 14–15-fold and 10–11-fold, respectively, compared with the control. In contrast, the heat-sensitive genotypes Aran and Gyzyl bugda exhibited substantially lower induction, reaching only about 3-fold and 5-fold, respectively. The stronger activation of *HSP17.3* in tolerant genotypes suggests a positive association between *HSP17.3* expression and thermotolerance. Similar findings have been reported in wheat and other crop species, where heat-induced accumulation of small heat shock proteins was associated with enhanced stress tolerance and improved protection of cellular proteins against thermal damage (Kang et al., 2022; Peters et al., 2024). As molecular chaperones, sHSPs contribute to thermotolerance by preventing protein aggregation and maintaining protein homeostasis under elevated temperatures. Heat stress also significantly affected *WRKY14* expression (Fig. 1B). The highest transcript accumulation was detected in the tolerant genotypes Murov 2 and Zirva 85, whereas only weak induction was observed in Aran and Gyzyl bugda. The genotype-dependent activation of *WRKY14* indicates its potential involvement in heat stress adaptation. *WRKY* transcription factors are recognized as important regulators of stress-responsive gene networks and participate in the control of antioxidant defense, signal transduction, and hormonal responses under adverse environmental conditions (Li et al., 2024). Enhanced *WRKY14* expression in tolerant genotypes may therefore contribute to the activation of downstream protective mechanisms required for adaptation to heat stress.

A pronounced genotype-dependent response was also observed for *WRKY36* (Fig. 1C). The strongest induction occurred in the heat-tolerant genotype Murov 2, where transcript levels increased approximately 30-fold relative to the control. A moderate increase of about 5-fold was detected in Zirva 85, whereas little or no induction was observed in the sensitive genotypes Aran and Gyzyl bugda. The substantial upregulation of *WRKY36* in Murov 2 suggests that this transcription factor may play an important role in the regulation of heat stress responses and stress adaptation mechanisms.

Table. Sequences of primers used for qRT-PCR.

Gene		Primer sequence (5′–3′)	Reference
Elf1-α	F	CAGATTGGCAACGGCTACG	Rustamova et al., 2021
	R	CGGACAGCAAAACGACCAAG	
HSP17.3	F	ATGGGGGGCATGGTGTTCG	Khokhlova et al., 2015
	R	TTGTCGAGGGTGAGGGTGAG	
WRKY36	F	GTCAGCAGCCAGCCTTCCCTTAGCC	Isgandarova et al., 2024
	R	CGTCGCCACGAGTATGGTCTTGTCC	
WRKY14	F	GATGACATAGATGCTGGAGGTGG	
	R	TGTGGCGTCGCTGTGGTT	

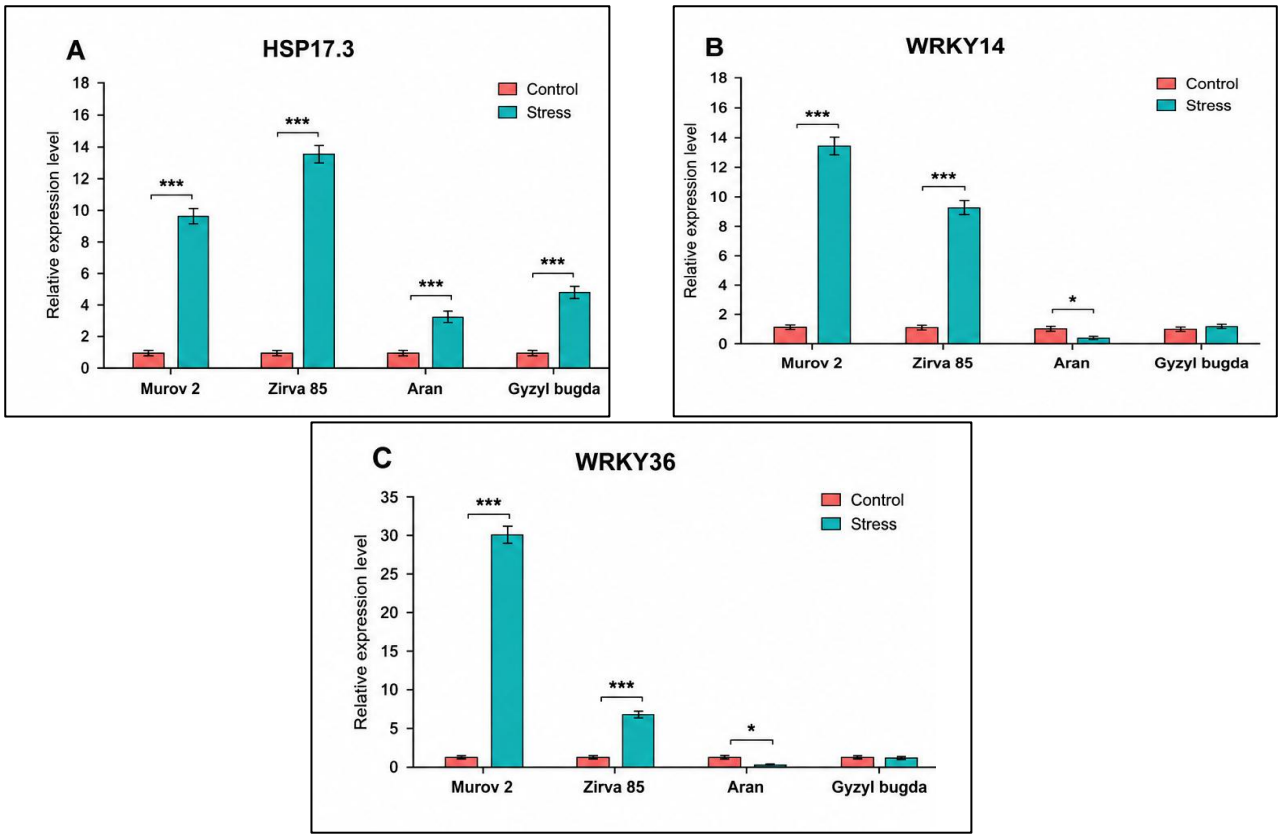

Fig. 1. Relative expression of HSP17.3 (A), WRKY14 (B), and WRKY36 (C) genes in four bread wheat genotypes differing in heat tolerance after heat stress treatment. Relative transcript abundance was determined by RT-qPCR using the $2^{-\Delta\Delta Ct}$ method and normalized to Elf1-α. Data represent mean ± SE (n = 3 biological replicates). Statistical significance between control and heat-treated plants was determined using Student's t-test * $p < 0.05$; *** $p < 0.001$.

Strong stress-induced activation of *WRKY* genes has been reported previously, with several members of the *WRKY* family exhibiting marked increases in expression under abiotic stress conditions (Zhang et al., 2025).

Notably, He et al. (2016) demonstrated that the wheat transcription factors *TaWRKY1* and *TaWRKY33* showed expression increases exceeding 30-fold under stress conditions, confirming the ability of *WRKY* genes to undergo rapid and substantial transcriptional activation in response to environmental challenges. In addition, *WRKY* transcription factors have been reported to participate in plant responses to high-temperature stress by regulating ROS-related signaling, hormone-mediated pathways, and downstream stress-responsive genes (Cheng et al., 2021).

Therefore, the approximately 30-fold increase in *WRKY36* expression observed in Murov 2 appears biologically plausible and may reflect an efficient activation of regulatory networks associated with heat stress adaptation and thermotolerance. The weak response detected in Aran and Gyzyl bugda suggests a limited capacity to activate these protective signaling pathways under heat stress, which may contribute to their lower stress tolerance. The coordinated induction of *HSP17.3*, *WRKY14*, and *WRKY36* observed in the heat-tolerant genotypes Murov 2 and Zirva 85 suggests the existence of an integrated molecular response to elevated temperature involving both protective chaperone systems and transcriptional regulatory networks. While *HSP17.3* likely contributes directly to thermotolerance by stabilizing denatured proteins and preventing irreversible protein aggregation, *WRKY14* and *WRKY36* may function as upstream regulators controlling the expression of stress-responsive genes involved in antioxidant defense, signal transduction, and cellular protection. The simultaneous activation of these genes in tolerant genotypes indicates a more efficient stress-response system compared with the sensitive genotypes Aran and Gyzyl bugda, which exhibited substantially weaker transcriptional responses. A similar relationship between heat shock proteins and stress-responsive transcription factors has been reported in wheat and other crop species, where enhanced activation of protective molecular networks was associated with improved tolerance to high temperature stress (Hasanuzzaman et al., 2020).

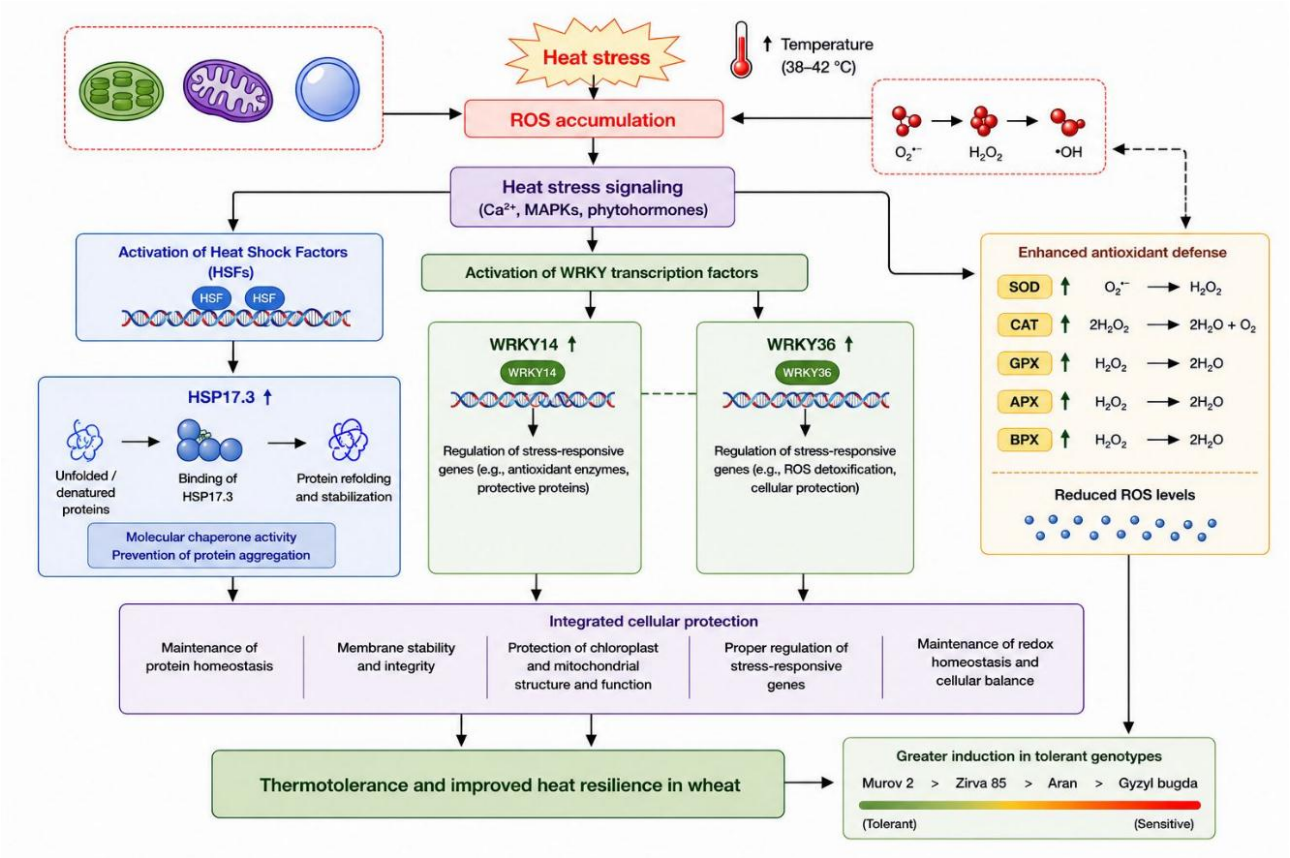

Fig. 2. Proposed molecular mechanism of heat stress response in bread wheat. Heat stress promotes reactive oxygen species accumulation and activates heat stress signaling pathways, resulting in the induction of HSP17.3 and WRKY transcription factors. HSP17.3 functions as a molecular chaperone to stabilize proteins, whereas WRKY14 and WRKY36 regulate stress-responsive genes involved in antioxidant defense and cellular protection. The coordinated activation of these pathways contributes to cellular homeostasis and thermotolerance. Abbreviations: ROS, reactive oxygen species; HSFs, heat shock transcription factors; HSP17.3, 17.3 kDa heat shock protein; WRKY14 and WRKY36, WRKY transcription factors; SOD, superoxide dismutase; CAT, catalase; GPX, guaiacol peroxidase; APX, ascorbate peroxidase; BPX, benzidine peroxidase.

Furthermore, recent studies have demonstrated that *WRKY* transcription factors play important regulatory roles in coordinating antioxidant defense and stress signaling pathways under abiotic stress conditions (Isgandarova et al., 2024). Therefore, the strong induction of *HSP17.3* together with *WRKY14* and WRKY36 in tolerant wheat genotypes may represent a key molecular mechanism contributing to cellular homeostasis and thermotolerance under heat stress conditions.

To integrate the expression patterns observed in the present study into a unified conceptual framework, a schematic model of the proposed molecular mechanism underlying heat stress tolerance in bread wheat is presented in Figure 2. Heat stress promotes the accumulation of ROS, which activates heat stress signaling pathways and induces the expression of HSP17.3 and WRKY transcription factors. Increased HSP17.3 expression may contribute to protein stabilization through its molecular chaperone activity, whereas WRKY14 and WRKY36 are likely involved in regulating downstream stress-responsive genes associated with antioxidant defense and cellular protection. The coordinated activation of these pathways may help maintain cellular homeostasis and enhance thermotolerance, particularly in tolerant genotypes such as Murov 2 and Zirva 85. This proposed mechanism is consistent with our previous findings on the integrated physiological, molecular, and ultrastructural responses of wheat to heat stress (Zulfugarova et al., 2026).

CONCLUSION

The present study showed that heat stress induces clear genotype-dependent changes in the expression of *HSP17.3*, *WRKY14*, and *WRKY36* genes in bread wheat. Heat-tolerant genotypes displayed stronger transcriptional activation than heat-sensitive genotypes, indicating that these genes may be associated with more effective molecular responses to elevated temperature. The marked upregulation of *HSP17.3* in tolerant genotypes suggests its involvement in chaperone-

mediated protection and maintenance of protein stability under heat stress. At the same time, the enhanced expression of *WRKY14* and especially *WRKY36* indicates that WRKY transcription factors may participate in the regulation of heat-responsive pathways in wheat. Overall, the coordinated induction of *HSP17.3*, *WRKY14*, and *WRKY36* in tolerant genotypes suggests that both protective chaperone systems and transcriptional regulatory mechanisms contribute to wheat thermotolerance. These genes may therefore be considered promising candidate expression markers for the evaluation of heat stress tolerance in bread wheat. However, further studies involving larger genotype collections, additional stress conditions, and functional validation are needed to confirm their role in heat adaptation and their usefulness in breeding programs.

AUTHOR CONTRIBUTIONS

SZ: Conceptualization, methodology, experimental investigation, data collection, formal analysis, and manuscript drafting. *SR:* Experimental validation, qRT-PCR analysis, data interpretation, visualization, and manuscript review. *İH:* Study supervision, project administration, conceptual development, interpretation of results, critical revision of the manuscript, and final approval of the submitted version. All authors have read and approved the final manuscript.

FUNDING

This research received no external funding.

DATA AVAILABILITY STATEMENT

The data supporting the findings of this study are available from the corresponding author upon reasonable request.

CONFLICTS OF INTEREST

The authors declare no conflict of interest.

ETHICS APPROVAL

This study did not involve human participants or animals. Therefore, ethical approval was not required.

AI STATEMENT

AI-assisted tools were used only for language translation, grammatical editing, and reference formatting.

REFERENCES

Cheng Z., Duan Y., Cao J., Chen J., Peng H., Liu J., Li Y., Zhou S., Zeng H., He Y., Chen J. (2021) The role of WRKY transcription factors in plant abiotic stress responses. *Plant Cell Reports*, **40:** 1983–1996.

El-Shehawi A.M., Alotaibi S.S., Elseehy M.M. (2020) Heat shock proteins expression is regulated by promoter CpG methylation/demethylation under heat stress in wheat varieties. *Pakistan Journal of Biological Sciences*, **23:** 1310–1320.

FAO (2023). The State of Food and Agriculture 2023.

Garg D., Sareen S., Dalal S., Tiwari R., Singh R. (2012) Heat shock protein-based SNP marker for terminal heat stress in wheat (*Triticum aestivum* L.). *Australian Journal of Crop Science*, **6:** 1516–1521.

Hasanuzzaman M., Bhuyan M.H.M.B., Zulfiqar F., Raza A., Mohsin S.M., Mahmud J.A., Fujita M., Fotopoulos V. (2020) Heat stress tolerance in plants: An overview. *International Journal of Molecular Sciences*, **21:** 1910.

He G.H., Xu J.Y., Wang Y.X., Liu J.M., Li P.S., Chen M. (2016) Drought-responsive WRKY transcription factor genes TaWRKY1 and TaWRKY33 from wheat confer drought and/or heat resistance in Arabidopsis. *BMC Plant Biology*, **16:** 116.

IPCC (2023) Climate Change 2023: Synthesis Report.

Isgandarova T.Y., Rustamova S.M., Aliyeva D.R., Rzayev F.H., Gasimov E.K., Huseynova I.M. (2024) Antioxidant and ultrastructural alterations in wheat during drought-induced leaf senescence. *Agronomy*, **14:** 2924.

Isgandarova T.Y., Rustamova S.M., Allahverdiyev T.I., Huseynova I.M. (2024) Proline accumulation and WRKY14/WRKY36 gene expression dynamics during drought-induced flag leaf senescence. *Journal of Life Sciences and Biomedicine*, **14:** 45–56.

Jagadish S.V.K., Murty M.V.R., Quick W.P. (2021) Rice responses to rising temperatures. *Journal of Experimental Botany*, **72:** 5143–5162.

Kang Y., Khan S., Ma X. (2022) Molecular bases of heat stress responses in plants. *Frontiers in Plant Science*, **13:** 837152.

Khokhlova L.P., Valiullina R.N., Mider D.R., Akberova N.I. (2015) Membrane thermostability and expression of small heat shock protein genes under high temperature and water deficit. *Biol. Membr.*, **32:** 59–71.

Kumar A., Sharma S., Chunduri V., Kaur A., Kaur S., Malhotra N. et al. (2020) Genome-

wide identification and characterization of heat shock protein family reveal roles in development and stress conditions in wheat. *Scientific Reports*, **10:** 7858.

Li S., Khoso M.A., Xu H., Zhang C., Liu Z., Wagan S., Dinislam K., Liu L. (2024) WRKY transcription factors as key regulators of plant resilience to environmental stresses: Current perspective. *Agronomy*, **14:** 2421.

Livak K.J., Schmittgen T.D. (2001) Analysis of relative gene expression data using real-time quantitative PCR and the $2^{-\Delta\Delta CT}$ method. *Methods*, **25:** 402–408.

Ma Z., Hu L. (2024) WRKY transcription factor responses and tolerance to abiotic stress in plants. *International Journal of Molecular Sciences*, **25:** 6845.

Mahajan S., Thakur P., Das S., Sharma R.P., Manuja S., Jha P.K., Fayezizadeh M.R. (2025) Impression of contemporary heat stress complexities in agricultural crops: A review. *Plant Growth Regulation*, **105:** 1805–1823.

Mittler R., Finka A., Goloubinoff P. (2017) How do plants feel the heat? *Plant Physiology*, **173:** 3–14.

Ohama N., Sato H., Shinozaki K., Yamaguchi-Shinozaki K. (2017) Transcriptional regulatory network of heat stress response in plants. *Trends in Plant Science*, **22:** 53–65.

Peters C., Haslbeck M. (2024) Catchers of folding gone awry: A tale of small heat shock proteins. *Trends Biochemical Sciences*, **49:** 989–1002.

Rustamova S.M., Shrestha A., Naz A.A., Huseynova I.M. (2021) Expression profiling of DREB1 and evaluation of vegetation indices in contrasting wheat genotypes exposed to drought stress. *Plant Gene*, **25:** 100266.

Rustamova S.M., Suleymanova Z.J., Isgandarova T.Y., Zulfugarova S.T., Mammadov A.C., Huseynova I.M. (2019) Identification of stress responsive genes by using molecular markers to develop tolerance in wheat. In: *Wheat Production in Changing Environments: Responses, Adaptation and Tolerance*, pp. 421–442.

Sankar M.S., Satyavathi C.T., Barthakur S., Singh S.P., Bharadwaj C., Soumya S.L. (2021) Differential modulation of heat-inducible genes across diverse genotypes and molecular cloning of a small heat shock protein from pearl millet (*Pennisetum glaucum*). *Frontiers in Plant Science*, **12:** 659893.

Temel A., Janack B., Humbeck K. (2017) Drought stress-related physiological changes and histone modifications in barley primary leaves at the HSP17 gene. *Agronomy*, **7:** 43.

van Montfort R.L.M., Slingsby C., Vierling E. (2001) Structure and function of the small heat shock protein/α-crystallin family of molecular chaperones. *Advances in Protein Chemistry*, **59**: 105–156.

Waters E.R., Vierling E. (2020) Plant small heat shock proteins. *Annual Review of Plant Biology*, **71:** 539–564.

Yadav M.R., Choudhary M., Singh J., Lal M.K., Jha P.K., Udawat P. et al. (2022) Impacts, tolerance, adaptation, and mitigation of heat stress on wheat under changing climates. *International Journal of Molecular Sciences*, **23:** 2838.

Zhang X.Y., Wang Y., Li J. et al. (2025) WRKY transcription factors participate in abiotic stress responses by regulating sugar metabolic pathways. *Frontiers in Plant Science*, **16:** 1646357.

Zhao C., Liu B., Piao S., Wang X., Lobell D.B., Huang Y. et al. (2017) Temperature increase reduces global yields of major crops in four independent estimates. *Proceedings of the National Academy of Sciences USA*, **114:** 9326–9331.

Zheng Y., Cai Z., Wang Z., Maruza T.M., Zhang G. (2025) The genetics and breeding of heat stress tolerance in wheat: Advances and prospects. *Plants*, **14:** 148.

Zulfugarova S.T., Rustamova S.M., Pashayeva A.N., Rzayev F.H., Gasimov E.K., Huseynova I.M. (2026) Integrated assessment of physiological, molecular and ultrastructural responses to heat stress in wheat. *Plants*, **15:** 1896.

ORCIDs:
Saida Zulfugarova: https://orcid.org/0000-0002-1772-8327
Samira Rustamova: https://orcid.org/0000-0001-5337-7109
Irada Huseynova: https://orcid.org/0000-0001-9766-9381

Note: *This manuscript was reviewed by two independent external reviewers who are not members of the journal's Editorial Board.*

Utilization of eucalyptus (*Eucalyptus* spp.) plant in value-added cosmetic, health and food products: Biological activities, industrial potential and economic importance

Musa Karadağ[1*], Kadir Sinan Aslan[2], Zübeyir Güneş[3], Halil İbrahim Ünsal[3], Necmettin Aktepe[4], Beşir Dağ[5]

[1]*Department of Chemistry and Chemical Processing Technologies, Technical Sciences Vocational School, Iğdır University, Iğdır, Türkiye*
[2]*Department of Biology, Science Faculty, Dicle University, 21280, Diyarbakır, Türkiye*
[3]*Field Crops Department, Kiziltepe Faculty of Agricultural Sciences and Technologies, Mardin Artuklu University, Mardin, Türkiye*
[4]*Kayapınar Parkorman Family Health Center, Diyarbakır, Türkiye*
[5]*Department of Nursing, Faculty of Health Sciences, Mardin Artuklu University, Mardin, Türkiye*

[*]***For correspondence:*** *musa.karadag@igdir.edu.tr*

Received: May 12, 2026; Received in revised form: June 12, 2026; Accepted: June 20, 2026

The present research aimed to characterize the phenolic composition of eucalyptus (*Eucalyptus* spp.) leaf extract and to investigate the possible industrial applications of these bioactive constituents. Phenolic compounds were identified and quantified through high-performance liquid chromatography coupled with a diode-array detector (HPLC-DAD). Analytical findings demonstrated the presence of nearly twenty distinct phenolic substances within the extract. Among the detected compounds, alizarin exhibited the highest concentration (265.72 ng/µL), followed by gallic acid (86.73 ng/µL). Several additional phytochemicals, including ascorbic acid, hydroxybenzoic acid, rutin, naringin, hesperidin, resveratrol, and quercetin, were also detected at varying levels. The diverse phenolic profile obtained from eucalyptus leaves suggests a substantial reservoir of biologically active molecules with notable functional properties. Many of these compounds are recognized for their capacity to neutralize reactive oxygen species, suppress microbial growth, and modulate inflammatory processes. Consequently, eucalyptus-derived extracts may represent promising natural ingredients for incorporation into pharmaceutical preparations, cosmetic products, and health-related formulations. Moreover, their potential role as naturally derived preservatives and oxidation inhibitors may support the development of cleaner-label food products and reduce dependence on synthetic additives. Overall, the findings highlight eucalyptus leaves as a valuable source of phenolic constituents with broad applicability in natural product research. The observed phytochemical richness further supports the utilization of eucalyptus biomass in environmentally friendly production systems, sustainable biotechnology, and green chemistry-based innovation strategies aimed at developing high-value bioactive products.

Keywords: *Eucalyptus spp., phenolic Compounds, HPLC-DAD, cosmetics, healthcare sector*

INTRODUCTION

The growing demand for sustainable technologies and naturally derived ingredients has increased scientific interest in bioactive compounds obtained from plant resources. In recent years, natural products have become key components in the development of environmentally compatible formulations for the pharmaceutical, cosmetic, nutraceutical, and food industries. Medicinal and aromatic plants are particularly valued because they synthesize a wide range of secondary metabolites, including phenolic acids, flavonoids, tannins, and essential oils, which exhibit diverse biological activities and functional properties (Başar et al., 2024; Ekor, 2014; FAO, 2021).

Among these botanical resources, eucalyptus (*Eucalyptus* spp.), a member of the Myrtaceae family, has attracted considerable attention due to its rich phytochemical composition and broad spectrum of biological effects. Numerous investigations have demonstrated that eucalyptus leaves contain substantial amounts of phenolic constituents capable of contributing to antioxidant defense mechanisms. Analytical studies have identified compounds such as ascorbic acid, gallic acid, hydroxybenzoic acid, vanillic acid, p-coumaric acid, rutin, naringin, neohesperidin,

 DOI: https://doi.org/10.62088/timbb/10.1.10

quercetin, hesperidin, and resveratrol within eucalyptus extracts. Chromatographic evaluation using HPLC-DAD further confirmed the occurrence of these metabolites and revealed particularly elevated levels of alizarin (265.7 ng/µL) and gallic acid (86.7 ng/µL). The abundance of these compounds suggests a strong antioxidant potential and an enhanced capacity to counteract reactive oxygen species. Previous studies have emphasized that phenolic metabolites contribute significantly to oxidative stress regulation while also exhibiting antimicrobial and anti-inflammatory activities that may support human health (Karadağ et al., 2024; Silva et al., 2003; Dhakad et al., 2018).

The replacement of synthetic preservatives and artificial antioxidants with plant-derived alternatives has become an important objective in modern product formulation. Owing to their high phenolic and flavonoid content, eucalyptus leaf extracts may provide multiple functional benefits in different industrial sectors. These benefits include protection against oxidative deterioration, inhibition of microbial growth, and mitigation of free-radical-mediated cellular damage associated with skin aging. Consequently, eucalyptus-derived bioactive compounds are increasingly considered promising candidates for incorporation into cosmetic products, food preservation systems, and health-promoting formulations (Aras & Karadağ, 2024; Bakkali et al., 2008; Draelos, 2019). Furthermore, compounds such as ascorbic acid and rutin are known to support collagen biosynthesis and skin regeneration processes, thereby enhancing the efficacy of dermocosmetic preparations.

The primary objective of the present study was to characterize the phenolic profile of eucalyptus leaf extract and to assess the potential significance of the identified compounds in terms of antioxidant functionality and industrial applicability. Figure 1 lists some keywords related to studies on eucalyptus (*Eucalyptus* spp.) in value-added cosmetic, health, and food products. These findings contribute to a better understanding of the potential use of eucalyptus as a natural source of active ingredients, functional additives, and preservatives. In addition, the results support the growing interest in eucalyptus biomass as a valuable renewable raw material for sustainable biotechnology, green chemistry applications, and the development of high-value natural products with economic and commercial relevance. Biological applications that have been and are planned to be carried out with the extracts and oils of the eucalyptus (*Eucalyptus* spp.) plant are clearly presented in Fig. 1 for the attention of researchers.

Chemical composition of eucalyptus plant

Eucalyptus (*Eucalyptus* spp.) is a medicinal and aromatic plant notable for its volatile oils and biologically active secondary metabolites, particularly those accumulated in its leaves. The volatile oil content varies between 0.5% and 3% depending on the species, climate, soil structure, harvest time, and distillation method (Dhakad et al., 2018). These oils generally consist of volatile components such as monoterpenes, sesquiterpenes, and phenolic compounds; polar compounds such as tannins, flavonoids, alkaloids, and phenolic acids also contribute to the composition (Batish et al., 2008; Brooker and Kleinig, 2006). Table 1 shows that eucalyptus (*Eucalyptus* spp.) is used as a value-added product ingredient across a wide range of applications from skin and hair care products to phytotherapeutic applications, and from natural flavorings to functional foods in the cosmetic, health, and food industries, thanks to its antiseptic, antimicrobial, anti-inflammatory, and antioxidant properties.

Major chemical constituents of eucalyptus

The biological and commercial value of eucalyptus is largely associated with the composition of its essential oil. Among the volatile constituents, 1,8-cineole (commonly referred to as eucalyptol) is recognized as the predominant compound, frequently accounting for approximately 60–85% of the total oil fraction depending on species and environmental conditions (Cox & Markham, 2007). This oxygenated monoterpene possesses a characteristic aromatic odor and has been extensively investigated for its pharmacological properties, including antimicrobial, anti-inflammatory, mucolytic, and analgesic activities (Juergens, 2014).

Besides *eucalyptol, eucalyptus* essential oils contain numerous terpenoid compounds that contribute to both fragrance characteristics and biological performance. These constituents include α-pinene, β-pinene, limonene, camphene, p-cymene, terpineol, globulol, and spathulenol, among others (Dorman & Deans, 2000). Such molecules play an important role in determining the overall bioactivity of the oil. In particular, α-pinene and limonene have attracted considerable attention due to their antioxidant and antimicrobial capabilities, making them promising candidates for incorporation into natural preservative systems used in pharmaceutical and cosmetic formulations (Aras et al., 2024; Bakkali et al., 2008).

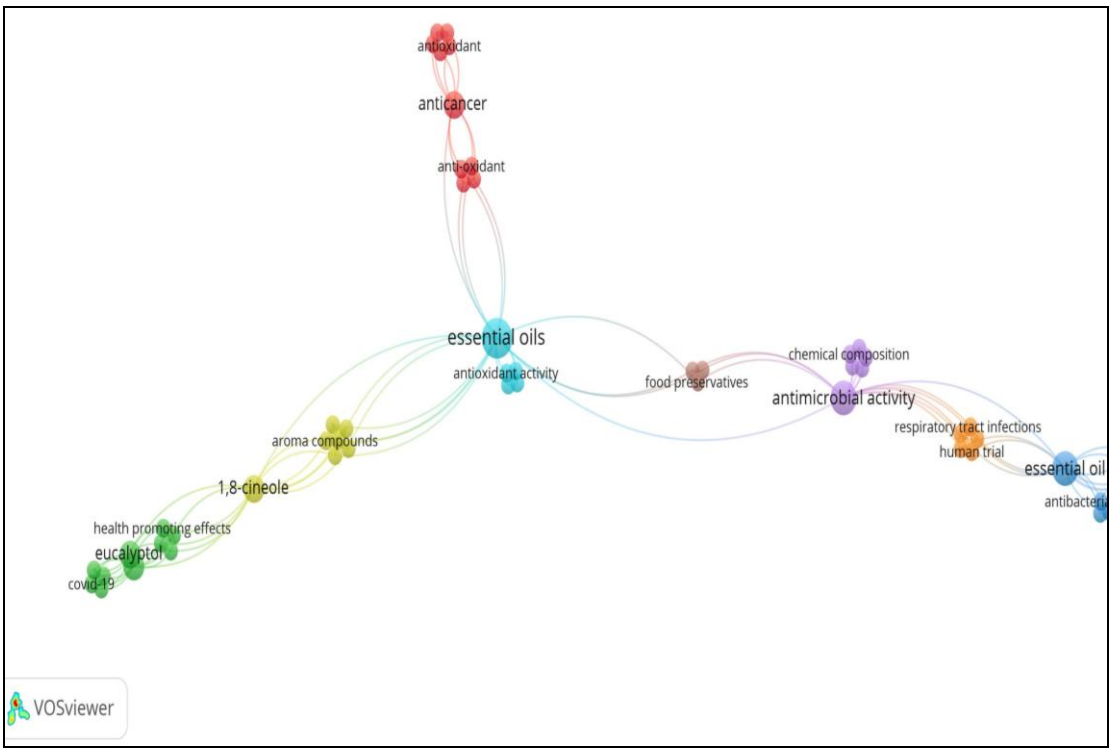

Fig. 1. Academic Studies on Eucalyptus (*Eucalyptus* spp.) (Web of Science database).

Table 1. Use of eucalyptus (*Eucalyptus* spp.) plant in value-added cosmetic, health and food products.

Sector	Application Area	Biological/Functional Effect	Formulation and Dosage Amount	References
Cosmetics	Skin care products	Antiseptic, anti-inflammatory, acne and pimple preventative	Creams, lotions, gels (0.5–2% eucalyptus oil or extract)	Juergens et al., 2003; Santos et al., 2017
	Hair care products	Anti-dandruff, scalp refreshing, antimicrobial	Shampoos, hair tonics (0.5–1.5% essential oil)	Santos et al., 2017
	Aromatherapy products	Relaxing, improves mental focus, provides a pleasant scent	Massage oils, perfumes, spa products (0.2–1% essential oil)	Esposito et al., 2016
Health	Natural preservatives & perfume agents	Antioxidant and microbial balancer	Cream, lotion and gel formulations	Juergens et al., 2003
	Phytotherapeutic applications	Expectorant, bronchodilator, anti-inflammatory, antimicrobial	Tea, inhalers, lozenges, ointments	Santos et al., 2017; Sadlon and Lamson, 2010
	Topical and aromatherapy	Wound healing, mental relaxation, antimicrobial	Massage oils, ointments, inhaler products	Esposito et al., 2016
Food	Natural flavorings	Enhances flavor and aroma in food and beverages	Tea, herbal extracts (0.1–0.5%)	Mehdizadeh et al., 2016
	Natural preservatives	Extends product shelf life with antimicrobial and antioxidant effects	Food supplements, functional foods	Santos et al., 2017
	Functional food and beverages	Provides antioxidant and metabolic support	Herbal beverages, tea blends	Sadlon and Lamson, 2010
	Food safety	Use in accordance with EFSA and FDA limits	Standardized extract and essential oil tests	Mehdizadeh et al., 2016

In addition to volatile terpenes, eucalyptus leaves are rich in non-volatile phytochemicals, including flavonoids, phenolic acids, and tannin derivatives. Representative flavonoids include quercetin, luteolin, and apigenin, whereas gallic acid and chlorogenic acid are among the most commonly reported phenolic acids. Tannins such as gallotannins and ellagitannins are also frequently detected (Silva et al., 2003). These compounds significantly contribute to antioxidant defense through free-radical neutralization and oxidative stress reduction. Moreover, flavonoid-rich extracts have gained increasing interest in dermocosmetic applications because of their photoprotective effects and their potential to support skin renewal processes (Draelos, 2019).

Extraction technologies and essential oil production

Steam distillation remains the most widely employed technique for the commercial production of eucalyptus essential oil. In this study, the

extraction of Eucalyptus plant extract and its phenolic content determination by HPLC are schematically shown in Fig. 2. During this process, volatile compounds are released from fresh or dried plant material through steam exposure and subsequently condensed to obtain the oil fraction (Lucchesi et al., 2004). Extraction efficiency and final oil composition are strongly influenced by operational variables such as processing duration, temperature, pressure, and moisture content of the leaves (Karadağ et al., 2024; Dhakad et al., 2018).

Recent technological developments have introduced alternative extraction approaches designed to improve yield and product quality. Techniques such as microwave-assisted extraction (MAE), supercritical carbon dioxide extraction ($SC\text{-}CO_2$), and ultrasound-assisted extraction (UAE) have become increasingly popular due to their reduced energy requirements, shorter extraction times, and enhanced preservation of heat-sensitive constituents (Chemat et al., 2017). Several studies have demonstrated that microwave-assisted processes may produce eucalyptus oils with elevated concentrations of 1,8-cineole compared with conventional distillation procedures (Koçak et al., 2021; Lucchesi et al., 2004).

Following extraction, essential oils are generally stored under controlled conditions to minimize oxidative degradation. Dark-colored glass containers and low-temperature environments are commonly preferred to preserve chemical stability during storage. Analytical quality assessment is typically performed using gas chromatography coupled with mass spectrometry (GC-MS), which provides detailed information regarding purity, component distribution, and compositional consistency (Karadağ et al., 2024; Silva et al., 2003).

Influence of species, geography, and environmental conditions on chemical composition

The phytochemical profile of eucalyptus essential oil is highly dynamic and can vary considerably according to botanical species, geographic location, climatic conditions, soil properties, and developmental stage of the plant (Dhakad et al., 2018; Batish et al., 2008). As a result, significant differences may be observed in both qualitative and quantitative composition among eucalyptus populations.

Distinct species are characterized by different dominant constituents. For instance, oils obtained from *Eucalyptus globulus* are generally characterized by high concentrations of 1,8-cineole, often representing between 60% and 85% of the total oil content. In contrast, *Eucalyptus citriodora* is primarily distinguished by its citronellal-rich profile, where citronellal may account for up to 90% of the volatile fraction (Oyedeji et al., 1999). Oils derived from *Eucalyptus camaldulensis* frequently exhibit elevated levels of p-cymene and α-terpineol compared with other species (Sefidkon et al., 2007).

Leaf maturity also contributes substantially to compositional variation. Younger leaves generally contain larger proportions of monoterpenes, whereas the accumulation of sesquiterpenes tends to increase as leaves age (Dorman & Deans, 2000). Environmental conditions further influence metabolite biosynthesis. Comparative investigations have shown that *Eucalyptus globulus* cultivated in Mediterranean regions may possess lower cineole concentrations than populations originating from Australia, indicating a strong geographical effect on secondary metabolite production (Silva et al., 2003).

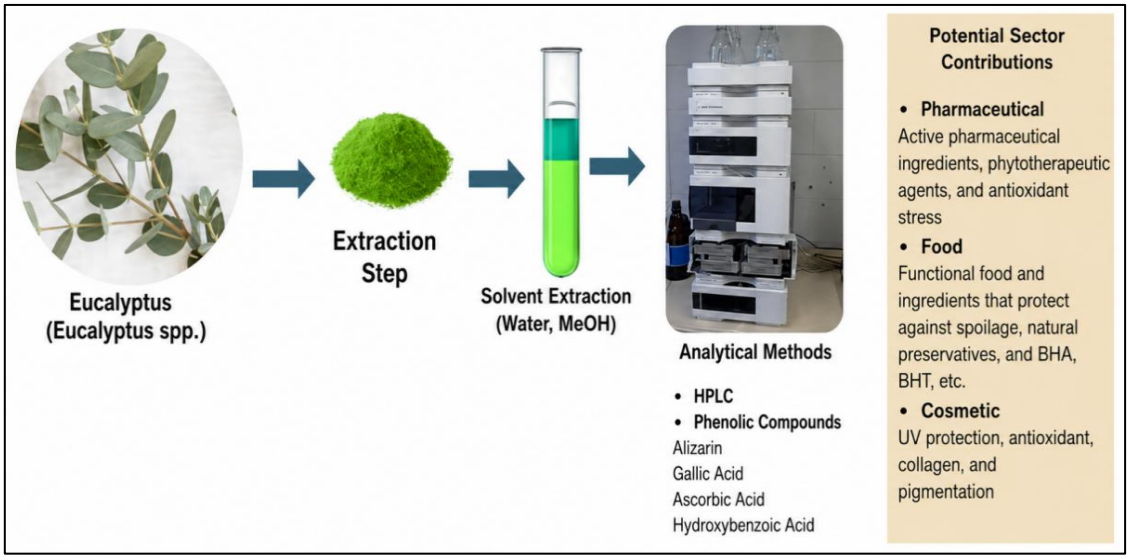

Fig. 2. Eucalyptus (*Eucalyptus* spp.) Workflow Diagram.

MATERIALS AND METHODS

Sample Collection and Extraction

The eucalyptus (*Eucalyptus* spp.) leaves used in this study were purchased, dried in the shade at room temperature, and then ground to a homogenous consistency. The extraction process was carried out by adding an 80% methanol: water (v/v) solution to 10 g of dry leaf sample. The mixture was extracted on a magnetic stirrer at room temperature for 24 hours. The filtered extracts were then concentrated by removing the solvent in a rotary evaporator at 40°C and stored at 4°C before analysis (Karadağ, 2025; Başar et al., 2024). The workflow diagram for the study is given in Fig. 3.

HPLC Analysis

An Agilent Technologies brand HPLC-DAD (Diode Array Detector) system was used to identify and quantify phenolic compounds. The analysis conditions are specified below: Chromatographic separation was performed on a C18 column with a length of 250 mm, an inner diameter of 4.6 mm, and a particle size of 5 µm. Two different solvents were used as the mobile phase: Mobile Phase A, water containing 0.1% phosphoric acid; and Mobile Phase C, 100% acetonitrile. During the analysis, the flow rate was set to 0.8 mL/min, the column temperature to 30°C, and the injection volume to 10 µL. DAD was used as the detector; analyses were performed at 300 nm and 200 nm wavelengths, with a reference range of 500/100 nm (Karadağ, 2025). Calibration was performed using 20 standard phenolic compounds (ascorbic acid, gallic acid, hydroxybenzoic acid, vanillic acid, p-coumaric acid, rutin, naringin, neohesperidin, quercetin, hesperidin, resveratrol, etc.). Calibration curves were generated using the external standard method, and the amounts of the compounds were calculated in ng/µL. Figure 2 shows that phenolic-rich extracts from eucalyptus (*Eucalyptus* spp*.)* are obtained through extraction and analytical characterization processes, and that these extracts can be utilized as antioxidants, preservatives, and functional ingredients in the pharmaceutical, food, and cosmetic industries.

RESULTS AND FINDINGS

The chromatographic evaluation performed using the HPLC-DAD system demonstrated that eucalyptus (*Eucalyptus spp.*) leaf extract contains a diverse spectrum of phenolic constituents. Approximately twenty individual phenolic compounds were identified, indicating a complex phytochemical composition and a substantial reservoir of antioxidant molecules. The concentrations of the detected compounds are summarized in Table 2.

Among all quantified constituents, alizarin was determined to be the predominant compound, reaching a concentration of 265.72 ng/µL. This anthraquinone-derived metabolite is recognized for its remarkable radical-scavenging capacity and its ability to protect biological systems against oxidative damage. Previous studies have reported that alizarin may contribute to the reduction of inflammation-related cellular injury by limiting oxidative stress and stabilizing cellular functions (Yoon et al., 2020). The elevated concentration observed in the present analysis suggests that alizarin may play a major role in the antioxidant effectiveness of eucalyptus leaf extract.

Gallic acid was identified as the second most abundant phenolic compound, with a measured concentration of 86.73 ng/µL. Owing to its well-documented antioxidant and antimicrobial activities, gallic acid is frequently associated with protection against oxidative deterioration and microbial contamination. The considerable amount detected in the extract highlights its potential value for applications related to food preservation and dermocosmetic formulations. Furthermore, the polyhydroxylated structure of gallic acid enables efficient inhibition of lipid oxidation processes, thereby contributing to cellular redox homeostasis (Mokhtari et al., 2021).

Several additional phenolic constituents were detected at intermediate concentrations. Ascorbic acid was quantified at 22.25 ng/µL, while hydroxybenzoic acid reached 19.67 ng/µL. Ascorbic acid is widely recognized as an essential antioxidant involved in collagen biosynthesis and tissue repair, making it particularly relevant for cosmetic and dermatological applications. Hydroxybenzoic acid, on the other hand, is known for its antimicrobial effectiveness and has attracted interest as a naturally derived preservative component.

The analysis also revealed the presence of various flavonoid and polyphenolic compounds in lower concentrations. These included rutin (6.33 ng/µL), hesperidin (2.72 ng/µL), naringin (2.26 ng/µL), resveratrol (2.15 ng/µL), and quercetin (1.28 ng/µL). Although present at comparatively lower levels, these metabolites are known to exert significant biological effects. Their combined action may contribute to the overall antioxidant performance of the extract through synergistic interactions among different phenolic molecules. In particular, resveratrol and quercetin have been extensively studied because of their protective roles against oxidative aging processes and their beneficial effects on cardiovascular health (Li et al., 2020).

Based on the quantitative data obtained from chromatographic measurements, the cumulative phenolic content of the eucalyptus leaf extract was estimated to be 417.76 ng/µL. This relatively high value confirms that eucalyptus leaves constitute a rich source of naturally occurring phenolic substances. The abundance and diversity of these compounds provide strong evidence for the considerable antioxidant potential of the extract.

Overall, the findings indicate that eucalyptus leaf extract represents a promising natural source of bioactive compounds with potential applications in multiple industrial sectors. The predominance of alizarin and gallic acid, together with the presence of numerous supporting phenolic constituents, suggests that the extract may be useful as a natural antioxidant ingredient in cosmetic, nutraceutical, pharmaceutical, and food-related formulations (Başar et al., 2024). Moreover, the broad diversity of identified phytochemicals supports the view that eucalyptus possesses multifunctional biological properties and considerable potential for the development of value-added natural products.

Application potential and ındustrial relevance

The phytochemical composition of eucalyptus (*Eucalyptus spp.*) leaves suggests that this plant may serve as a valuable natural resource for multiple industrial sectors. Quantitative HPLC-DAD analysis revealed substantial concentrations of bioactive constituents, particularly alizarin, gallic acid, ascorbic acid, and hydroxybenzoic acid (Karadağ et al., 2024). Because these compounds possess diverse biological functions, eucalyptus-derived extracts have attracted increasing attention as functional ingredients in products designed for health, cosmetic, and food-related applications (Zhang et al., 2023). The combination of antioxidant, antimicrobial, and protective activities enhances the commercial attractiveness of this botanical resource and supports its integration into sustainable product development strategies.

Table 2. Phenolic compounds studied.

No	Compound	Retention Time (min)	Amount (ng/µL)	Chemical Class	Biological Activity	Potential Uses
1	Alizarin	38.64	265.72	Anthraquinone Derivative	Powerful Antioxidant, Anticancer, Anti-inflammatory	Health products, anti-aging cosmetic formulations
2	Gallic Acid	4.27	86.73	Phenolic Acid	Antioxidant, Antimicrobial, Anti-inflammatory	Food preservatives, skin care products
3	Ascorbic Acid (Vitamin C)	3.31	22.25	Vitamin (Ascorbate Derivative)	Antioxidant, Collagen Synthesis Supporter	Skin rejuvenating cosmetics, food supplements
4	Hydroxybenzoic Acid	7.88	19.67	Phenolic Acid	Antimicrobial, Antioxidant	Cosmetic preservatives, natural antimicrobial agents
5	Rutin	18.88	6.33	Flavonoid Glycoside	Capillary Protector, Anti-inflammatory	Vascular strengthening drugs and cosmetic products
6	Neohesperidin	29.74	3.93	Flavonoid Glycoside	Antioxidant, Taste Regulator	Functional beverages, pharmaceutical formulations
7	Hesperidin	36.81	2.72	Flavonoid	Anti-inflammatory, UV Protector	Sunscreen products, anti-aging formulas
8	Resveratrol	32.40	2.15	Stilbene Derivative	Antioxidant, Cardioprotective, Anti-aging	Skin care products, food supplements
9	Naringin	26.95	2.26	Flavonoid	Lipid Lowering, Antioxidant	Functional foods, cosmetic products
10	Quercetin	35.06	1.28	Flavonol	Antioxidant, Antiallergic, Anticancer	Cosmetic serums, supplements
11	*p*-coumaric Acid	17.25	1.96	Hydroxycinnamic Acid	Antioxidant, UV Absorber	Food preservatives, natural sun filters
12	Vanilic Acid	10.24	1.27	Phenolic Acid	Antimicrobial, Flavoring	Food flavoring, pharmaceutical formulation
13	Flavon	40.45	0.37	Flavonoid	Antioxidant, Pigment Regulator	Cosmetic coloring, biotechnological studies

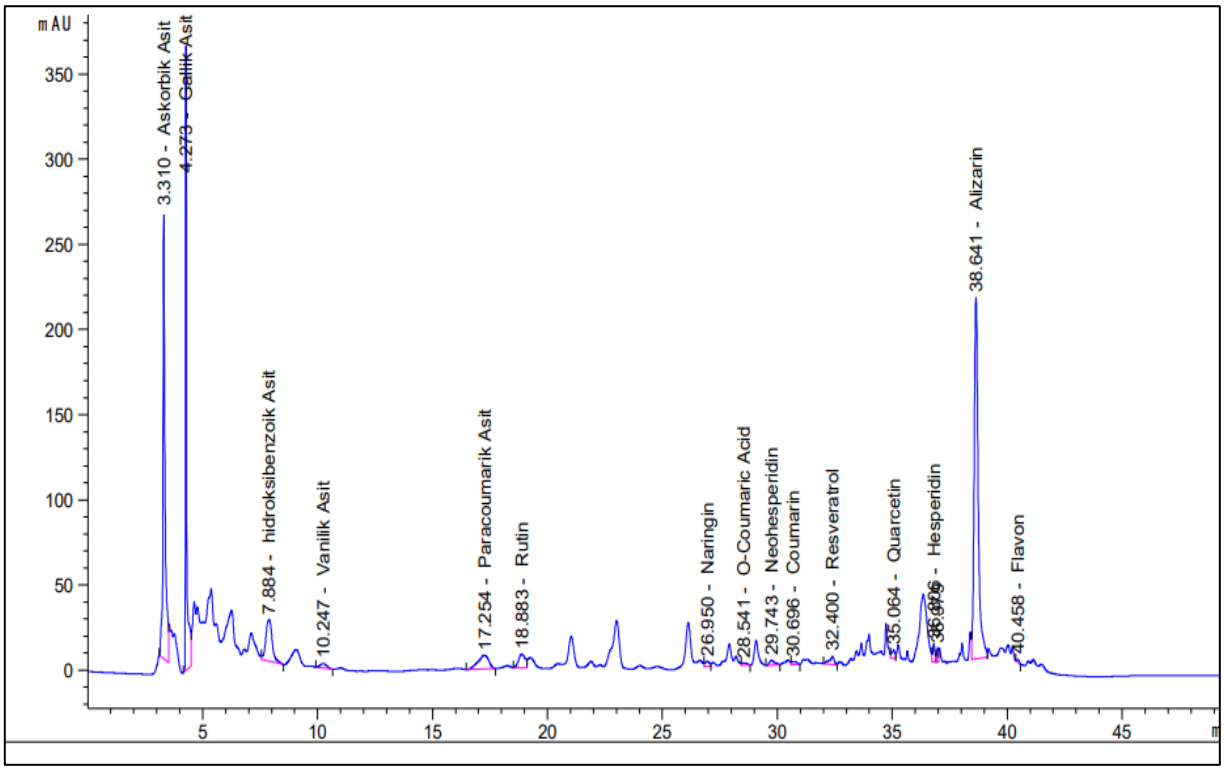

Fig. 3. HPLC Phenolic Chromatogram of Eucalyptus Plant.

Relevance to healthcare and pharmaceutical applications

The bioactive profile of eucalyptus extract indicates considerable potential for pharmaceutical and nutraceutical utilization. Phenolic constituents are known to contribute to the mitigation of oxidative damage through their capacity to neutralize reactive oxygen species and regulate inflammatory pathways (Karadağ et al., 2021). High concentrations of alizarin and gallic acid may provide protective effects against cellular deterioration associated with chronic oxidative stress. Such mechanisms are frequently linked to disorders including cardiovascular diseases, diabetes mellitus, and neurodegenerative conditions. Furthermore, the presence of ascorbic acid may enhance immune function and support tissue regeneration processes, increasing the potential value of eucalyptus-derived products in health-supporting formulations.

Opportunities in cosmetic formulations

Natural antioxidants have become increasingly important ingredients in modern cosmetic products due to consumer demand for safer and plant-based formulations. The phenolic compounds identified in eucalyptus extract, including gallic acid, rutin, hesperidin, and quercetin, are recognized for their ability to protect skin tissues against oxidative stress and environmental damage. These compounds may help reduce the detrimental effects of ultraviolet radiation, support collagen production, and contribute to maintaining skin integrity and appearance. Consequently, eucalyptus extracts may be incorporated into anti-aging creams, antioxidant serums, photoprotective products, and skin-care formulations. In addition, the aromatic characteristics of eucalyptus essential oil can provide sensory and aromatherapeutic benefits when combined with phenolic-rich extracts.

Potential uses in the food industry

From a food technology perspective, eucalyptus-derived phenolic compounds may function as natural alternatives to synthetic preservatives and antioxidants. Oxidative degradation is one of the major causes of quality loss in food systems, and phenolic compounds can delay these reactions by scavenging free radicals and inhibiting lipid oxidation. As a result, eucalyptus extracts may contribute to prolonged shelf life and improved product stability. Their antimicrobial properties may further assist in controlling spoilage microorganisms in food products such as meat, dairy products, and functional beverages. The incorporation of natural plant-based preservatives aligns with current consumer preferences for clean-label products while simultaneously enhancing food safety and nutritional preservation (Karadağ & Doğan, 2024).

Economic significance and industrial perspectives

The abundance of biologically active phenolic compounds in eucalyptus leaves presents important economic opportunities for the development of value-added products. The utilization of locally available botanical resources may reduce dependence on imported synthetic additives and promote domestic production capacity. Advances in extraction, purification, and standardization technologies further increase the feasibility of producing high-quality eucalyptus-derived ingredients suitable for industrial applications. In addition, the integration of eucalyptus biomass into biotechnology and green chemistry initiatives may contribute to sustainable manufacturing systems and environmentally responsible production practices (Karadağ et al., 2025).

Overall, the results demonstrate that eucalyptus leaf extract possesses considerable potential as a multifunctional natural ingredient. Its antioxidant-rich composition and broad biological activity profile support applications in healthcare, cosmetics, food preservation, and sustainable biotechnology. Consequently, the valorization of eucalyptus resources may generate both economic benefits and scientific opportunities while promoting environmentally conscious production approaches.

DISCUSSION

The present investigation employed HPLC-DAD analysis to characterize the phenolic composition of eucalyptus (*Eucalyptus spp.*) leaf extract and revealed a substantial abundance of bioactive constituents. The analytical results confirmed that alizarin and gallic acid were the dominant phenolic compounds within the extract. These findings are consistent with previous reports describing eucalyptus species as important reservoirs of phenolic metabolites with notable biological activity (Dhakad et al., 2018; Silva et al., 2003).

Phenolic compounds are widely recognized as plant-derived secondary metabolites involved in defense responses against environmental stressors. Beyond their ecological functions, these molecules have attracted considerable attention because of their antioxidant, antimicrobial, anti-inflammatory, and potential anticancer properties. The remarkably high concentration of alizarin observed in the current study may represent one of the principal factors responsible for the biological effectiveness of eucalyptus extract. Earlier investigations have demonstrated that alizarin can reduce oxidative injury by scavenging reactive species and protecting cellular structures from molecular damage, including DNA degradation (Yoon et al., 2020). Consequently, the abundance of this compound reinforces the potential application of eucalyptus as a natural antioxidant source.

Gallic acid was identified as the second most abundant phenolic constituent. This compound has been extensively documented for its antimicrobial activity and its ability to suppress lipid peroxidation processes. Compared with concentrations reported for numerous other medicinal and aromatic plants, the gallic acid level measured in this study is relatively high (Mokhtari et al., 2021). Such findings suggest that eucalyptus leaves may represent an attractive raw material for the development of natural preservative systems and functional bioactive ingredients.

Moderate concentrations of ascorbic acid and hydroxybenzoic acid were also detected. These compounds contribute significantly to the overall antioxidant potential of the extract. Ascorbic acid functions as a key participant in cellular redox regulation and is widely utilized in cosmetic products because of its role in collagen biosynthesis and skin repair mechanisms (Suh et al., 2019). Hydroxybenzoic acid, meanwhile, possesses antimicrobial characteristics that may enhance the preservative capacity of plant-derived formulations.

Although flavonoids such as rutin, hesperidin, quercetin, and resveratrol were present at comparatively lower concentrations, their contribution should not be underestimated. Numerous studies have demonstrated that interactions among different phenolic compounds can produce synergistic effects, leading to enhanced antioxidant performance beyond the activity of individual constituents. Resveratrol and quercetin, in particular, are frequently associated with anti-aging activity, cellular protection, and cardiovascular health benefits (Li et al., 2020).

The total phenolic concentration calculated for the eucalyptus extract reached 417.76 ng/µL, confirming the plant as a rich source of naturally occurring phenolic substances. Previous studies involving different *Eucalyptus* species have reported substantial variability in phenolic content, largely influenced by environmental conditions, genetic background, cultivation region, and extraction methodology (Kumar et al., 2012; Bakkali et al., 2008). Therefore, the relatively high phenolic concentration observed in the present work may also reflect the effectiveness of the extraction and analytical procedures employed.

Taken together, the results demonstrate that eucalyptus leaf extract contains a diverse and abundant phenolic profile capable of providing strong antioxidant functionality. The predominance

of alizarin and gallic acid, combined with the presence of additional bioactive compounds, highlights the potential of eucalyptus as a natural source of antioxidants, antimicrobial agents, and functional ingredients. These findings support the growing interest in utilizing plant-derived resources within sustainable biotechnology, green chemistry initiatives, and environmentally responsible industrial production systems.

CONCLUSIONS AND FUTURE PERSPECTIVES

The present study investigated the phenolic composition of eucalyptus (*Eucalyptus spp.*) leaf extract through HPLC-DAD analysis and demonstrated that the extract contains a diverse range of bioactive phytochemicals. Quantitative evaluation revealed that alizarin and gallic acid were the predominant phenolic constituents, reaching concentrations of 265.72 ng/µL and 86.73 ng/µL, respectively. In addition to these major compounds, several other phenolic substances, including ascorbic acid, hydroxybenzoic acid, rutin, hesperidin, quercetin, and resveratrol, were identified and contributed collectively to the antioxidant profile of the extract.

The overall results confirm that eucalyptus leaves represent a rich source of naturally occurring phenolic compounds with considerable biological activity. The abundance of antioxidant molecules suggests that eucalyptus-derived extracts may be utilized in a variety of industrial applications where protection against oxidative degradation is required. The identified phytochemicals possess properties that may support product stability, cellular protection, and functional performance in formulations intended for food, pharmaceutical, and cosmetic purposes.

Particularly noteworthy is the high abundance of alizarin and gallic acid, which are recognized for their strong antioxidant and protective characteristics. These compounds may contribute to the mitigation of oxidative stress, enhancement of skin-care formulations, and extension of shelf life in oxidation-sensitive products. Consequently, eucalyptus extract emerges as a promising candidate for the development of natural alternatives to synthetic preservatives and antioxidant additives.

From an economic and environmental perspective, the utilization of eucalyptus biomass may create additional value through the transformation of renewable plant resources into commercially relevant products. Considering the widespread cultivation and availability of eucalyptus species in Türkiye, the plant may serve as an important domestic source of phenolic compounds for sustainable industrial production. Increased exploitation of locally available botanical resources could support environmentally responsible manufacturing practices while reducing reliance on imported synthetic ingredients.

Recommendations for future research

- Advanced extraction technologies such as ultrasound-assisted extraction, microwave-assisted extraction, and supercritical carbon dioxide extraction should be investigated to optimize phenolic recovery and improve extraction efficiency.
- The biological properties of the identified compounds should be evaluated through comprehensive in vitro and in vivo studies to further validate their antioxidant, antimicrobial, anti-inflammatory, and potential therapeutic activities.
- Additional research should focus on the formulation and stabilization of eucalyptus-derived extracts for incorporation into cosmetic products, including creams, serums, lotions, and photoprotective preparations.
- The suitability of eucalyptus phenolic extracts as functional ingredients or natural preservatives should be assessed in different food matrices under real storage conditions.
- Comparative investigations involving multiple *Eucalyptus* species and different cultivation regions are recommended to better understand the influence of genetic and environmental factors on phenolic composition.
- The phenolic profile data generated in this study may serve as a reference source for future projects involving natural antioxidant production, green chemistry technologies, and sustainable biotechnology applications.

In summary, eucalyptus leaves constitute a valuable reservoir of phenolic compounds with substantial antioxidant potential. Their multifunctional biological properties and broad industrial applicability support their consideration as a natural, cost-effective, and environmentally sustainable alternative for use in biotechnology, cosmetics, pharmaceuticals, and food-related industries.

ACKNOWLEDGEMENTS

The authors would like to thank all individuals and institutions that provided support or insights during the preparation of this study.

ETHICAL CONSIDERATIONS

This study complies with internationally accepted research ethics standards. No human participants, personal data, or confidential information were involved, or all ethical approvals were obtained where required.

AUTHOR CONTRIBUTIONS

All authors contributed significantly to the conception, design, analysis, and writing of this manuscript. All authors have read and approved the final version and agree to be accountable for the content of the work.

FUNDING

This research did not receive any specific grant from funding agencies in the public, commercial, or not-for-profit sectors.

CONFLICT OF INTEREST

The authors declare no conflict of interest related to this study.

REFERENCES

Aras A., Karadağ, M. (2024) Analysis of secondary metabolite contents of some plants by HPLC. *Journal of Agriculture*, **7(2):** 157-167.

Bakkali F., Averbeck S., Averbeck D., Idaomar M. (2008) Biological effects of essential oils – A review. *Food and Chemical Toxicology*, **46(2):** 446–475.

Başar Y., Gül F., Karadağ M., Alma M.H., Demirtas İ., Tel A.Z. (2024) Determination of the volatile, phenolic and fatty acid contents of Helichrysum plicatum by chromatographic methods. *Turkish Journal of Biodiversity*, **7(2):** 83-94.

Dhakad A.K., Pandey V.V., Beg S., Rawat J.M., Singh A. (2018) Biological, medicinal and toxicological significance of Eucalyptus leaf essential oil: A review. *Journal of the Science of Food and Agriculture*, **98(3):** 833–848.

Draelos Z.D. (2019) The science behind skin care: Moisturizers. *Journal of Cosmetic Dermatology*, **18(4):** 1136–1141.

Ekor M. (2014) The growing use of herbal medicines: Issues relating to adverse reactions and challenges in monitoring safety. *Frontiers in Pharmacology*, **4:** 177.

FAO (2021) The State of the World's Forests 2020: Forests, biodiversity and people. Food and Agriculture Organization of the United Nations.

Karadag M., Doğan S. (2024) Mask for moisturizing skin and body made from cold-pressed paste of peanuts (*Arachis hypogaea* L.). *Adv. Biol. Earth Sci.*, **9(1):** 155-160.

Karadağ M., Omarova S. (2024) Use of *Prunus armeniaca* L. seed oil and pulp in health and cosmetic products. *Adv. Biol. Earth Sci*., **9(1):** 105-110.

Karadag M., Baran A., Güneş Z. (2024) Production of value-added cosmetic products from cold-pressed *Helianthus annuus* L. oil and pulp. *Advances in Biology & Earth Sciences*, **9:** 35-39.

Karadağ M. (2025) Phenolic compound profile of *Mentha arvensis* L. (wild peppermint) samples. *Turkish Journal of Technical Sciences and Innovation*, **1(1):** 12-23.

Karadağ M., Güneş Z., Çelik S. (2025) Chemical composition of essential oil obtained from rosemary (*Rosmarinus officinalis* L.) growing in Iğdır and its use in cosmetics. *Journal of Agriculture*, **8(1):** 53-64.

Karadağ M., Koyuncu M., Atalar M.N., Aras A. (2021) SPME/GC-MS analysis of *Artemisia campestris* subsp. *glutinosa*, *Lavandula angustifolia* Mill., and *Zingiber officinale* volatiles. *Erzincan University Journal of Science Institute*, **14:** 41-49.

Koçak M.Z., Karadağ M., Çelikcan F. (2021) Essential oil composition of Salvia officinalis and *Rosmarinus officinalis*. *Journal of Agriculture*, **4(1):** 39-47.

Kumar A., Ilavarasan R., Jayachandran T., Decaraman M., Aravindhan P., Padmanabhan N., Krishnan M.R.V. (2012) Phytochemical investigation on a tropical plant Eucalyptus globulus (L.). *Int. Journal of Pharmaceutical Sciences Reviews and Research*, **6(2):** 42–45.

Li Y., Yao J., Han C., Yang J., Chaudhry M.T., Wang S., Liu H., Yin Y. (2020) Quercetin, inflammation and immunity. *Nutrients*, **8(3):** 167.

Mokhtari Z., Baluchnejadmojarad T., Roghani M. (2021) Neuroprotective effect of gallic acid in a rat model of diabetic neuropathy: Involvement of oxidative stress and inflammation. *Iranian Journal of Basic Medical Sciences*, **24(2):** 180–187.

Silva J., Abebe W., Sousa S.M., Duarte V.G., Machado M.I., Matos F.J. (2003) Analgesic and anti-inflammatory effects of essential oils of Eucalyptus. *Journal of Ethnopharmacology*, **89(2–3):** 277–283.

Suh D.H., Lee S., Heo J. (2019) Ascorbic acid and its antioxidant function in plants. *Antioxidants*, **8(6):** 180.

Yoon S., Park Y., Kim S. (2020). Antioxidant and anti-inflammatory properties of alizarin isolated from *Rubia cordifolia*. *Pharmaceutical Biology,* **58(1):** 715–722.

Zhang N., Baran A., Valioglu F., Teng L., Atalar M.N., Keskin C., ... Beilerli A. (2023) Antioxidant, AChE inhibitory, and anticancer effects of *Verbascum thapsus* extract. *Cellular and Molecular Biology*, **69(14):** 211-216.

ORCIDs:
Musa Karadağ: https://orcid.org/0000-0003-2498-3403
Kadir Sinan Aslan: https://orcid.org/0000-0003-4564-1285
Zübeyir Güneş: https://orcid.org/0000-0002-9170-7006
Halil İbrahim Ünsal: https://orcid.org/0009-0006-6791-3754
Necmettin Aktepe: https://orcid.org/0000-0003-2192-9049
Beşir Dağ: https://orcid.org/0000-0002-5208-3552

MINISTRY OF SCIENCE AND EDUCATION REPUBLIC OF AZERBAIJAN

TRANSACTIONS

OF THE INSTITUTE OF MOLECULAR BIOLOGY & BIOTECHNOLOGIES

PUBLISHER: INSTITUTE OF MOLECULAR BIOLOGY

Volume X, No 1 2026

CONTENT

Ministry of Science and Education
of the Republic of Azerbaijan
Institute of Molecular Biology

11 Izzat Nabiyev Str.,
AZ1073, Baku, Azerbaijan
Tel: +994 12 538 1164
Fax: +994 12 510 2433
E-mail: imbb@science.az
www.timbb.az